Gas Phase Formation and Photodissociation Spectroscopy of Mass Selected Nitrogen and Oxygen Substituted Carbon Clusters

IM FACHBEREICH PHYSIK
DER FREIE UNIVERSITÄT BERLIN
EINGEREICHTE DISSERTATION ZU ERLANGUNG DER GRADES
EINES DOKTORS DER NATURWISSENSCHAFTEN

Von
Matthieu Lalanne

Berlin, July 2015

Hiermit erkläre ich, dass ich vorgelegte Dissertation selbst verfasst und mich dabei keiner anderen als der von die bezeichneten Quellen bedient habe. Weiterhin erkläre ich hiermit, dass ich an keiner anderen Stelle ein Prüfungsverfahren beantragt bzw. die Dissertation in dieser einer anderen Form bereits anderweitig als Prüfungsarbeit verwendet oder einer anderen Fakultät als Dissertation vorgelegt habe.

Berlin den,

. . . . . .
Unterschrift

DISPUTATION: 10.11.2015

Erstgutachter: Prof. Drs. Ludger Wöste
Zweitgutachter: Priv.-Doz. Dr. Albrecht Lindinger

Contents

Abbreviation x

Introduction **1**
1. Panspermia and exogenous theories 1
2. Anions and amino acids in interstellar medium 3
3. Synthesis in quasi interstellar conditions: Carbon Sputtering 4
Outline of the thesis 7

1. Theoretical basis **9**
1.1. Cluster formation in sputtering process 9
1.1.1 Sputtering process 9
1.1.2 Clusters' formation 12
1.1.3 Clusters' growth 13
1.2. IR vibration spectroscopy 18
1.2.1 Classical approach 19
1.2.2 Quantum approach 20
1.2.3 Vibrations modes 23
1.2.4 Infrared photodissociation 24
1.3. Theoretical Calculations 26
1.3.1 *Ab initio* method 26
1.3.2 DFT methods 27
1.3.3 Basis set 28

2. Experimental setup **31**
2.1. The magnetron sputter source 31
2.2. Mass selection and trapping 37
2.3. Laser system 43

3. Ions production and mass spectra **45**
3.1. Ions production 45
3.1.1 Non-linear gas pressure dependency 45
3.1.2 Time evolution of the charged sputter yield 46
3.2. Comparison between the sputter process with O_2 and N_2 47
3.3. Mass spectra by sputtering in the presence of N_2 49
3.3.1 Negatively charged ions 49
3.3.2 Odd/ even effect in the $C_xN_y^-$ anions 51
3.3.3 Anions with the oddmasses 54
3.4. Mass spectra by sputtering in the presence of O_2 55
3.4.1 Negatively charged ions 55
3.4.2 Positively charged ions 58
3.5. Conclusion 59

4. Dicyanocarbanions $C_xN_2^-$ **61**
4.1. IRPD spectra of $C_xN_2^-$ 62
4.2. Vibrational pattern 64
4.3. Review of the different $C_xN_2^-$ 65
CN_2^- 65
$C_3N_2^-$ 65
$C_4N_2^-$ 66
$C_5N_2^-$ 66
$C_6N_2^-$ 68
$C_7N_2^-$ 68
$C_8N_2^-$ 69
$C_9N_2^-$ 69
$C_{10}N_2^-$ 69
$C_{11}N_2^-$ 69
4.4. Conclusion 70

5. Tetracyanocarbanions $C_xN_4^-$ **71**
5.1. IRPD spectra of $C_xN_4^-$ 72
5.2. Nitrile, imine carbene/carbyne vibrations pattern 73
5.3. Geometries shared by the $C_xN_4^-$ 75
5.4. Review of the different $C_xN_4^-$ 76
$C_3N_4^-$ 76
$C_4N_4^-$ 76
$C_6N_4^-$ 77
$C_8N_4^-$ 78
$C_{10}N_4^-$ 79
5.5 Conclusion 80

6. Carbanions C_x^- **81**
6.1. IRPD spectra of C_x^- 82
6.2. Parity discrepancy in the structure of C_x^- 84
6.3. Absorption band characteristics 85
Matrix shift 87
Particular sensitivity of the IRPD method 88
6.4. Identification of C_{11}^- 88
6.5. Conclusion 89

7. Oxocarbanions C_xO^- and $C_xO_2^-$ **91**
7.1. IRPD spectra of C_xO^- 92
7.2. Bands intensity 95
7.3. IRPD spectra of $C_xO_2^-$ 96
7.4. Conclusion 97

8. Masses of 75, 89 and 115 amu **96**
8.1. The masss 75 99
8.2. The mass 89 102
8.2.1 IRPD spectra with N_2 103
8.2.2 IRPD spectra with O_2 106
8.3. The mass 115 108
8.4. Conclusion 111

9. NCO^- and NC_3O^- **112**
9.1. IRPD spectra of NCO^- and NC_3O^- 113
9.2. Cyanate CNO- and linear C_3NO^- 114
CNO^- 114
C_3NO^- 112
9.3. Dicussion fort he absorption band at 2178 cm^{-1} 115
9.4. Predicted hydogenized form of NCO^- and NC_3O^- 117
9.5. Conclusion 120

Annex: Amino acids embedded in Helium droplets **121**
L-glycine 122
L-valine 124
Lvaline and L-tryptophan 125
L-histidine and Ltryptophan 128
Conclusion 131

Summary **133**
Future perspectives 135

References 138

Appendix 153

Abreviations:

aug-ccpVTZ augmented correlation consistent polarized Valence Triple Zeta

CID Collision Induced Dissociation

DFT Density Functional Theory

DC Direct Current

FTIR Fourier Transformation Infra-Red

Gly Glycine

HF Hartree Fock

His Histidine

HV High Voltage

IR Infra-Red

IM Interstellar Medium

IRMPD Infra Red Multi Photon Dissociation

IVR Internal Vibrational Redistribution

IRPD Infrared Photo Dissociation

LDA Locale Density Approximation

OPA Optical Parametric Amplifier

OPO Optical Parametric Oscillator

QMS Quadropole Mass Spectrometer

TOF Time Of Flight spectrometer

RET Ring Electrode Trap

RF Radio Frequency

TCNE Tetracyanoethylene

Trp Tryptophan

UV Ultra-Violet

Val Valine

Introduction

Space remains an essentially unexplored environment. The tiny fraction of its enigmatic essence that it has yet unveiled fascinates and captivates us. Its extreme dimensions and conditions demand of the physicist ever more astute methods to gather knowledge to shed light upon the darkness beyond earth. Space is not empty, but its constituents as well as its chemistry remain essentially unknown to us. The goal to comprehend space on a molecular level has inspired this work. This dissertation presents synthesis and identifications of molecules in conditions approaching those of the interstellar medium. The spectroscopic identifications of anions carried out in this work deliver valuable information in the quest for the identification of interstellar molecules. The experimental synthesis of molecules in gas phase, here observed, is translatable to hypotheses about the interstellar medium and its chemistry. This work contributes to an ongoing investigation into the chemistry of formation of amino acids, which has a wide scientific relevance within and beyond physics.

1-Panspermia and exogenous theories

In 2006, NASA's spacecraft Stardust returned gases and particles captured from the Comet *Wild 2*. Extracted from the foils of the spacecraft, the samples revealed the presence of glycine, and α-alanine [1]. This represented the first observation of amino acids residing on a comet, although a variety of extraterrestrial amino acids were found many times on meteorites. Some meteorites as old as the solar system, the chondrites, are particularly rich in carbon and entail diverse organic compounds such as amino acids [2]. The meteorite of Murchison, which crashed in 1969 in Australia, contained more than 70 amino acids. Of those 70, there were 8 that correspond with those involved in the biochemistry of life, such as alanine, glycine and serine [3]. The discovery of amino acids incited a resurgence of interest in exogenous theories defending the extraterrestrial origin of pre-biotic molecules.

Already in the nineteenth century, theories which oriented the origin of the life in the universe found scientific support. The hypothesis that life exists throughout the universe was then defined as panspermia, a term borrowed from the Greek philosopher Anaxagoras in reference to his consideration of the related origin of nature and the cosmos [4]. In 1863, Pasteur's experiment showed that even blood in aseptic conditions remains free from bacteria, and brought the discussion about spontaneous generation to a close [5]. The spontaneous generation theories were then completely discredited, also as an explanation of the birth of life. Pasteur's conclusion that living organisms come only from living organisms (biogenesis) paved the way for theories arguing an extraterrestrial origin of life.

However, in 1952 the Miller-Urey experiment showed the synthesis of amino acids in a "primitive soup [6]." This soup [composed of the gaseous methane (CH_4) ammoniac (NH_3) water (H_2O) and hydrogen (H_2)] resembled the primitive atmosphere. The electric discharges applied to it may repel atmospheric lightening. Glycine and alanine were among the most abundantly organic molecules produced through this effort. Miller postulates a formation of amino acids from aldehyde (R-CHO), ammoniac (NH_3), and hydrogen cyanide (HCN) [7], known as the Strecker reaction. With different strong sources of energy, this experiment was reproduced many times in order to simulate, for example, cosmic radiation [8], UV (Ultra Violet) irradiation [9] or volcanism [10]. From the many attempts to simulate the primitive atmosphere and its chemistry it has been shown that a *sine qua non*-condition of organic molecule production remains the reductive property of the atmosphere. Recent geologic findings suggest that the primitive atmosphere was already non-reductive [11], arguing against the atmospheric origin of the amino acids.

With the evidence of the presence of organic molecules in space, soft panspermia theories emerged, which argued that pre-biotic molecules originate from space. These theories upheld that the extraterrestrial pre-biotic molecules were distributed on earth when life began (abiogenesis). Recent studies investigated the isotopic ratio of chlorine in oceanic dorsal in order to find evidence of the formation of the ocean [12]. It was concluded that most of the water on Earth has an extraterrestrial origin. Pre-biotic molecules such as amino acids may have arrived on earth within this water.Very recently the European mission Rosetta reported a high deuterium /hydrogen ratio in the water of the Jupiter family comet Churyumov-Geramienko [13]. This discovery precludes the idea that all the water of earth's ocean originates entirely within Jupiter family objects. Further attempts of the Rosetta mission will be focused on the presence of organic compound within the comet's water. The panspermia theories also find resonance in biology. One focus of synthetic biology is to observe the capacity of life to integrate exogenous constituents. In 2010 Venter et al. reported the creation of cells controlled by a chemically synthetized genome [14]. The created "mycoplasma mycoid", which is a half synthetic organism, was able to replicate itself like any normal cells. Thereby, the synthetic biology demonstrates ever more the capacity of life to integrate exogeneous constituents.

Parallel, since the 1970s the synthesis of amino acids in conditions similar to interstellar space became subject of many studies and experiments [15-17]. Recently the bombardment of heavy ions on ice composed of methane and carbon monoxide produced glycine in similar conditions to those present in the interstellar regions [15]. The photolysis of carbon dioxide, carbon monoxide and methanol was another successful way for amino acid synthesis [16]. Through the sputtering of carbon target in quasi-interstellar conditions Marcel Devienne and his collaborators observed the formation of alanine and glycine [17,18]. This experiment is highly interesting, because it is only achieved from carbon atoms and the elementary gases nitrogen, oxygen and hydrogen. Its represents one of the bases of the studies described in this dissertation. A reproduction of a similar experiment with a more precise identification method aims to bring new elements into the question of the formation of amino acids in gas phase and in interstellar medium.

2- Anions and amino acids in interstellar medium

Not only did lone atoms exist throughout the universe, but polyatomic molecules and dust were also present. Polyatomic molecules up to 70 atoms (fullerenes) were already detected [19]. Despite the intense cosmic radiations occurring in space, molecules exist and form interstellar clouds. These clouds present an onion-form, where the external layers protect the denser center. Starting diffuse, the cloud become denser, making up a part of the star formation cycle. The electromagnetic waves constitute the main source of information on their composition. Depending on the density of the clouds, absorptions and the emissions are detectable in different ranges, from UV (ultra violet) to GHz. The diffuse clouds, characterized by a very low density (10^2 to10^3 particles /m^3) and cold temperatures (30 to 50 K), are active in the UV and IR ranges. The dense clouds (10^3 to 10^5 p /m^3 and 20-30 K) remain opaque to the UV radiations. In the centers of these, larger molecules are formed, which are detectable in the range of microwave, corresponding to rotational signatures of molecules.

Figure 1: Picture of the interstellar Cloud W5 hosting multiple generations of stars. The picture was taken in IR range from the *Spitzer Space Telescope*.

In the myriad of interstellar clouds, some are particularly solicited by astronomy, the Taurus Molecular Cloud (TMC-1) in the Taurus constellation for example. Some dense clouds evolved in hot cores (200K to 300K) through intense chemical reactions in their center, representing the first phase of star formation. These are also praised for molecular identifications, as the Sagittarius Cloud (Sgr2) located in the center of our own galaxy. Although the major part of interstellar identification occurs in microwave region, the IR emissions and absorptions are valuable to the astronomers. The infrared (IR) regions revealed the transition between vibrational levels, which are propitious to the identification of the molecules without permanent dipole moment. Principally impossible from the earth, the interstellar IR radiation detection utilizes a spatial

telescope such as the *Spitzer Space Telescope,* launched in 2003, in order to collect observations in the range of 5-40 μm. For radiodetections, telescopes are installed around the world, as for example in Europe *IRAM* (in Spain) and *MPIfr* (in Germany). In 2001 the data furnished by these two observatories enabled the discovery of C_6H^- in TMC-1. C_6H^- was the first anion detected, inciting new attention to the interstellar negatively charged spaces [20].

Until this discovery, anions were considered too fragile to exist among the intense cosmic radiation made principally of protons. The postulations of anions in space [21-22] remained strongly hypothetic as long as they remained transparent in astronomic observations. The actual inventory of interstellar detected molecules reveals 160 molecules, a great majority of which includes carbon atoms [19]. The list presents also 30 ions, only five of which are anions. Many negatively charged counterparts of the already identified species were suspected to exist in space. For example, many of the carbon chains C_x are identified interstellar molecules. The rate of radiative attachment of electron is predicted high for the carbon chain. This allows for a lifetime of up to two weeks for some C_x^- [23]. The lifetime is estimated to be even longer for carbon chains presenting an additional oxygen atom [24]. Therefore C_xO^- are considered potential interstellar species. The carbon nitrides**,** including many nitrogen atoms, have recently caught the attention of many astronomers. The dense atmosphere of Titan, Saturn's largest moon, was revealed by *Voyager 1* to be composed of 97 % Nitrogen and 2% Methane [25]. Carbon nitrides, as for example C_2N_2 and C_4N_2 are likely to be present in Titan's atmosphere chemistry [25-26]. The lack of IR experimental data on negatively charged systems was one of the main reasons for the delay in the discovery of interstellar anions, as presented by McCarthy in 2012[27].

Such was not the case for amino acids, also potentially present in interstellar medium. Glycine, the smallest amino acid, is especially well investigated. In the laboratory, two conformers of Glycine, called I and II, were observed in the gas phase. The two conformers presented two different dipole moments, 0.93 D and 4.50 D respectively [28]. Both of the conformers were sought for years in vain, until 2003 when the detection of the glycine I in a hot molecular core was reported [29]. The absence of conformer II, the most active for the absorption, was the subject of many discussions [30]. Recently, a theoretical study revealed the synthesis in the interstellar gas phase of alanine and glycine as strongly underprivileged [31]. *Ab initio* calculations were applied on more than twenty isomers of glycine and of alanine. The alanine arrived only at the sixth position, 0.46 eV higher than another amino acid, which was not present in life. Glycine arrived in the third position of the energy scale, 0.39 eV higher than a carbanic methyl. Due to this controversial results amino acids formations and existence in the interstellar medium still need more investigations.

3-Synthesis in quasi-interstellar conditions: Carbon Sputtering

The synthesis of glycine reported by Devienne et al. represents a key experiment in the understanding of the synthesis of amino acids in quasi-interstellar conditions. In this experiment a carbon target was bombarded with highly energetic ions and oxygen, hydrogen and nitrogen gases. Such bombardments are called sputtering (in reference to the atom ejected from the

surface). After hours of bombardment, the accumulated ions were electromagnetically extracted from the target and identified. Then the ions were fragmented through Collision Induced Dissociations (CID). The fragments of molecules which resulted from sputtering were compared with molecules of interest. Thereby several organic molecules were identified. Glycine was for example identified through its 12 principal fragments. To enhance the understanding of synthesis in gas phase, a more powerful IR identification is setup in a similar experiment, which is described in this dissertation. Beyond the identification method, the experiment presented differs in some points from those previously made.

	(In this work)	/	(Devienne et al.)
-Projectiles energy:	<1 keV	/	10-15 keV
-Gas sublet:	on the sputtering head	/	molecular beams (O_2) and (H2/N2)
- Identification:	Infrared spectroscopy	/	CIDs

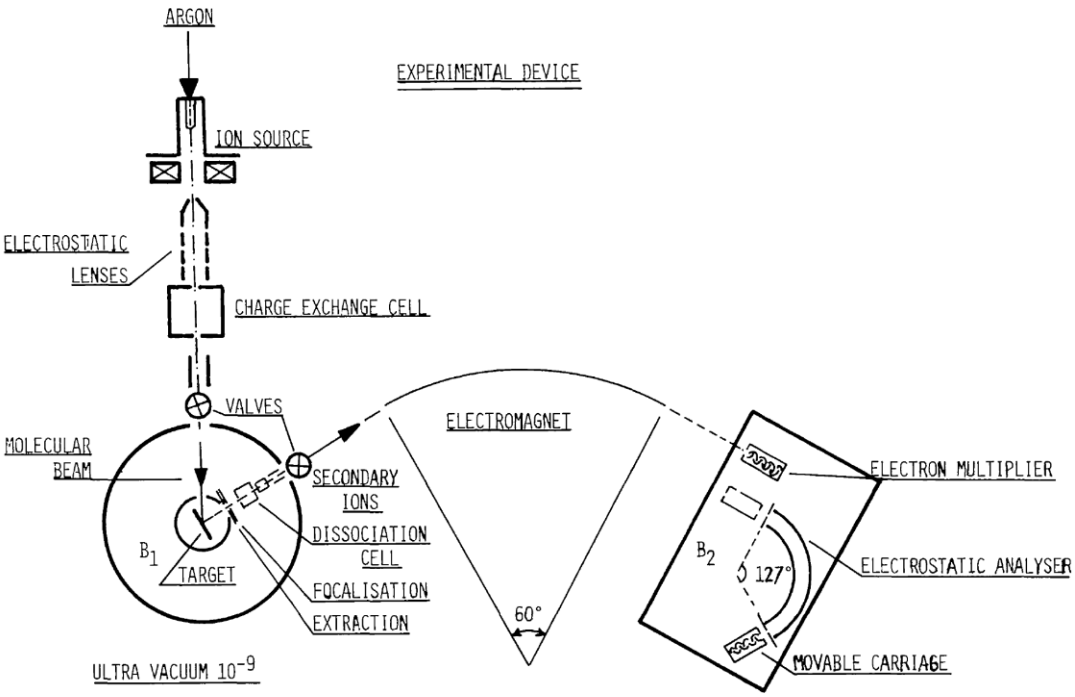

Figure 2: Schema of the experimental device employed by Devienne et al., picture extracted from [18].

Such experiments are conducted under a high vacuum in the range of 10^{-5} to 10^{-7} mbar. The pressure of 10^{-7} mbar corresponds to the vacuum reigning at 200 km from earth. Some dark interstellar clouds were estimated to attain the pressure of 10^{-8} mbar, as for example the Orion Molecular Cloud [32]. Differing from interstellar conditions, the source produced many masses corresponding to the species identified in space (figure 3). The sputtering products clearly corroborates the interstellar identifications. The CN, C_6H^-, and C_8H^- represent three of the five interstellar anions detected. The addition of the other five species (H_2O^+ CO^+, HCO^+, NO^+,

HCO_2^+) brings to eight the number of interstellar charged species [19] formed in the source. Furthermore, many of the ions abundantly produced by the source present their neutral homologues in space (blue in the figure 3). In the past several years, a great increase in the identification of interstellar molecules was registered. New identifications will certainly enrich this description. Conversely, the species produced by the source form hypothetic interstellar ions. Thereby, the sputtering appeared to be a particularly adequate source to investigate the interstellar chemistry.

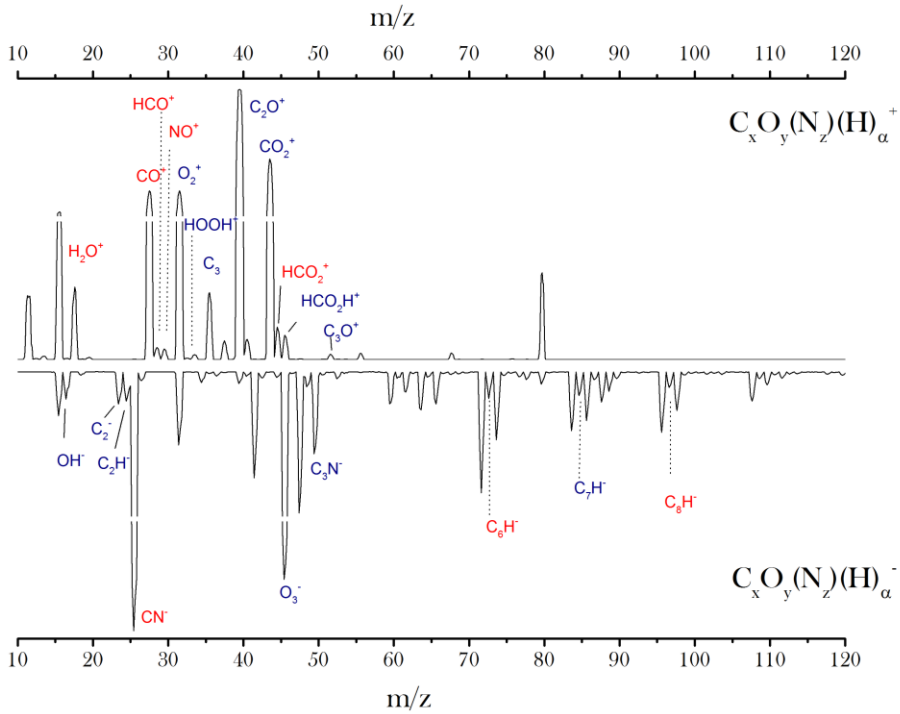

Figure 3: Mass- spectra of positively (top) and negatively (bottom) charged ions produced by sputtering in the presence of O_2. Eight ions (in red) have already been identified in the interstellar medium. The neutral homologues of many produced anions are also interstellar (in blue). The nitrogen and hydrogen atoms were present by contamination and only a very restricted quantity of them was present in the sputtering process. By these preliminary spectra, the species assigned represent the most plausible combination of the elements in presence. The infrared identification of many of these systems confirmed these first suspicions from mass-spectrometry. Thereby the species attributed on the figure, when not confirmed, are highly probable.

As often occurs in physics, observations far from earth find similarities at the microscopic levels observable on earth. The property of many materials at microscopic level constitutes a great catalyst for technological development. This development profits from the different properties offered by the multitude of existing clusters. An extension of the production or of the understanding of the clusters is of great technological interest. The sputter source produced many valuable clusters. Carbon nitrides, including four nitrogen atoms, are particularly

promising. The graphitic C_3N_4 was considered an attractive free-metal photocatalyst, using solar energy for the extraction of hydrogen from water, which represents a future source of energy independent from fossil reserves [33]. The band gap of the g-C_3N_4 is sufficiently large to overcome the endothermic reaction of water splitting and remain in the UV visible domain of absorption. Furthermore, complexes of C_3N_4 or $C_{11}N_4$ are predicted with a high bulk moduli, which determine the hardness at a microscopic level [34, 35]. These could dethrone diamond from its place as the hardest material. Similarly, carbon chains of carbyne type are predicted to be the stiffest material known [36]. Carbyne molecules were proposed many times for a variety of applications including nanoelectronics [37], the synthesis of complexes [38], and hydrogen storage [39]. The oxo-carbon clusters (C_xO) and (C_xO_2), which include more than one carbon atom, represent a challenge for chemists. Only a few of them were observed recently [40-45]. Thus the examination of the production of sputtering shows huge potential, not only for astronomers.

OUTLINE OF THE THESIS

As introduced above, the lack of anionic spectroscopic information evocated by astronomers and the understanding of the formation of amino acids in quasi-interstellar gas phase constitute challenging objectives. In this context a reproduction of the Devienne experiment with an infrared identification appeared to be a highly promising concept. This dissertation presents a setup of this concept and its results.

The low ionic density of the produced ions requires the use of a specific IR spectroscopic method: the Infrared Photodissociation (IRPD). The experimental work consists of the combination between a sputtering source a tandem mass spectrometer-ring trap and IR laser system. The success of the investigation was based on the establishment of adequate conditions to synthesize the anions in question. The efficient data collection allowed for IR identification of more than 30 ions. Furthermore valuable information about the chemistry in the sputtering process could be gained. The computational facilities offered by the Freie Universität Berlin were strained in order to perform DFT (Density Functional Theory) calculations on the investigated anions allowing for structural identification of the investigated systems. These theoretical data facilitate a greater understanding of the experimental results, presented within several chapters of this dissertation.

The first chapter begins with the basics of the sputtering process before introducing vibrational spectroscopy and the messenger IRPD method. It then presents briefly the theoretical calculations utilized. In chapter 2 the ions are followed from their formation in the sputtering source to their investigation by infrared spectroscopy through the detailed description of the different elements that compose the experimental setup. Chapter 3 presents the behavior of the source and the mass spectra of the ions obtained by using different gases. Deductions made from these spectra reveal evidences of their chemistry and indicate probable paths of ion formation.

Chapter 4 reports the spectroscopic results on the dicyano-carbanions ($C_xN_2^-$) and their bent geometries in case of anions with less than four carbon atoms. . Chapter 5 focuses on an essentially uninvestigated group, the tetracyano-carbanions, $C_xN_4^-$. The IR absorption values allowed for the unveiling of the branched geometries of these carbon nitrides. Chapter 6 presents the naked carbanion chains C_x^-, including the last anions, which have not yet been investigated by IR spectroscopy in the gas phase. Numerous reports offer many ways to compare with the IRPD method and reveal some of its specificities. Chapter 7 reports the identification of carbon anions cluster with one or two oxygen atoms and presents their cumulene-like structure. Concurrent anions in the spectra inform on the reactivity of formation for C_xO^-. Chapter 8 focuses on the detection of species of 75, 89, 115 amu, which correspond to the masses of amino acid. These anions including a hydrogen atom or a heavy isotope present absorption spectra valuable for the future IR identification of amino acids. Chapter 9 presents C_xNO^- anions, which entail the same composition of carbon, nitrogen, and oxygen atoms as in organic molecule. The hydrogenation of the ions was the subject of theoretical computational investigations in order to apprehend their relation with organic molecules. In annex a complementary experiment is presented, where amino acids are embedded in helium droplets. Through mass spectrometric observations, associations of several amino acids, fragments of amino acids and water molecules are examined.

Chapter 1:

Theoretical basis

The technologically-advanced methods employed in this work exist on account of the understanding of the physics behind them. A brief theoretical presentation of the key elements of the experiment introduces the physical concepts employed in this study.

1.1. Cluster Formation in sputtering process

1.1.1 Sputtering process

The sputtering process, the bombardment of amorphous or polycrystalline sample with ions, was described by Sigmund and Thomson [46]. In the Sigmund collisional sputter theory, the ions bombarded (primary ions) practice a series of collisions against material. By this linear collision cascade, the material experiences recoiling atoms. The impinging ions lose their energy through the nuclear and electronic stopping power of the material. The recoil atoms also experience ionizations. The energy of the recoil decreases with the order of the collisions. The energy of the recoil atom could help in overcoming the surface potentials energy barrier. The escaped atoms are described as sputtering particles. Sigmund defined the ratio of sputtering particles on the impinging particles through the sputter yield Y:

$$Y(E) = \Lambda\alpha\, N\, S_n(E) \tag{1.1}$$

Where Λ is a material constant, which includes the ejection probability of atoms, α a correction factor and S_n the nuclear stopping cross section as a function of the energy of incident particles, and N the density of the atomic density of the targeted material. By an energy inferior to 1 keV:

$$\mathrm{Y(E)} = 1 + \frac{3}{4\pi^2}\alpha\frac{\gamma E}{U_0} \tag{1.2}$$

Where U_0 is the surface of binding energy (representing the minimum energy necessary to be release from the surface) and γ is a transfer mass factor defined:

$$\gamma = \frac{4\mathrm{M}_1 M_2}{(\mathrm{M}_1 + M_2)} \tag{1.3}$$

where M1 and M2 define the masses of respectively the incident particle and the target atom. When the energy rises above 1keV:

$$Y(E) = \frac{(0.042)\alpha\, S_n(E)}{U_0} \tag{1.4}$$

S_n, the nuclear stopping power, varies as a function of the energy of incident particles:

$$S_n(E) = \frac{\pi a_L^2 \gamma}{\varepsilon/E}\, S_n(\varepsilon) \tag{1.5}$$

where Lindhard's reduced energy ε is a function of the atomic numbers Z_1 and Z_2, defined in case of a non-homonuclear stopping :

$$\varepsilon = \frac{32.53\, M_2 E}{Z_1 Z_2 (M_1 + M_2)\left(Z_1^{2/3} + Z_2^{2/3}\right)^{1/2}} \tag{1.6}$$

and the Lindhard's screening parameter a_L is related to a_0 the Bohr radius:

$$a_L = 0.8853\, a_0\, (Z_1^{2/3} + Z_2^{2/3})^{-1/2} \tag{1.7}$$

The sum of nuclear stopping power $S_n(E)$ and electronic stopping power $S_e(E)$ defines the energy lost per unit of length:

$$\frac{dE}{dx} = -N\,(S_n(E) + S_e(E)) \tag{1.8}$$

With low energies of the impinging ions, the nuclear stopping power increases linearly. Beyond a plateau this stopping power decreases by intermediate energies. In this range of energy the electronic stopping power, which were negligible by lower energies (except for small projectiles), becomes dominant. The increase of the electronic stopping power follows the Lindhard and Scharff model:

$$S_e(E) \approx \xi_e 8\pi e^2 a_0 \frac{Z_1 Z_2}{Z} \frac{v}{\frac{e^2}{\hbar}} \tag{1.9}$$

Where a_0 represents the Bohr radius, v the projectile velocity, ξ_e is a function of the atomic number Z. The electronic stopping attained a maximum by some tenth of MeV. By higher energies the impinging ions enter in the Beth regime:

$$S_e(E) = \frac{4\pi e_1^2 Z_e}{m\,v}\left(log\frac{2mv^2}{I} + correction\ terms\right) \tag{1.10}$$

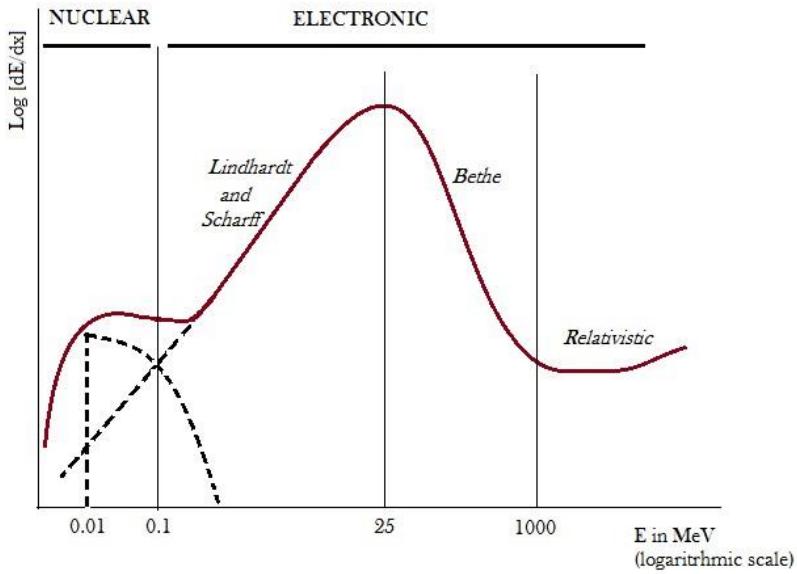

Figure 1.1: Representation of the stopping power of an impinging ion as a function of its energy. Nuclear stopping power dominates by low ion energy (not exceeding several keV). At these energies, light ions also experience the electronic stopping power. By higher energies the electronic stopping power dominates in accord within the equation (1.8). In this regime the efficiency of sputtering becomes better with neutral projectile. The Bethe regime appeared after the maximum of stopping power in accord to equation (1.9). With extreme energies the power increases again in the relativistic regime [46].

The range of energies, which occur in the Bethe and relativistic regimes, are far beyond the experiment reported in this work. In the range of energy up to ten keV, different impacts are generated on the target material by the bombardment and different regimes are defined.

Single knock-on regime occurs particularly under low energies or low masses (H, He). The energy transferred remains low but high enough to provoke the ejection of several atoms. The

collision series are limited to few events and reflections of ions from the sub layers ensue frequently.

Linear cascade regime originates from energies of a few hundred eV. In this case the collision cascade turns into a long series of events. The sputter yield remains linearly dependant on the energy (cf. equation 1.1), such as in the single knock-out regime. The main difference between both regimes remains the abundance of moving atoms by the linear cascade.

Collision spike regime is attained with stronger energies up to 10 keV and heavy atoms. Intense cascades put in motion a majority of atoms in volume of collision of the target. The transition between the linear cascade and the spike regime are observed through sputter yields. In the spike regime, sputter yields experience a super-linearity as a function of the energy.

1.1.2 Clusters' formation

Empirical findings

For the first time in 1958, Richard E. Honig reported the formation of Ag_x^+ (x = 2,3) through the bombardment of noble gas ions carrying an energy not exceeding 400 eV [47]. Ten years later Ag_{60}^- clusters were obtained with krypton ions of 15 keV. Cluster Cu_x^+, Au_x^+, Ag_x^+ with more than 200 atoms were observed in 1986 [48]. Recently, clusters containing more than 500 atoms were reported by Staudt et al [49]. Numerous experimental attempts furnished a collection of evidence concerning the formation of cluster. The cluster sputter yield experiences a power law dependency:

$$Y(x) \propto x^{-\delta} \tag{1.11}$$

Where the δ exponent depends on the nature of the target [51] and the experimental conditions (energy and the nature of the projectiles) [52]. Considering the total yield:

$$Y_{Tot} = \frac{Y}{n_p} \propto \tag{1.12}$$

where n_p is the number of projectiles. Experimental observations showed the inverse correlation between the exponent sigma and the total yield Y_{Tot}. In both the condition with large and small Y_{Tot}.the exponent was observed respectively small and large [51]. The major production of neutral sputter atoms has been experimentally established. The ratio of ions was estimated [53]:

$$\frac{C_{+/-}}{C_{neutral}} = 10^{-3} - 10^{-4} \tag{1.13}$$

The production of ions was greatly enhanced by the bombardment of reactive oxygen (O_2^+) [54] and nitrogen ($N_2^{+)}$ [55]. The ions ratio in the sputter yields produced by different material (Ag, Ta, Nb, Ge) was the subject of recent studies [56]. By the cluster size exceeding 10 atoms the probability of the positively charged atoms was under 10^{-3}. By the cluster size smaller than 10 atoms, an increased probability of charged cluster was observed and for all material investigated. The abundance of positively charged clusters prevails clearly over the negatively charged clusters in the sputter yield [52].

Experimental model

In order to explain the numerous empirical findings different models were proposed.

Direct Emission Mechanism (DEM)
This model considers a collision of a recoil atom and a second atom already in the target material [57]. The recoil atoms receive sufficient energy to also provoke the ejection of second atom. The model remains useless for case of material possessing a dissociation energy of dimer inferior to the binding surface energy as for example metals and semi-conductors. In the case of carbon sputtering target, the measurement of the surface binding energy suggests a direct emission mechanism of performed clusters [65].

Atomic Combination Mechanism (ACM)
By this model, the formation of dimer results from two atoms already ejected from the target surface [57]. Such collisions require proximity and closeness of both atoms. A kinetic energy smaller than the binding energy constitutes also a condition for this mechanism. The ACM explain successfully the distribution of several systems composed of dimers and trimers [58]. This model could not explain further characteristics of the sputtering.

Thermodynamic model
The thermal effects of large collision cascades, which occur in small volumes, are taken in account in this model [59]. From the thermalization of the surface, atoms are vaporized. The density of the material irradiated and evaporated close to the target plays a crucial role in the distribution of the size. For intermediate energies, the distribution of the cluster size produced follows a polynomial decay. The thermodynamic model explains relatively well the mass distributions of Ar_x^+, N_x^+ and Ni_x^+ [60].

Shock wave model
This model was carried out in order to explain the formation of large cluster by heavy atoms. The collision cascade of heavy atoms increased the density of energy on the target. The

overlapping of several elastic collision cascades provokes shock waves [61]. This model explains well the power dependency of the yield (equation 1.10). The large exponent σ, which was many times observed, are not explained by the shock wave model nor by any other model. The recent formations of clusters, with a size exceeding 500 atoms [49], correspond to σ ≈ 2, in accord with the shock wave model.

1.1.3 Clusters' growth.

The phase transition theory admitted a critical size of nuclei, which are able to form a base for further growth [62]. And dimers are predicted stable enough to constitute a base for cluster growth [63]. The formation of dimers in the vicinity of the sputter target could be describe through a three-body collision:

$$C + C + Ar \rightarrow C_2 + Ar \tag{1.14}$$

where C represents metal atom, and Ar represents buffer gas atom. The subsidiary energy of the collision is released by the intermediate of the buffer gas. The next size increase results from different processes [63-69].

Attachment of atoms

This process results from collisions between atoms. The buffer gas allows the evacuation of the subsidiary energy of collision. The attachment of atoms could be described:

$$C_x + C \rightarrow C_{x+1} \tag{1.15}$$

The rate of the process depends on the size of the cluster. Considering k_x as constant rate:

$$k_x = k_0 x^{2/3} \tag{1.16}$$

where k_0 is a constant rate depending on the material as well as the experimental conditions.

A parameter G (dimensionless) characterize the process

$$G = \frac{k_0}{k\, N_{Ar}} \tag{1.17}$$

Where N_{Ar} represents the density of argon.

The average size of the clusters are correlated with this parameter [66]:

$$\bar{x} = 0.31G^{3/4} \tag{1.18}$$

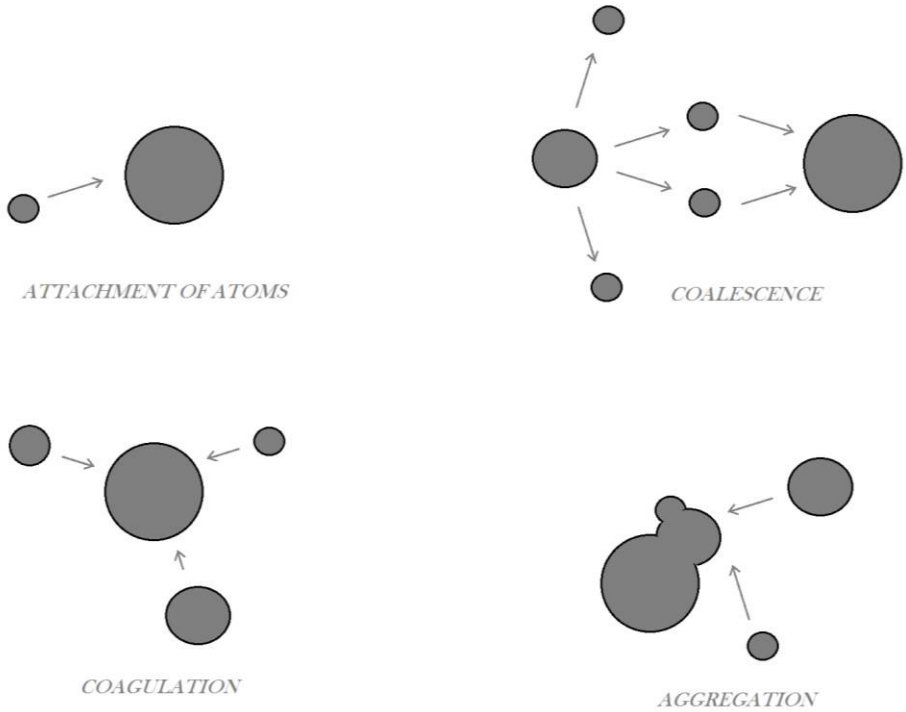

Figure 1.2: Main processes of cluster growth occurring in supersaturated vapor. Inspired from [68]

Coagulation

This mechanism considers the cluster under liquid state. Droplets of different sizes collide and form larger clusters:

$$C_{x-y} + C_y \rightarrow C_x \tag{1.19}$$

Single interactions between two droplets form a kinetic regime. A diffusion regime also occurs when several molecules interact simultaneously. The density of the bound atoms influences the regime occurring. In accord with theoretical studies' estimations of the density of bound atoms N_b[66], the kinetic regime remains possible in the source present in this work and the average size of the cluster is described:

$$\bar{x} = 6.3(N_b k_0 t)^{1.2} \tag{1.20}$$

Coalescence:
In this process, clusters experience two kind of behavior depending of their size. Smaller than the critical size, the clusters lose their atoms through evaporation. The reduced saturation provokes this evaporation. The larger clusters grow further. The critical size delimits the growth from the decreasing clusters. The critical radius could be defined:

$$r_{cr} = \frac{\alpha}{\Delta} \tag{1.21}$$

where Δ delta is the degree of saturation and α is described:

$$\alpha = \frac{2\sigma_t}{kT} V_M C_\infty \tag{1.22}$$

where C_∞ determines the concentration of the saturated solution, V_M the atomic volume of the cluster and σ_t the interphase tension and T the temperature.

The relationship between the critical radius r_{cr} and the critical x_{cr} is expressed:

$$r_{cr} = r_W \, {x_{cr}}^{1/3} \tag{1.23}$$

where r_W represents the Wigner-Seitz radius, which corresponds to a sphere with a volume equal to the mean volume per atom in solid. In a diffusion regime of coalescence the average of distribution:

$$\bar{x} = 1.35 \, x_{cr} \tag{1.24}$$

Aggregation

This growth involved attachment of clusters, which partially conserve their initial configuration. The sputtering method is mainly used to produce non-agglomerated metallic nanoparticles. Experimental examinations of the shape of copper and silver clusters produced in a magnetron reveal the absence of aggregates [69]. The aggregation of carbon nanoparticles synthesized by sputtering required a HV deposition chamber to be observed [64] and after long time of deposition only rare case of aggregations were observed. By these studies, the absence of isolated nano-particles around the aggregated structures implied that the aggregation are synthetized in the gas phase.

Clusters' charging

In accord with theoretical investigations, different ways of cluster charging are considered [67,70,71],:

$$e^- + C_x \rightarrow C_x^- \tag{1.25}$$

$$e^- + C_x^+ \rightarrow C_x \tag{1.26}$$

$$A^+ + C_x \rightarrow C_x^+ + A \tag{1.27}$$

$$A^+ + C_x^- \rightarrow C_x + A \tag{1.28}$$

Utilizing balance equation the ratio of the negatively charged clusters could be expressed:

$$\frac{C_-}{C_0} = \sqrt{\frac{T_e m_i}{T_i m_e}} \frac{N_e}{N_i} \frac{1}{1 + z_0(T_i)} \tag{1.29}$$

with:

$$z_0 = \frac{1}{4\pi\varepsilon_0} \frac{e^2}{r_c} \frac{1}{kT} \tag{1.30}$$

where m_i, N_i, T_i, m_e, N_e, T_e represent the respective masses, densities, and temperature of ions and of electrons, r_c represents the radius the cluster C, where C-represent its negatively charged counterparts.

Only the single charged products of sputtering are considered. Multi-charged species were not yet reported and are assumed to be absent or produced in negligible quantity. The magnetron sputter sources generate a plasma in the proximity of the surface of the target and multicharged dust are usually present in the plasma chemistry [72]. In this work carbon clusters with a charge exceeding 1 were not observed in accord with the tacit assumption that multi-charged system are absent from the sputtering yield.

1.2 Vibration Spectroscopy

IR absorption spectroscopy constitutes a powerful technique to characterize the structure of molecules and belongs to the conventional methods of identification of molecules [73-75]. The traditional procedure involves irradiating a sample of investigated molecules with an electromagnetic field and measuring the intensity after interaction with the sample. The process is repeated for different wavelengths. Graphic representations of absorption as a function of wavelength or of frequencies are carried out in order to obtain IR absorption spectra (figure 1.3). Classically in IR spectroscopy the frequency is expressed through the wavenumber, noted ω, in cm^{-1}, equal to the inverse of the wavelength. The infrared electromagnetic spectrum covers the range between the visible and the microwaves, which includes frequencies from 0.5 to 300 THz, or 20 to 10,000 cm^{-1}. The spectrum could be divided arbitrary into three sub-ranges the far IR 10-2000 cm^{-1}; mid IR 2000-6000 cm^{-1} and near IR 600- 10,000 cm^{-1} (visible). From the Planck's law, $E= h\nu$, the energies of the IR radiations are relatively weak from 0.0025 eV to 1.25 eV. For comparison the value of 0.0025 eV corresponds to the thermic energy at 30 K ($E = k_b T$). The infra-red electromagnetic absorptions involve the movement of the atomic nucleus. Generally, the electronic states are excited by higher energetic radiations than infrared. The first electronic excitation is particularly low for metals and, for example, appears with about 5000 cm^{-1} for K_2 but needs 40,000 cm^{-1} for acetylene [76]. The systems investigated in this work present electronic excitations definitely outside the IR range of energy employed. An empiric interpretation of IR spectra derived from collected experimental measurements. In more than 100 years of history, millions of spectra were reported and showed that many functional groups absorbed in the same wavelength range. As presented on the figure 1.1 the collection of data showes that single bonds involving carbon, oxygen and nitrogen atoms typically absorb until 1600 cm^{-1}, whereas the double bonds absorb from 1600 cm^{-1} to 1800 cm-^{1} and the triple bonds from 2000 to 2500 cm^{-1}. The bonds involving a hydrogen atom generate absorption in higher range from 2500 to 4000 cm^{-1}. Finer spectral signatures, inventories and tables exist, which provide many variations of functional groups [77-78]

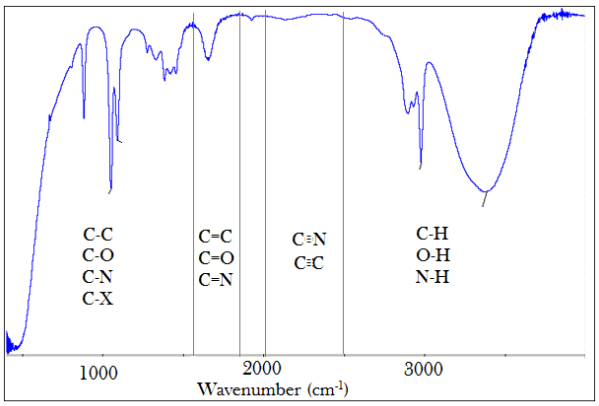

Figure 1.3: IR absorption spectrum of ethanol. In addition the typical region of absorption of single, double and triple bonds introduce an empiric interpretation of the spectra

Classical Approach

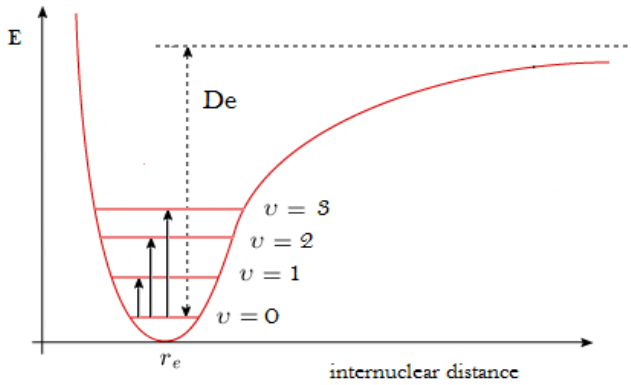

1.4: The Morse potential with the first three vibrational levels and the excitations $\upsilon_{(1\text{-}3)}$, from the fundamental level υ_0. *De* represented the difference between the fundamental level and a dissociation threshold.

Around the equilibrium, the Morse curve takes the form of Taylor series where the first not null term is of second order, considering r_0 the minimum distance and k a proportionality constant:

$$E = \frac{1}{2}\, k(r - r_0)^2 \tag{1.31}$$

In a barycentric referential, the masses of two atoms could be expressed under a unique reduced mass μ (product of the masses divided by their sum) and r, the internuclear distance related to the centre of inertia. The law of conservation of Energy could be applied, considering the Galilean reference frame is isolated:

$$E = \frac{1}{2}\, \mu\, \dot{r}^2 + \frac{1}{2} k\, r^2 \tag{1.32}$$

The evolution in function of the time was obtained by derivation of the equation 1.29:

$$\ddot{r} + \omega^2 r = 0 \tag{1.33}$$

with:

$$\omega = \sqrt{\frac{k}{\mu}} \tag{1.34}$$

Considering that a the equilibrium r_0 is non nul, the solutions of the differential equation take the form:

$$r(t) = A\ \cos(\omega(t) + \varphi) \tag{1.35}$$

with:

$$A = \sqrt{\frac{E}{k}} \tag{1.36}$$

In accord with the solution of the equation, the relation between the wavelength, k and μ remains:

$$\frac{1}{\lambda} = \frac{1}{2\pi}\sqrt{\frac{k}{\mu}} \tag{1.37}$$

By the molecules, k represents the strength the bond. Thereby, the frequency values and differences observed between the different functional groups are explainable through the different masses as well as the order and the strength of the bonds in presence.

Quantum approach

The schrödinger equation of the system [79]:

$$\left(-\frac{\hbar^2}{2\mu}\ i\,\nabla^2 + \frac{1}{2}\,k\,r^2\right)|\Psi_r\rangle = E\,|\Psi_r\rangle \tag{1.38}$$

The wave function Ψr is interpreted as the amplitude of the probability of presence. This equation of second order admits an infinite number of solutions and the energy do not restrict some values for the energy. Some limits have to be carried out (negative energies) to obtain the allowed some discrete values of energies:

$$E = h\,\upsilon_0\ \left(n + \frac{1}{2}\right) \tag{1.39}$$

This expression shows that even at 0 K, the energy of the system is non-null and a molecule continue to have energy. The thermal energy at a temperature of 30 K corresponds to 0.0025 eV and constrains the molecule to remain in the fundamental level of vibration. The wave function presents an eigenvector containing a Hermite polynomal H_n:

$$|\Psi_n(r)\rangle = \sqrt{\frac{\beta}{\Pi\pi 2^n\, n!}}\ H_n\ (\ \beta x)\ e^{\left(-\frac{1}{2}\beta^2 x^2\right)} \tag{1.40}$$

where:

$$\beta = \sqrt{\frac{\mu\omega}{\mathrm{k}}} \tag{1.41}$$

The Hermite polynomal H_n corresponds to:

$$H_n = (-1)^n \, e^{r^2} \frac{d^n}{dr^n}\left(e^{-r^2}\right) \tag{1.42}$$

which follows the recursion relation:

$$H_{n+1}(z) = 2\, z\, H_n(z) - 2\, n\, H_{n-1}(z) \tag{1.43}$$

The part of the eigenvector constituted by the Hermite polynomal is relevant for the rest of the development. A variation of the dipole moment constitutes a sine qua non condition for the absorption and could be expressed:

$$\frac{\delta\mu}{\delta r} \neq 0 \tag{1.44}$$

An electromagnetic wave is given respectively with the dipolar momentum μ and the magnetic momentum $\mu_b$by the following formula:

$$\vec{E}_{\,dipole} = \mu\vec{E} + \mu_b\,\vec{B} \tag{1.45}$$

The magnetic term is neglected in relation to the electric component of the electromagnetic wave. The Hamiltonian H_{int} describing the perturbation by the electromagnetic wave could be represented:

$$H_{int}\,|\Psi_r\rangle = \left(-\frac{\hbar^2}{2\mu}\nabla^2 + \frac{1}{2}\,k.r^2 + \mu\,E\right)|\Psi_r\rangle = E\,|\Psi_r\rangle \tag{1.46}$$

and

$$H_{hr} = -\frac{\hbar^2}{2\mu}\nabla^2 + \frac{1}{2}\,k.r^2 \tag{1.47}$$

where H_{hr} describes the harmonic Hamiltonian.

Here the assumption is made that the eigenstate of the harmonic oscillator is not modified by the electric perturbation, rather it only inducts a transition from one state to another, which are approximated by the harmonic oscillator. The transition from an *i* state to a *j* state is considered. The probability of transition from one state to other is proportional to the product:

$$P_{i\to j} \propto \langle \Psi_j | H_{hr} | \Psi_i \rangle + \langle \Psi_j | \mu | \Psi_i \rangle \, E \tag{1.48}$$

The first term is nul, when $i \neq j$ because the eigenfunction of the oscillator harmonic are orthogonal. The second term could be expressed:

$$P_{i\to j} \propto \left(\langle \Psi_j | \mu_0 | \Psi_i \rangle + \frac{\delta\mu}{\delta r} \langle \Psi_j | r | \Psi_i \rangle \right) E \tag{1.49}$$

From equation 1.37:

$$\langle \Psi_j | r | \Psi_i \rangle \;\propto \int_{-\infty}^{+\infty} H_j\ (z)\, z\, H_i(z) e^{-z^2} dz \tag{1.50}$$

In accord with the Hermite polynomal recursion relation (equation 1.40):

$$\int_{-\infty}^{+\infty} H_j\ (z)\, z\, H_i(z) e^{-z^2} dz \;=\; i \int_{-\infty}^{+\infty} H_j\ (z)\ H_i(z) e^{-z^2} dz \;+\; \frac{1}{2} \int_{-\infty}^{+\infty} H_j\ (z)\, H_i(z) e^{-z^2} dz \tag{1.51}$$

so that:

$$\int_{-\infty}^{+\infty} H_{n'}\ (z)\, H_n(z) e^{-z^2} dz \;= 0 \; if \; n' \neq n \tag{1.52}$$

The first term of the equation (1.47) is non nul if $j = i\text{-}1$ corresponding to the emission and the second term if $j = i+1$ corresponding to absorption. This explains the quantized energies involving two successive vibrational levels in the absorptions.

Vibration modes

In a molecule, the atomic movement of each atom is described in a local Cartesian space (A, x, x z) by three axes corresponding to three degrees of freedom. Molecules composed of N atoms possess 3 N degrees of freedom. Taking away 3 translation modes and the 2 or 3 rotation modes (if the molecule is respectively linear or non-linear), a molecule possesses 3N-5 or 3N-6 modes of vibration. The modes described here are normal modes, where the frequency is the same for the atoms taking part in the vibrations. The vibrations appear under many configurations: figure 1.5

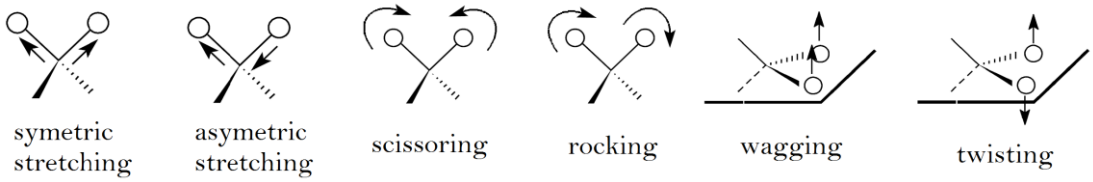

Figure 1.5: representation of several vibration modes occurring.

Not all the vibrations are active for IR absorption. As mentioned before (equation 1.41), a variation of the dipole moment during the vibration is necessary for IR absorptions. Several modes of vibration do not fulfill this condition.

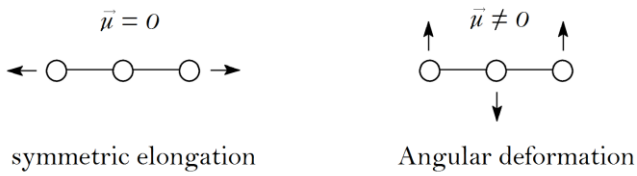

Figure 1.6: Representation of two vibration modes in a linear molecule. A symmetric elongation on the principal axis (left) preserves the dipole moment μ of the molecules, which remains inactive to IR absorption, whereas an angular deformation (right) induces a modification of the dipole moment and the IR activity.

In order to apprehend the IR active modes in three dimensions, the orthogonality and the symmetries of the wave functions of both vibrational states, initial and final, are taken into account. Considering the dipole moment is a function *f* of the three axes x, y, z in a Cartesian space, the intensity of the transition *I* is proportional to:

$$I \propto \langle \Psi_j | f | \Psi_i \rangle \tag{1.53}$$

The intensity is not nul when:

$$\Gamma\,\Psi_f \otimes \Gamma\, f \otimes \Gamma\,\Psi_i \subset A1\ symmetry\ total \tag{1.54}$$

where Γ is the matrix representation of the symmetry operation. In this work, the initial vibrational states remain the fundamental states and present a total symmetry (A1). In this case, in order to absorb light, the symmetry of the excited vibrational state has to correspond to the symmetry of the dipole moment. The symmetries of the vibrational excited states are described in the group theory, where the different elements of symmetry present on molecules are taken into account [81]. The denomination Schoenfliess is used for these elements where C is for axis, sigma for plan, i for center, I for identity and S for rotation-reflexion. The molecules sharing the same typical combination of symmetry elements are disposed in point groups. For each point group, the modifications of the symmetry operable are resumed in character tables (figure 1.5).

C_{2v}	E	C_2	σ_v (xy)	σ_v (yz)		
A_1	1	1	1	1	z	x^2, y^2, z^2
A_2	1	1	-1	-1	R_z	xy
B_1	1	-1	1	-1	x, R_y	xz
B_2	1	-1	-1	1	y, R_z	yz

Figure 1.7 Character table for the point group C_{2v}. The four columns represent the symmetry elements, the identity (E), the axis on 180° (C2) and two plans (σ). The four lines presented the symmetry A_1 A_2 B_1 B_2. The two right-hand columns inform about the symmetries species (left) and the polarizability (right). By the point group C_{2v}, only the excitations in direction of states, which present a symmetry species of an axis x,y,z (corresponding to the symmetry A_1, B_1 and B_2) are subject of IR absorption (in the case of initial state is the fundamental).

Infrared Photodissociation

In 1985 Okumura et al. reported a predissociation state of hydrogen clusters reached by IR excitation [82]. This discovery paved the way for the development of a new indirect method to measure the IR absorption through dissociation. The high sensitivity of this background-free detection of the Infrared Photodissociation (IRPD) is limited by thresholds of covalent bond dissociation, usually higher than the IR range of energy. The dissociations occurring in IR range

result from multiphonic dissociation (IRMPD) by high energies level or from the presence of bond of weak energy.
The early experiments of multiphotonic IR dissociation with CO_2 laser characterized the IRMPD process [83]. The absorption process is semi-resonant. For ions larger than 10 atoms the ions are excited to a quasi-continuum state by the resonant IR photons. In the quasi continuum the density of state rises with the absorbed photon [84] provoking the absorption of almost any IR photons. An intramolecular vibrational redistribution (IVR) occurred in a short time scale in the range of 10^{-11} to 10^{-12} s [85]. This rapid redistribution of the energy caused the depopulation of the excited levels and the absorption of more photons. The dissociation threshold attained, the energy was redistributed over all degrees of freedom. Experimentally the dissociation followed a decay function of the ion density, reported by Dundan [86]. In the case of smaller ions, vibrational intermode anharmonicities bring shifts in the sequential absorption of infrared photons [87]. In the system presenting weak bonds, the dissociation could occur with the excitation of a single photon. In this case the IR activated systems remain first in a metastable state. The distribution of internal energies of the metastable state is common with the other process of excitation, as for example CID [88]. Dynamically the IVR process is slower than the excitation process. The kinetic studies revealed dissociation times up to some µs [89], which limit a broadening caused by short lifetimes. The dissociation of the metastable state possesses concurrent path of relaxation. A deactivation by collision could occur. Radiation and photon emission could represent also another path for the molecule to recover her initial energy. Such relaxations appear in single photon processes, but only rather exceptionaly [90].

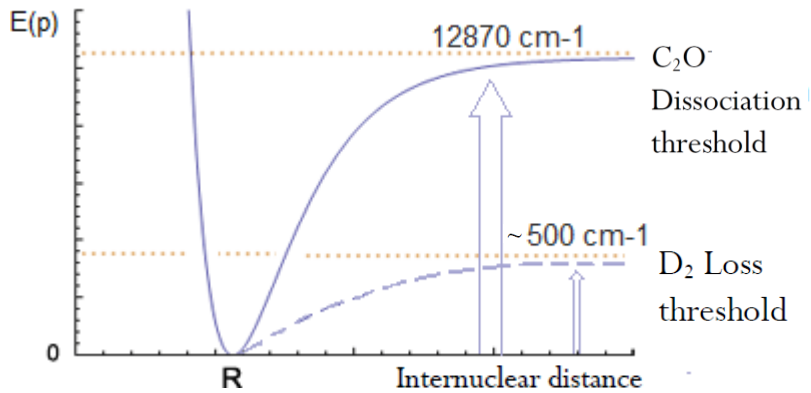

Figure 1.8: Schematic representation of the fragmentation of C_2O and the loss of D_2 tagged on C_2O energies. The low energy of separation of D_2 allows the one photonic IRPD.

One approach to overcome the energetic barrier of the dissociation consists of the attachment of a messenger (also called "tagging"). This method has been developed by Okomura and Lee [91]. An inert gas atom attaches to the molecule or cluster of interest and formed a non-covalent bond [92,93]. The non-covalent bonds occurred only in molecules presenting a low energy of vibration.

Different molecules are suitable to form non covalent bonds. The inert gas atoms present fully occupied subshells, which predispose them to form van der Walls interactions with the molecules of interest. The noble gases He, Ar or Ne, which possess low polarizabilities and small masses, only slightly influence the IR spectra and prove to be efficient messengers. Studies combining different messengers revealed the preferential attachment of different messengers to different isomers [93, 94]. The utilization of the heavy inert gas Xe or CH_4 or N_2 revealed higher perturbations and showed additional band features [92, 94]. The influence of the messenger on the structure of water clusters was revealed by the different vibration spectra of Ar-$H^+(H_2O)_2$, compared to Ne-$H^+(H_2O)_2$ [94]. The tagging could also be isomer dependent, as for example by the isomer of LiH_2O_4 [95]. For the choice of messenger in this work, a preliminary tagging test revealed that noble gases do not properly tag the carbon chain. The deuterium dimer (D_2) revealed itself as an adapted messenger for the method applied. The tagged deuterium dimer brings its own vibration frequency close to 3000 cm^{-1}. In this work, the molecules investigated are hydrogen-free (except a few of them) and the range of interest examined is located at 1200 to 2400 cm^{-1}.

1.3 Theoretical Calculations

Computational chemistry plays a decisive role in the research. Developers of computational methods (W. Kohn, J. Pople, M. Karplus, M. Levitt, and A.Warshell) were honored by two Nobel Prizes in chemistry in 1998 and 2013. Slightly less than ninety years ago, two German scientists, W. Heitler and F. London [97], initiated the quantum chemistry through their study of the hydrogen chemical bond. The development of computers considerably expanded the power of computational chemistry, particularly through the elaboration of efficient computer programs (ATMOL, Gaussian, IBMOL and POLYATOM). The continuous elaboration of solutions of the wave equation offers a wide range of calculation methods. The most frequently used computational methods could be classified in two categories: when the wave function is the subject of the calculations, the method is known as Wave Function Theory also called *ab initio* method; when the density of electrons is targeted by the method, it carries the name DFT (Density Function Theory). A brief description of methods will be presented in the following paragraphs.

Ab initio methods

Almost all the *ab initio* methods use the Hartree-Fock approximation, which is based on the Born-Oppenheimer approximation. In the Hartree Fock method the colombic repulsion is averaged through the main field approximation, where only the correlation between electrons of the same spin are taken into account. Any relativistic effects are neglected. In some methods, the correlation between the electrons is established through a perturbation of the solution HF. The second order of perturbation (MP2) is particularly successful and is often employed, but needs an adequate HF approximation [98]. Other methods are used to simulate more exactly the coupling between the electrons and to introduce the number of excitation degrees needed, but the price for their achievement remains high. The strategy to include a cluster operator is known as "coupled cluster" CC. The wave function of the fundamental state is as follows:

$$|\Psi_{cc}\rangle = e^{\hat{T}}|\phi_0\rangle \tag{1.55}$$

where Φ_0 is the Hartree Fock wave function and T the operator allowing the inclusion of all the excitations from occupied orbits to virtual orbits. T operator is expressed:

$$\hat{T} = \hat{T}_1 + \hat{T}_2 + \cdots + \hat{T}_n \tag{1.56}$$

where n is the number of electrons in the system. Usually the approximation called CCSD using T=T1+T2 is largely employed with T1, the operator of mono-excitation, and T2, the operator of the bi-excitation [99].

DFT methods

The DFT methods were developed in order to overcome the difficulty of *ab initio* methods to calculate systems with a high number of atoms or transition metal atoms. The calculation of the energy in the DFT starts from the electronic density. The wave function in comparison is a purely mathematical invention and requires functions depending on 3N variables, with N being the number of atoms. In DFT methods the density of electrons is a function of only three variables: the x-position, the y-position and the z- position of the electrons, regardless of the number of electrons. The energy of a molecule takes the form of a functional ("function of a function").

$$E = F\,[\,\rho(x,y,z)] \tag{1.57}$$

The value of the functional F needs to be approximated. The multiple strategies to obtain the functional F define different DFT methods. In the 1960s, P. Hohenberg and W. Kohn develop a density theory by the use of the Thomas-Fermi theorem [100]. The theory was adapted by W. Kohn and by L. J. Sham in 1965 to a practical version [101], where the electronic density is composed of a correlation of different molecular energies:

$$E[\rho] = T[\rho] + E_{ne}[\rho] + J[\rho] + E_{xc}[\rho] \tag{1.58}$$

Where T is the kinetic energy of the electrons, E_{ne} nuclear-electron attraction, J the electron-electron repulsive energy, E_{xc} the electron-electron exchange correlation energy. The last element of the functional remains the most difficult to approximate. The orbital model determines the other three elements T, E_{ne}, J :

$$\rho = \sum_{i=1}^{n} |\phi_i|^2 \tag{1.59}$$

where the wave function is considered with only one determinant:

$$\Psi_s = |\Phi_1 \Phi_2 \dots \Phi_n| \tag{1.60}$$

Several approximation methods exist. The local density approximation LDA constitutes one example. In this approximation E_{xc} is approximated through the functional for a uniform electron gas:

$$E_{xc}^{LDA}[\rho] = \int_v \rho(r)\ \epsilon_{xc}(\rho) dV \tag{1.61}$$

With

$$\epsilon_{xc}(\rho) = \epsilon_x(\rho) + \epsilon_c(\rho) \tag{1.62}$$

Where ϵ_x *(ρ)* is the exchange energy from P. Dirac [102], and ϵ_c *(ρ)* correlation energy obtained through the adjustment from uniform electron gas [103]. The expression proposed by S.H. Vosko, L. Wilk and M. Nausair is largely employed (VMN) [104]. The LDA deliver generally overestimated energies and underestimated bond length between atoms [105].

One strategy consists of combining *ab initio* and DFT methods to form a hybrid method. This is the case of the B3LYP, one of the standard methods, often classified as a DFT method. The concept originated in the work of C. Lee, W. Yang, R.G. Paar and A. Becke, who named this method with first letters of their family names. The 3 represents the three parameters used in the approximation of the fourth subsequent part of the functional (equation 4):

$$E_{xc} = E_x^{LDA} + a_0 E_x^{HF} + a_x E_c^{B88x} + a_c E_c^{LYP88c} + (1 - a_c)\ \text{VWN80c} \tag{1.63}$$

Where $a_0 = 0.2$, $a_x = 0.72$, $a_c = 0.81$(experimentally determined). The x refers to the electron exchange and the c to electron correlation. The B88x, LYP 88c, VWN80c correspond to a low density approximation and two gradient corrected approximations [104,106,108].

The Basis set

The calculations require a first representation of atomic orbitals in the form of basis functions. The basis set is formed of the combination of several basis functions, improving the quality of the calculation. A panel of basis sets is available, from the minimum basis set to the extend versions, resulting from more than seventy years of improvement. Different classes of basis sets exist, originating from the different strategies to calculate the orbital function. The utilization of the Slater type orbital constitutes one the first strategy employed. These orbitals take into account only the radial part in the solution of the Schrödinger equation. Thereby, the Slater type of orbital could be expressed by the function:

$$R_l(r) = N_{n,l}\ r^{n-1}\ e^{(-\zeta r)} \tag{1.64}$$

where N represents a normalisation constant, n and l the principal and the angular momentum quantum numbers, ζ the constant related to the effective charge of the nucleus. The equation of the Slater type orbital (1.58) could be replaced by the Gaussian function:

$$R_l(r) = N_{G(n,l)}\ r^{n-1}\ e^{(-\alpha\, r^2)} \tag{1.65}$$

Where N_G is the normalized constant adapted to the Gaussian function and the exponent α was fitted to ζ. The calculations in the Hartree-Fock include several products of four orbital functions. The product of Gaussian functions revealed itself more easily than the function of the Slater type orbital. The mathematics facilities with the Gaussian functions reduced considerably the computational resources necessary in comparison with the Slater type orbital. Different generations of basis sets were developed involving more or fewer orbital functions. For example the small basis sets (STO-*X*G) are composed of the combination of *X* Gaussian functions. Usually the basis sets, from STO-3G to STO-6G are employed but remain obsolete. The split valence basis (*X*-Y1G) utilized only three Gaussian functions, where two of them include *X* and *Y* primitives for simulatating respectively the core and the valence orbitals. The 6-31G basis set is largely employed and declined with different extensions.

Recently, the complete basis sets, which takes into account larger shells (d, f, g, or higher) were carried out. In accord with the partitioning of S. Huzinaga and T.H. Dunning, the number of functions increased greatly. The carbon atom for example, will be treated with ten basis functions in the case of double zeta. The order of zeta describes the number of different ζ exponents (equation 1.58) employed in the Gaussian functions. The declination of functions with different exponents helps particularly to represent the close energetic differences of

several atomic configurations, as for example s^1d^9 or d^{10} by some metal. To simulate the anions including a delocalized electron in the external shell, a diffuse Gaussian function is added. The method could be also enhanced by an added perturbation corresponding to the electron correlation similarly to the post Hartree Fock methods, (as for example the couple-cluster method). The aug-cc-pVTZ basis set employed throughout this work represents an augmented (aug- for the diffuse function), correlation-consistent-polarized (cc-p for the perturbation taken into account), Valence (correlation applied on valence electron), Triple Zeta (three zeta exponents included) basis set.

Chapter 2:

Experimental Setup

The successful IR measurement of cyanocarbanions and oxocarbanions was afforded by the conjunction of a magnetron sputter source with a tandem (ring ion trap / mass spectrometer) and a tunable IR laser system. This conjunction was made possible in the framework of a collaboration between the Freie Universität in Berlin and the Fritz Haber Institute in Berlin. The source using the sputtering technology, well established for the deposition of metallic layers, revealed itself also as a fruitful way to generate small carbon aggregations in gas phase. The reaction of those clusters with nitrogen or oxygen produced the useful ions of interest. However, the small density of ions produced rendered the IR photodetachment particularly pertinent for this experiment. Crucial in the attempt to investigate the molecules of interest, the sputter source is described in depth. Therefore follows a description of the successive elements encounter by the ions during their flight in the experimental setup until their detection.

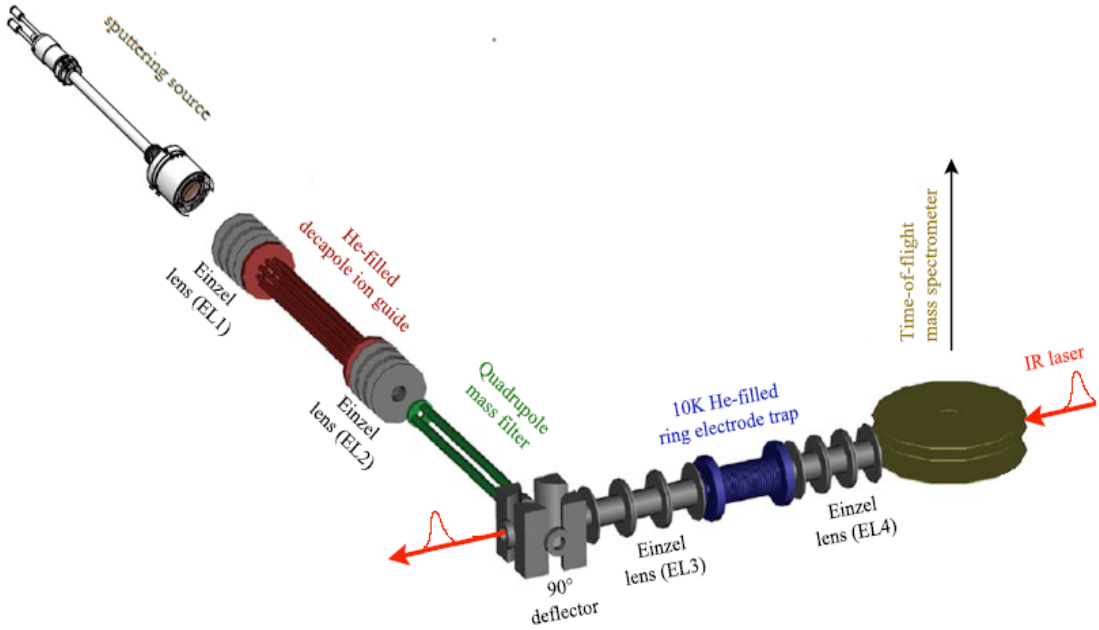

Figure 2.1: Representation of the experimental setup composed of the sputtering source and tandem mass spectrometer trap. High vacuum chambers surrounded the experimental setup and the introduction of gases in the different sections supported the reactions of formation, the cooling and the tagging. The guiding elements of the picture were copied from [108].

2.1 The magnetron sputter sources

Development

Magnetron sputtering constitutes a widely used industrial process for a wide range of coatings. The disintegration of a cathode electrode through the bombardment by energetic ions constitutes the basic process of sputtering. This process has been development for over more than a century. In 1852 Sir William Grove studied the effect of a glow discharge on a silver surface [109]. A few years later, Julius Plücker demonstrated experimentally the cathode rays [110]. In 1921 J.J.Thomson used the term "spluttering" [111] to designate the impact of ions on a target in his theory prefiguring the collision cascade model (cf. chapter 1). Then, the process (preferentially called by the metaphor "sputtering") experienced a remarkable development through the concept of J.M. Penning, which associated a crossfield electron trap (made of magnetic and electric fields) [112]. The development of this concept leads to the establishment of magnetron sputter source. The cylindrical magnet is designed in order to form electromagnetic fields able to trap the ions. Classically, central and external poles guarantee concentric magnetic field-lines (figure 2.3). The sputtering process forms a plasma in the vicinity of the target. The plasmas are composed of a quasi-neutral gaseous mixture of the ions, where positively and negatively charged ions remain unbounded. The simultaneous presence of an electric field and a magnetic field in the magnetron sputter source influences the charged molecule of the plasma. According to the Lorentz force, the ion experienced a drift movement [113]:

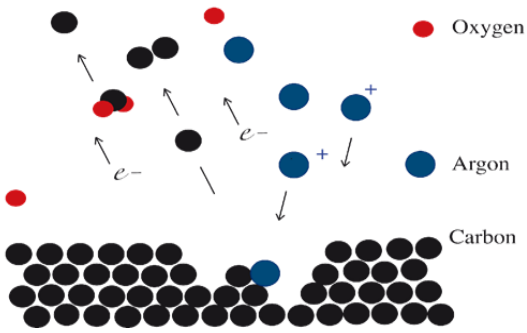

Figure2.2: Representation of sputtering process with disintegration of the carbon cathode. The impinging argon ions provoke the escape of carbon atoms. The presence reactive oxygen gas allow formation of cluster with substituted atoms. Details of the process are presented in chapter1.

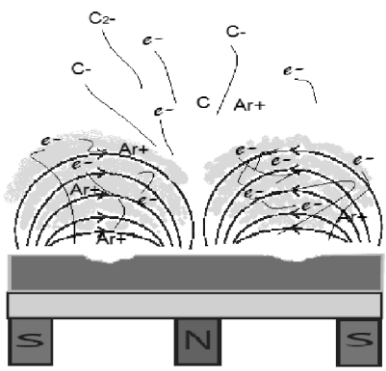

Figure 12.3: Representation of a magnetron sputter source with the magnetic fields lines originated from the central and external poles and the plasma resulting (light grey color)

$$\vec{v}_{E\times B} = \frac{\vec{E}\times\vec{B}}{B^2} \tag{2.1}$$

The experimental conditions are set up to constrain the secondary electrons in the vicinity of the collision region. Thereby the collision, the density, and the rate of collision are enhanced. Additional ionizations by electron-atom collisions also occur in the plasma.

Sputtering Source

The source employed in the experiment was a conventional and commercial magnetron sputter source (*TORUS 2"HV from Kurt J. Lesker company*). The circular head, made of steel and copper, included a circular carbon target with a diameter of 2 inches. The 0.25 inch thick target came from originated also from Lesker Company, which guarantees a purity of carbon at 99,999%. The thickness of the target is adapted to the rare earth magnet located under the stand of the target. The head of the source possessed a sputtering gas inlet close to the surface of the target. This lateral inflow was distributed all around the target through a groove on a ring holding the target (nr. 3 in the figure 2.4). A power supply warranted a power of the target up to 500 W DC on the cathode (nr. 10 in the figure 2.4). A water-cooling in contact with the copper cooling well kept the sputtering head cool.

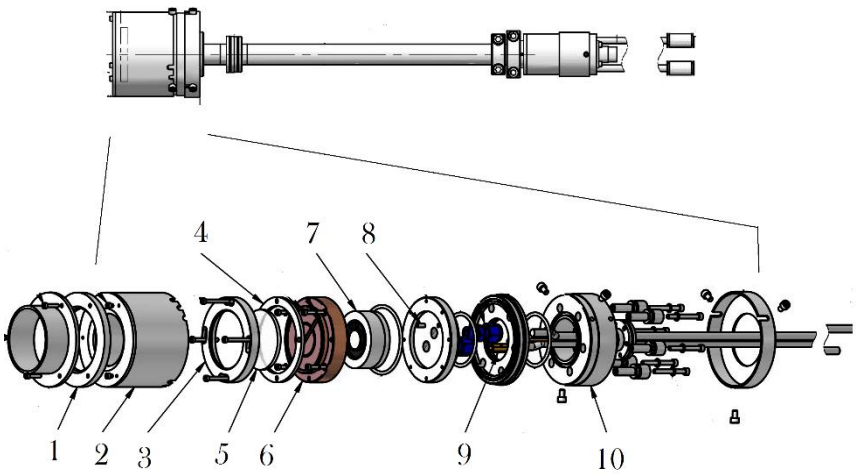

Figure 2.4: Representation of the sputter source and the principal elements, which compose the sputter head : 1) gas distribution ring, 2) space shield weldment, 3) and 4) target hold rings, 5) target, 6) copper cooling well,7) magnet, 8) water inlet 9) high voltage wire,10) cathode. Picture adapted from [114].

The sputtering head is mounted inside a vacuum chamber (figure 2.3). The source is axed strictly perpendicular to the lateral flanch of the chamber, ensuring the axial alignment of the emission in the chamber. The connection of the source with the flanch is located on the extension tube of the source. At this connection, an o-ring permits an adjustment on the transversal axe. The optimal distance of the sputter head distance from the skimmer constitutes an influencing parameter in the distribution of the cluster detected. As determinant parameter, is constituted by the pressure surrounding the sputter head. The growth process of cluster is greatly influence by the pressure of the buffer gas as well as the

pressure of the reactive gas and of the vapour originated from the target (cf. chapter 1). In the chamber, a recipient surrounds the sputtering head. This recipient, where the gases were introduced, supports a gradient of pressure. The buffer gas and reactive gas and sputtering gas inlet are located inside the recipient, which is separated from the rest of the chamber, where a deeper vacuum exists. The turbo pump connected to the rest of the chamber ensures a vacuum usually 1.10^{-4} to $4\ .10^{-4}$ mbar (during the experiment with gas introduction). The higher pressure supported the reactions with the reactive gas and the production of larger clusters, whereas the lower pressure in the chamber supported the purity, where a very restricted quantity of remaining gas could react with the clusters.

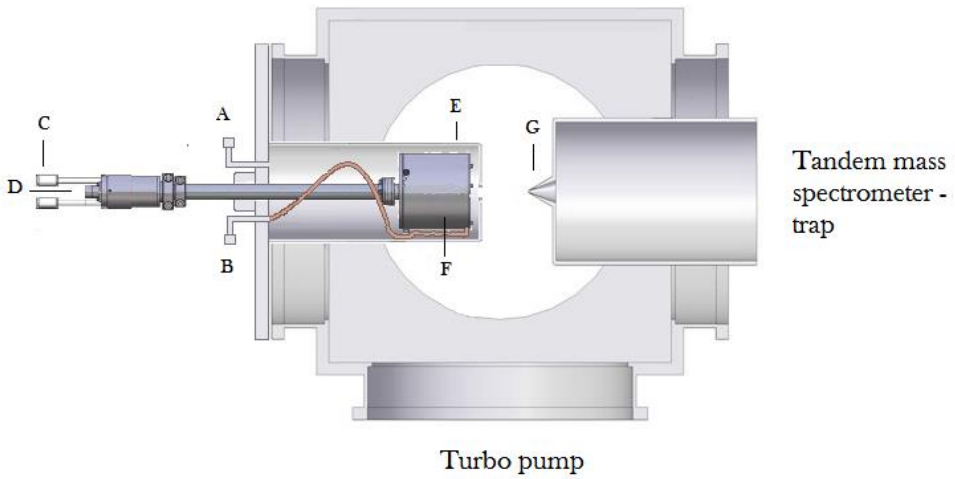

Figure 2.5: sectional representation of the source in the high vacuum chamber. A) buffer gas inlet, B) Sputter gas inlet C) Water cooling D) power supply, E) recipient F) sputter head G) 3mm skimmer Sputter gas inlet.

The whole chamber was connected with a turbo pump TMH 1601 P *(Pfeiffer vacuum)* associated with a rotary vane pump Typ E2M18 (*Edward*). The pressure 1.10^{-6} mbar could be attained in a few hours without sputtering operations and gases inflows.

Reactive gas introduction in sputtering process

The addition of reactive gas in the sputtering process is necessary to obtain the clusters of interest in this work. The sputtering carried out with O_2^+ and N_2^+ was already reported for the enhanced production of charged sputter yield [54-55]. The introduction of the reactive gases is carried out in same place as the argon gas inlet. The design of the gas inlet allows a supply of the gas all around the target, close to the region of the plasma. The productions of the targeted clusters, which are structurally approaching organic molecules, require different gases. Therefore, a set was built in order to control and secure the purity of the introduced gases (Figure 2.6).

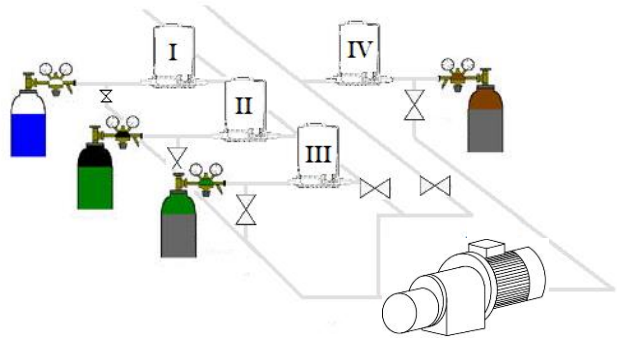

Figure 2.6: representation of the gas inlet composed of four mass flow controllers (I, II. III. IV). The gas argon, oxygen and nitrogen share the same inlet arriving on the gas distribution ring (figure 2.4) The Ne buffer gas is connected to an extra inlet arriving at the bottom of the recipient surrounding the sputter head (B on the figure 2.5).

The flows of the different gases are handled through a set of digital mass flow controllers of different capacities 10 sccm, 50 sccm and 100 sccm *(company Aera)*. Each gas is connected to its own mass flow controller. The mass flow controllers are tuneable through increments of 0.5 sccm and guarantee an accuracy of 0.5%. To limit contamination, the gas lines were connected to a rotary vane pump.

The sputtering process is dependent on the pressure, which itself the dependents on the pumping and reaction of the reactive gas with the target and with the sputter yield. Thereby the sputtering could be described as non-linear process. In order to describe the behaviour of the sputter source, a model, known as Berg Model, was completed [115]. In this model the influence of the reactive gas on the pressure is taken into account. Parallel, the influence of the contamination of the target, is described by a fraction Θ_t of the target, which is contaminated by the reactive gas. The sputter yield may have originated from two fractions, contaminated or not, respectively Y_{mc} and Y_{mm}. Through balance equations, the rate F of sputtering could be expressed:

$$F = \frac{J}{q}[Y_{mc}\Theta_t + Y_{mm}(1 - \Theta_t)] \tag{2.2}$$

Where J represents the current ion density and q an elementary charge.

Very recently an upgrade was made on the Berg model, where in addition to the chemisorptions different poisoning processes are taken into account [116]. The reactive gas molecules are considered to not only contaminate the surface, but also deeper layers (up to 50 angstroms).

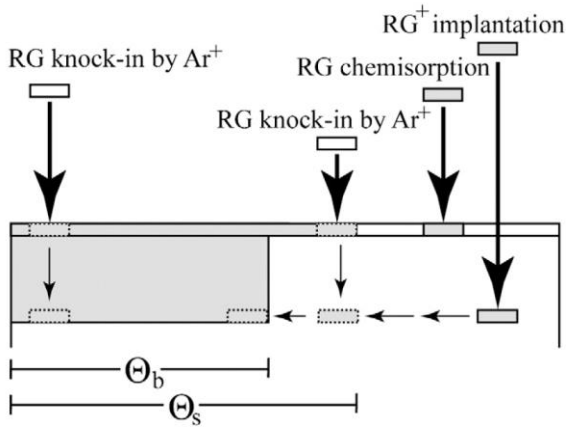

Figure 2.7: Representation of the different process of contamination of reactive gas (RG) on metal target. Θ_s and Θ_b represent the contaminated fraction of target respectively at the surface and at the sublayer. Picture copied from [119].

The impinging ions collide with atoms of the reactive gas located at the surface of the target. Thereby, reactive atoms are pushed to deeper layers in the target. This contamination process is defined as knock-in. The reactive gas atoms are ionized in the plasma and become projectiles similarly to argon ions. Thereby the ions attain a deeper layer, where they could remain. In this case a contamination occurs known as an implantation. Taking in account these different contaminations, the balance equation could be written for the surface and the sub layer as:

$$2\alpha_i \frac{J}{q}\left(\frac{P}{P_A + P}\right)(1-\Theta_b) + \frac{J}{q} Y_k \Theta_s (1-\Theta_b) = \Theta_b \frac{J}{q}[Y_{mm}(1-\Theta_s) + Y_{mc}\Theta_s] \quad (2.3)$$

$$\frac{J}{q} Y_c \Theta_s + \frac{J}{q} Y_k \Theta_s = 2\alpha_s F(1-\Theta_s) + \Theta_b \frac{J}{q}[Y_{mm}(1-\Theta_s) + Y_{mc}\Theta_s] \quad (2.4)$$

where P_A is the argon pressure, Y_k the knock-in yield, Y_c the sputter yield compose of reactive gas atoms, Θ_s contaminated fraction of the surface Θ_b contaminated fraction of the sublayer, α_i direct implantation probability α_s sticking coefficient.

2.2 The mass selection and the trapping

The IRPD method employed in this work requires a mass selection and a trapping of the systems of interest. After the production, the ions are guided through different RF multipole elements. Upstream, a decapole collimated the beam, followed by a quadrupole mass filter selecting the masses, then the ring electrode trap confines the ions in order to support the tagging. The spectroscopy is performed by a laser beam, which attains the ions shortly after the extraction from the trap before the detection through the TOF mass spectrometer.
The concept and the design of the combination mass spectrometer/ ring ion trap originated from Gerlich and coworkers [117]. The experimental setup has been built and develop in the group of Prof. Knut R. Asmis at the FHI in Berlin. With the present instrumental set up the ions investigated are leaded through a succession of guiding elements (cf. the figure 2.1), which are described below. The elements, which constitutes the system have been several times in depth reported [96,108,117-118].

Decapole

In order to collimate the beam of ions, a decapole is located close after the source. The decapole belongs to the RF multipoles, where $2n$ poles influence the ions trajectory. The $2n$ pole (n =5) take the form of parallel rods, arranged in a circle with a radius r_0. The center of the circle is aligned with the ions beam. The same potential is applied to all the electrodes with the charge alternation on the successive rods. In vacuum, from the derivation of the Maxwell equation, the Laplace equation describes the electric potential Φ:

$$\Delta\Phi(r) = 0 \tag{2.5}$$

which could be expressed in polar coordinates (r, ϕ):

$$\Phi(r,\phi) = \Phi_0 \left(\frac{r}{r_0}\right) \cos(n\phi) \tag{2.6}$$

If only a continuous potential is applied on the rods, this potential take the form of three dimensional saddle. In this characteristic saddle form, the center of r_0 corresponds to the intersection of the maximum and the minimum of the potential originated from the rod supplied with respectively a positive and a negative potential. The ions do not remain at the center attracted by the rods of the opposite sign. To constrain the ions in the center of the area delimited by the rods, a RF frequency is added:

$$\phi_0 = U + V\cos(2\pi f t) \tag{2.7}$$

The effective potential, which govern the ions motion, depends of the number of rods:

$$V^* = \frac{n^2 q^2 V^2}{4m(2\pi f t)^2 r_0^2}\left(\frac{r}{r_0}\right)^{2n-2} + qU\left(\frac{r}{r_0}\right)^n \cos(n\phi) \tag{2.8}$$

Where m represents the mass of the charged molecules involved. The effective potential experiences a minimum on the center of the circle inscribed in the rods.

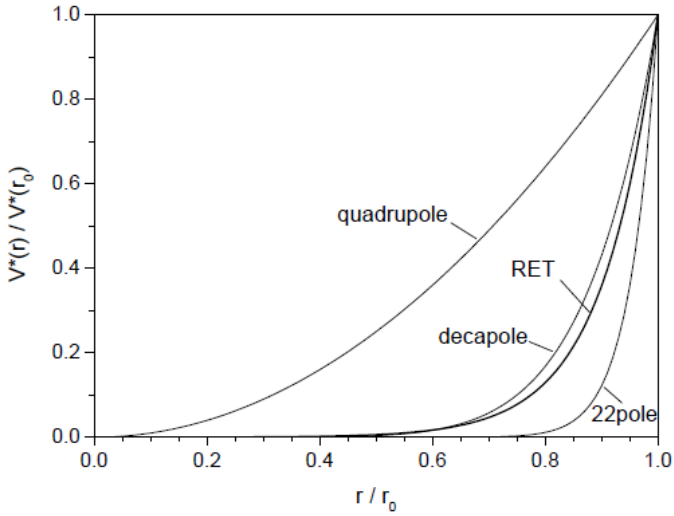

Figure 2.8: Radial dependency of the effective potential in different RF multipoles: decapole (5*n*) and 22 poles as well as elements also present in the experimental setup: quadrupole (2*n*), and the ring electrode trap. Picture copied from [108].

Increasing the number of the rods, the centered minimum of effective potential become larger and its lateral slop become steeper on the side and closer to the rods. The multipoles are able to increase the collisional cooling and to collect the ions more efficiently than a multipole composed of four rods. The decapole is particularly efficient in a way to guide simultaneously a large mass range. The decapole used is 22 cm long supplied with 3.9 MHz and Umax of 400 V. Helium is introduced in the guiding chamber to improve the collimation, attaining a pressure close to 1.10^{-4} mbar.

Einzel lens

The guiding of the beam was also sustained by einzel lenses placed before and after the RF mass filter. The name einzel, which means single in German introduce the fact that only one potential between the central and the outer electrodes is sufficient to characterize the lens. Three electrodes composed the lenses, where the first and the third carry the same voltage. Usually the two outer electrodes are grounded and the central electrode is put on a voltage of the same charge as the ions of the beam. In the case of a higher voltage applied on the central electrode the einzel lens first decelerate and then accelerate the beam. Two lenses were also located before the trap and before the TOF.

Quadrupole

The quadrupole mass filter utilizes the trajectory stability to separate the ions in function of the mass/charge ratio. The quadrupole belongs to RF multipole composed $2n$ (n=2) rods. The rods usually present an elliptical cross section. In this case the Laplace condition are respected:

$$\nabla^2 \phi_0 = 0 \tag{2.9}$$

Where:

$$\phi = \frac{\phi_0}{r_0^2}(\lambda x^2 + \sigma y^2 + \gamma z^2) \tag{2.10}$$

Where λ, σ ,γ represent the weighting factors. In the case of the quadrupole: λ = - σ and γ = 0. The movement of the ions within the quadrupole could be expressed:

$$m\ddot{x} + 2\, e(U + V\ \cos \omega t)\ \frac{x}{r_0^2} \tag{2.11}$$

$$m\ddot{y} - 2\, e(U + V\ \cos \omega t)\ \frac{x}{r_0^2} \tag{2.12}$$

Through the definition of two parameters a and q (along both axes x and y)

$$a_x = -q_z = \frac{8eU}{mr_0^2\Omega^2} \tag{2.13}$$

$$q_x = -a_z = -\frac{4eV}{mr_0^2\Omega^2} \tag{2.14}$$

where Ω represents the radial frequency of the potential applied made of a RF and a DC component, the movement of charged particles could be represented by Mathieu equation involving oscillating parameters [119]:

$$\frac{d^2u}{d\xi^2} + [a_u - 2q_u\cos(2\xi)]u = 0 \tag{2.15}$$

Where $2\,\xi = \omega t$.Depending on the parameters a and q the equation forms stable and non-stable solution. The limit between stable and unstable solution could be represented in stability diagrams. Assuming the Mathieu equation is taken into account along two dimensions, a stability area could be delimited (picture 2.9).

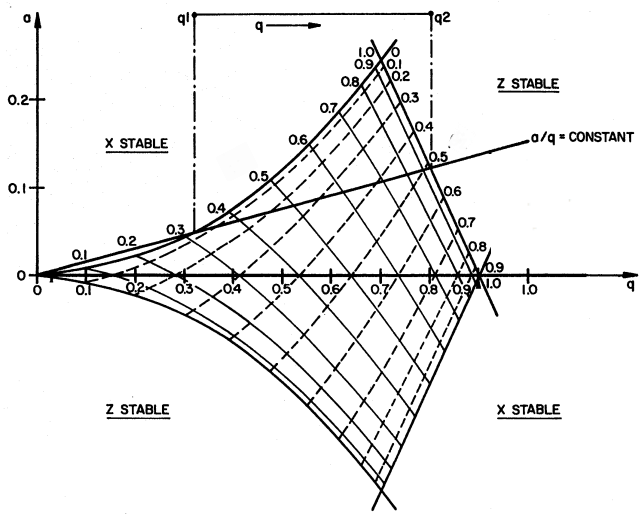

Figure 2.9. Stability area of the ions in the quadrupole as function of the a and q parameters. The ratio a/q remains constant and represent the operating line, which delimit the stability conditions between q_1 and q_2 and thus defines the bandwidth of the filter. Picture adapted from the patent of the ion trap mass spectrometer system and method (US 5420425 A)

Depending on the operating ratio $a\ /q$, the stability area is more or less restricted (figure 2.9). This allows a discrimination of the ions in function of their ratio mass/charge.

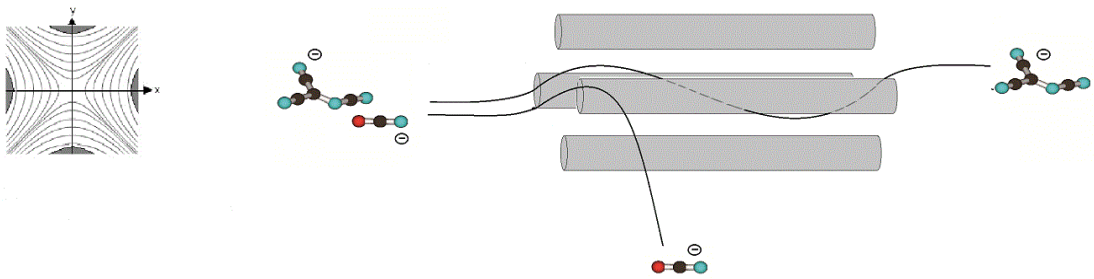

Figure 2.10 Representation of the quadrupole, sectional with the field lines (links) in perspective with ions ways. Only a limited ratio mass/charge experiences a stabile oscillation in the quadrupole and continue their way through the experimental setup.

The experimental setup was equipped with a CMS quadrupole mass tri-filter (Extrel). The tri-filter mass contained a pre and post filter to increase the transmission. With the operating radio frequency of 1.2 MHz, the quadrupole covered a range from 2 to 2000 amu.

Ring Ion trap

The ring ion trap also belongs to the RF multipole element. In this case the weighting factors (equation 2.10) correspond to: $\lambda = \sigma = 1$ and $\gamma = -2$. The ions oscillate transversally in the z axis in the trap. Two potentials form barriers at the entrance and the exit of the trap. The barrier at the entrance is low enough to permit the entrance of the incident ions. In the trap the ions lose energy through collision with buffer gas along their path to the trap. Thereby the entrance barrier is high enough to constrain these trapped ions inside the RF multipole. The ring ion trap was designed to confine the ions in a cylindric space of 10mm in diameter and 50 mm in length. 24 ring 1mm thick electrodes surrounding the trapping space. Isolation disks are interposed between the electrodes and each electrode became the opposite voltage phase -350 V/ 17 MHz of the adjacent electrodes. The messenger D_2 is introduced under the gaseous form of deuterium dimer, which represents ~1% of the gas present in the source. The messenger attachment:

$$C_x + \ D_2 \ \rightarrow \ C_x - D_2$$

corresponds to a weak bond (van der Walls). The weak nature of the bonding attachment requires a low intern energy of the ions. The access of temperature of down to 10 K is supported by the closed cycle helium cryostat (*Sumito Heavy Industries*). The control of the temperature is practiced through a heating mounted between the cold head of the cryostat and the trap. The extraction and the detection of the ions imposes the control the ion packet. A surrimposed DC potential allow for transverse control of the ion packet. Six segments of the trap formed a gradient and the DC potential guided the ion packet in the trap. The extraction mode was generated by the remove of the energy barrier at the exit of the trap, which remained strong enough to constrain ions in the trap throughout the filing phases. In the whole trap a gradient of potential forms a ramp, which focuses the ions cloud in space as well as in time. This collimation remains crucial for TOF detections. An einzel lens placed between the trap and the TOF spectrometer assists the collimation.

TOF spectrometer

The Time of Flight (TOF) spectrometer deduces the mass of the detected ions from the traveling time. Submitted to electric field, the kinetic energy of the ions is proportional to the squared ratio mass/charge. The TOF presents the major advantage, to detect a whole spectrum from a single bunch of extracted ions. By the extraction from the trap, the kinetic energy of the ions is controlled by the voltages apply on the trap and the pressure in the chamber. The system mounted in this work is a Wiley-McLaren TOF mass spectrometer. Two steering plates are able to induce a potential of 5000 V and to steer the ions into the TOF flight perpendicular to the axe of extraction of the trap. The steering voltages are set on the form of 50 µs pulses delivered by a fast high voltage transistor switch (*Behlke Power Electronics GmbH*). This system used the principle of push-pull circuit and delivered pulses with a rise time and fall time of 10 ns. The opening of 20 mm in the plate permits to detect the ion packets. After a flight of 55 cm, the packets of pulled out ions attain and hit the Multi Channel Plates (MCP). A Pre-amplifier amplified the signal before than a 12-bit high speed digitizer sampled connected on the computer. A second way of ions detection was available through a channeltron placed on the axe of the trap extraction. The steering plates are grounded and the ions could attain unperturbed the channeltron electron multiplier. The flow of electrons induced by the channeltron is sent to a counter under TTL (transistor-transistor-logic) pulse.

2.3 The laser system

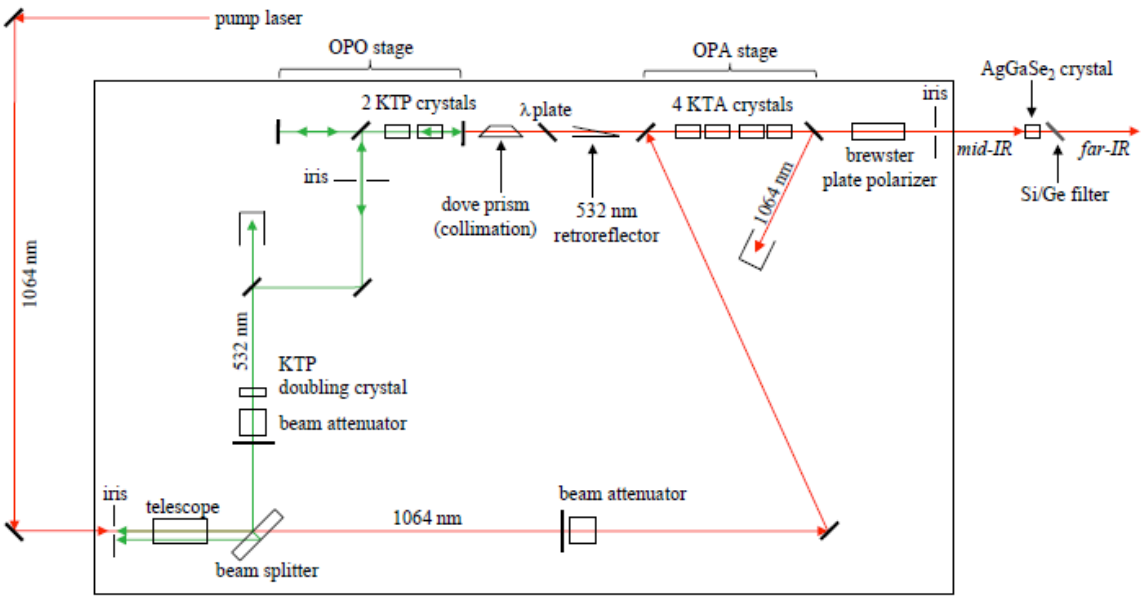

Figure 1.6: Representation of the laser system.. The red color represents the IR beam, and the green represents the beam of 532 nm. The picture is copied from [121]. Helium atmosphere is carry out in the experimental setup in order to avoid water absorption.

The infrared beam employed in the experiment is delivered from a system combining an Optic Parametric Oscillator (OPO) and an Optic Parametric Amplifier (OPA) following the design of Gruyer and coworkers [120]. The fundamental wavelength at 1064 nm delivered by Nd:YAG laser (*innolas, spitelight*) pumps the system with pulse of 7 ns and a repetition rate of 10 Hz. The beam is splitted, and two third of it are doubled through a KTP (Potassium Titanyl Phosphate) crystal. The wavelength of 532 nm experienced a Difference Frequency Mixing in the KTP crystal and the incident photons were splitted in signal and idler.

$$\frac{1}{\lambda_{PUMP}} = \frac{1}{\lambda_{SIGNAL}} + \frac{1}{\lambda_{IDLER}}$$

The orientation of the axes of the crystals influenced the wavelength emitted. By the horizontal rotation of the crystal, the wavelength of the signal sweeps a range of 710 nm to 880 nm, whereas the idler wavelength took the corresponding values from 2120 nm to 1350 nm. A second DFM process takes place in the OPA stage. The idler, which originated from the first frequency mixing by the OPO and the split part of the pump laser arrived are

focused on another set of KTP crystals. The tilted polarization of the OPO idler was corrected in the same polarization as the pump beam through a plate λ/2. The pulse emitted could sweep the domain from 2056 cm^{-1} to 5020 cm^{-1}. A brewer window was employed in order to filter the signal emitted by the OPA. The domain of IR 1000 to 2400 cm^{-1} is crucial for this work, corresponding to the absorption band resulting from the stretch mode of the anions investigated. For attaining the far IR another DFM process is set up through an $AgGeSe_2$ crystal receiving the idler and signal of the OPA (the brewer window is in this case removed). This extension allow for cover a region between 1000 and 2137 cm^{-1}, which is targeted in this work. The investigations are made with the two lasers setup in order to cover the range of 1000 cm^{-1} to 2400 cm^{-1}.

Chapter 3:

Ions production and spectra

The present work focuses on different types of ions: carbanions, cyanocarbanions, oxocarbanions and oxocyanocarbanions. Based on carbon atoms, these ions were produced by the sputtering of a graphite target. Oxygen and nitrogen were employed as reactive gas and influenced the sputtering process. The sputtering process in presence of reactive gas was the subject of many experimental and theoretical studies [54-55, 115-116 122-125]. The high efficiency of the clusters production was crucial for the whole experiment. The observations and the control of the ions production under the different conditions constituted a preliminary and necessary step of the experiment, which is presented in the first paragraph. The panel of the clusters produced by the source was revealed through mass spectrometry. The examination of those mass spectra evidenced the nature and the formation process of the ions.

3-1 Ions production

3-1-1Non-linear gas pressure dependency and hysteresis

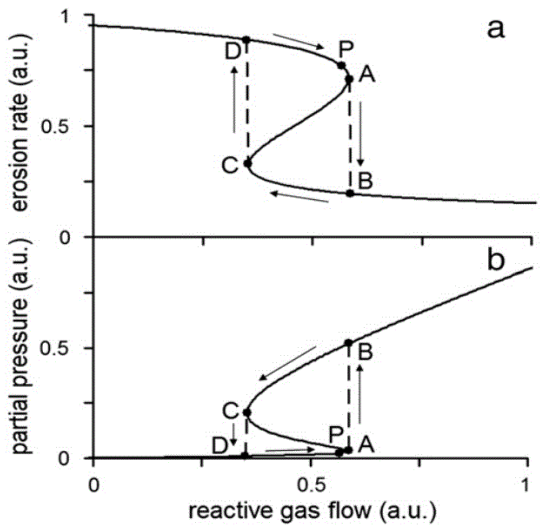

Figure 3.1: Schematic processing curves for erosion rate (a) , and partial pressure of reactive gas (b) as a function of the reactive gas flow. The metal mode corresponds to the transition from D to A and the compound mode from B to C, the preferred processing point P correspond to high erosion with stochiometric composition and abundant formation. Schema taken from [123]

The sputtering process is controllable through the regulation of different actors, mainly through the power of the source, the flow of the gases and the concentration of the gas mix. The reactive gas is consumed by the reaction with the sputtered atoms, by the reaction on the target, and by the pumping of the chamber. In the Berg-model [116] (cf. chapter 2) the flow of reactive gas influences dramatically the process and the activity of the source, creating a hysteresis behavior. Abrupt transitions appear between three different modes. In the presence of low reactive gas flows, the metal mode occurs, which presents abundant cluster formations but with sub-stoichiometric composition. By high gas flow, the compound mode, also named poisonous mode, is observed, with low formation and stoichiometric composition. The mode in between presents the favored properties of high formation with stoichiometric composition. At the start of the sputter source, the path to find the optimal

conditions is not direct. Some intermediate conditions, principally a high flow of reactive gas, have first to be fulfilled to then attain a stable and optimized sputtering. This experimental behavior of the source used for this thesis describes a hysteresis behavior similar to the Berg-model.

3-1-2Time evolution of the charged sputter yield

Beyond the balance between different regimes inevitable during the start, the production of ions changes slowly over the hours of experimentation. The conditions are permanently adjusted to obtain the optimal ions formation over the time. The voltage measured on the skimmer is dependent on the flow of charged particles produced by the sputter head, and reveals the activity of the source. The evolution of this activity compared to the evolution of the optimal gas flows and the power applied to the source are presented in the figure 3.1.

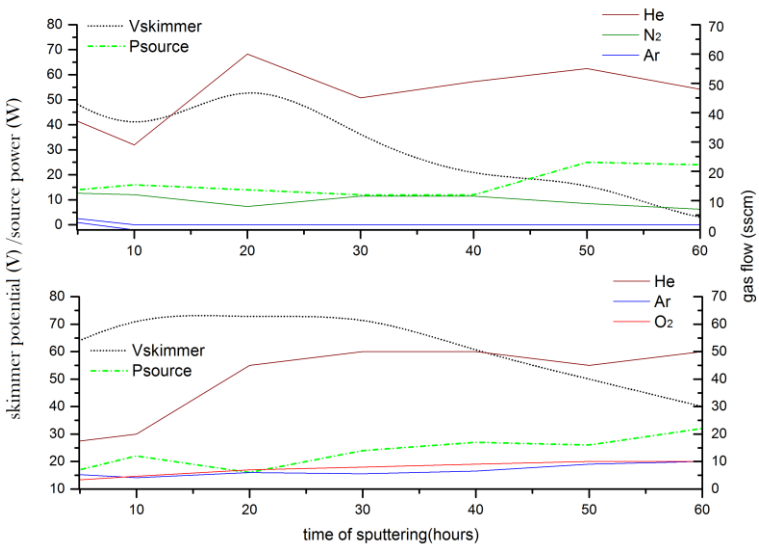

Figure 3.2: The activity of the source represented by the voltage on the skimmer and the optimal conditions represented by the gas flows and the power of the source over the time of sputtering, in the presence of N_2 (up) and of O_2 (down). The mounting of the target on the source defines the time 0 on the graph.

The source production reaches a maximum after 20 hours in the presence of O_2 as well as in the presence of N_2. After the maximum, the source production decreases slowly. To obtain the strongest signal, the gas flows and the power of the source are increased in the course of the hours of sputtering. The helium flow is regularly increased until the cap of 20 hours and only slightly increased after this cap. The power of the source needs to be increased after 20 hours. The sputter source is generally employed 10 hours in a row, with breaking time of 14 hours in between. Respecting the same procedure for each sputtering sequence excludes the influence

of some parameters on this evolution. The temperature of the head, the vacuum in the chamber and the pumping strength are similar at the beginning of each sequence. The structure of the target experiences a continuous evolution principally through the poisoning and the erosion. The chemisorption of the reactive gas is high enough to play an important role in the sputtering efficiency [116](cf. chapter 2). The contact with the free-air before the mounting of the target in the vacuum chamber certainly affects its surface. It's already known that the sputtering erosion concerns single atoms and that the metallic atoms of the target are snatched more easily than contaminating atoms of reactive gas implanted in the structure [52]. The air-poisoned layer can slow down the sputtering process and explains the maximum production after 20 hours. The erosion of the target surface concerns principally a restricted area, where an annular deepening is formed (figure 3.3.) The hours of erosion of the surface could explain the slow decreasing of the ions production after the maximum.

3-2 Comparison between the sputter process with O_2 and N_2

Already from the start of the sputtering process, the use of O_2 and N_2 influences differently the procedure. Focused on the anions production, the adjunction of the reactive gas N_2 strongly increases the signal. The argon usually employed as sputtering gas, could be totally replaced by the N_2, which plays both the role of sputtering gas and of reactive gas. This way, the production of anions containing many nitrogen atoms is sustained. For the case of O_2, its addition in the source dramatically disturbs the production of anions. The procedure requires at the start of the source the absence of O_2 and the presence of only argon, as sputtering gas. The flow of O_2 has to be introduced slowly and progressively. The detections of anions using O_2 as reactive gas is clearly less efficient than with N_2. Oxygen atoms present a 3 eV smaller ionization potential than the nitrogen. Thus, the positively charged oxygen ions and the oxygen atoms with electronegative characters could capture the electrons efficiently reducing the presence of anions. Oxygen atoms are also smaller (60 pm) than nitrogen atoms (71 pm). The poisoning on the target is certainly influenced by the nature and the size of the reactive gas. As shown on the photography of the used targets (picture 3.3), the print of erosion caused by a sputtering in N_2 differs completely from the print of an identical carbon target in the presence of O_2. The flat surface presenting grey shine results on the extraction zone after the sputtering with N_2. For his part the process with O_2 leaves the surface of the target rough and black. The quantity of carbon extracted from the target after the same time and under very similar conditions and source power is higher with O_2 than N_2. The poisoning of sputter targets was recently considered as a more complex process than from chemisorption, which is the only poisoning process taken into account in the first Berg Model [115]. The neutral contaminating atoms could be knocked down in sub-layer through the ions bombardment, and an implantation of reactive gas under the ionic form directly into the sub-layer is also suggested [116]. Theoretical study simulated the contamination processes with different compositions target/reactive gas [124] and confirmed experimental observations [123]. The conclusion of these studies and of our experimental suggests that the target/reactive gas composition which

present low reactivity favor implantations, whereas compositions with high reactivity, produce more chemisorption at the surface and this difference increases under low argon pressure.

Picture 3.3: The surface of the two carbon targets, after 120 hours of sputtering in the presence of O_2 (left) and in the presence of N_2 (right).

The observation of the two targets in the presence of O_2 and of N_2 indicates different kinds of poisoning (see picture 3.3 and 3.4). A predominant contamination on the surface is suspected with regard to the regular flat surface of the target with N_2. The rough structure with O_2 suggested a greater implication of sub-layers.

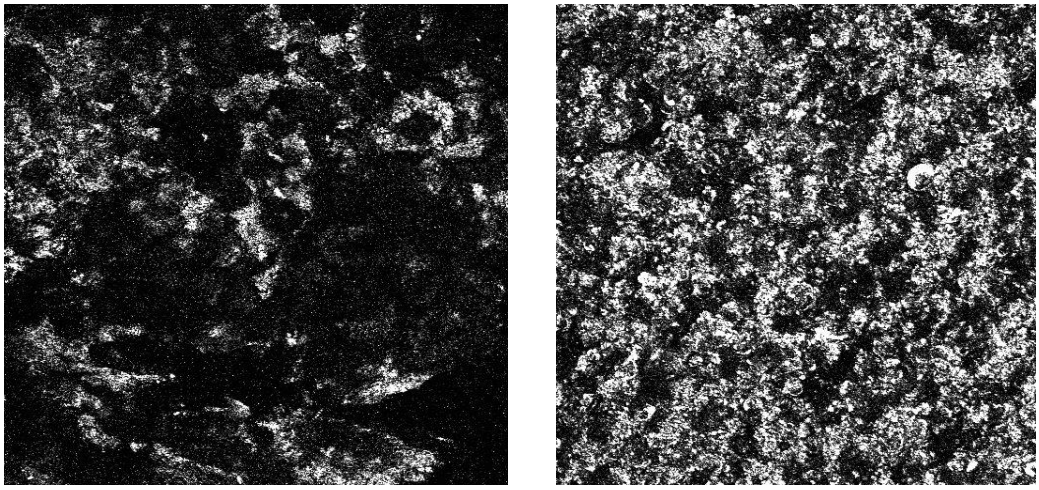

Picture 3.4: The surface of carbon targets presented in picture 3.3 observed with an aggrandizement with a factor 20. [Sputtering in the presence of O_2 (left) and in the presence of N_2 (right)]

The extraction print of the target is not the only different behavior of the source reactive gas dependency. A strong deposition of a black layer is observed on the plates of the sputter head, on the front plate of the cooling recipient and on the skimmer after sputtering with N_2. This deposition layer was completely absent by the sputtering with O_2, even though more material was extracted from the target (see picture 3.3). The strong influence of the gas flow of O_2 on the deposition rate and the composition of the deposition were already reported previously [56]. The sudden fall in the deposition rate with O_2 gas flow > 25 % partial pressure was demonstrated and attributed to the poisoning regime. The plasma takes a different color depending of the present gas. A red-orange to red-purple plasma is observed in helium and nitrogen and white with in the mixture of O_2, Ar and He. The color of

the plasma results from the relaxations of the energy levels involved depending on the atoms. These colors are comparable with the usual pale yellow color of plasma in O_2 and red to yellow of plasma in N_2 used in the industry.

3.3 Mass spectra in the presence of N_2

3.2.1 Negatively charged ions

Using N_2 as reactive gas and sputtering gas, the source produces abundant anions as revealed by the mass-spectra. The clusters produced by the source are mainly formed of nitrogen and carbon atoms, C_xN_y. Formation of doubly charged anions is possible, but none of them were clearly detected. The doubled ionized $C_5N_2^{2-}$ corresponding to the very abundant $C_5N_2^-$ could be expected. The signal of the mass 44 corresponding to $C_5N_2^{2-}$ was less than 500 times weaker than the signal of the single charged anions and not distinguishable from the experimental noise. The multiply charged anions will be thus neglected over the experimentation.

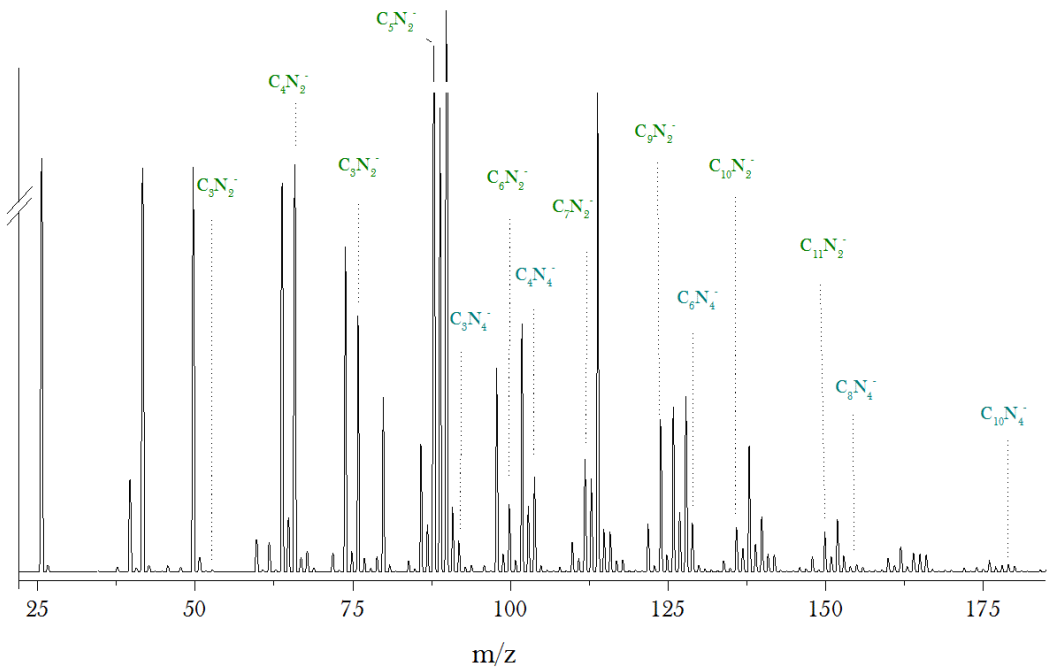

Figure 3.5: Mass spectrum of negatively charged anions produced by the sputtering source under 25 W with 14.5 sccm N_2 und 33.6 sccm He.

The distribution remains centered at 100 amu and the three masses 88, 90 and 114 were particularly abundant corresponding to $C_5N_2^-$, $C_4N_3^-$ and $C_6N_3^-$ respectively. After 100 amu, the ion signal decreases with the size but remains high enough for numerous systems up to 200

amu. Beyond this mass the ion yields are negligible. The decreasing part of the distribution on the side of the large cluster is explainable through:

-a) Only lone carbon atoms escape the target surface and the growth of clusters is time dependent process (cf. chapter 1)

-b) The size of the cluster in the sputter process is power dependent (cf chapter 1) and the power utilized in this work is up to some hundreds eV.

-c) The greater ratio of charged/neutral particles for the size up to 10 atoms was systematically observed by the sputtering of different target composition [56].

The low signals of the small anions are explainable by:

-The coalescence, which could take part in the cluster growth (cf chapter 1), where the cluster larger than a critical size grows and smaller sizes evaporates.

- The electronaffinity of the carbon chain as well as carbon chain containing nitrogen, which becomes larger with the size [23,24].

The low signal of C_x^- reveals a very strong reactivity of the nitrogen on the negatively charged carbon clusters. The $C_xN_y^-$, which include small number of nitrogen, are particularly abundant and the formation of anions with up to 5 nitrogen atoms is clearly identified. The anions, which present a smaller number of carbon atoms than nitrogen atoms are disfavored. Thereby the number of strong peaks grows for larger masses. Six series of peaks are observed spaced by 12 amu, which correspond to the $C_xN_y^-$ y = 0 to 5. The anions with more than 5 nitrogen atoms present the same masses as the systems with a smaller number of nitrogen atoms. For example, the $C_xN_6^-$ presents the same mass as C_{x+7}^-. The low signal of the C_x^- could mask only a few $C_{x-7}N_6^-$ and by extrapolation all the anions y > 6 should be very rarely formed. For each number y of nitrogen atoms the distribution of the anions as a function of the number x of carbon was examined (figure 3.6). Different levels of nitrogenation share a strong odd/even effect as well as a similar distribution based on a maximum with a roughly symmetrical decreasing signal on each side of the maximum.

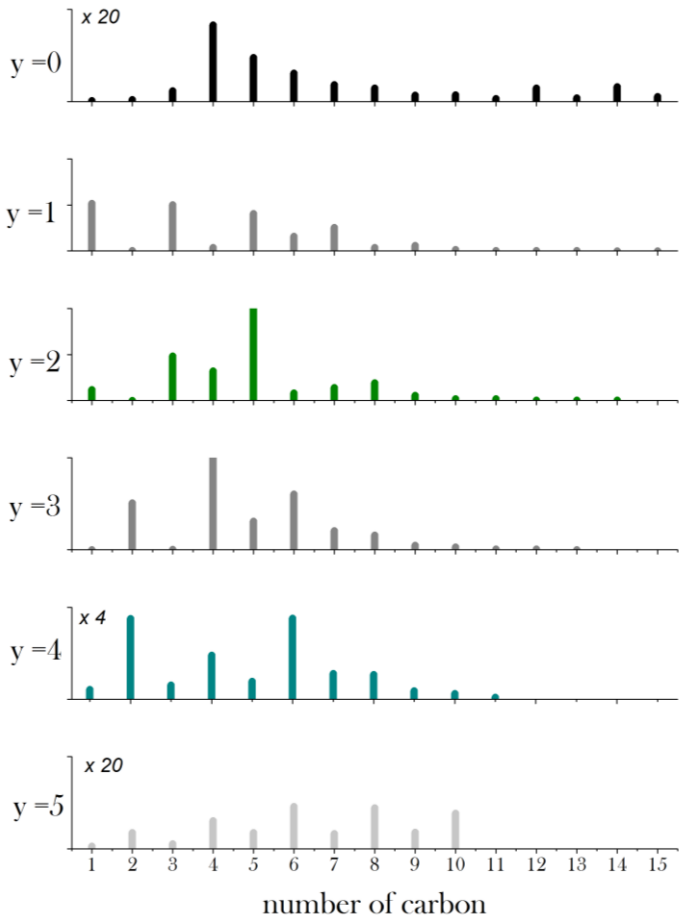

Figure 3.6 Comparison of the signal between the different levels of nitrogenation of carbon chain as function of the number of carbon.

The general odd/even effect of the $C_xN_y^-$ was already evocated previously [125].

3.3.2 Odd/Even effect in the $C_xN_y^-$ anions.

C_xN^-

The anions including one nitrogen atom present a clear preference for the system with an odd number of carbon atoms. Theoretical and gas phase experimental investigations in the IR range on the C_xN^- presented the structure depending of the size [96-118]. The privileged production of C_xN^- with an odd number of carbon atoms in comparison to their homologues with an even number was observed by sputtering process [96]. In this report the odd/even effect was related to the more stable singlet state which present a pronounced polyyne characteristic (-C≡C-) than the triplet state with an accentuated cumulene characteristic (=C=C=).

$C_xN_2^-$

The group containing two nitrogen atoms presents a strong maximum at x = 5 and a preference also for odd numbers of carbon atoms, except for x = 8. This is one rare exception in the odd/even rule that the other carbon nitrides follow. The calculations at the B3LYP aug-cc-pVTZ level reveal the dinitrile structures and the doublet multiplicity for the lowest isomers of all anions in this group (chapter 4). The main systematic odd/even difference in the structure resides in the alternation of bond lengths. The calculated bond lengths of $C_xN_2^-$ for the odd x include two consecutive C-C bonds of the same length hindering the polyyne characteristic. For even x, a strict alternation of the bonding length is possible. The predicted structural differences dependent on the number of carbon atoms remain minimal. In order to explain the odd/ even effect, the way of formation of the $C_xN_2^-$ is examined. Anions can be produced by electron attachment in the sputter source region (where the subsidiary energy resulting from the collision could be evacuated under the form of radiation or by collision with the buffer gas):

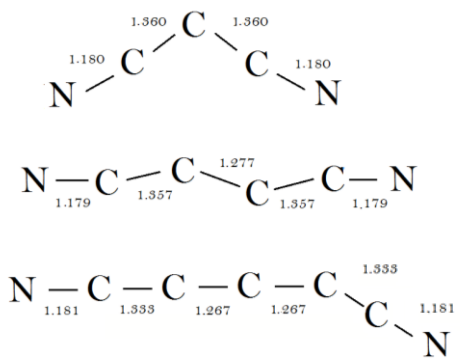

Figure 3.7: Representation of the geometries and bond lengths of the $C_xN_2^-$ (x = 3-5). Schema made from B3LYP/aug-cc-pVTZ calculations presented (in the chapter 4)

$$C_xN_2 + e^- \rightarrow C_xN_2^- + h\upsilon \tag{3.1}$$

Theoretical studies on neutral C_xN_2 structures reveal a singlet ground state for the clusters with the even x and a triplet ground state for the odd x [126]. Not only the HOMO-LUMO gaps and ionization potentials (AIP) are strongly influenced by the number of x but also the electron affinity. The electron affinity (EA) is calculated clearly stronger for the odd x than the even, and increases with the cluster size. In this sense the particularly low electron affinity of C_2N_2 could explain the quasi absence of $C_2N_2^-$. Other ways of formation could happen as well. The introduction and presence of an abundant quantity of nitrogen makes another way of clustering possible:

$$C_xN^- + N \rightarrow C_xN_2^- + h\upsilon \tag{3.2}$$

Here, the electron attachment happened on the lower cluster and the growth by N addition to the anions. In this case, the odd preference of the C_xN^- is transferred to the odd preference by the anions with one nitrogen atom more. However the relative abundance of the C_xN^- / $C_xN_2^-$ is fluctuating and is in favor for the dinitrile x = 4, 5. The anions $C_2N_2^-$, which remain extremely weak in this work, have been observed as the most abundant species in collision between a beam of N^+ and N_2^+ and one of C_x^- issue of laser ablation [127]. Thereby, in this

work, the formation of clusters differs from the direct reactions between positively charged nitrogen atoms and carbanions.

$C_xN_3^-$

The distribution of tricyano-anions presents a maximum at x = 4 and a strict even preference. Studies investigated the stability of the $C_xN_3^-$ through DFT calculations [128]. The incremental binding energies reported by Chen et al, reflects the relative stabilities of the anionic clusters. The stabilities of the anions, which present a even numbers of carbon atoms are clearly higher than with an odd number of carbon atoms. These stabilities match the experimental observations (except for low $C_2N_3^-$ observed, which is predicted with high stability).

$C_xN_4^-$, $C_xN_5^-$

As the $C_xN_3^-$, the anions with $C_xN_y^-$ (y = 4, 5) follow also a preference for the even x. The maximum recorded for the y = 3, 4, 5 are increasing with the number of contained for respectively x = 4, 6, 10. For the $C_xN_y^-$ with y > 3 the theoretical and experimental information reported is scarce.

C_x^-

The signal of the C_x^- (x = 1-3) is very weak and does not present a clear odd/even effect. The anions with (x > 8) follow a slight even preference. The spectra, which results from the sputtering of the graphite target solely with Ar (figure 3.6), showed the C_x^- distribution free of odd/even preference and with a clear maximum at x =5 (figure 3.8).

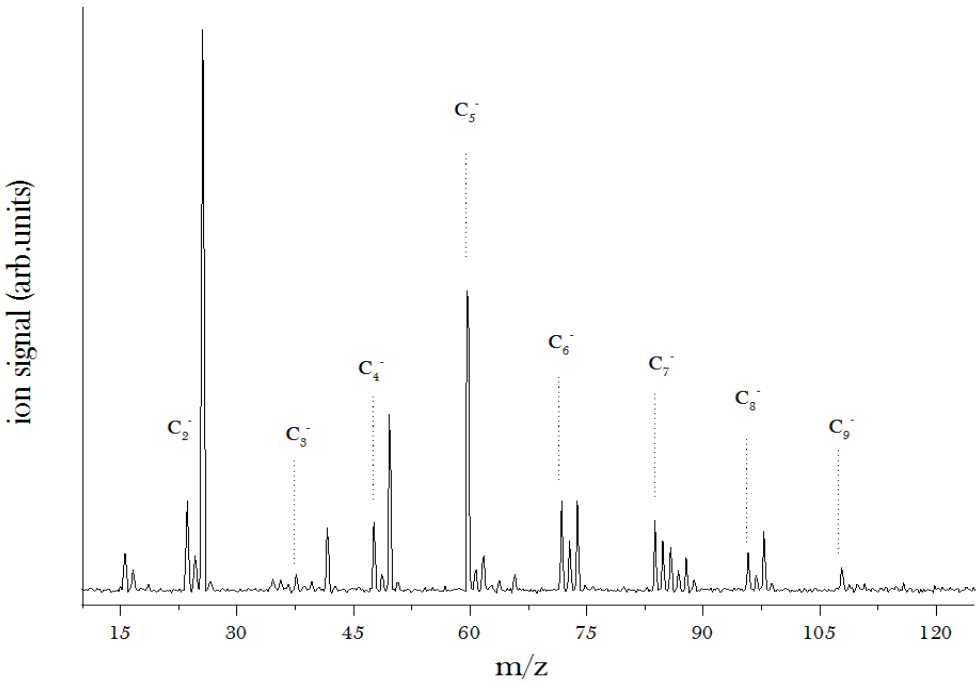

Figure 3.8: Mass spectrum of negatively charged anions produced by the sputtering source under 25 W with 14.5 sccm Ar und 33.6 sccm He

As reported by the group of J.P. Maier, the C_x^- (x=2-9) anions present a similar linear structure with a doublet multiplicity in their ground state [129]. The slight odd preference observed by the C_x^-, (figure 3.6) can be explained by the appearance of the $C_{x-7}N_6^-$ anions which present the same mass as the pure carbon clusters.

3.3.3 Anions with the odd masses

The C^{13} and N^{15} are naturally present with a portion of 1,1% and of 0.37% respectively. All the other isotopes of C and N atoms are extremely rare and neglected. The heavier isotopes can only partly explain the odd mass intensities observed for the ions with odd masses (figure 3.9). Alternatively, the presence of H atoms can explain the presence of such odd masses. Reactivity studies between H and nitrogen-containing carbananions report that none of these react with H_2, but with H, on the following way [130]:

$$CxN_y^- + H \rightarrow CxNyH^- \tag{3.5}$$

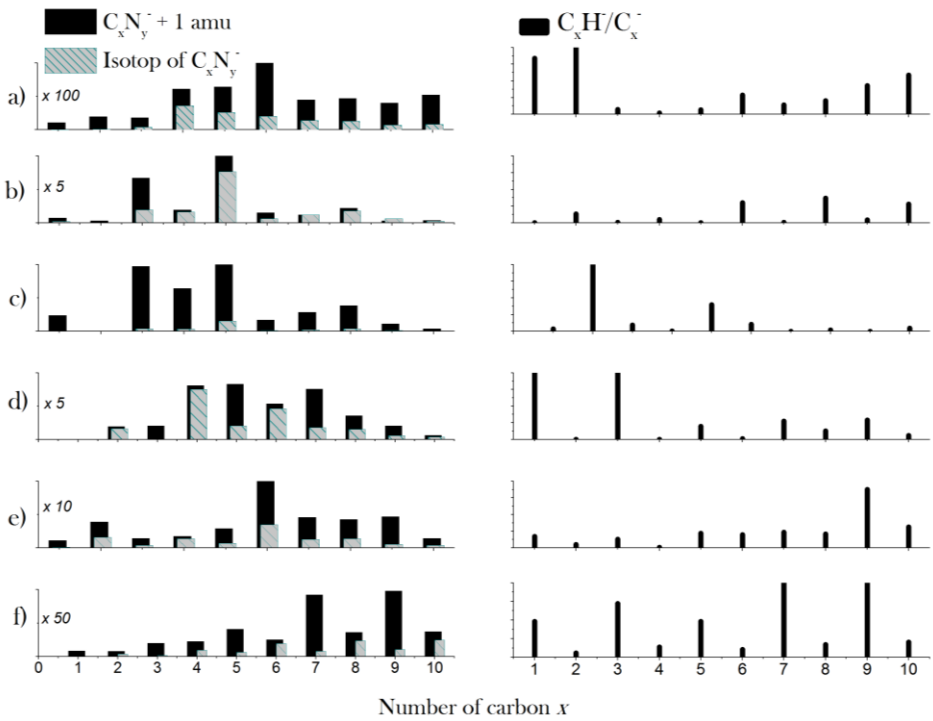

Figure 3.9: The left part represents the detected intensity of the masses corresponding to the masses of $C_xN_y^-$ + 1 amu (black bars) and the isotopically substituted cluster masses (grey bars). The right part presented the portion of hydrogenated anions $C_xN_y^-$. The lines; a, b, c, d, e, f present the level of nitrogenation y = 0 – 5.

The figure 3.9 presents the portion of the signal responsible for the isotope substituted C^{13} and N^{15} clusters. These intensities were calculating based on the known natural isotopic distribution and C^{12}/N^{14} cluster yields.

By comparing the calculated intensities for the isotopically substituted clusters with the one observed in the mass spectra, the origin of the measured signal can be determined. Thus, some of the masses can be explained solely by the isotopically substituted cluster, however many of the masses observed present a higher intensity than the one calculated, meaning that additional clusters must hide under the same mass. The hydrogenation presents a clear preference as function of the parity of carbon atoms for y = 1, 3 and 5. This preference is inverted in comparison to the one observed in the formation of the H-free structures (figure 3.6). The inversed parity preference of the hydrogenated structure indicates an easy hydrogenation of the less stabile anions, with a triplet ground states. The experimental and theoretical reactivity studies of H and carbanions concluded that C_xN^- (x = 1-6) and $C_xN_2^-$ (x = 1, 3-5) present moderate reactivity and $C_xN_3^-$ (x = 2, 4) are not reacting at all [130]. As seen on the figure 3.9, the C_xNH^- (x = 1-5) and the $C_xN_2H^-$ (x = 1, 3-4) are weak < 16% and $C_xN_3H^-$(x = 2, 4) are very weak <10%.

The systems with the odd masses 89, 75 and 115 amu are targeted on this experiment (due to their equivalence with the masses of amino acids cf. chapter 8). All these masses are a mixture of anions containing one heavy isotopic atom and the hydrogenated carbanions. The estimation of the proportion for each of these species is performed based on the measured spectra and calculated probabilities for the natural appearance of the isotopically substituted clusters as follows:

75 amu: 91.8 % of C_5N^- containing a heavy isotope (16.2 % for each five forms with one C^{13} atom and 10% with one N^{15} atom) and 8.2 % of C_5NH^-.

89 amu: 13.2 % of $C_5N_2^-$ containing a heavy isotope (2.3% for each of the five C^{13} configurations and 0.7% for each of the two N^{15} configurations) and 86.8% of $C_5N_2H^-$.

115 amu: 86.2% of $C_6N_3^-$ (12.3 % for each of the six forms with C^{13} and 4.0% for each of the three forms with N^{15}) and 13.8% of $C_6N_3H^-$.

3.4 Mass spectra in the presence of O_2

3.4.1 Negatively charged ions

The reactive sputtering with oxygen remains clearly less productive for anions than with nitrogen. Small sizes anions are abundantly formed, however the intensity of the signal decreases strongly with the size. The sputtering in the presence of O_2 does not produce large anions as with N_2 and the anions bigger than 125 amu are only detected in small quantities. The

highest intensity are observed for 26 and 46 uma, which correspond to CN^- and NO_2^- clearly revealing the presence of nitrogen atoms, which are only present by contamination with air and are thus present in minor quantity. The presence of C_x^- in greater quantity than in the sputtering with N_2 indicates the stronger reactivity of carbon anions with nitrogen than with oxygen. The spectra are not only composed of $C_xO_z^-$ but also of $C_xN_yO_z^-$. The coincidences of many masses complicate the interpretations of the mass spectra. Due to their overlap, the systems cannot be separated by mass spectrometry, IR spectroscopy can aid in the interpretation of theses peaks. To clarify the interpretation, the different anions of interest for this work were separately examined.

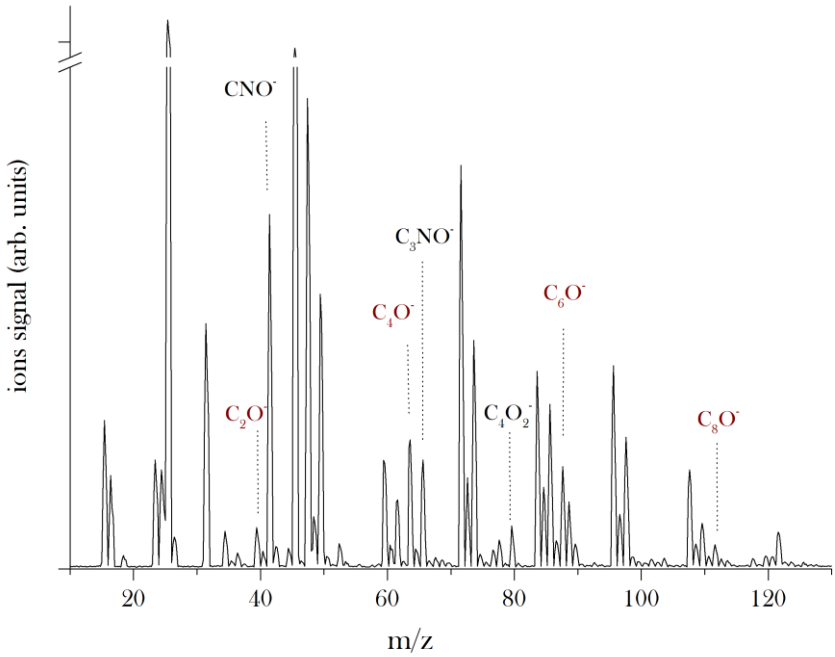

Figure 3.10: Mass spectrum of negatively charged anions produced by the sputtering source under 24 W with 8.5 sccm of O_2, 5.5 sccm of Ar und 50 sccm He.

C_x^-

The masses corresponding to the carbanions are abundantly present up to 132 amu corresponding to C_8^-. Beyond 48 amu, these masses might also correspond to $C_xO_3^-$. The presence of nitrogen in the experiment allowed the formation of other systems with the same masses. Also the following combinations: the $C_xO_2N_2^-$, the $C_xON_4^-$ and the $C_xN_6^-$ are possible from the respective masses of 60, 72 and 84 amu. The distributions of the C_x^- in presence of oxygen and nitrogen are compared in figure 3.11. The favored formation of anions, which contain small numbers of nitrogen atoms argues against the interpretation of these signals to $C_xN_y^-$ anions, where a large number of N atoms would be required for the same masses.

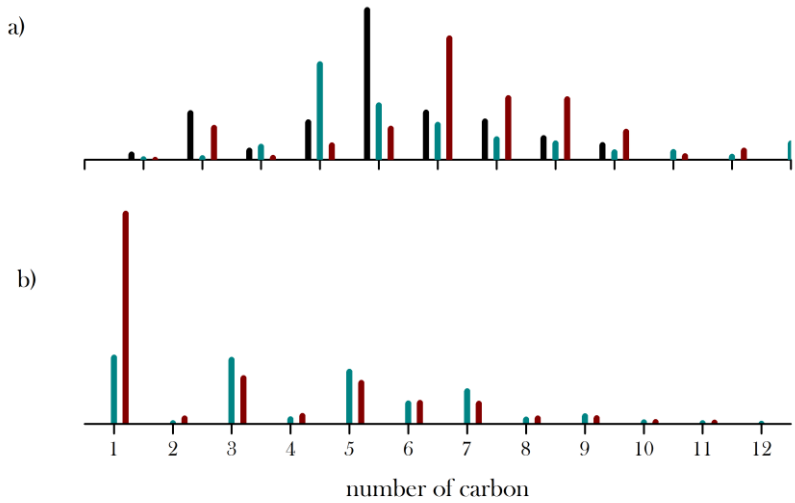

Figure 3.11: Distribution of a) C_x^- and b) C_xN^- as as a function of the number of carbon atoms in the presence of different reactive gas: black without reactive gas, turquoise with N_2, red with O_2.

C_xO^-

The mass corresponding to the C_xO^- presents a strong preference for an even number of carbon atoms. The $C_{x-1}N_2^-$ share the same masses and are indistinguishable from the C_xO^- in the mass spectra. With the assumption that the O_2 does not play an important role in the distribution of $C_xN_2^-$, the comparison of the distribution allowed the estimation of the upper limit of dicyanocarbanions present under one peak. The similar distribution of C_xN^- under the different conditions (figure 3.11) argued in favor of this assumption. The peak mass 76 amu was particularly small in the sputtering with O_2, whereas this mass represents the strongest signal of the $C_xN_2^-$ with an even number of carbon atoms. With this mass as reference, the maximal contamination by $C_xN_2^-$ can be estimated (figure 3.10). For the C_xO^- (x= 2,4,6,8) the $C_{x-1}N_2^-$ are potentially present and could represent respectively up to 5%, 70%, 60% and 4% of the signal. The mass of C_4O^- corresponds also to the mass of O_4^-, a system supported by the high O_2^----O_2 binding energy 10.49 eV of [64].

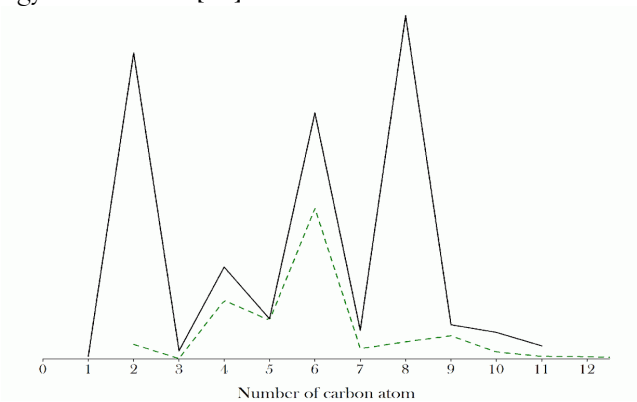

Figure 3.12: Upper limit of the $C_{x-1}N_2^-$ (green broken line), which are potentially present in the signal observed from the sputtering in oxygen (black line), where the C_xO^- are expected.

C_xNO^-

The masses of C_xNO^- are also shared by $C_{x-1}N_3^-$. The two anions, CNO^- and C_3NO^- represent are targeted in this work. The succession of C, N, O atoms is abundantly present in the organic molecules. Their examination is valuable in the understanding of the gas phase formation of organic molecules. Under the mass of C_3NO^- (66 amu), the simultaneous presence of the $C_2N_3^-$ remains possible. In the sputtering in the presence of nitrogen, the ratio $C_2N_3^-/C_4N_3^-$ is close to 0.30. In the sputtering in the presence of oxygen, the ratio mass 66 amu / mass 90 amu (which corresponds principally to $C_4N_3^-$) is close to 3. Considering that the distribution of the $C_xN_3^-$ remains the same in the sputtering in nitrogen and oxygen, a majority of C_3NO^- in the mass 66 is expected.

$C_xO_2^-$

The $C_xO_2^-$ share the same masses with the $C_{x-2}N_4^-$ and the $C_{x-1}N_2O^-$. Under the mass 80, not only $C_4O_2^-$ could be present, but also $C_2N_4^-$ or $C_3N_2O^-$. The minor formation of the $C_2N_4^-$ by the sputtering with N_2 argued against a significant amount of the tetracyano-system.

3.4.2 Positively charged ions

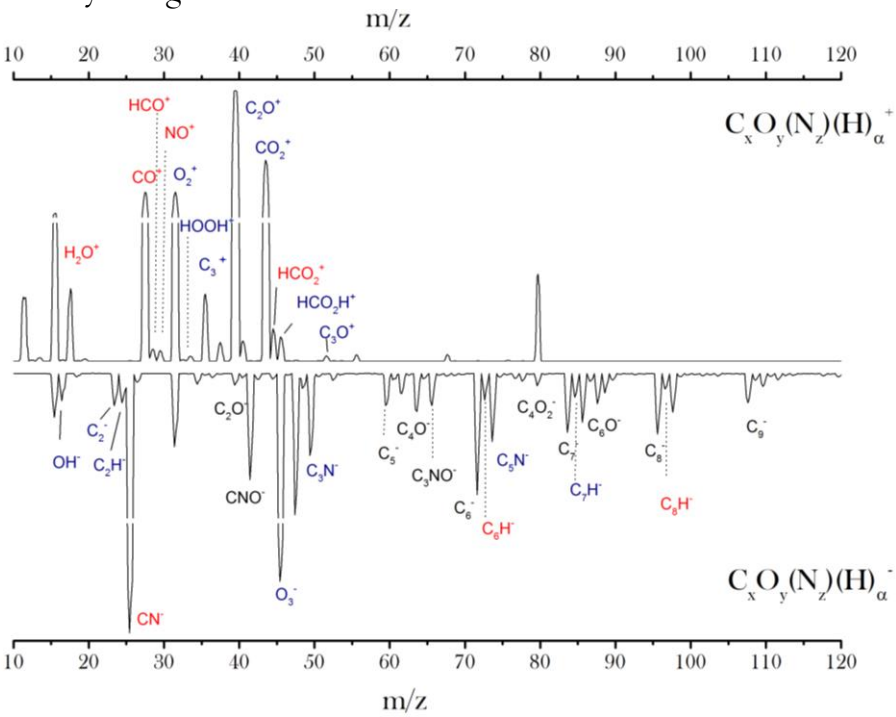

Figure 3.13: Mass spectra of the anions and cations formed through the sputtering of carbon targets in the presence of oxygen as reactive gas The red color marked the ions identified in interstellar medium (IM) and the blue color marks some of the species also identified in IM as neutrals.

The examination of cations reveals supplementary evidences about the chemistry of the sputter source. The positively charged ions in oxygen present a higher yields than its negative counterpart. This matches with previous reports [52]. The masses below 48 amu were particularly abundant. The diatomic (C_2^+, O_2^+, CO^+, NO^+) and triatomic molecules (H_2O^+, HCO^+, C_3^+, C_2O^+, CO_2^+) compose the major part of the produced cations. The presence of hydrogen is revealed by the presence of hydrogenated forms for several cations in large quantities. Larger masses are also detected which could correspond to $C_4O_2^+$ C_3O^+, $C_2O_2^+$, $C_3O_2^+$. Beyond 80 amu, the presence of cations is not detected.

The cations produced in large yields are generally nonexistent or produced in small quantities under anionic form and vice versa (except for O and O_2). The C_3^+ is the only bare carbon cluster cation formed in remarkable quantities. From a combination of DFT, coupled cluster method and the statistical model Metropolis Monte Carlo, the dissociation energy of C_3 was predicted the strongest of the C_x (x = 2-20) [132], and the electron affinity was estimated the smallest of the C_x (x = 2-20) [133]. For the small cations including oxygen, the occurrence of cations is related to the ionization potentials, which values were measured for example at 14.1 eV and 13,78 eV for CO and CO_2 , respectively [134]. The anionic homologue of CO_2 is not observed in the mass spectra, which match with experimental studies reporting the formation of CO_2^- only with the help of the Rydberg electron transfer and considering the free electron attachment as impossible [135].

3.5 Conclusion

The sputtering process depends on the gas flow in accordance with the Berg model, where the erosion rate as function of the gas flow follows a hysteresis behavior. The charged sputter yields admitted a maximum after 20 hours of sputtering and required increased gas flows and power in order to maintain its efficiency. A two phase start up process was used to obtain the best sputtering conditions by the increasing the gas flow and thus, the pressure in the chamber and secondly by increasing the source power. The presence of a different reactive gas (O_2 or N_2) influences strongly the process. The formation of negatively charged yield is supported in N_2 whereas its production is hindered in O_2. The reactivity of the formation of carbanions containing nitrogen atoms remains greatly stronger than carbanions containing oxygen atoms. The sputtering process leaves different nature of erosion print as function of the gas employed. This difference matches the theoretical and experimental studies, which revealed a contamination made of chemisorption in the case of the high reactivity of the couple target/reactive gas and of implantations in the case of low reactivity of the couple. In the Devienne experiment, the formation of glycine occurs on the target surface and was then extracted. The examination made on the sputter surfaces remains certainly important in understanding the chemistry of formation of amino acids.
In the presence of N_2, the preliminary mass spectra permit the identification of several $C_xN_y^-$ (y = 0-5) up to 15 atoms. The $C_xN_y^-$ (y = 1-5) show clear odd /even preferences in their distributions as a function of the number of carbon atoms. The preference shared by the $C_xN_y^-$ (y = 1, 3, respectively odd and even) could clearly be explained by favored structures. The

parity preference of the other $C_xN_y^-$ (y = 2, 4) respectively odd and even) could be explained from reactions of formation occurring in the sputtering process. Beside the major peaks of the $C_xN_y^-$, the presence of hydrogenated clusters is observed. The hydrogenated anion distribution as a function of the number of carbon atoms also presents a parity preference for y = 1, 3. These parity preferences (respectively even and odd) are inversed in comparison of their hydrogen-free homologues.

In the presence of O_2, the nature of the charged sputter yields depends on the sign of the charge. The small cations of up to three atoms are favored and masses never exceed 80 amu, whereas the anions of up to 11 atoms are produced in great quantity. Several clusters are present under both charges (positive and negative). The ratio (positive / negative) follows generally the eletronaffinities and ionization energies differences. The reactivity of oxygen atoms on carbanions remains lower than nitrogen atoms. Under the mass detected by the sputtering in oxygen, clusters containing nitrogen (resulting from contamination) are observed. In addition to the carbon anions containing oxygen, clusters, -which include nitrogen atoms- are expected.

The optimal conditions of the source are carried out and permit the IR identifications of several anions, which constitute the subject of the following chapters. From the sputtering in nitrogen, $C_xN_2^-$ (x= 1,3-11), $C_xN_4^-$ (x = 3,4,6, 8,10) are IR examined and from the experiment in oxygen, C_x^-(x = 5-9,11), C_xO^- (x = 2,4,6,8), $C_4O_2^-$ and C_xNO^- (x = 1,3) as well as anions, which share the same mass as three amino acids (75,89,115 amu).

Chapter 4:

The dicyano carbanions $C_xN_2^-$

In 1910 the Yerkes Observatory revealed that the spectra of Halley's Comet showed very prominent cyanogen bands. The article published in the New York Times [137] was praised as an important discovery for astrophysics and astrochemistry. The cyanogen C_2N_2 was already well known since the early nineteenth century, when Gay-Lussac first synthetized it and paved the way for its use as a fertilizer or as handsoap to remove silver clusters after the manipulation of photographic paper. Cyanogen is very poisonous and its potassium salt is enough to cause instant death when ingested, as was also mentioned in the article. The expected meeting between the earth and the tail of Halley′s Comet, which contains cyanogen, incited public fear regarding a possible poisoning of earth′s atmosphere. Whether «anti-comet pills» were taken or not, no effect from the poisonous tail was noted. The tail missed the earth by more than 197,000 miles. One century later, astronomists focused again on the cyano-carbon molecules. Recently, Voyager 1 provided details about the atmosphere of Titan, a satellite of Saturn. With a dense atmosphere, rich in nitrogen (1.5 times denser than that of the earth), with liquid phases on and under the surface, Titan intrigued astronomists. Titan also seemed to display dunes, seasons and coastlines, and to resemble the Earth as no other known planet of the solar system. The interstellar chemistry with nitrogen has been the subject of very recent publications on the experimental reactions and computational studies [138,139]. From laboratory simulations and astronomic observations, the dicyano structures C_2N_2 and C_4N_2 are likely to be present in Titan's atmosphere chemistry [25-26]. DFT calculations reported the possible structural of the neutral, cationic and anionic form of samll C_xN_2 clusters with x= 1-4 [140]. Through B3LYP/cc-pVTZ calculations determined the ground-state energies and bonding in C_5N_2 and C_6N_2 was determined, where the odd numbered carbon clusters have triplet ground states and are more cumulenic, whereas the even clusters are singlets in the ground state and acetylenic in structure [141]. The detection of cyanopolyyne anions C_3N^- and C_5N^- in the interstellar medium of a carbon-rich star [142-143] turned the attention to the negatively charged molecules also relevant for the astronomy [142]. Investigations of nitrogen-containing carbanions were carried out in order to understand the interstellar chemistry. Jiang′s theoretical DFT study on $C_xN_2^-$ (x =1-12) revealed that $C_xN_2^-$ (x = 6–14) anions form linear conformer with $D_{\infty}h$ symmetry whereas $C_xN_2^-$ (x = 1–5) anions form chain-like arrangements. Two N atoms favor to bond at ends in linear and chain-like configurations [144]. Experimentally the $C_xN_2^-$ anions in the gas phase produced from different sources were observed [145-146] but experimental structural and vibrational information is limited to CN_2, which present an asymmetric CN stretch at 1467 cm^{-1} [148].

The $C_xN_2^-$ (x=1, 3-12) anion in this study have been produced by the sputtering source, whereas the $C_2N_2^-$ was essentially absent. In an experimental study it was observed that by the collision of N^+/N_2^+ on a plume of laser ablation on a graphite target, $C_2N_2^-$ anions were the most abundant species [147]. The $C_xN_2^-$ (x=1, 3-12) were investigated through the IRPD method using D_2 as messenger. The results of these investigations in the range of 1600 to 2300 cm^{-1} are presented and discussed on the next figures and paragraphs.

4.1: The IRPD Spectra of $C_xN_2^-$

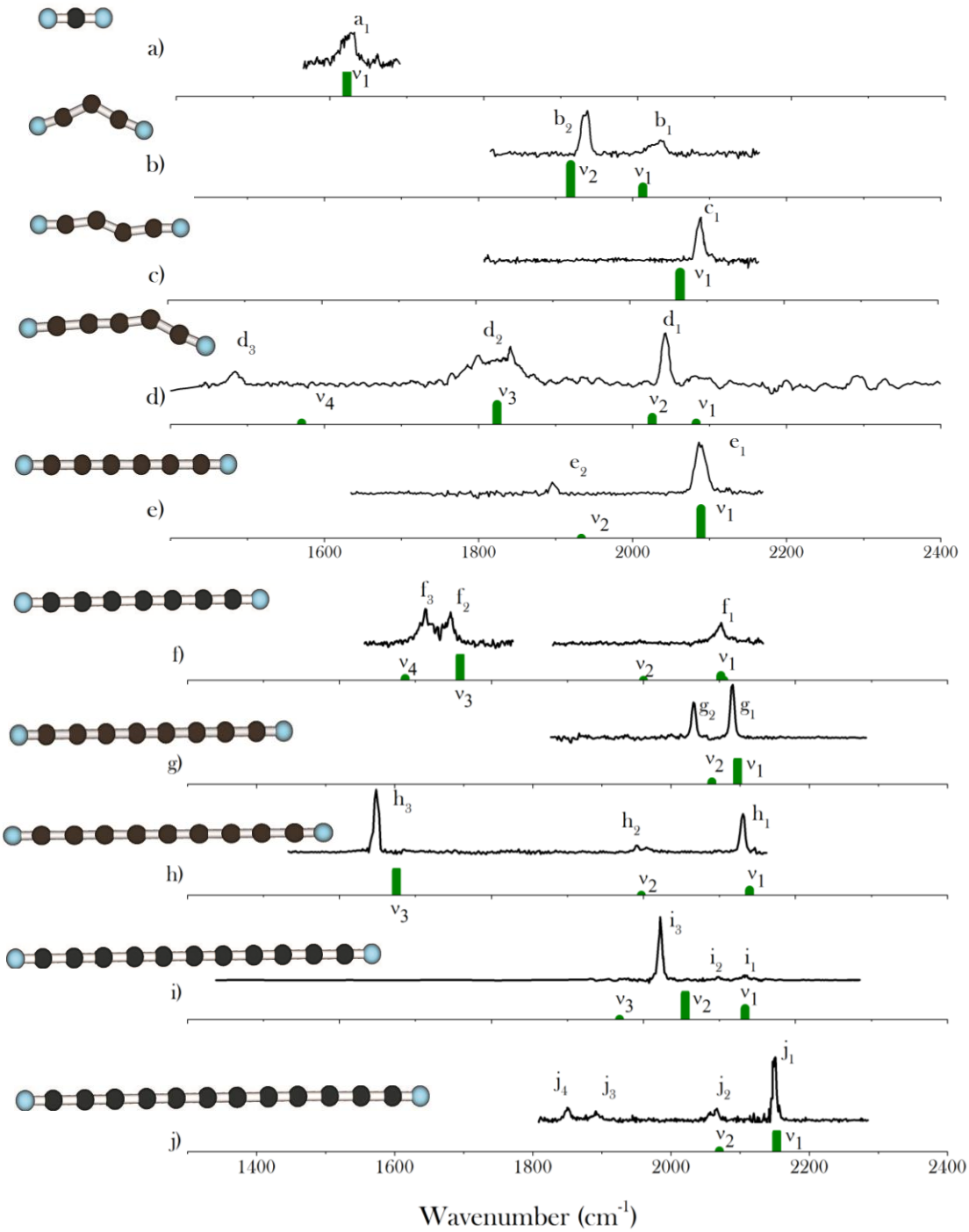

Figure 4.1: IRPD spectra of $C_xN_2^-$ - D_2: a,b-j represent x = 1,3-11 The green bars represent the absorption frequencies obtained from B3LYP/aug-cc-pVTZ calculations (scaling factor of 0.968). The geometries presented originate also from the calculations.

Anions	Stretch mode	IRPD	HWHM	B3LYP
CN_2^-	ν_1 C=N	1631	18	1622.2(126)
$C_3N_2^-$	ν_1 -CN 1-2	2031(25)	24	2013.3 (80)
	ν_2 -CN ½	1938(100)	13	1919(383)
$C_4N_2^-$	ν_1 -CN 1/2	2082(100)	11	2065.0 (893)
$C_5N_2^-$	ν_1 -CN 1-2	--	-	2082.8 (88)
	ν_2 -CN 1/2	2043(100)	11	2025.6(459)
	ν_3 -CC 3	1819 (68)	77	1824.6 (1268)
	ν_4 -CC # 4	1483 (27)	19	1570.5 (98)
$C_6N_2^-$	ν_1 -CN 1/2	2086 (100)	13	2089.0 (2290)
	ν_2 -CC #	1994 (12)	12	1933.5 (6.3)
$C_7N_2^-$	ν_1 -CN 1/2	2098(-)	12	2102.0 (718)
	ν_2 -CC 3	1751(90)	11	1759.0 (3572)
	ν_3 -CC # 4	1716(100)	10	1686.7 (263))
$C_8N_2^-$	ν_1 -CN 1/2	2091 (100)	6	2096.2(3900)
	ν_2 -CC #	2035(67)	8	2059.0(388)
$C_9N_2^-$	ν_1 -CN ½	2136(61)	7	2139.6 (1302)
	--	2008(8)	8	--
	ν_2 -CC	1994(12)	6	1997.15 (13)
	ν_3 -CC#	1651(100)	7	1675.0 (6300)
$C_{10}N_2^-$	ν_1 -CN 1/2	2133 (8)	5	2133.7(1557)
	--	2098 (5)	7	--
	ν_2 -CC	2022(100)	5	2059.1 (5611)
	ν_3 -CC	--	-	1968(25)
$C_{11}N_2^-$	ν_1-CN 1/2	2150(100)	6	2153 (2039)
	ν_2-CC	2067(19)	6	2070 (97)
		2054(14)	6	--
		1891(12)	8	--
		1850(20)	8	-

Table 4.1: IRPD experimental frequencies, with the relative IR intensities given in parenthesis in percent, and B3LYP/aug-cc-pVTZ geometries and frequencies with the predicted intensities given in parenthesis in Km/mole. 1/2 and 1-2 specify the coupling respectively out of phase and in phase of both CN stretches. # indicates the CC stretch mode involving only each second bond of the carbon chain.

The $C_xN_2^-$ investigated in this thesis present one to four absorption bands in the range from 1600 to 2300 cm^{-1}. A discrepancy between the odd and even number of carbon atoms appears and the size of the anions influences the pattern of absorption. The anions with an odd number of carbon atoms are responsible for a larger number of bands than the structures with an even number of carbon atoms. A strong band between 2040 and 2200 cm^{-1} is shared by all the species, which remains the strongest among the anions with an even number of carbon atoms. Second bands between 1900 and 2000 cm^{-1} were present in several anions and were the strongest absorption band of some (x = odd) anions. Only the structures presenting an odd number of carbon atoms formed bands in the region between 1500 and 1900 cm^{-1}.
The computational predictions explain the absorption bands obtained in most cases. The B3LYP/aug-cc-pVTZ calculations reveal the bend geometries of the small anions $C_xN_2^-$ x = 3, 4, 5, which is not shared by the linear structure of the anions including more than 6 carbon atoms. The $C_xN_2^-$ present ground states with a doublet multiplicity. They include the nitrogen atoms systematically at the end of the carbon atoms forming a chain. The chains are close to polyyne-configurations, where the bond lengths alternate between single and triple bonds. The bond lengths between N and C correspond to nitrile functions (C ≡ N) for all of them except for CN_2^-, where the bond lengths represent a diimide structure (N=C=N). Stretches of nitrile functions are detected for each $C_xN_2^-$ in the range of 1938 to 2136 cm^{-1} (except for CN_2^-). Other absorption bands originate from stretches of carbon atoms. The vibrational patterns of absorption are presented in the following paragraph.
However, the concordance of the theoretical and experimental values for the $C_xN_2^-$ (table 4.1) remains the worst compared to all groups of molecules presented in this work. The distance between the theoretical and the experimental values exceeds several times 20 cm^{-1} and in some extreme case reaches 90 cm^{-1}. Three bands were also observed particularly broad, which correspond to the CN stretch (ν_1) of $C_3N_2^-$, the both CC stretches (ν_3) of $C_7N_2^-$ and (ν_3) of $C_7N_2^-$. The origins of singular bands are examined and discussed in the paragraph, which presents the detailed review of each anions.

4.2 Vibrational pattern

The nitrile stretches between 1938 and 2136 cm^{-1}, find their origin at the carbon-nitrogen triple bond located at the end of the chains. Except for CN_2^- including double bonds, the stretches of the nitrile functional groups absorb strongly for every $C_xN_2^-$. They represent the strongest absorption detected among the anions (x= 1, 3-6) in the range of 1600 to 2300 cm^{-1}. They are overstepped by some stronger CC stretches observed for the anions with more than seven carbon atoms. The stretches of two nitrile functional groups are systematically coupled, also in the long chains. A coupling out of phase of the two nitrile groups is symbolized with a "1/2" in Table 4.1. These coupled stretches are responsible for stronger absorptions than the in phase coupling, symbolized "1-2". This second coupling is predicted and observed at a higher frequency than the other mode, for example 97 cm^{-1} higher for $C_3N_2^-$ and 57 cm^{-1} higher for $C_5N_2^-$. A coupling in phase in the linear chains constitutes a

symmetric vibration mode, which remains IR inactive. For larger anions, the absorption frequencies become higher. The evolution of the frequencies as a function of size differs depending of the even or odd character of the anion. The clusters with an even number of carbon atoms present a roughly asymptotic evolution. Taking the $C_xN_2^-$ (x = 3, 5, 7, 9, 11) in account, the frequency difference between two successive sizes are respectively 105, 55, 48, 14 cm^{-1}. By the anions containing an even number of carbon atoms, the evolution is successively by the $C_xN_2^-$ (x = 4, 6, 8, 10) were observed with differences of 4, 5 and 41 cm^{-1}.

The CC stretches between 1483 and 2035 cm^{-1} are responsible for absorptions by the anions containing more than four carbon atoms. These stretch modes in the carbon chain involved several bonds. The stretch mode can be described by the bonds principally involved in the vibration. The numbers associated with CC stretches in Table 4.1 indicated the location of the bond, which is mainly involved. The CC bonds are counted starting from one end (in the case of bent anions starting from the shortest end). The vibration modes constitute two kinds of patterns. Each successive bond could be out of phase forming an alternating stretch mode. When the vibration skips each second atom, other modes could be formed, which are symbolized by "#" in table 4.1. The alternating mode is observed only in the structures presenting an odd number of carbon atoms. With two nitrile functions located at the extremities, the polyyne-like chains (C-C ≡ C-) allow a strict alternation of the size of the bonds only with an even number of carbon atoms. The chains with an odd number of carbon atoms contain two successive bond of the same length, which are located on both sides of the central atom. The strict alternation of the bond lengths seemes to hinder the alternating stretching mode. As the size of the chain increases, the frequency of the alternating stretching mode become lower. The second mode absorbes at frequencies, which increase with the size of the structures.

4.4 Review of the different $C_xN_2^-$

CN_2^- is clearly identified with an observed absorption band at 1631 cm^{-1}, which is predicted by the calculations to be only 9 cm^{-1} lower in frequency. The absorption band results from the asymmetric stretch of the two CN bonds forming a diimide linear structure. CN_2^- remains the only $C_xN_2^-$ anion measured in this work without a nitrile functional group. The isomer CNN is revealed by the B3LYP/aug-cc-pVTZ calculations energetically 1.97 eV higher than the configuration with the central carbon atom and is clearly not expected in the experiment. The neutral CN_2 has already been investigated by gas phase IR spectroscopy and presents an absorption at 1467 cm^{-1}, 164 cm^{-1} red shifted in comparison to the anion [148]. This concords with the MP2 (fc)/6-311+G* calculations of Munreraah et al, which represents the anions structure very similar to the neutral form, with slightly larger C-N bonds [140].

$C_3N_2^-$ forms a bend structure with an angle of 126° and belongs to the C_{2v} point group. In and out of phase nitrile stretches are expected to be IR active. Two bands appear at 2031

cm^{-1} and at 1938 cm^{-1}, which can be attributed to these two stretch modes. The calculations at the B3LYP/aug-cc-pVTZ level predict two absorption frequencies ≈ 20 cm^{-1} lower than the observations. The absorption band at 2031 cm^{-1} is asymmetric and 24 cm^{-1} wide. The implication of other molecules, which could be responsible for a band close to 2031 cm^{-1}, is examined. The mass selection allows the presence of other anions having the same mass of 64 amu, for example C_4O^- or O_4^-. The supposed absence of oxygen in the chamber rendered the O_4^- strongly improbable. The anion containing four oxygen atoms was reported with cyclic form and the absorption of the highest frequency came from the O=O stretch at 1292 cm^{-1} [145]. The C_4O^- was investigated in this work (chapter 7) and reveals two strong absorption bands at 2172 cm^{-1} and 1877 cm^{-1}, thus not explaining the asymmetry observed for $C_3N_2^-$. The Other structures as the $[H_2O...NO_2]^-$ could be also dismissed in regard of the very low signal of H_2O^- and of NO_2^- in the mass spectra. From the calculations, the linear isomer of $C_3N_2^-$ is clearly underprivileged by 0.21 eV, and should present only one strong absorption at 1857 cm^{-1}. The observed bands are attributed to the $C_3N_2^-$. The influence of the negative charge on the spectra is revealed by the comparison of absorption frequencies of neutral C_3N_2, which is reported with two bands corresponding to a symmetric and an asymmetric CN stretch mode respectively 84 cm^{-1} and 190 cm^{-1} lower than $C_3N_2^-$[146].

$C_4N_2^-$ presents only an absorption band in the range from 1600 to 2300 cm^{-1}, which is observed at 2082 cm^{-1}, 17 cm^{-1} higher than the computational predictions. The symmetric CN stretch is expected to be inactive in relation to its C_2h geometry. The carbon chain presents two symmetric angle of 146°. The B3LYP /aug-cc-pVTZ calculations reveal the linear isomer energetically 0.05 eV higher in energy.

$C_5N_2^-$ is responsible for three absorption bands at 2043 cm^{-1} (d_1), 1819 cm^{-1} (d_2), 1483 cm^{-1} (d_3) corresponding to the three predicted stronger absorptions. However, the difference between the calculations and the experimental results remain important for the d_2 band. This band is expected clearly stronger than the b_1 band. The band d_2 has a width 80 cm^{-1} and is composed of few peaks, which cannot be resolved. A band measured with low laser power reveals a similar width and indicated the absence of broadening resulting from the intensity of the laser (figure 4.3).

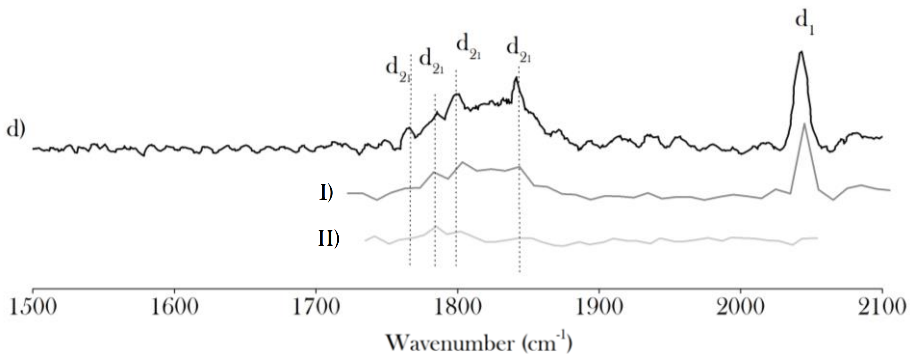

Figure 4.2: IRPD absorption spectra of $C_5N_2^-$ measured under different laser intensity: d) 0.52 mJ/pulse, I) 0.30mJ/pulse, II) 0.06 mJ/pulse [laser intensity measured at 1820 cm^{-1}].

This absorption band results from a stretch mode involving the carbon bonds on each side of the bend. The IR investigation was also carried out for the mass of 89 amu (figure 4.3). In the spectra corresponding to the mass 89 amu, a similar absorption centered at 1820 cm^{-1} appears, which presents a similarly large width of 80 cm^{-1}.

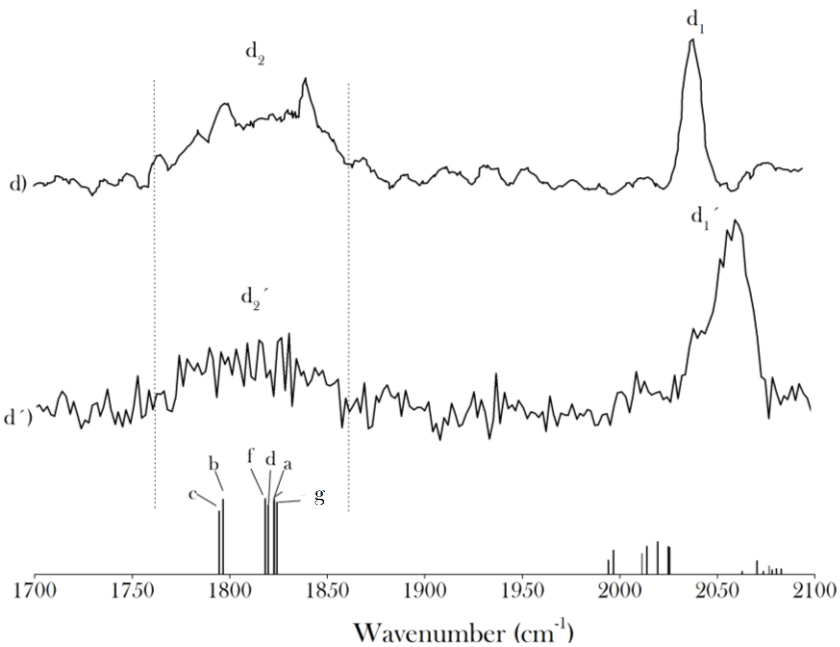

Figure 4.3: IRPD absorption spectra corresponding to the mass 88(d) and the mass 89 (d') in the region from 1700 to 2100 cm^{-1}. The B3LYP aus-cc-pVTZ calculations of the isotopomers C_5N_2 containing one ^{13}C or one ^{15}N are presented: (a) $N^{13}CCCCCN^-$, (b) $NC^{13}CCCCN^-$, (c)$NCC^{13}CCCN^-$, (d) $NCCC^{13}CCN^-$, (e) $NCCCC^{13}CN^-$, (f) $^{15}NCCCCCN^-$, (g) $NCCCCC^{15}N^-$ [where the bend * located. NC(C*) $CCCN^-$].

By comparing the experimental and the predicted IR frequencies for mass 89 amu, $C_5N_2H^-$ as well as the isotopomers of $C_5N_2^-$, which contain a ^{13}C or a ^{15}N (chapter 8) could be identified. In the case of the $C_5N_2H^-$, by comparison of the experimental and the theoretical calculations, the hydrogen atom is attached to the carbon atom mainly involved in the stretch in question (the details are presented in chapter 8). A similar vibration mode is predicted in the $C_5N_2H^-$, which is responsible for an absorption band at 2055 cm^{-1} composing part of the band (d'_1) (cf. chapter 8). This band remains thin with a low bandwith.

The isotopomers of $C_5N_2^-$ containing one ^{13}C or one ^{15}N have been investigated by means of B3LYP/ aug-cc-pVTZ calculations (chapter 8, table 8.2). The influence of the heavy isotopes differs as a function of the implication of the atoms in the stretch mode. In this case, two ^{13}C locations have a particularly large influence and reduce the frequency of absorption, which are predicted 30 cm^{-1} lower than in the ^{13}C-free anions. All of the other five isotopomers are estimated with as small influence not exceeding 7 cm^{-1}. The band observed for the mass 89 presents also a width of 80 cm^{-1}. The second minor band at the red side expected from the calculations was not observed. Or this second part is too weak to be observed, or the influence of the heavy isotopes are much smaller than predicted, or the isotopes limit the broadening observed. An influence of the messenger could be taken into question, which could be experimentally tested with a complementary investigation with another messenger. These suppositions reveal themselves as hypothetic, and invite future investigations.

In previous IRPD and IRMPD studies, the double peaks of several absorption bands could be attributed to rotationally unresolved P, Q, R branches [118,121]. The case of to a partially resolved rotational structure was also associated to an absorption band, which present similarities with the absorption band d_2 of $C_5N_2^-$. The antisymmetric NH stretching vibration of $NH_4^+.H_2O$ were in good agreement with the simulations using the program PGOPHER with the rotational constant originating from B3LYP calculations (with the rotational constant of bare NH_4^+) [121]. This absorption band, which appear to be composed at least of nine equidistant small peaks, was attributed to a partially resolved rotational structure with a characteristic spacing of ~11 cm^{-1}, which correspond to a Q branch progression in quantum number K. The experimental and computational result were obtained for temperature of 100K. On the experimental setup presented in this work, previous studies estimated the molecule temperature at 75K [118]. For the band of $C_5N_2^-$, the different attempts of simulation with the program PGOPHER were not in agreement with the experimental results and conditions.

$C_6N_2^-$ is the smallest investigated dinitrile $C_xN_2^-$ anion with a linear structure. The strong CN stretch is measured at 2086 cm^{-1} and is in accord with the calculations with a deviation of 3 cm^{-1}. The second band is observed at 1994, which is 60 cm^{-1} higher than the predictions. This second band remains also stronger than the expectations. In order to investigate other possible origins of this band, other anions, which carry the mass of 100 amu are subject to calculations. The next two isomers of $C_6N_2^-$ in the energy scale are estimated with more than 1 eV higher and the respective strongest bands expected are located at 1841 cm^{-1} and 2216 cm^{-1}. The $C_7NH_2^-$ carries also the same mass of 100 amu, and the mass of C_7N was particularly abundant in the mass spectrum, which makes the presence of this anion, even if in small amount possible. From the calculations, the $C_7NH_2^-$ anions should absorb strongly at 2035 cm^{-1} and at 2169 cm^{-1} and are clearly not observed. However the second band of $C_6N_2^-$ originates from CC stretches located in the center of the molecule. The same kind of

vibration pattern in other $C_xN_2^-$ presents calculations, which also underestimate the frequency.

$C_7N_2^-$ could be clearly identified through two absorption bands. The band (f_1) at 2098 cm^{-1} originating from the CN stretch and the band (f_2) at 1751 cm^{-1} from one of the CC stretch modes, which presents a frequency in very good agreement with the calculations with a deviation of 4 cm^{-1}. The frequency of the second CC stretch is observed at 1716 cm^{-1} and 19 cm^{-1} overestimated. This band reveals itself to be the strongest band in the spectra, whereas the calculations predict a weak band. Other anions carrying the mass 112 are examined. The two next isomers in the energetic scale are predicted more than 0.8 eV higher than the isomer, which represent the global minimum and remain improbable. The $C_8NH_2^-$ favored isomer is estimated to present a strong absorption at 1944 cm^{-1}. The spectra of $C_7N_2^-$ remains an exception in this work. The bands (f_2) and (f_3) are completely saturated by laser intensities which allow the observation of (f_1). The peaks corresponding to (f_3) remains also saturated with a lower intensity than (f_2) (figure 4.4). The spectra presented in figure 4.1 were recorded at a very laser intensity to avoid saturation and thus, power broadening.

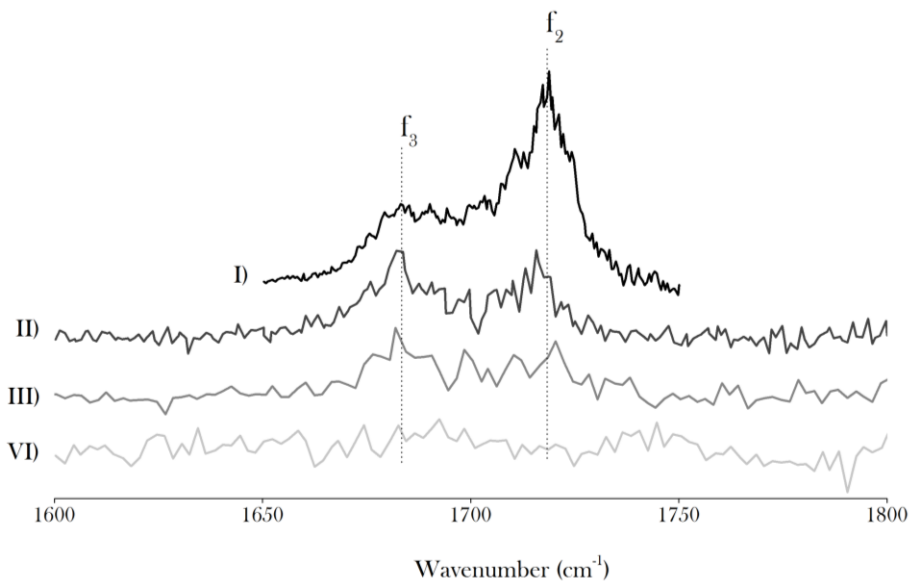

Figure 4.2: IRPD absorption spectra of $C_5N_2^-$ measured under different laser intensity: I) 0.18 mJ/pulse, II) 0.076 mJ/pulse III), 0.059m mJ/pulse, IV) 0.046 mJ/pulse. [laser intensity measured at 1700 cm^{-1}].

$C_8N_2^-$ could be identified by the two bands coming from two vibration patterns similar to $C_6N_2^-$ .The CN stretch was observed at 2091 only 5 cm^{-1} lower than the computational expectations. The frequency of the second band remains 59 cm^{-1} overestimated.

$C_9N_2^-$ presents an absorption spectra, which resemble $C_7N_2^-$. The CN and a CC stretch mode (strictly alternating phase) remain close to the estimations at. Anew the second CC stretch experience an overestimation of its frequency.

$C_{10}N_2^-$ is identifiable through the two stretch modes CN and CC expected from the linear structure. The deviation between the theoretical and the experimental results remain smaller than 1 cm^{-1} for the CN stretch. In the case of the CC stretch, the deviation approaches the value of 48 cm^{-1}. Such large deviations have been observed several times for the smaller dinitride anions. The presence of a small band at 2098 cm^{-1} suggests the presence of another anions.

$C_{11}N_2^-$ is responsible for two absorption bands, which clearly match the calculations with a difference not exceeding 3 cm^{-1}. The bands resulting from the CN stretch at 2153 cm^{-1} present the highest frequency for the investigated dinitrile anions. Two other bands are observed in the spectra and reveal the presence of a different structure not yet identified.

4.5 Conclusion

The (x = 1,3-11) are produced by the sputtering of carbon target with the use of gaseous nitrogen as reactive and sputtering gas. The IRPD absorption spectra are identified by comparison with the calculation at the B3LYP aug-cc-pVTZ. The most stable structures are N terminated, presenting a nitrile group for all systems with x>2. This nitrile functions lead to observation of stretching vibrations in the region of 1938 to 2150 cm^{-1} and are coupled leading to in and out of phase stretching mode. The anions with more than 6 atoms are responsible for absorption resulting from CC stretch modes. For systems with an odd number of atoms, CC stretches involving successive bonds are observed. Other CC stretch involving every second bond, are detected for all systems (x > 6). These second modes present absorption frequencies systematically overestimated at the B3LYP/aug-cc-pVTZ level. The deviations between the experimental and computational results of the $C_xN_2^-$ remain the largest observed compared to all anions investigated in this work. The CC stretch of $C_5N_2^-$, which involves mainly carbon atoms located close to the bend of the carbon chain, present a surprising width of 80 cm^{-1}. Further investigations involving different isomers or isotopes cannot explain this broadening. Additional molecular dynamics studies involving the tag anion might explain this band and excite further studies.

Chapter 5:

Tetracyano-carbanions $C_xN_4^-$

The carbon nitride clusters, which contain four nitrogen atoms, present fully promising properties. The graphitic C_3N_4 was considered as an attractive free-metal photocatalyst, using solar energy for the extraction of hydrogen from water, which represents a future source of energy independent from fossil reserves [31]. The band gap of the g-C_3N_4 is sufficiently large to overcome the endothermic reaction of water splitting and stay in the UV visible domain of absorption. C_3N_4 became the focus of physicists as early as in the 1990s. Predictions which were based on ab initio computational methods, conjectured a hardness stronger than diamond for a covalent complex ß-C_3N_4 [32]. Similar to ß-Si_3N_4, the complex including sp^3 hybridized carbon atoms, was suspected to present a bulk moduli, which determines the hardness at a microscopic level, superior to 440 GPa. The quest of superhard materials stimulated many experiments. A cubic phase of C_3N_4 was synthesized in 2006 under hard pressure conditions [149]. The hardness of other carbon nitrides was also investigated, as for example $C_{11}N_4$ [33]. C_6N_4, named tetracyanoethylene (TCNE) is already fully employed by the industry of supraconductor materials. Its acetylenic-like structure present CN triple bonds with weak π bonds of weak energy. The four combined nitrile functional groups render TCNE an interesting electron acceptor character. Similarly to the $C_xN_2^-$, the $C_xN_4^-$ is suspected to take part in the interstellar chemistry. The information about the C_xN_4 in gas phase is very scarce. The TCNE, under neutral and ionic forms, is the only system of the group, which have been investigated by theory and experiment [150-152]. IR absorption neon matrix studies revealed two absorption bands for $C_6N_4^-$ anions at 2163 .9 cm^{-1} and 2108.4 cm^{-1} [151]. Experimentally the synthesis of C_3N_4 cations by combination of laser ablation and a nitrogen molecular beam has been reported [153]. The theoretical DFT and CCSDT calculations revealed the ground state of C_8N_4 and its ions. Surprisingly the ground state calculated for the neutral C_8N_4 is an open shell $^5A_1$ state and the geometry of the anionic ground state exhibit two five-numbered rings attached by a six-numbered ring [154].

In order to understand the vibrational behavior of gas phase negatively charged anions containing four nitrogen atoms, the IRPD spectra of $C_xN_4^-.D_2$ was set up. The lack of previous structural and vibrational information rendered the results particularly valuable. The investigation on the $C_xN_4^-$ x=3, 4, 6, 8, 10 are reported in this work.

5.1 IRPD spectra

The $C_xN_4^-$ (x = even) were produced abundantly and the $C_3N_4^-$ was the only (x = odd) anion presented from the group. In the region between 2000 cm^{-1} to 2140 cm^{-1} allows measuring the same peaks with both laser guaranteeing the correct relative intensities of the bands.
The spectra are presented and are compared to the predicted frequencies.

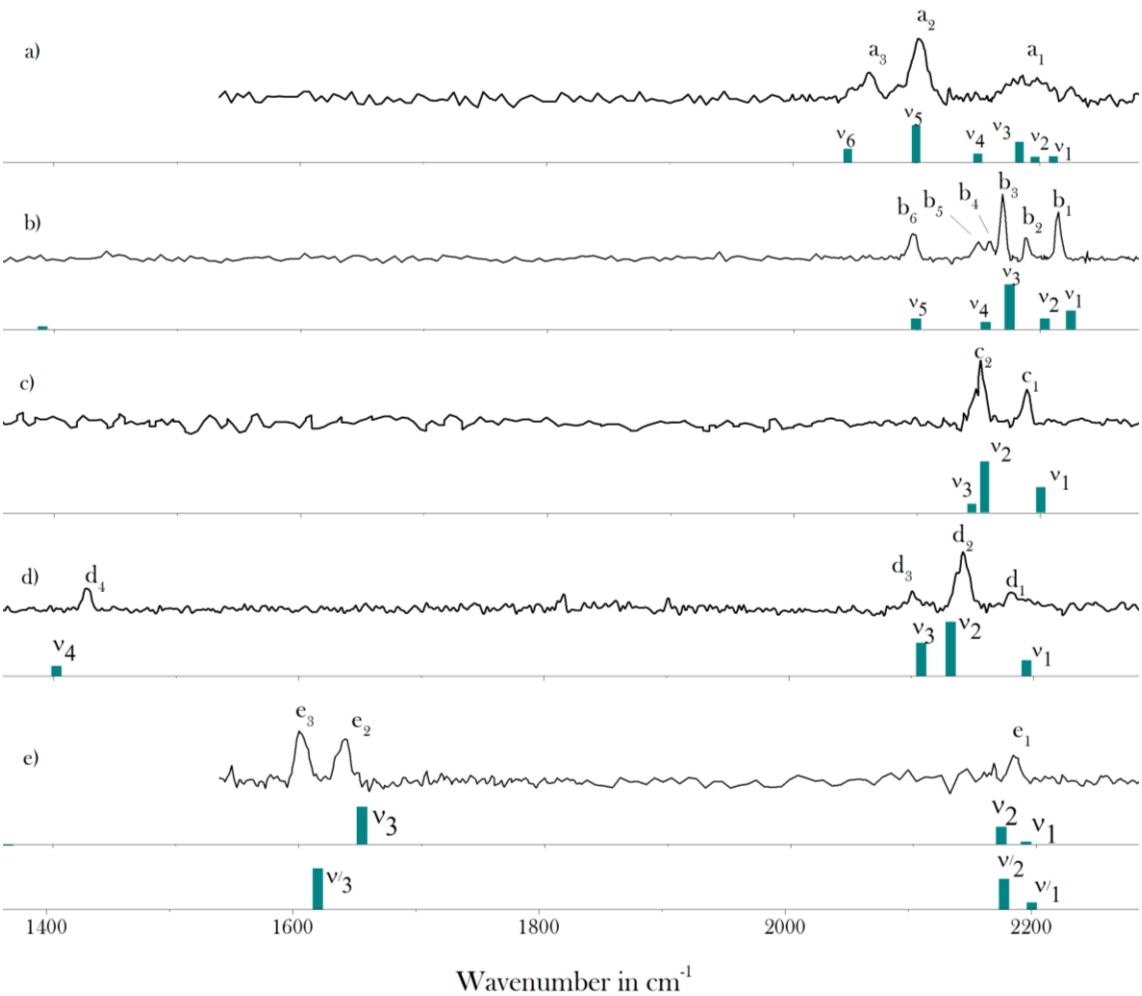

Figure 5.1: IRPD spectra of $C_xN_4^-$. D_2: a, b, c, d, e are the spectra with x = 10, 8, 6, 4, 3, respectively. The turquois bars represent the absorption frequencies obtained from B3LYP/AUG-cc-pVTZ calculations. In the case of $C_3N_4^-$, the computational frequencies of the two deepest isomers were presented.

The agreement between the theoretical and the experimental values allows a clear identification of the investigated systems. The region between 2050 and 2220 cm^{-1} is particularly propitious for the IR absorption of the anions containing four nitrogen atoms. For the two smaller systems, few absorption bands appeared close to 1600 cm^{-1} and to 1400 cm^{-1}. The vibrations patterns responsible for all the absorptions measured are attributed to the stretches of different kinds of functional groups: nitrile; imine; and from the carbon chains.

	Geometries	Stretching mode	IRPD Experiment Frequency / Width	B3LYP Frequency
$C_3N_4^-$	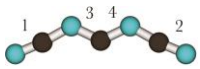	ν_1 -C≡N 2 ν_2 -C≡N 1 ν_3 -C=N- 3/4	2179(49) / 9 1636(100) / 10	2191.6 (188) 2171.3 (871) 1650.4(1800)
$C_3N_4^-$	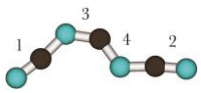	ν'_1 -C≡N 2 ν'_2 -C≡N 1 ν'_3 -C=N- 3/4	1602 (100) / 11	2200.5(99) 2178.0 (1231) 1620.4 (1719)
$C_4N_4^-$	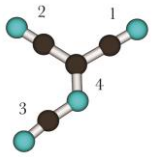	ν_1 -C≡N 1 ν_2 -C≡N 2 ν_3 -C≡N 3 ν_4 -C=N- 4	2173(42) / 13 2142(100) / 10 2105 (36) / 8 1428 (41) / 8	2194.0 (70) 2132.2(302) 2108.0(176) 1402.2 (36)
$C_6N_4^-$	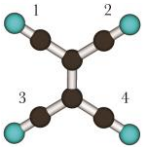	ν_1 -C≡N 1-2 /3-4 ν_2 -C≡N 1-3 /2-4	2188 (40) / 7 2151 (100) / 8	2200.5 (167) 2154.9 (389) 2144.4 (26)
$C_8N_4^-$	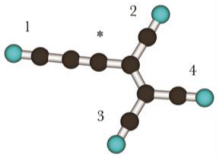	ν_1 -C≡N 1-2 ν_2 -C≡N 3-4 ν_3 -C≡N 3/4 ν_4 -C≡N 1/2 ν_5 -CC- *	2216 (73) / 5 2190 (87) / 4 2170 (100) / 5 2159 (26) / 6 2150 (25) / 8 2094 (40) / 6	2224.8 (280) 2203.8 (138) 2175.2 (789) 2155.7 (79) 2099.3 (137)
$C_{10}N_4^-$	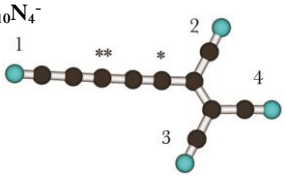	ν_1 -C≡N 2 ν_2 -C≡N 3-4 ν_3 -C≡N 1 ν_4 -C≡N 3/4 ν_5 -CC- * ν_6 -CC- **	2191(69) / 28 2103(100) / 14 2063 (44) / 11	2216.2 (78) 2210.0 (52) 2197.4 (798) 2163.3 (206) 2112.8 (1632) 2057.0 (452)

Table 5.1: IRPD experimental frequencies, with the relative IR intensities given in parenthesis in percent relative to the strongest one, and B3LYP /AUG-cc-pVTZ geometries and frequencies with the predicted intensities given in parenthesis in km/mole. The numbers on the structure precise the location of the CN stretches (the (../..) and (..-..) specify the coupling of the modes in and out of phase respectively).

5.2: Nitrile, imine and carbene/carbyne vibration patterns

The CN nitrile stretches between 2105 and 2200 cm^{-1}, result from the vibrations of the carbon and nitrogen atoms located at the end of a chain or of a branch and are observed for all the $C_xN_4^-$. The number of the bands reveals the number of terminal nitrogen atoms. For example the three bands (d_1), (d_2), (d_3) of $C_4N_4^-$ correspond to a branched structure with three nitrile functional groups. The CN stretches are also coupled together in the anions with an even number of nitrile functional groups. An in phase coupling of two CN stretches is symbolized in the table by a dash (..-..) and an out of phase coupling by a slash (../..). The anion with 6 carbon atoms has a D_{2h} symmetry. In this case all the four CN bonds were coupled together and form two different modes, which result in two absorption bands, (c_1) and (c_2).

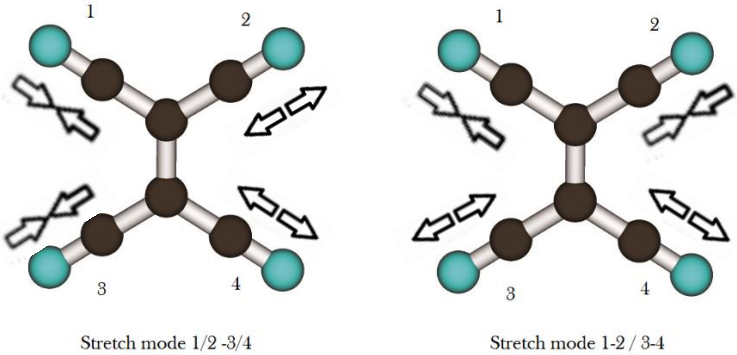

Figure 5.2: Representation of two modes resulting of the coupling between the four nitrile stretches in the $C_6N_4^-$.

In the $C_8N_4^-$, the coupling was limited to two CN bonds placed on the same side of the bridge formed by the two *sp*^{2} carbon atoms. Each side labeled on the table with 1, 2 and 3, 4 could form two different modes and the four bands ((b_1), (b_2), (b_3), (b_4)) were observed. The anions with ten carbon atoms presents only one large band in the investigated region caused by the nitrile functional groups. The overlapping of the absorption of several isomers could explain the feature of the absorption band, detailed in the paragraph dedicated to $C_{10}N_4^-$. By the structure containing 10 carbon atoms, the DFT calculations revealed the absence of coupling of the nitrile function located at the longest extremity. The nitriles (1) and (2) are expected to be independently at the origins of two absorption bands of the system. The two last bands are predicted originating from the two coupling modes of (3) and (4).
The intensities of each nitrile band are different. Generally the strongest bands came from the nitrile function at the end of the longest branch or coupled out of phase with the other nitrile on the same side of the carbon bridge (nitrile (1) and (2)). The bands with the highest frequencies are the result of the coupling between two in phase coupled nitrile functions on the same side of the bridge, or come from the CN (2) on the same side of the bridge with the longest branch ($C_{10}N_4^-$).

The CC stretches between 2063 and 2103 cm^{-1}, were only observed for the (x ≥ 8) anions. The stretches placed on the longest branch involved several CC bonds. The chains structures (between polyyne-like and cumulene-like) presented alternatively long and short bond lengths. The first carbon atom attached after the *sp^2* carbon bridge on the first carbon (labeled * in the table 5.2) is the center of the CC vibration (ν_4) absorbing at 2094 cm^{-1} (b_6) by $C_8N_4^-$. The same center is observed in one of the two IR active vibrations (ν_5) et (ν_6) in $C_{10}N_4^-$ measured at 2063 cm^{-1} (a_2). The other band (a_3) at 2103 cm^{-1} originates from a vibration centered in the middle of the chain (labeled with **).

The CN imine stretches around 1400 and 1600 cm^{-1}, take place in the two smallest systems presented. The anions containing at least as many nitrogen as carbon atoms share a nitrogen atom between two carbon atoms forming an imine function. Attached on a *sp^2* carbon in $C_4N_4^-$, the central double CN bond leads to the lowest stretching band here observed at 1428 cm^{-1}. In $C_3N_4^-$, two central C=N bonds could also be out of phase coupled and absorb in the region of 1600 cm^{-1} (at 1602 and 1636 cm^{-1}, depending of the isomer).

5.3 Geometries shared by the tetracyano-carbanions

All the ground states of the $C_xN_4^-$ present a doublet multiplicity and share important similarities. As already observed for the $C_xN_y^-$, the nitrogen atoms are located at the end of a carbon chain or branch. For the $C_xN_4^-$ with x = 6, 8, 10, the nitrogen atoms are preferably located on each end of the branched anions. The structure with 6 carbon atoms is composed of four branches having the same length, which are attached by two *sp^2* carbon atoms. For x = 8 and 10, the structures were similar to $C_6N_4^-$, differing only in the length of one branch. For the anions containing 4 carbon atoms, the structure is composed of only three branches and the geometry appears as a hybrid between $C_6N_4^-$ and $C_3N_4^-$. Two branches of $C_4N_4^-$ resemble to $C_6N_4^-$ with two nitrile functional groups and the third branch resembles to $C_3N_4^-$ (with a nitrile and an imine function). $C_3N_4^-$ forms a chain alternating nitrogen and carbon atoms.

The anions of this group include two parts containing two nitrogen atoms connected by the two *sp^2* carbon atoms. These dicyano-carbene parts possess an odd number of carbon atoms. Except for C_3N_4, a dicyano-tricarbene part was systematically present attached by the *sp^2* hybridization of its median carbon. In the case of $C_8N_4^-$ or $C_{10}N_4^-$, a longer part containing five or seven carbon atoms, were attached on the second carbon atom from an extremity. The $C_xN_2^-$ containing an odd number of carbon atoms were produced particularly abundantly by the sputtering process (see chapter 3). Composed of two (x = odd) parts, the (x = even) $C_xN_4^-$ were predominantly observed. Considering the geometries, it was conceivable that the dicyano-carbanions played an important role as reagent in the formation of $C_xN_4^-$. For $C_3N_4^-$ the structure alternated the atoms C and N. The alternation was also shared by smaller clusters: the $C_2N_3^-$ [62] and the neutral or the cationic form of C_2N [73]. A formation of $C_3N_4^-$ from anions as $C_2N_3^-$ or CN^-, also abundantly present in the sputtering yield, could be suspected as well.

5.4 Detailed review of the $C_XN_4^-$

Each system of the group presented specificities and the systems were examined separately in the following paragraphs.

For *$C_3N_4^-$*, a large number of isomer is predicted with a variety of different structures and geometries. The structures of smaller clusters containing more nitrogen than carbon atoms were already discuss in the literature [140]. Two successive terminal nitrogen atoms at the end are predicted for CN_3^-, a cyclic structure as for CN_4^- and nitrogen in the middle of a chain as for $C_2N_3^-$. All these structural characteristics are conceivable also for $C_3N_4^-$ and thus, many different geometries and their frequencies have been calculated with the B3LYP/aug-cc-pVTZ method and compared to the experimental spectrum. The lowest energy isomer of $C_3N_4^-$ presents a ground state with doublet multiplicity and forms a chain of alternating carbon and nitrogen atoms. This chain is not linear and forms a flattened "M". The nitrile functional groups at the end are predicted to be responsible for two absorption peaks. Experimentally only one band coming from the nitrile functional group is observed at 2179 cm^{-1} representing a difference of 9 cm^{-1} with the estimations. The absence of the second band corresponding to ν_1 can be explainable by the predicted weak intensity. For the band resulting from the middle CN is lower than the predicted values with 15 cm^{-1}. A second experimental absorption band is observed at 1602 cm^{-1}. In order to explain this band the next isomer has been considered. The isomer is only 0.22 eV higher in energy and presents a similar structure to the global minimum forming a flattened "S" (see figure 5.4). The band corresponding to the imine functions of the second isomer was predicted 31 cm^{-1} deeper than the first isomers, in very good agreement with the experimentally bands, which are predicted to be shifted by 34 cm^{-1}. The two isomers differs by their conformations, and the influence of the tagging and the conformation or the conformation on the tagging is thinkable. A tagging with a species other than D_2 could reveal the possible influence of the messenger.

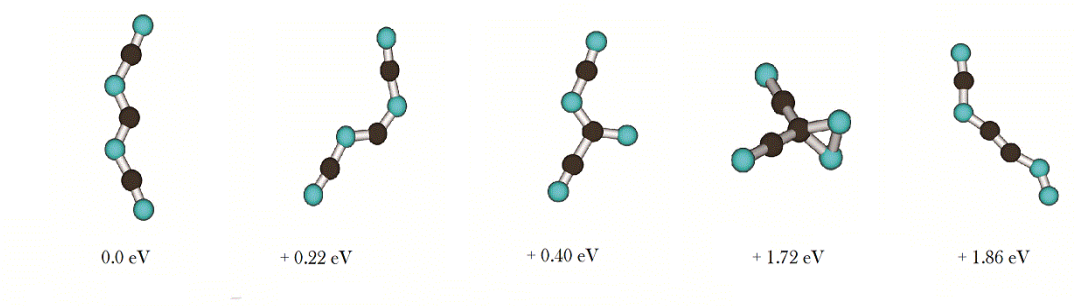

Figure 5.3: Five deepest isomer of $C_3N_4^-$ predicted by the B3LYP / aug-cc-pVTZ calculations.

The $C_4N_4^-$ could also form many isomers. The energetically lowest structure presents three branches with three terminal nitrile functions. The fourth nitrogen is located between two carbon atoms, the sp^2 carbon and the carbon involved in the nitrile functional group. The branch containing the two nitrogen atoms includes a bond length at the extremity slightly

longer than in the two other branches. The absorption due to the vibration of this third nitrile function was observed at 2105 cm^{-1}, which represents a difference of only 3 cm^{-1} with the expectations. This remains the lowest absorption frequency originating from the nitrile functional groups by the $C_4N_4^-$. Another nitrile group (labeled with 2 in the table 5.1) absorbs at 2142 cm^{-1} and is with a factor 0.6 more intense and 32 cm^{-1} deeper than the third nitrile functional group (labeled with 1). The imine function bound to the sp^2 carbon includes a longer bond length and absorbed at 1428 cm^{-1}. The calculations present a deviation not exceeding 12 cm^{-1} by the three bands resulting from the nitrile functional groups and 28 cm^{-1} resulting from the imine functional group rendering the identification clear. The different possible isomers of this anions are completely underprivileged, for example the isomer with three branches and the four nitrogen atoms at the extremities was 1.82 eV higher, or the structure with a sp^3 carbon presented a ground state 3.12 eV higher.

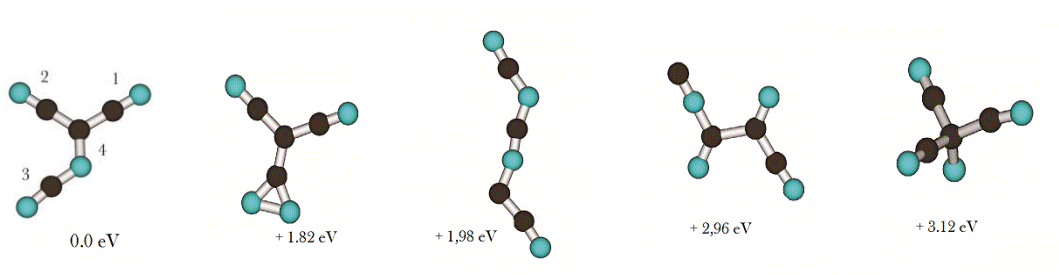

Figure 5.4: Four isomers of $C_4N_4^-$ predicted by the B3LYP / aug-cc-pVTZ calculations. The energies were compared with the ground state of deepest energy calculated presented in the table 5.2

The $C_6N_4^-$ reveals absorption bands in accord with the calculations. The two stronger expected bands exhibit only a deviation of 5 cm^{-1} and 12 cm^{-1} from theory. The third absorption expected is not observed which can be explained by the low intensity expected. The geometry revealed by the B3LYP/aug-cc-pVTZ is corresponding with the theoretical calculations already reported. Available neon matrix absorption spectra show bands at 2163 .9 cm^{-1} and 2108.4 cm^{-1} which were attributed to the $C_6N_4^-$ [151]. In this experiment the molecules were obtained by an irradiation of a tungsten lamp several hours long on the cationic TCNE. These results obtained in matrix presented a difference of 43 and 25 cm^{-1} relative to the results obtained here by the IRPD method.

The $C_8N_4^-$ ground state was proposed as a tricyclic form with two five-membered rings connect each other via a six membered ring [154] presented in the figure 5.4.

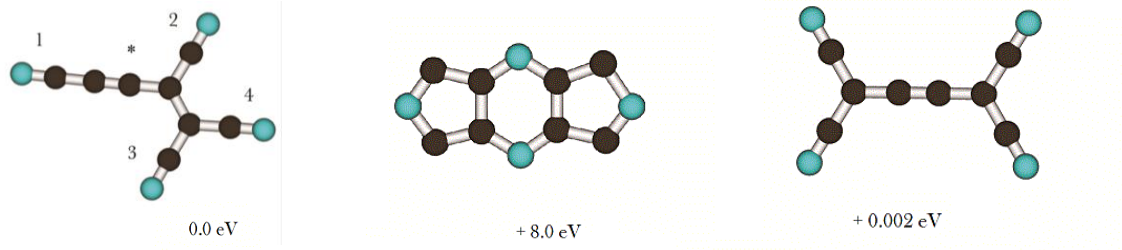

Figure 5.5: Isomers of $C_8N_4^-$ predicted by the B3LYP / aug-cc-pVTZ calculations. On the left side the isomer as proposed in the literature is shown [92] and on the right the side the second isomers in energy is presented. The energies were compared with the ground state of deepest energy calculated presented in the table 5.1.

The DFT calculations reveal the tricyclic anions 8.0 eV higher in energy than the lowest energy geometry, indicating that this compact structure is energetically unfavorable. This is supported by the IR frequencies. The predicted characteristic band for the cyclic structure at 1338 cm^{-1} is not observed in the experimental spectrum. Additional two different branched structures are calculated with a very small energetic difference of 0.002 eV. The measured bands allowed the identification of the favored branched geometry, the experimental bands presenting a deviation smaller than 15 cm^{-1} from the calculated values. The measured intensities are in accord with the expectations. Four absorption bands should originate from the nitrile functional groups, coupled in phase or out of phase$^-$, where only the nitrile groups on the same side of the sp^2 carbon bridge are coupled together (table 5.1).The CC stretch is predicted responsible for an absorption band at 2099 cm^{-1} .Only the bands predicted at 2224. 8 cm^{-1} and 2203.2 cm^{-1} were observed slightly stronger than the estimations. The isomer 0.002 eV higher in energy is predicted with two absorptions at 2223.5 cm^{-1} and 2208 cm^{-1}, which could overlap the absorption bands of the lowest energy isomer. An additional band at 2150 cm^{-1} was detected in the IRPD spectrum. This band is not predicted for either of the calculated geometries. This band could be explained by the combination between two IR active absorption bands predicted at 849.7 cm^{-1} and 1290.1 cm^{-1} which forms a peak estimated at 2139.8 cm^{-1}(figure 5.6). Such combination band have been observed by the C_xN^- [62] and thus, their presence is not surprising.

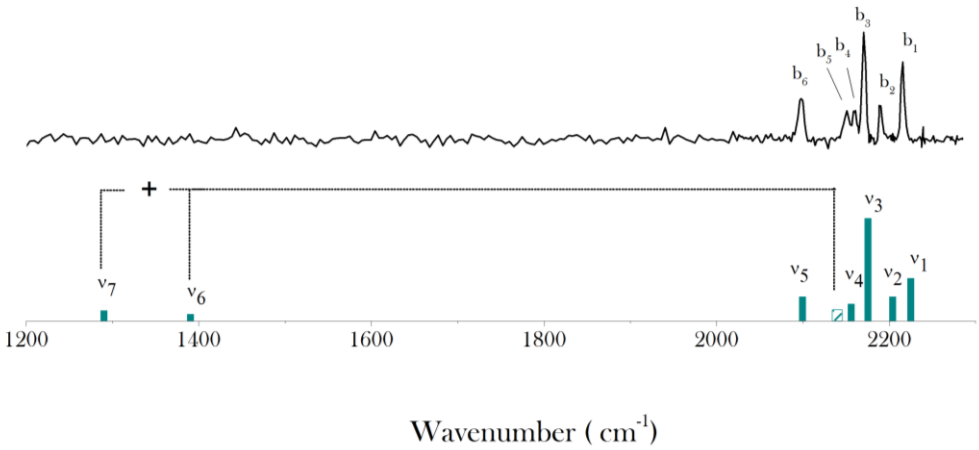

Figure 5.5: IRPD spectrum of $C_8N_4^-$ (top) from B3LYP/aug-cc-pVTZ calculations (bottom) including the assignment with the band coming from the combination of two modes of vibration.

The $C_{10}N_4^-$ presents plenty of possible isomers. The absorption spectra indicated structure with similar to $C_8N_4^-$. The DFT calculations reveal four isomers < 0.15 eV higher than the energetically deepest isomer (figure 5.6). The experimental absorptions match the calculations of the isomer of deepest energy. Indeed the band observed at 2063 cm^{-1} coincids only with the ν_5 of the isomer of smallest energy (table 5.2). The two features corresponding to the CC stretches are wide and asymmetric, suggesting the presence of an additional band. The band at 2103 cm^{-1} possesses an asymmetry on the red side, explainable by the presence of another isomer. The ν_4 band and the ν_5 band of different isomers were estimated close to 2100 cm^{-1}. The width of the bands seems to reveal the presence of the other isomers but avoid a precise identification of other isomers potentially present. The overlapping of many bands of several isomers in the region between 2150 and 2220 cm^{-1} could explain the 28 cm^{-1} large band centered at 2191 cm^{-1}.

isomer	ν_5 CC Stretch	ν_4 s CC Stretch	ν_3 Stretch	ν_3 CN Stretch	ν_2 CN Stretch	ν_1 CN Stretch
a	2057.0 (452)	2112.8 (1632)	2163.3 (206)	2197.4 (798)	2210.0 (52)	2216.2 (78)
b	--	2105.1(362)	--	2182(1360)	2222.9 (800)	--
c	2098.7(80)	2106.0 (139)	2177.1(223)	2182.7(833)	2219.0 (267)	2229.3(177)
d	2092.2(575)	2131.5(2)	2159.0(102)	2193.6(1412)	2203.6 (167)	2203.4 (317)
e	2115.5 (124)	2146.6(412)	2179.5(129)	2195.2(461)	2215.3(578)	2237.0(370)

Table 5.2: Frequencies of absorption predicted for the isomers $C_{10}N_4^-$ of obtained by the B3LYP / aug-cc-pVTZ calculations. The isomer a,b,c,d,e are presented in figure 5.6.

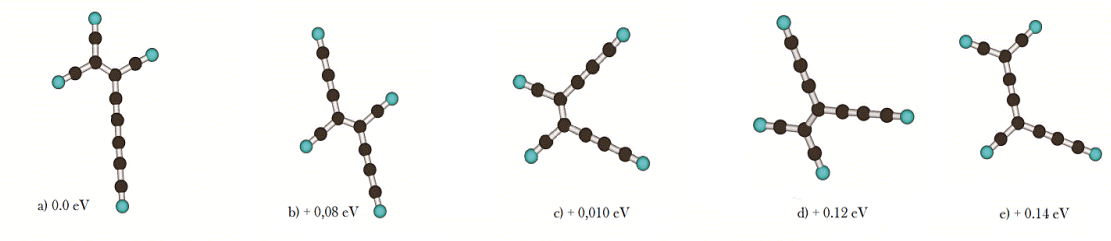

Figure 5.6: Isomers of $C_{10}N_4^-$ predicted by the B3LYP / aug-cc-pVTZ calculations. The energies were compared with the ground state of deepest energy (a).

5.5 Conclusions of the $C_xN_4^-$

The sputtering of carbon target in nitrogen produced abundantly the tetracyano-carbanions identified by the IRPD method. The production of anions with an even number of carbon atoms was strongly favored, but the presence of anions containing an odd number of carbon atoms was also observed. The IRPD experiment revealed the absorption frequencies of the $C_xN_4^-$ anions, x = 3, 4, 6, 8, 10. By comparison with DFT calculations, the structure of the isomers favored in the gas phase could be determined.
The structures with a lowest energy estimated by B3LYP / aug-cc-pVTZ calculations were always favored. The presence of other energetically closed isomers was proposed by $C_{10}N_4^-$. In the case of $C_3N_4^-$, the IR spectra can be explained by an energetically less favored isomer. This assignment requires additional investigations.
The geometries of the measured anions are similar to the $C_6N_4^-$, having a longer branch in case of larger number of carbon atoms. The two systems presenting four and three carbon atoms included one and two imine functional groups, respectively.
The experiment also allowed a comparison with the literature on the $C_xN_4^-$. The IRPD experiment on $C_6N_4^-$ identified a deeper ground state in accord with the prediction [150] but cast the doubt on the experimental bands attributed to the anion in neon matrix [151]. The measurement and the calculations on $C_8N_4^-$ disapproved the structure already proposed [154]. The IR vibrational information about the tetracyano-carbanions is strongly enhanced through this work.

Chapter 6

Carbanions C_x^-

Carbon constitutes a perfect illustration of allotropism. For example, the well-treasured diamond is an insulator with a large band gap and is most likely the hardest material on earth, whereas the more brittle graphene presents high electron mobility. The strong physical and electronic differences arise from the arrangement of the carbon atoms. A sp^2 hybridization of carbon atoms is the base of graphite and carbon nanotubes, whereas a sp^3 hybridization could form diamond or lonsdaleite depending on the lattice arrangement (respectively tetrahedral or hexagonal). Carbon exists also under the carbyne form, a long chain of *sp* hybridized carbon. In the carbyne chains, transitions were predicted to occur between two configurations: the cumulene =C=C= and the polyyne –C≡C–, known as Peirels transitions [154]. DFT calculations performed for an infinite chain estimated the polyyne configuration as favored by 2 meV per atom compared to the cumulene configuration [36]. Carbyne molecules were proposed many times for a variety of applications including nanoelectronics [37], the synthesis of complexes containing an active metal [38], and hydrogen storage [39]. Recent theoretical studies predicted the carbyne chain as the stiffest material known [36]. Carbyne chains were observed stable at high temperatures (up to 3000 K) [156] and were identified more than fifteen years ago in the interstellar medium [157]. Following this discovery in astronomy, carbon chains and their ions were subject of many theoretical and experimental studies in the nineties. The rate of radiative attachment of electron to naked carbon was predicted in the order of $2 .10^{-7}$ cm^3 s^{-1} and the life time of C_x^- up to several weeks under interstellar conditions [22]. In the gas phase, cyclic molecules were reported; their occurrence depends on the size of the chain. From 10 carbon atoms and up, cyclic structures were favored over chain structures [158]. The capacity to form cycles for smaller clusters increases with positively charged carbyne structures. For example under certain conditions, positively charged rings of 3 atoms were observed [161] and the chain structures were completely underprivileged beyond C_{10}^+. Concerning anions, the linear chains were more widespread and were still observed for important masses (for example C_{30}^-). Anionic systems exist also with cyclic geometry from 9 to 29 carbon atoms, as identified by photoelectron spectroscopy studies [159], where the linear anions presenting more than 9 atoms were only a minor product of laser vaporization. The IR absorption spectra of the small C_x^- (x = 5-10, 12) chain-forms were already published, observed by FTIR spectroscopy in neon [164] and argon [162-163] matrix. The photoelectron detachment applied on the linear chains for x = 12-21 reported the absorptions spectra in the region of 5500 to 11000 cm^{-1} and the transparency of the ring forms [160]. One of the few experimental data on C_{11}^- resulted from a U.V. photodetachment study, where the photoelectron pattern of C_{11}^- presented anomalous double peaks, attributed to an experimental artifact [159]. In this work the IRPD measurements of C_x^- (with x = 5-9, 11) provide IR absorption frequencies in gas phase. Starting from 9 carbon atoms, the anions start to form rings. C_{11}^-, not yet investigated in matrix presents a particularly interesting structure.

6.1. IRPD Spectra

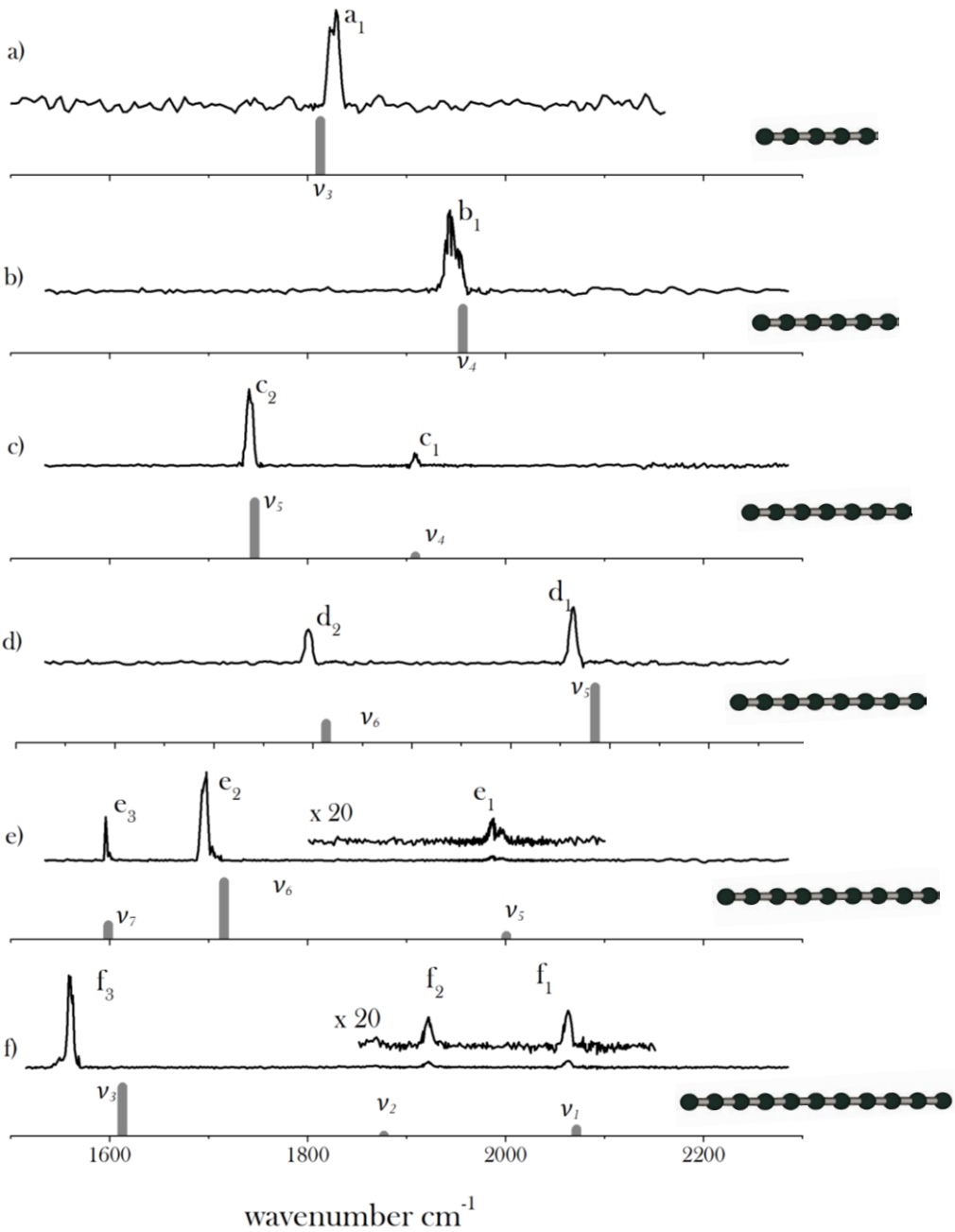

Figure 6.1.: a) to f) IRPD spectra of C_x- (x = 5-9, 11). The grey bands symbolize the frequencies as predicted by the B3LYP calculations using the aug-cc-pVTZ basis set (scaling factor 0.968).

All the systems present strong absorption bands in the region from 1500 to 2100 cm^{-1}. The full power of the laser, up to 1.0 mJ, per pulse leads to a fragmentation ratio of the tagged carbanion of up to 80%. Such absorptions match with the strong intensities of some thousands of km/mol as predicted by the DFT calculations (table 6.2). The spectra presented in the figure 6.1 are obtained with a reduced light intensity (up to 16 times) in order to avoid saturation and to conserve the correct relative intensities of the bands. The here presented IR-range is investigated with both available IR laser setups. All the bands are situated in the far IR region or in the overlapping region of both laser setups and the relative intensities between the bands are guaranteed.

Ion		Matrix Neon / Argon	Gas phase IRPD	B3LYP aug-cc-pVTZ
C_5^- (X $^2\Pi_u$)	ν_3	1822.3 / 1831.8	1826	1813.0 (1107)
C_6^- (X $^2\Pi_u$)	ν_4	1938.5 / 1936.7	1947	1957.0 (930)
C_7^- (X $^2\Pi_g$)	ν_4	- / -	1910 (44)	1909.3 (109)
	ν_5	1736.4 / 1734.8	1742 (100)	1746.5(3049)
C_8^- (X $^2\Pi_g$)	ν_5	2067.8 / 2064	2068 (100)	2085.5(1975)
	ν_6	1796.0 / -	1801 (47)	1813.4 (660)
C_9^- (X $^2\Pi_u$)	ν_5	- / -	1987 (4)	2001.0 (333)
	ν_6	1692.6 / 1686.7	1696 (100)	1715.8(4926)
	ν_7	- / 1583.3	1594 (69)	1598.7(1228)
C_{11}^- (X $^2\Pi_g$)	ν_1	- / -	2063 (7)	2072.0 (1310)
	ν_2	- / -	1922 (6)	1877.2(46)
	ν_3	- / -	1560 (100)	1612.1(9954)

Table 6.1: Absorption frequencies observed in the gas phase by IRPD, in neon and argon matrix, and predicted frequencies from B3LYP/aug-cc-pVTZ calculations. All the values are given in cm^{-1}. The errors were estimated at +/- 1 cm^{-1} in neon [164] and in argon matrix [162-163|. The relative intensities of the experimental bands and the predicted intensities in km/mol are given parenthesis.

The number of bands grows with the size of the systems. One band is measured for the clusters with 5 and 6 carbon atoms, two bands for 7 and 8 atoms, and three bands for 9 and 11 atoms. The two bands of highest frequencies come from C_6^- and C_8^-. The strongest bands correspond to the bands of higher frequency by the system containing an even number of carbon atoms. On the contrary, the bands of higher frequency containing an odd number of carbon atoms are

weaker. Except for C_{11}^-, the absorption bands observed in matrix are in good agreement with the results from the matrix studies confirmed clearly the identification (table 6.2). All observed bands in the region from 1560 to 2068 cm^{-1} are attributed to CC stretches. The DFT calculations predict the vibration frequencies close to the observed absorption for x = 5-9 and reveal information about the modes of vibration responsible for each band.

6.2 Parity discrepancy in the structure of C_x^-

Cumulene and polyyne

In accordance with previous reports, C_x^- from 5 to 9 form linear chains. The alternating bond lengths in the structures are consistent with the transitions reported between the cumulene-form and the polyyne-form [93]. All the chains are symmetric in regards to the center of the chain. Starting from the extremity, the first bond is short and the second bond is by all anions the longest of the chain. The structures with an even number of carbon atoms are closer to the polyyne-form and several bonds are predicted with a length under 1.25 A°, equivalent to a triple bond. Starting from the extremities, the triple bonds are located between the third and the fourth atoms in C_6^- and in C_8^-. The other bonds alternated between longer and shorter lengths. The shorter lengths are between simple and double bonds and the longer between double and triple bonds. An odd number of carbon atoms have a configuration, which is closer to the cumulene-form. The interatomic distances between 1.272 and 1.314 A° correspond to double bonds and there is still an alternation in bond length. This alternation is symmetric to the center of the molecule, and the two adjacent bonds of the same length are located at the center of the chain. The two successive bonds of same length are shorter in C_7^- and C_{11}^- and longer for C_5^- and C_9^-. In the figure 6.3, the configuration of the chains and the kind of the bonds are also represented.

Size dependent evolution of the stretching modes and frequencies

All the vibration modes that are IR active and measured by the IRPD method are composed of antisymmetric stretching vibration from the center of the chain. A discrepancy in the vibration patterns between odd and even numbers of carbon clearly exists (figure 6.3). The IR active vibration patterns of the even number of carbon atoms includes bonds placed on either side of the central bond. The central bond isn't involved in the vibration. For C_6^-, two successive bonds on each side of the central bond were involved in the IR active vibration. The only mode of vibration resulted from the alternating phase of the stretches of the two bonds. This mode forms the absorption peak at 1934 cm^{-1}. For C_8^- three bonds were situated on each side of the central bond. The three bonds were able to form two IR active modes. The three bonds could alternate successively the phase of stretch and are responsible for the stronger absorption of C_8^- at 2067 cm^{-1}. The two external bonds in opposite phase formed another mode of vibration whereas the bond in between conserved a similar length. This second mode is responsible of an absorption band two times smaller and 266 cm^{-1} lower than the other band.

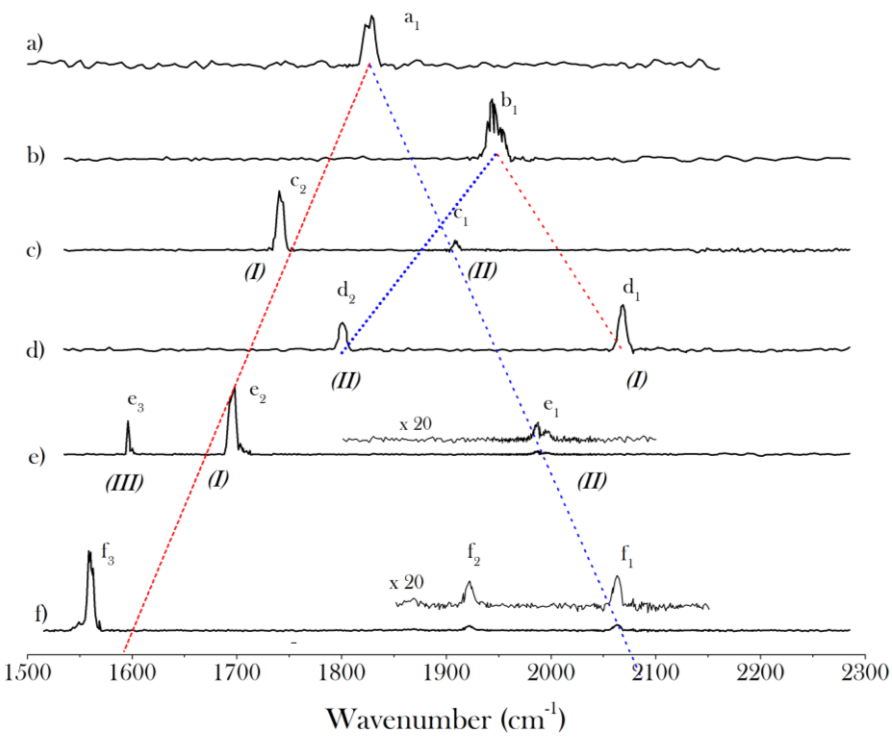

Figure 6.2 :a) to f) IRPD spectra of C_x- (x = 5-9, 11), respectively from a) to f) with broken line link the same king of vibration mode: stretch mode involving nearby bonds *(I)* in red and involving every second atom (II) in blue.

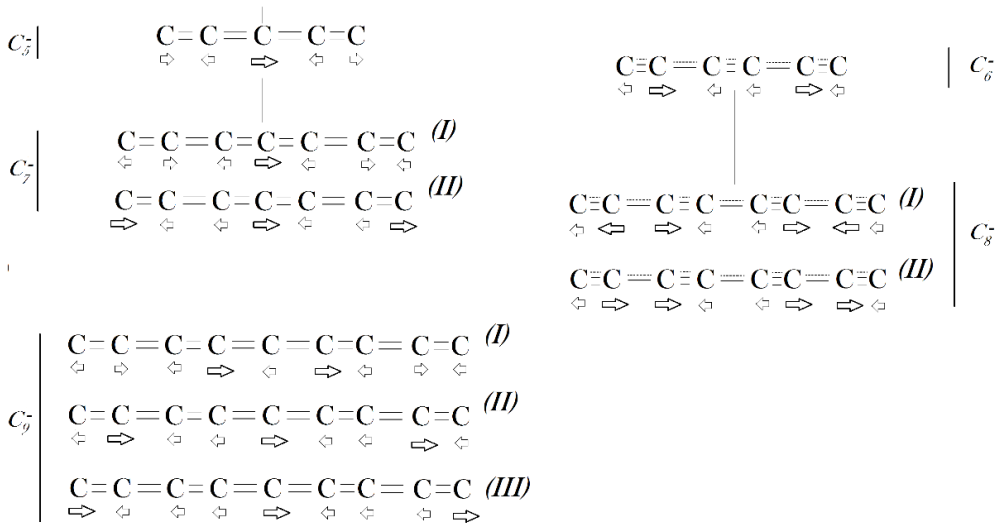

Figure 6.3: Vibration modes from B3LYP/ aug-cc-pVTZ of C_x^- (x = 5-9, 11) anions, strict atlernative stretch mode *(I)* stretch mode with jump of two atom (II) ,stretch mode with jump of three atom (III) . The dark arrows are located at the center of the vibration mode.

With chains containing an odd number of carbon atoms, an atom is located in the middle of the chain. For the chains with an even number of carbon atoms, all the IR active modes are antisymmetric to the center of the chain. In order to simplify the explanation, only one side is described. The IR active modes of vibration are made in most cases with a coupling between the bond of the central atom and the other bonds on either side. C_5^-, which presents two bonds on each side of the center, forms a mode with an alternating stretching phase of these two bonds. The chain with two atoms more (C_7^-) presented three bonds on each side. The two active modes measured on C_7^-. The anions with an odd number of carbon atoms could vibrate with a strict alternating stretch of each bond, including the central atom. This strict alternating mode absorbs at 1742 cm^{-1}. The second mode occurs when the bond in the middle of the three conserves its similar length and the two lateral bonds oscillated with an opposite phase. This second mode is 168 cm^{-1} higher in frequency, and has a six times lower intensity than the first mode of C_7^-. The C_9^- possesses four bonds on each side of the central atom of the chain. These four bonds have many possible modes of vibration, three are IR active and are revealed by three peaks in the IRPD spectra. In a way to clarify the explanation, the bonds could be numbered from 1 to 4 from the extremity to the center. The first mode of vibration involves bond 1 and bond 4 in opposite phase. The absorption is observed at 1595 cm^{-1} and with two third of the intensity of the following second mode of vibration. Bonds 2 and 3 are in opposite phase, responsible for the stronger absorption of C_9^- at 1696 cm^{-1}. In the third mode bond 4 and bond 1 are vibrating in phase, while bond 2 was in opposite phase. The absorption of this third mode was more than ten times weaker than the two others and located at 1987 cm^{-1}.

To sum up, the modes with alternating stretching phase are responsible for the strongest absorption bands and occur for each size of carbon chain from C_5^- to C_{11}^-. A discrepancy exists between the odd numbers and the even numbers of carbon atoms in the chains. The alternating modes involve all the atoms in the chains with an odd number of carbon atoms and the frequencies of absorption decreases with the size of the chain. For the chains with an even number of carbon atoms, the central bond is not involved in the vibration and the alternation is not complete. In this case the alternating modes absorb at higher frequencies than for the odd number chains and the frequencies of the alternating modes increase with the size of the chain. From C_7^- and C_8^- a second kind of vibration mode appears where the alternation skips two atoms. The second modes absorbs at a higher frequency for C_x^- (x = 5, 7, 9), and at a lower frequency for C_x^- (x = 6, 8). A third mode appears from C_9^- with a skip of three atoms in the coupling of the stretches and possesses a lower frequency of absorption than the two other modes.

6.3 Absorption band characteristics of C_x^-

Matrix shifts

The values obtained with the IRPD method are close to the values measured in matrix. The matrix to gas shift is systematically on the red side and is under 8 wave numbers in neon matrix and under 11 wave numbers in argon matrix. The shifts are commonly observed in matrix and resulted from the attractive effect caused by the induced dipoles on the matrix. The red shifts are understood by the stronger attractive forces of the $\nu = 1$ state than the $\nu = 0$ state. Typically the red shift increases with electronegativity differences along the molecule and with matrix polarizability [165]. By comparison with the present IRPD investigation, the neon measurements form only red shifts. These red shifts, coming from the neon matrix, are between 0.5 cm^{-1} and 8 cm^{-1} and are not clearly influenced by the size or the parity of the anions. In the spectra of the anions containing 8 carbon atoms, two different shifts are observed for different bands of the same system. The mode which successively alternates the phase of vibration is observed with a smaller shift than the other mode. Different shifts observed on different modes of vibration in a same system are often reported and the sign of the shift could also change for different stretches as for example with SO_2 [165]. The argon matrix influences the frequency of absorption more strongly, and except for C_5^-, results in red shifts, which are larger than for the neon matrix. The only different behavior comes from C_5^- where the argon matrix forms a 5 cm^{-1} blue shift in regards to the IRPD measurements. The blue shifts coming from the matrix were already observed in small carbanions as for example with C_4^- in neon matrix from the group of J. P. Maier [129].

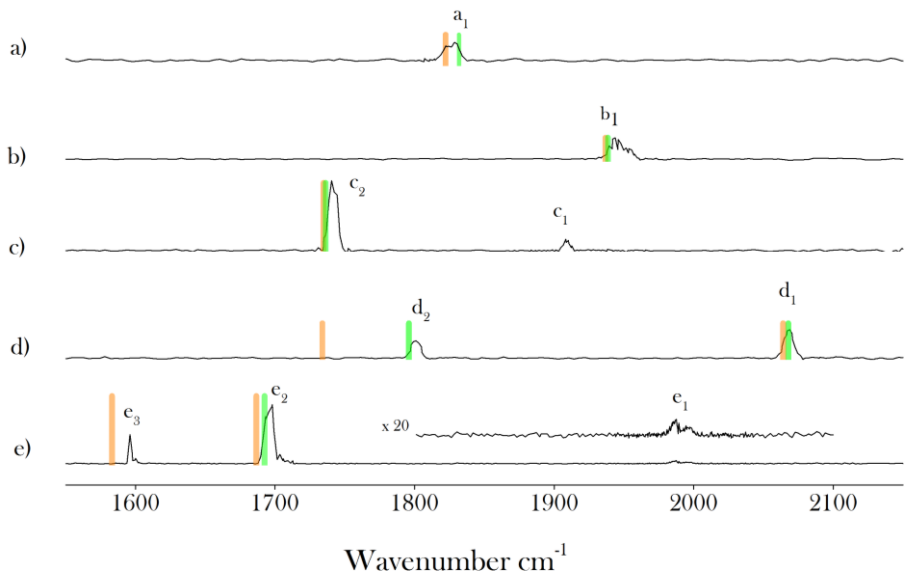

Figure 6.4: IRPD spectra and results of measurement in neon (green bars) and in argon (orange bars) matrix.

The IRPD measurements are coherent with the studies in matrix. The argon or neon matrix produce a majority of red shifts and one blue shift. The biggest shifts from the neon matrix were observed with C_6^- and C_7^-. The lack of bands in the neon and argon matrix investigations rendered a deeper analysis of the shifts difficult.

Particular sensitivity of the IRPD method

The experimental relative intensities are in good agreement with the order of intensities predicted at the B3LYP/aug-cc-pVTZ level. The vibration modes presenting two atoms moving in parallel are estimated with a weak intensity. The computational results predict these modes 30 times weaker than the strongest band by C_7^- and 4 times weaker by C_9^-. The experimental relative intensities differs from the theoretical results. The bands located at 1910 cm^{-1} for C_7^- and at 1594 cm^{-1} for C_9^- represent 44% and 69% relative the strongest band of each anion. The two stretch modes underestimated by theory present a similar pattern of vibration, which involve in particular the extreme and the central bond of either side. Following previous B3LYP/aug-cc-pVTZ calculations, the D_2 messenger is predicted with a favored location at the end of the carbon chain [112]. In the neon and argon matrix experiments, these bands were not observed suggesting the particular sensitivity of the employed IRPD method for the modes of vibration involving in particular the external bonds. An enhance sensitivity of the IRPD method could be suspected when the location of the messenger coincides with the vibration and demand further investigations.

6.4 Identification of C_{11}^-

The chain with eleven carbon atoms forms absorption spectra with three bands within the experimental range of this study. A first band at 1560 cm^{-1} is more than 10 times stronger than the two other bands at 1922 cm^{-1} and 2063 cm^{-1}. The B3LYP / aug-cc-pVTZ calculations also predicted three bands, but presented a consequent deviation with the experimental data. The strong absorption is predicted at 1612.8 cm^{-1} and the two weak bands at 1877.2 cm^{-1} and at 2072.0 cm^{-1}. The calculations reveal intensities for the two weaker bands, which are 7 and more than 100 times weaker than the stronger band. The experimental intensities reveal a less pronounced difference. The relative intensities represent respectively a factor of 14 and 16 with regard to the strongest bands. In regard of the important differences between the experiment and the calculations, other systems, which might be potentially present, are examined. The cyclic configuration of C_{11}^- is also investigated with the same computational method. With 0.65 eV higher energy than the chain form, the ground state of the cyclic anion is clearly underprivileged. The cyclic C_{11}^- should absorb at 1865 cm^{-1} and at 1995 cm^{-1}. The spectra confirmed the absence of the cyclic anion, as already reported in other experiments [159]. The mass selection allowed the detection of other systems presenting the same mass of 132 amu. The $C_7O_3^-$ is possible, because O_2 is employed as reactive gas in the sputtering process. The deepest isomer predicted by the B3LYP/ aug-cc-pVTZ calculations presents strong absorption bands at 2184 cm^{-1} and at 2119 cm^{-1} (figure 6.4). $C_7O_3^-$ can be clearly

exclude to play a role in these spectra.

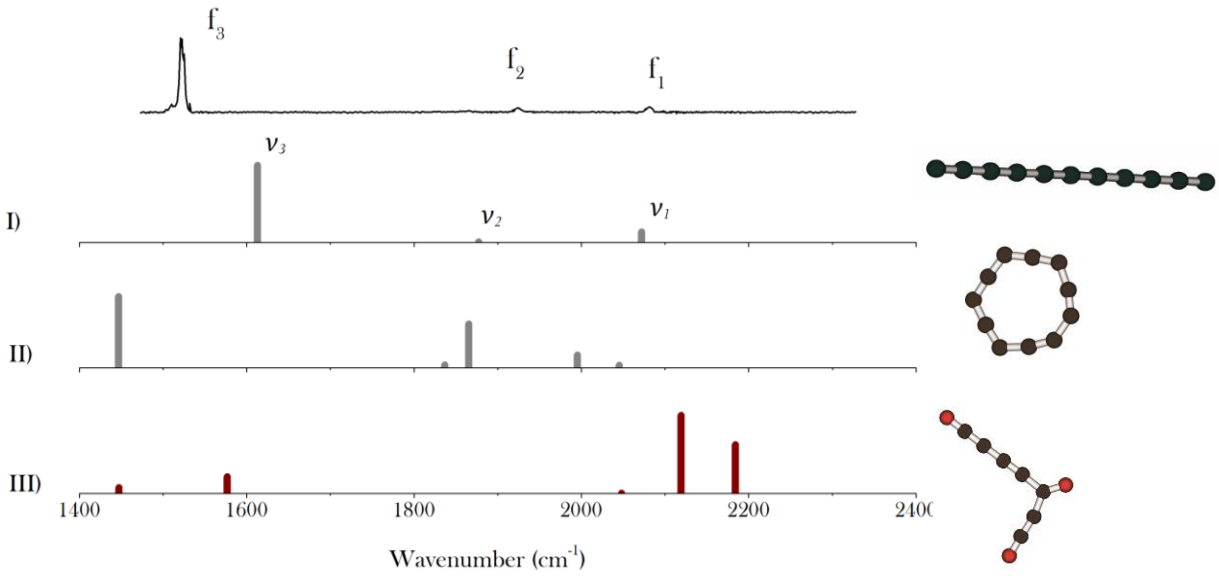

Figure 6.4: IRPD spectrum of C_{11}^-, and the B3LYP/ aug-cc-pVTZ calculations of I) the linear C_{11}^-, II) the cyclic C_{11}^- and III) $C_7O_3^-$

Regarding the evolution of bands as a function of the size of the chains, the spectrum of C_{11}^- is coherent with the other linear anions containing an even number of carbon atoms. The band resulting from the alternating mode of vibration is lower in frequency with 44 cm^{-1} than for C_9^- , whereas C_9^- was 48 cm^{-1} lower than C_7^-. The higher frequency band also follows the behavior of the other smaller chains. This band is 76 cm^{-1} higher than in the C_9^-, whereas the C_9^- higher band is 77 cm^{-1} higher than the C_7^-. The computational deviations are on the blue side by the even numbers of carbon and on the red side by the odd numbers. The greater deviations where already observed by C_9^- (19cm) and C_7^- (17cm), The deviations of the calculations seem to increase with the size of the chain and more significant deviations could be expected for C_{11}^- . Despite the poor calculation values, in regard of the spectra of other C_x^-, there is a high probability that the structure C_{11}^- detected presents a linear structure.

Conclusion of the C_x^-

The sputtering process efficiently produced carbanions. The linear negatively charged carbon chains were detected for all the carbanions containing from 5 to 9 and 11 carbon atoms. The IRPD pre-dissociation investigations matched the precedent neon and argon matrix experiments [159-160]. This experiment revealed new bands for the well-studied carbanion, in agreement with the calculations at the B3LYP/ aug-cc-pVTZ level. The new bands resulting from similar modes of vibration, show a particularly sensitivity with the IRPD technique, which employs D_2 as messenger. The analogy between the bands and vibration modes in the anions containing 5 to 9 carbon atoms revealed a systematic evolution of the spectra depending on the size. A clear discrepancy is observed as a function of the number carbon atoms in the chain. This systematic evolution of the spectra aid the interpretation of the C_{11}^- linear structure despite the poor agreement with the theoretical frequencies. Therefore the correct scaling of the IRPD method, employed within this work on uninvestigated systems is confirmed.

Chapter 7:

Oxo carbanions, C_xO^- and $C_xO_2^-$

CO is one of the most abundant gas in interstellar cloud. Its presence is also used for the detection of H_2 due to the reaction between these two. In 2011 carbon monoxide was discovered on Pluto's atmosphere [166]. This sudden detection of CO, absent in precedent observations, allowed speculations about a fast evolution of Pluto's atmosphere regarding its nature and its size. The smallest monoxide, the well-known poisonous carbon monoxide, remains the only C_xO presenting a triple bond (CO). The monoxides including more carbon atoms present double bonds (-C=O). In contrary to CO, which has been observed and utilized by chemists for centuries, the C_xO consisting of more than one carbon atom required modern technology to be observed. For the first time in 1965 the formation of a longer monoxide was reported: C_2O was synthetized from a reaction from the photolysis of cyanazid in presence of CO [40]. Several years later, C_3O was observed by reaction of graphite vapor on CO [41]. By electrical discharge on the C_3O_2 or photolysis of C_5O_2, the C_4O, C_5O, C_6O, C_7O C_9O were successsively identified [42,167,168]. By Fourier-transform spectroscopy in microwave region, the C_xO x = 2, 4-9 revealed their rotational spectra [167, 168]. Their linear structures was found to become more uniform cumulene-type with increasing the number of carbon atom and converge to constant length. In 1984, the C_3O was identified in the dark cold cloud TMC-1 [169]. In the same cloud, 6 years later, the presence of C_2O was also detected [170]. The actual list of identified interstellar molecules present an underrepresentation of anions. Theoretical studies estimated that C_xO should attach electrons at least as efficiently as the C_x^- [171]. The carbon chains with more than six carbons are predicted to have a lifetime of up to two weeks [23]. By increasing their size, the carbon chains present higher electronegativity and more degrees of freedom. Both of them delay the electron detachment and thus the formation of anions [23]. The additional oxygen atoms provide even more degrees of freedom. Thereby the life time of the C_xO^- is expected to be comparable with that of the C_x^- [171]. Theoretical calculations at a CCSD (T)/aug-cc-pTVZ level and at a B3LYP/aug-cc-pVDZ level revealed the structure of for C_xO^- anions (x = 2-8) [24,171]. With the exception of C_3O^-, the anions present a linear structure, which appear to become more cumulene-like with increasing the size of the chain. Experimentally, the C_2O^- was the subject of photoelectron spectroscopy studies [172] and several electronic absorptions in Neon matrix reported [173]. C_3O^- was investigated by slow photoelectron velocity-map imaging spectroscopy [174]; his structure, which displays a Renner-Teller distortions is reported. Transition states of the C_4O^- assigned to $A \leftarrow X$ and $B \leftarrow X$, were reported by absorption spectroscopy in neon matrix [173], which represent the only experimental absorption spectra of C_xO^- anions (x > 4) yet reported.

Carbon dioxide is one of the bases of organic chemistry and involved in the fundamental process of respiration in life. The well-studied CO_2 is ubiquitous on Earth. The carbon dioxides including more carbon atoms required strategic chemical processes to be observed. The C_xO_2 (x > 1) present a cumulene-like carbon chain and carry the name of carbene dione. Four of them have already been successively discovered during the last two centuries. In 1873, C_3O_2 could be formed through the application of electric discharge on CO. C_3O_2, also called carbon suboxide, presents a boiling point at 6.8°C and is described as gas with a pungent odor. One century later, several larger dioxides were

obtained by photolysis and thermic processes on pseudo-oxocarbon, (oxocarbon containing also nitrogen atoms). In 1988 the successful synthesis C_5O_2 [43] revealed a molecule surprisingly stable, which could be maintained for a short time in a solution at room temperature and forms a yellow solid at temperature below -90°C. C_7O_2 was discovered three years later [44] also through a photolysis process. For the even number of carbons, only one species has been observed in the laboratory. Maier et al. also synthesized C_4O_2 through the photolysis of a carbon cycle containing oxygen and nitrogen, the cyclic diazoketone [45]. The ethylen dione (C_2O_2) has never been observed until now, despite many attempts, even as transients. Neither by neutralization of ionic forms nor by photochemical dimerization is C_2O_2 observable. The singlet ethylene dione is estimated to be inherently unstable and dissociates immediately (and barrier-free) in CO. The facile fragmentation of the triplet C_2O_2 state should explain the difficulty of observation. The lifetime of the triplet state is estimated to be in the order of 0.5 ns and gives hope of observation as transient [175]. For their part the ions $C_2O_2^{2-}$ and $C_2O_2^+$ are stable. A collection of vibrational frequencies was already reported for the carbene diones. The carbon suboxide was many times investigated and the quasi-linear structure of C_3O_2 is well known [176]. The tetracarbene dione neutral reveal experimentally another structure than the linear geometry of the triplet ground state predicted by theoretical studies [178]. The charged carbon diones were also subject to many experimental studies in IR range. Through photoelectron spectroscopy the cation of the carbon suboxide revealed a CO stretch absorption close to the neutral form [177]. Concerning the ethylene dione, both positively and negatively charged ions were investigated by IR absorption spectroscopy in neon matrix and argon matrix [179-180]. The a-stretch band of CO was founded in $C_2O_2^-$ circa 540 cm^{-1} higher than for $C_2O_2^+$. Vibrational absorption spectra of $C_4O_2^-$ anions were not yet reported.

7.1 IRPD spectra of the C_xO^-

The source produces the C_xO^- with a preference for the anions containing an even number of carbon atoms. Here, C_xO^- anions with (x= 2, 4, 6, 8) were subject to IRPD investigations. Their observed absorption bands are in very good agreement with the calculations (figure 7.1). Only two bands present a deviation from the theoretical values exceeding 10 cm^{-1}. Except for C_2O^-, the different bands of absorption occur at similar frequencies for the different anions. For all the C_xO^- (x = 4, 6, 8) the strongest bands are observed around 2180 cm^{-1}, which originate from the CO stretches. The others bands find their origin from the CC stretches. The spectra reveal also the clear presence of $C_{x-1}N_2^-$ in addition to C_4O^- and C_6O^-, indicated by the additional peaks observed in the IRP, which resemble those observed in the chapter 4. The spectra of the dicyano-anions, already discussed in Chapter 4, are compared to the present measurements in section 7.2

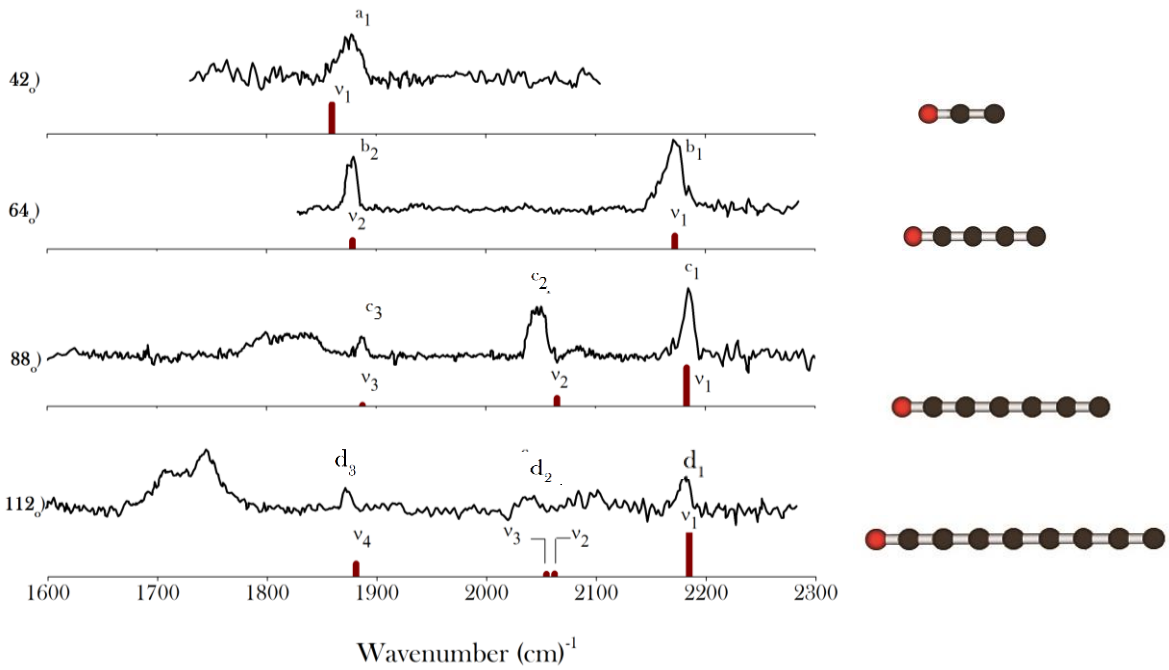

Figure 7.1: IRPD spectra of the masses 42, 64, 88,112 amu corresponding to the C_xO^- (x = 2, 4, 6, 8). The absorption frequencies and structures were obtained from B3LYP/aug-cc-pVTZ calculations (scaling factor of 0.968).

		Stretching bonds	IRPD Experiment Frequency / Width(cm^{-1})	B3LYP Frequency(cm^{-1})
C_2O^-	ν_1	-CO	1866 / 22	1859.6 (371)
C_4O^-	ν_1	-CO	2172 (-) / 14	2172.33 (880)
	ν_2	-CC	1877 (-) / 11	1878.3 (356)
C_6O^-	ν_1	-CO	2184 (100) / 11	2182.9 (2335)
	ν_3	-CC 4th bond	2046 (-) / 18	2064.7(498)
	ν_2	-CC term	1887 (36) / 8	1887.6 (68)
C_8O^-	ν_1	CO	2183 (100) / 10	2184.7 (4868)
	ν_3	CC 4th bond	2041 (44) / 15	2061.7 (165)
	ν_4	CC 6th bond		2054.5 (153)
	ν_2	CC term	1875 (66) / 9	1880.9 (26)

Table 7.1: IRPD experimental absorption bandwidth and frequencies, with the relative IR intensities given in parenthesis in per cent, and B3LYP /aug-cc-pVTZ frequencies with the predicted intensities given in parenthesis in Km/mole.

All investigated C_xO^- present similar cumulenic-like structures, which include double bonds between the atoms. However, the bonds present alternative lengths as presented on the figure 7.2. The longest CC bonds are located between the second and the third carbon (by starting to count from the C extremity of the chain). The CO bond become shorter by increasing the size of anions. However, the absorption involving principally the CO stretches are located at similar frequencies for the anions x = 4, 6, 8. In comparison to C_4O^- the bands corresponding to v_1 were measured at only 11 cm^{-1} and 12 cm^{-1} higher than for C_6O^- and C_8O^-. At the other end of the chain, the CC stretches present also similar IR absorption bands at 1872 cm^{-1} 1887 cm^{-1} and 1875 cm^{-1} for CO_4^-, CO_6^- and CO_8, respectively. For the two longest chains, other CC stretches appear additionally. One part of the band at 2046 cm^{-1} for C_6O^- is attributed to CC stretch involving the central bonds of the carbon chain. The other part of this absorption bands originates from the contaminating $C_5N_2^-$ (figure 7.3). A band at 2041 cm^{-1} for C_8O^- is attributed to the two calculated CC stretch modes, which occur in the middle of the carbon chain. The CCO^- is responsible for only one absorption band in the investigated region and this band at 2186 cm^{-1} result from the out of phase stretching vibrations of its two bonds.

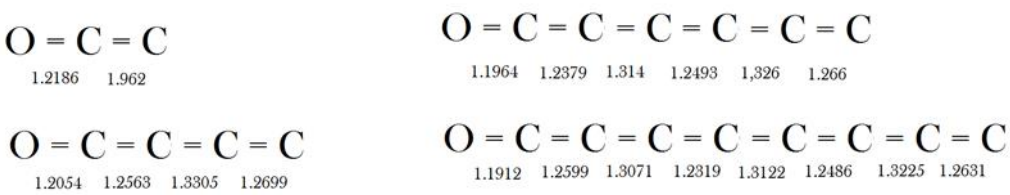

Figure 7.2: Interatomic distances predicted through B3LYP /aug-cc-pVTZ calculations on the C_xO^- (x = 2, 4, 6 ,8).

Particular sensitivity of the IRPD method depending of stretch mode

The observed bands match only partially the predicted intensities. For C_6O^- and C_4O^- , the order of intensities remains experimentally and theoretically the same, but the CC stretch at the end of the chain was clearly stronger than the predictions for C_6O^-. For the C_8O^-, the CC stretch at the end of the chain was responsible for a stronger absorption than the absorption coming from CC stretches in the middle of the chain and the order of the predicted intensities does not match the experimental observations. As was reported in the chapter 6, which concerned the C_x^-, certain stretch modes appeared more sensitive in the employed messenger spectroscopy than by the IR absorption spectroscopy measured in matrix. The particular sensitivity of IRPD method with D_2 as messenger for the modes of vibration, which involve the CC at the end of the chain could be anew suspected.

7.2 C_xO^- / $C_{x-1}N_2^-$ formation

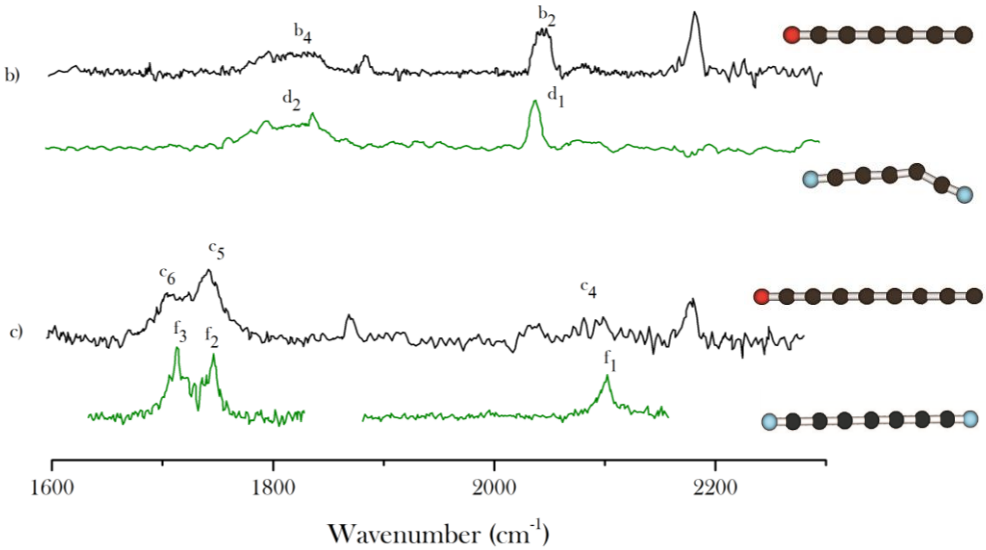

Figure 7.3: IRPD absorption spectra of sputter yield, which originate from sputtering in oxygen [in black], where C_6O^- (b) and C_8O^- (c) are expected. Under each curve IRPD pre-dissociation spectra corresponding to $C_{x-1}N_2^-$ from sputtering in nitrogen [in green].

The presence $C_5N_2^-$ and $C_7N_2^-$ are indubitably detected in the spectra corresponding to the molecular masses of C_4O^- and C_6O^-. The absorption pattern of two anions, which contain two nitrogen atoms, are clearly observed (figure 7.3). The bands (d_2) of $C_5N_2^-$ in addition with the CC stretch at 2146 cm^{-1} are responsible of the 18 cm^{-1} broad band (b_2). The intensities of the bands attributable to $C_7N_2^-$ in the spectra (c) differ from those observed in the presence of N_2 (green curve on the figure 7.3). The bands (c_5) and (c_6) present different relative intensities with the corresponding (f_2) and (f_3). This difference originate from the laser intensities employed in the two experiments. Focused on the detection of the small band C_xO^-, the laser intensity employed provoked the saturation of the band (c_6) corresponding to (f_3). The saturation of the band (c_5) occurred by higher laser intensities (cf. chapter 4). The band (c_4) corresponding to (f_1) appeared very also weak. In the figure 7.3, the relative intensities in the two parts of the absorption spectrum of $C_7N_2^-$ presented (green curve) are not respected and the intensity of band (f_1) is obtained with a strong laser intensity. For the strongest absorption intensities for $C_5N_2^-$ and $C_7N_2^-$, the predictions lie at 459 and 3572 km/mol. The same B3LYP method estimates larger intensities for C_6O^- and C_8O^- at 2335 and 4868 km/mol, respectively. In the presented spectra the strongest band for $C_5N_2^-$ represents about 69 % of the strongest band for C_6O^-. By comparison of the observed with the predicted intensities, the ratio $C_5N_2^-$ /C_6O^- should be 3.5. The strongest band of the $C_7N_2^-$ was also the strongest in the spectra, 1.2 times higher than the CO stretch of the C_8O^-. For his part, the ratio $C_7N_2^-/C_8O^-$ could be estimated at 1.70. These estimations carried out from the calculations remain hypothetic. The quantity of nitrogen (present from contamination of the target) is unknown. However the formation of $C_{x-1}N_2^-$ was definitely favored in comparison to C_xO^- for (x= 8) and for (x = 6).

7.3: IRPD spectra of $C_4O_2^-$

The mass spectra of the $C_xO_y^-$ reveal the consequent formation of anions with the mass of 80 amu. This is the only mass abundantly produced, which correspond to a $C_xO_2^-$.Figure 7.4 compares the IRPD absorption frequencies with the predicted absorption frequencies based on B3LYP/aug-cc-pVTZ calculations.

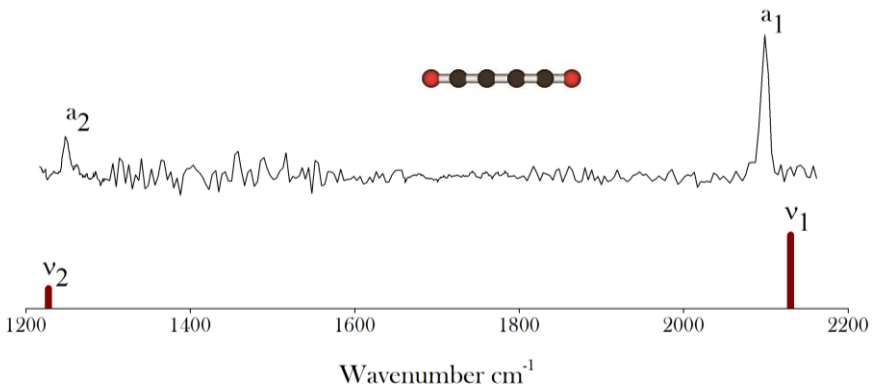

Figure 7.4: IRPD absorption spectra of $C_4O_2^-$ .The absorption frequencies were obtained from B3LYP/aug-cc-pVTZ calculations.

The two strong bands (a_1) and (a_2) are in good agreement with the predictions. The absorption (a_1) originates from a coupled out of phase stretch of both CO groups. The coupling of the in phase CO stretch does not influence the dipole moment of the anions and the vibration mode remains IR inactive. The absorption band at 2082 cm^{-1} presents an important deviation from the calculations (at 2130 cm^{-1}), whereas the band at 1231cm^{-1} resulting from the CC stretch mode matches the calculations with a difference not exceeding 10 cm^{-1}. In the case of the neutral C_4O_2, the absorption of the neutral was observed at 2130 cm^{-1}, 1277 cm^{-1} [45]. The favored structure of $C_4O_2^-$ presents a ground state with a doublet multiplicity. Its linear structure, which includes one oxygen atoms at each end, resembles its homolog containing one oxygen atom (C_4O^-). The CO bonds in $C_4O_2^-$ are predicted with a length of 1.2214 A° and the CC bonds alternate between 1.2607 and 1.3349 A°. The cumulenic form of carbon chain is more pronounced by the presence of a second carboxyl group at a terminal location on the chain.

7.4: Conclusion of the C_xO^- and $C_xO_2^-$,

.

Through the sputtering of carbon target in the presence of O_2, C_xO^- anions up to 9 atoms, could be produced. For the $C_xO_2^-$, only $C_4O_2^-$ could be detected. The IRPD method revealed the absorptions bands of the C_xO^- (x = 2, 4, 6, 8) appearing in the range of 1600 cm^{-1} to 2300 cm^{-1}. The C_xO^- (x = 4, 6, 8) presented a similar pattern of absorptions. These three anions have a similar cumulene-like linear structure. For all three, the carbonyl functional groups located at an extremity are responsible for absorption around 2180 cm^{-1}. At the other extremity, the stretch of the carbon atoms provokes an absorption band around 1887 $cm^{-1}$for all three observed systems. For the anions (x= 6, 8) additional bands resulting from the stretch of the carbon within the chain appeared around 2040 cm^{-1}. C_2O^- differs by the mode of vibration including the two bonds of the molecule and by its absorption at 1866 cm^{-1}. For $C_4O_2^-$, the cumulenic form of the carbon chain is accentuated in comparison to the monoxide structures. In this structure a vibration mode with both CO coupled absorbs at a lower frequency than in the C_xO^-.

Similarly to the observation on C_x^-, several stretch modes, involving in particular the external bond of the chains, were underestimated by the calculations. A particular sensitivity of the IRPD method, which employed D_2 as messenger, for the vibration located at the extremity may be anew suspected. The strong presence of carbon nitrides indicated the stronger reactivity of formation of $C_5N_2^-$ and $C_7N_2^-$ compared to C_4O^- and C_6O^-.

Chapter 8:

Masses of 75, 89 and 115 amu

The three masses of 75, 89 and 115 amu correspond to the masses of three amino acids, respectively glycine, alanine and serine. These three belong to proteinogenic amino acids. The bonding of proteinogenic amino acids form proteins. Fundamental to cells in their abundance and functions, the amino acids are considered to be among the "elementary bricks" of life. They are ubiquitous in life, present even in simple organisms and thereby belong to the family of pre-biotic molecules. The origin of these pre-biotic molecules is under investigation also in space (as presented in the introduction chapter). Glycine, alanine, and serine were found on several meteorites [2-3] and glycine and alpha-alanine were detected in the comet *Wild 2* [1]. In the laboratory, in quasi-interstellar conditions, the synthesis of glycine was several times reported [14-16]. On Earth, beside the 23 proteogenic amino acids and the handful more also present in cells, more than 500 amino acids are known. Amino acids are defined by their amine (NH2) and their carboxylic (COOH) functional groups. In solution, depending on the pH, the functional groups could take the form of ammonium and carboxylate in accord with the *equilibria* $COOH/COO^-$ and NH_2/NH_3^+. Thereby de-protonized and protonized forms exist presenting respectively a negative and a positive charge (figure 8.1). At neutral pH, the glycine, alanine and serine are under their zwitterionic forms. Astronomers foresee different possible forms in space [31]. The zwitterionic form is expected because of the presence of extraterrestrial ice. Abundant H^+ and e^- in space could generate respectively the protonized and the anionic form.

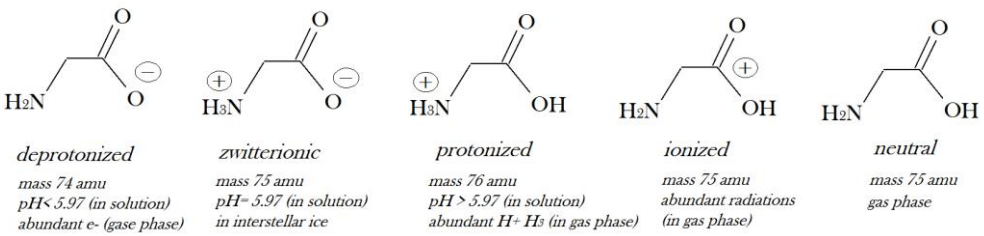

Figure 8.1: Different forms of glycine usully observed in the laboratory and expected by astronomers in space. The three first forms (left) are also observed in solution.

The identification of glycine reported by Devienne et al. corresponds to a mass of 75 amu (positively charged) [17]. In the sputtering source many species are produced under both the cationic and anionic forms. In this work the attention is focussed on the 75, 89 and 115 amu (corresponding to glycine, alanine, proline) negatively charged but not deprotonized. The aim of this work is to understand more the formation of amino acid in the gas phase. The first step consists to examine the sputtering target in the presence of nitrogen and in the presence of oxygen. In these conditions (without introducing H atoms) the presence of amino acids is not expected. The three amino acids, already mentioned, are composed of at least five hydrogen atoms. As shown in the above chapters, the sputtering source produce a wide range of clusters, as well as masses corresponding to this three amino acids. These three masses present an odd number of amu, whereas the C_xN_y and C_xO_y present exclusively an even number of amu

(isotope excepted). On account of the isotopic distribution, the presence of anions including hydrogen atoms in the clusters is also expected. The presence of hydrogen, which remains difficult to vanish completely from the experimental setup, is observed. The system C_5NH^-, ($C_5N_2H^-$ and C_4OH^-) $C_6N_3H^-$, or the hydrogen-free isotopomers including one ^{13}C and ^{15}N are expected for the mass of 75, 89, and 115 amu, respectively (cf the mass-spectrometric analysis in chapter3). The IR absorption spectra of these systems are relevant for the future IR investigations of the amino acids in the gas phase. The mass selection allows the presence of different systems of same mass, which are detected in the same IR absorption spectra. Furthermore, the carbon clusters, which present only one hydrogen atom, represent the first step of hydrogenation. The examination of the hydrogenations is particularly relevant in the understanding of the formation of organic molecule in gas phase.

8.1. The mass 75

Following the mass spectra analysis, the presence of the six isotopomers of C_5N^- and C_5NH^- is expected for the mass of 75 amu (see chapter 3). The hydrogenated form is supposed to represent less than 10%. The five isotopomers carrying a ^{13}C atom shared statistically the same occurrence estimated close to 16% and the isotopomer with ^{15}N should represent 10%. The C_5N^- is one of the first anions detected in the interstellar medium [21], through the IRAM 30-m telescope, which registered the spectral lines in the 80-115 GHz band of the dusty envelope of a carbon star IRC 10216, which has turned out to be the richest source of anions in the interstellar medium. The IRPD investigation of C_5N^- reveal its absorption frequencies in the region between 1800 and 2500 cm^{-1} [62]. An absorption at 2191 cm^{-1} was attributed to a stretch mode, which involve principally the nitrile bond, and two absorptions at 2116 and 1934 cm^{-1} were attributed to the stretch of CC bonds on the middle of the chain and at a terminal location, respectively.

IRPD Spectra of 75 amu

The IRPD absorption spectrum for the anions of 75 amu produced by the sputtering in the presence of N_2 is presented in the figure 9.1. These results are compared with the B3LYP / aug-cc-pVTZ calculations. For the six isotopomers and the hydrogenated form of C_5N^- in figure 9.1, the measured absorption bands are asymmetric, crumpled and resemble clearly the absorption pattern expected for the different isotopomers. The presence of hydrogenated anion is not excluded.

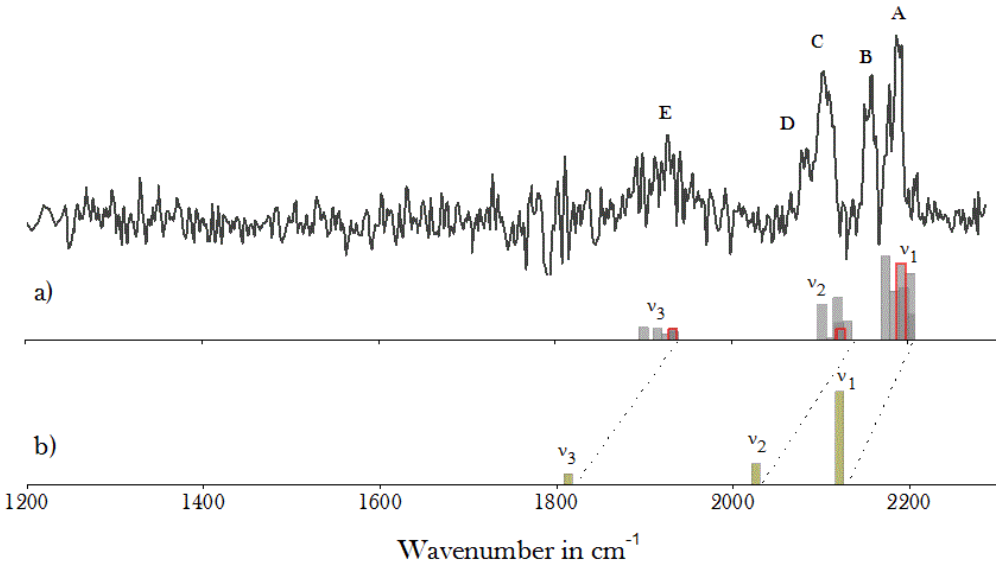

Figure 8.1. : IRPD spectrum of the mass of 75 uma obtained by sputtering of carbon target in presence of N_2. The B3LYP/ aug-cc-vptz calculations reveal the absorption bands of **a)** the isotopomers of C_5N^- and **b)** the C_5NH^- . The red bars represent the ^{15}N isotopomer.

The isotopomers of C_5N^-

The 6 isotopomers, which carry the mass of 75amu, are subject to computational analysis. In comparison with the isotope-free C_5N^-, the DFT calculations revealed strictly the same structures and the same geometries for each isotopomer. The potential energies between the ground state of the isotopomers are predicted with differences smaller than 0.003 eV (table 9.1) and should not influence the distribution of the heavy isotopes. Each location in the anions of the heavy atoms present the same probability of occurrence. The absorption frequencies of the isotopomers are systematically lowered in comparison with the isotope-free C_5N^-, by up to 38 cm^{-1}. The three expected strongest vibrations are the result of stretching modes.

CN stretches (ν_1) are coupled with the other bonds with an alternating stretching phase of the successive bond. The isotopic influences reveal the implication of each atom on the molecular vibration pattern pattern. The ^{13}C influence depends on its location in the anion. From the C-extremity to the N-extremity, this influence become progressively stronger, reaching 28 cm^{-1}. The ^{15}N influence is 10 cm^{-1} lower than the last carbon atom at the N-extremity. According to the calculations, the pattern of absorption is expected to be at least 30 cm^{-1} broad, centered at 2188 cm^{-1} and asymmetric possessing a second maximum on the red side.

Nature of anions	ν_1 CN stretch	ν_2 CC stretch	ν_3 CCt stretch	Energy
C-C-C-C-C-N	2202.8 (1571)	2134.8 (462)	1937.6(232)	-245.243350
^{13}**C** -C-C-C-C-N	2202.7 (589)	2131.7(420)	1916.3(257)	-245.243462
C-^{13}**C**-C-C-C-N	2202.6(1539)	2122.0(397)	1900.7(284)	-245.243525
C-C-^{13}**C**-C-C-N	2195.4(1213)	2102.7(815)	1935.2(187)	-245.243548
C-C-C-^{13}**C**-C-N	2184.7(1128)	2120.7(967)	1926.1(137)	-245.243531
C-C-C-C-^{13}**C**-N	2174.8(1936)	2112.7 (36)	1933.6(261)	-245.243525
C-C-C-C-C-^{15}**N**	2192.3(1761)	2124.2(251)	1933.5(240)	-245.243456

Table 8.1. : B3LYP/ aug-cc-vPTZ calculations of the C_5N^- and the isotopomers of the mass of 75 amu. The frequencies are expressed in cm^{-1} and the energy of the ground states in Hartree /particules.

CC stretches (ν_2) are principally resulting from the second and the third bonds starting from the C-extremity. In this pattern of vibration the fourth bonding is not involved. From the calculations, the absorption band is expected to be centered at 2119 cm^{-1} and also broad (>32 cm^{-1}) and asymmetric with two maxima.

CC-terminal (ν_3) stretches should be responsible for the smallest and brightest band, at least 38 cm^{-1}, centered on 1914 cm^{-1}. The fourth bond is not involved in this vibration and the strong influence of the last carbon should have created an asymmetry.

The experimental spectrum presents two dented bands at 2181 cm^{-1} (A) and at 2154 cm^{-1}(B). These two bands could be associated with the absorptions expected from the CN stretch. The experimental separation in two parts of the band reveals the stronger influence, as expected of some isotopomers. The pattern is then larger than predicted, close to 45 cm^{-1} and the values are 25 cm^{-1} lower than the calculations. The other band centered at 2096 cm^{-1} (C+D) is asymmetric and dented. The calculations of the isotopomers are in good agreement with the observed peaks. The 40 cm^{-1} large band is in accord with the peak expected for the CC stretch (ν_2) and also 25 cm^{-1} deeper than the computational values. The intensity of the peak (D) is stronger than expected and the presence of another specie, which increased the intensity of this absorption, could be suspected. The weak and large band at 1927 cm^{-1} (E) is in accord with the computational ν_3 frequencies, the absorption corresponded to the frequency theoretically calculated.

The C_5NH^-

From the Lewis rules, the hydrogen atom is optimally located on the C-extremity of C_5N^-. The DFT calculations on C_5NH^- predict the structure with the hydrogen atom located on the N-*terminus* energetically by 11.5 eV higher than with the hydrogen on the C-*terminus*. Contrary to the C_5N^-, the hydrogenated anion possesses a doublet ground state and is not linear. The chain presents a bend structure and the hydrogen forms a 144° angle with the chain. The bonds adopt a length slightly closer to the cumulene-form.

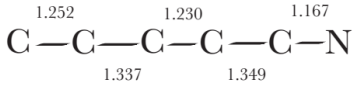

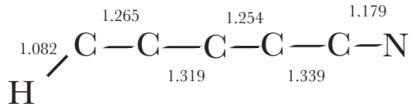

Figure 8.2: Structure predicted for C_5N^- and C_5NH^- from B3LYP/aug-cc-pVTZ calculations.

The C_5NH^- admits three similar configurations of vibration as C_5N^- (ν_1, ν_2, ν_3). The CC stretch (ν_3) is estimated at 1813.1 cm^{-1}, 124 cm^{-1} lower than for C_5N^-. The two other absorptions coming from the CC stretch (ν_2) and the CN stretch (ν_1) are estimated at 2026.0 cm^{-1} and at 2120.9 cm^{-1}. In comparison to the calculations on C_5N^-, they represent also two red shifts of 82 cm^{-1} and 108 cm^{-1} respectively. The intensities are estimated roughly two times weaker for the hydrogenated anion. Two new modes of vibration coming from the CH bond are revealed by the calculations: the CH stretch estimated at 3041.4 cm^{-1} and the CH bend at 669.8 cm^{-1} (outside the here investigated region).
The large dented peak observed at 2096 cm^{-1} (C+D) could contain the absorption of C_5NH^-. The peak at 2103 cm^{-1} (C) could match the expected strongest absorption band of C_5NH^-, estimated at 2121 cm^{-1}. The small predicted intensities of the other bands of the hydrogenated anions could explain their absence. The presence of C_5NH^- stays clearly hypothetical.

8.2. The mass 89

The mass corresponding to alanine is measured under two different sputtering conditions: in the presence of N_2 or in the presence of O_2. In the nitrogen experiment, the mass 89 is expected to be mostly composed of $C_5N_2H^-$ (see chapter 3). Through the sputtering with oxygen, beside C_4O^- the spectra reveal the abundant presence of $C_5N_2^-$ (see chapter 7). Not only are the hydrogenated and the heavy forms of C_4O^- expected to be present also those of the $C_5N_2^-$. The two systems $C_5N_2^-$ and C_4O^- were already examined in the preceding chapters, facilitating the interpretation of the IR spectra for mass 89.

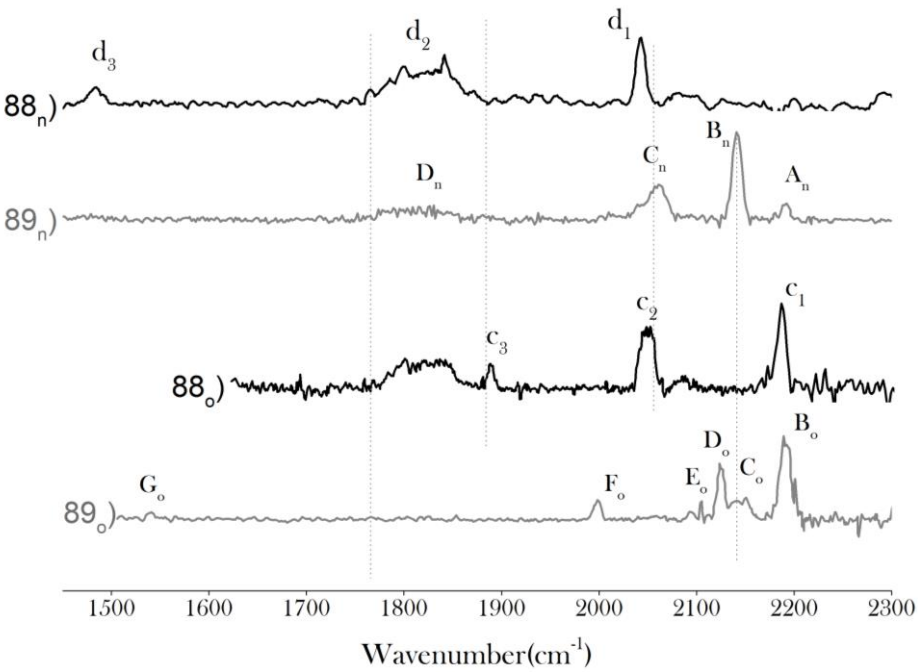

Figure 8.3: IRPD spectra of the mass of 88 amu (a) and (c) and the mass 89 uma (b) and (d). (88_n) and (89_n) are obtained by the sputtering of carbon target in the presence of N_2, whereas the (88_o) and (89_o) are obtained in the presence of O_2.

From the comparison of the spectra of the masses of 88 amu and of 89 amu, the new bands A_n B_n and C_o, D_o, F_o appear on the spectra of the mass of 89 amu. The presence of a heavy isotope in the structure modify only slightly the pattern of absorption leading to small red shift of the band. In the presence of nitrogen the band C_n and D_n revealed the presence of such isotopomers of $C_5N_2^-$. In the presence of oxygen, no evidence of presence of isotopomers is observed. In the spectra obtained in the presence of oxygen for systems of 88 amu, the $C_5N_2^-$ is not only present but also estimated the major anions. The ratio $C_5N_2^-/C_4O^-$ is estimated (with the computational values as reference) to 2.5 (chapter 3).

8.2.1. IRPD spectra of the mass 89 amu with N_2

The spectra reveal clearly the presence of the $C_5N_2^-$ isotopomers and of the $C_5N_2H^-$ as shown in figure 8.4.

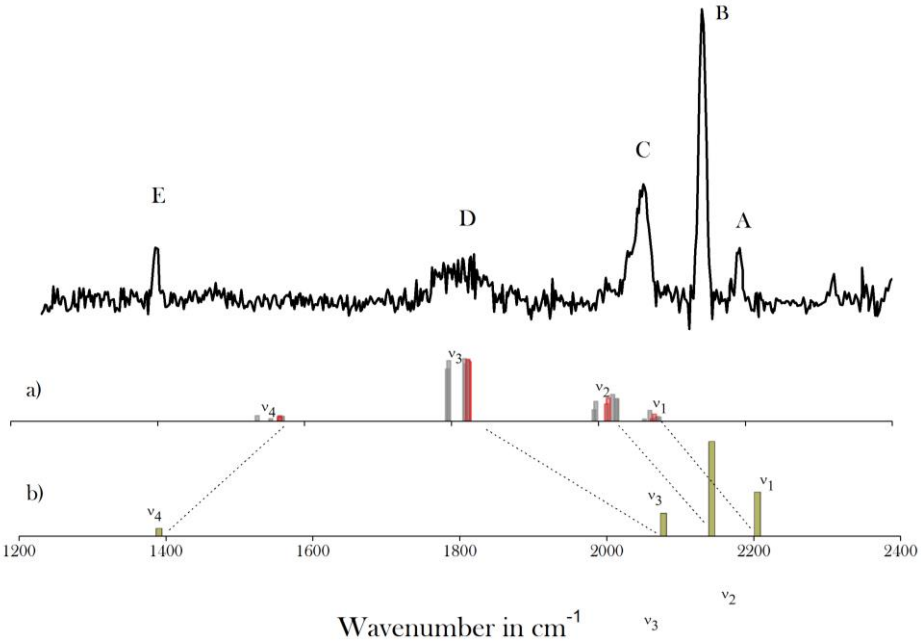

Figure 8.4: IRPD spectrum of the mass of 89 amu obtained by the sputtering of carbon target in the presence of N_2. The B3LYP/ aug-cc-pVTZ calculations reveal the position of the absorption bands of **a)** the isotopomers of $C_5N_2^-$ and **b)** the $C_5N_2H^-$. The absorptions expected for the ^{15}N-containing isotopomer were labeled in red.

The isopotomers of $C_5N_2^-$

The vibration pattern of $C_5N_2^-$ (88 amu) were already examined (chapter 4).The predicted influences of the isotopomers show a red shift of the frequencies up to 30 cm^{-1} for all absorption bands (table 8.2). For the mass 89 amu, the two bands centered respectively at 1820 cm^{-1} (D) and at 2055 cm^{-1} (C) are broad. They could be clearly associated with the absorptions caused by the heavy atoms, at the frequencies corresponding to (ν_3) and (ν_2). The band at 1820 cm^{-1} is expected from the calculations to be composed of two parts. The first part is expected to be only 3 cm^{-1} larger than for the isotope-free anion. The second part is expected to come from the influence of heavy isotopes, when they are located close to the bend of the structure. This second part should be situated 30 cm^{-1} deeper and 3 times weaker than the first part. The band (C) corresponding to (ν_3) is weaker, but with a width similar to the band for the mass 88, which is already 80 cm^{-1} broad. The second expected part, is not observed. The frequency (ν_2) concerns principally the CN stretch located on the long side of the anion. The influence of the isotopes is particularly strong for the two carbon atoms attached on the nitrogen atoms, exhibiting the participation of the two nitrile functions in this mode of vibration. The heavy nitrogen atom reduces the frequencies less than the terminal carbon atoms but more than the central carbon atoms. The pattern of absorption frequencies should form a 25 cm^{-1} band, asymmetric on the red side. The band (B) observed at 2055 cm^{-1} is 23 cm^{-1} broad and asymmetric. The absence of absorptions corresponding to ν_1 and ν_4 on the spectra may be

explained by the expected low intensities. Contrary to the C_5N^-, the calculations on $C_5N_2^-$ show an underestimation of the absorption frequencies coming from the isotopomers.

Anion configuration	ν_1 CN s Stretch	ν_2 CN l Stretch	ν_3 CC Stretch	ν_4 CC b Stretch
N-C-C*-C-C-C-N	2083.11(88)	2025.6 (459)	1824.3(1267)	1570.5 (98)
^{15}**N**-C-C*-C-C-C-N	2076.4(150)	2011.4(365)	1822.5(1295)	1566.8 (89)
N-^{13}**C**-C*-C-C-C-N	2070.3(231)	1994.1(241)	1818.2(1323)	1570.1 (98)
N-C-^{13}**C***-C-C-C-N	2080.2 (97)	2025.4(468)	1819.7(1210)	1536.0(118)
N-C-C*-^{13}**C**-C-C-N	2082.8 (87)	2019.5(568)	1794.6(1104)	1566.8(119)
N-C-C*-C-^{13}**C**-C-N	2078.0 (73)	2024.9(481)	1796.7(1281)	1554.3 (52)
N-C-C*-C-C-^{13}**C**-N	2062.8 (44)	1996.7(419)	1822.8(1315)	1569.9(103)
N-C-C*-C-C-C-^{15}**N**	2073.6 (48)	2013.8(489)	1824.2(1259)	1565.9(101)

Table 8.2: B3LYP / aug-cc-pVTZ basis set calculations of the $C_5N_2^-$ and the isotopomers of the mass of 89 amu. The frequencies are expressed in cm^{-1}. The location CN stretches is indicated by "s" and "l" (the small and the long branch respectively) and the CC stretch by a "b" (carbon on the bend of the molecule).

The hydrogenated form

The calculations reveal the energetically favored structure, which presents a ground state with a singlet multiplicity and with two nitrogen atoms at the end of the chain.

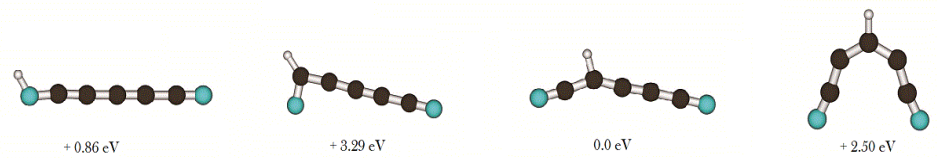

Figure 8.5: Structures of $C_5N_2H^-$ and the relative energy of their ground state from the B3LYP / aug-cc-pVTZ calculations.

The favored location of the hydrogen atom is on the second carbon of the chain, 0.86 eV lower in energy than the location on the nitrogen atom. A hydrogen atom placed on the other carbon atoms formed unprivileged systems with over 2.5 eV higher in energy than the global minimum. By comparison with the hydrogen free structure, the presence of the hydrogen atom reduces the angle of the bend and favors the polyyne character of the CC bonds. The bond lengths of the nitrile functional groups are also reduced.

The IR spectrum in figure 8.4 presents bands, which are clearly attributable to $C_5N_2H^-$. Three bands (A), (B) and (E) are sharp corresponding to the computational values and also absent in the spectrum of $C_5N_2^-$. The band (B) at 2153 cm^{-1} is more than five times stronger than the two other bands at 1397 cm^{-1} (E) and at 2190 cm^{-1}(A). Another band (C) seems to correspond to (ν_2) of $C_5N_2H^-$ but is overlapping the CN stretch of the isotopomers. The position of the

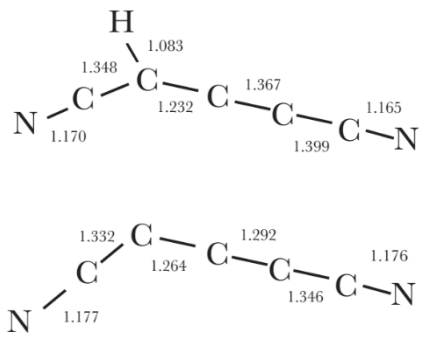

Figure 8.6: Structure predicted for $C_5N_2^-$ and $C_5N_2H^-$ through B3LYP/aug-cc-pVTZ calculations.

absorption coming form $C_5N_2H^-$ should be between 2040 cm^{-1} and 2074 cm^{-1}, which is in accord with the estimation at 2078 cm^{-1}. The hydrogenated structure presents also two CN stretching modes and a IR active CC stretching. Compared to the $C_5N_2^-$, the CN stretch on the short side (ν_1) is estimated eight times more intense and the CN on the long side (ν_2) four times more intense. For his part the CC stretching mode is estimated with an absorption more than four times weaker. A new mode appears at 1397 cm^{-1} corresponding to the calculated vibration at 1390 cm^{-1}. The vibration pattern is composed of the CH bending coupled with the stretching vibration of CC bonds. The measurements match clearly the calculations, except for the 16 cm^{-1} deviation of the band at 2191 cm^{-1} (A). The DFT calculations of $C_6NH_3^-$, which carry also the mass of 89 amu, reveal a strong absorption at 1869 cm^{-1}. The seven isotopomers, including one 13C or 15N and the $C_5N_2H^-$ are clearly identified. In regard of the experimental intensities and the predictions, the $C_5N_2H^-$ is the major product detected.

8.2.2. The IRPD spectra of the mass 89 amu in the presence of O_2

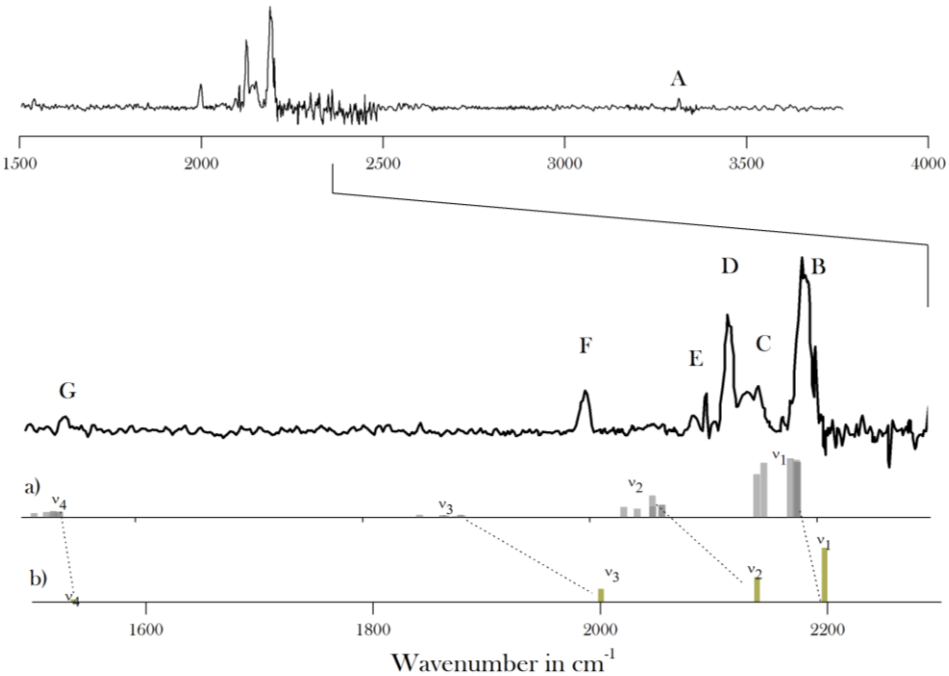

Figure 8.7: IRPD spectrum of the mass of 89 amu obtained by the sputtering of carbon target in the presence of O_2. The B3LYP/ aug-cc-pVTZ calculation of **a)** the isotopomers of C_6O^- and **b)** of the C_6OH^- .

The sprectrum presented in the figure 8.6 shows absorption bands corresponding to the expected absorption frequencies of the isotopomers of C_6O^- and of the hydrogenated anion. Contrary to measurements made with the mass of 88 amu, measurements made with the mass 89 reveal only a hypothetical and weak presence of nitrogen-containing systems of 89 amu.

The Isotopomers of C_6O^-

As expected, the heavy atoms reduce the absorption frequencies. The linear structure of C_6O^- was composed of a cumulene-like carbon chain with double bonds between C and O. The CO stretch is expected to absorb at 2183 cm^{-1}. Only the two closest locations of ^{13}C near the oxygen atom strongly affect the frequency. The absorption pattern expected from the calculations is composed of two parts, which are separated by 20 cm^{-1}. The two observed bands at 2191 cm^{-1} (B) and at 2151 cm^{-1} (C) match the computational values very well. The deviations from the calculations are below 10 cm^{-1}. The form of the absorption band at 2151 cm^{-1} is in good agreement with the predicted absorption frequency of the isotopomers. However, the absorption at 2051 cm^{-1} matches an absorption band of the C_5NH^-, which presents a strong absorption at 2053 cm^{-1}. The 25 cm^{-1} broad absorption peak at 2051 cm^{-1} on the spectrum with O_2 and the absence of other weaker absorption bands of the nitrile anions indicate the hypothetical and minor presence of C_5NH^-. The absorption at 2091 cm^{-1} is also located near the prediction made on HC_6O^-. The absorption coming from the isotopomers seems to be secondary (in comparison to HC_6O^-) but well and truly present.

Anion configuration	ν_1 CO	ν_2 CC	ν_3 CCt	ν_4 CC
C-C-C-C-C-C-O	2182.9(2335)	2064.7 (498)	1887.2(216)	1534.2(216)
^{3}**C** -C-C-C-C-C-O	2182.9(2330)	2063.3(487)	1870.4(73)	1528.2(230)
C-^{13}**C** -C-C-C-C-O	2182.9(2335)	2055.6(443)	1850.2(88)	1532.5(222)
C-C-^{13}**C** -C-C-C-O	2181.9(2445)	2030.0(419)	1873.2(56)	1521.9(206)
C-C-C-^{13}**C** C-C-O	2176.6 (2490)	2041.7(349)	1887.5(66)	1533.7(216)
C-C-C-C-^{13}**C** -C-O	2153.3(2304))	2063.8(525)	1886.3(90)	1511.0(164)
C-C-C-C-C-^{13}**C** -O	2147.0(1918)	2055.2(904)	1882.0(30)	1527.8(245)

Table 8.3: B3LYP with aug-cc-pVTZ basis set calculations of the C_6O^- and the isotopomers of the mass of 89 amu. The frequency values were expressed in cm^{-1}.

The HC_6O^-

The calculations reveal a linear structure for HC_6O^-, which is similar to C_6O^-. The hydrogen atom is located at the end of the C-*terminus*. With the hydrogen atom the chain become more similar to the polyyne-like structure made of alternating triple and single bonds. The vibration modes of the hydrogenated C_6O^- are similar to the hydrogen-free anion. The CC stretch in the

chain (ν_2) is estimated at 2138 cm^{-1} and the stretch involving the terminal carbon atom of the molecule (ν_3) at 2001 cm^{-1}. These values represent differences with C_6O^- of respectively 74 and 114 cm^{-1}. The absorption (ν_2) is also estimated as much stronger than one corresponding to C_6O^-. The CO stretch is estimated at 2197 cm^{-1}, which is 14 cm^{-1} greater than for C_6O^-. The very small elongation of the CO, of only 0.006 angstroms, resulting from the presence of the hydrogen atom is in accord with the small difference of absorption band attributed to the CO stretch (ν_1). The two sharp bands at 1998 cm^{-1} and 2125 cm^{-1} could be easily associated with the

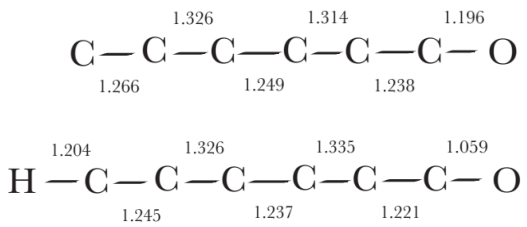

Figure 8.8: Structure predicted for C_6O^- and C_6OH^- through B3LYP/aug-cc-pVTZ calculations.

absorptions of HC_6O^-. The band observed at 2191 cm^{-1} (B) is attributed to the CO stretch and the large width likely comes from the superposition of the heavy C_6O^-. Corresponding to the computational value of 3369 cm^{-1}, the observed band at 3312 cm^{-1} (A) is associated to the CH stretch. The weak absorption of the CC stretch (ν_4) seems to be detected at 1539 cm^{-1} (G) with a deviation of only 2 cm^{-1} from the calculations. The experimental values are in very good agreement with the predictions and the identification of C_6OH^- was clear. Considering the high percentage of $C_5N_2^-$ identified in the IR spectrum of C_6O^-, for the hydrogenated anions, the formation of HC_6O^- was preferred over $C_5N_2H^-$.

8.3. The mass 115

The structures containing heavy isotopes and the hydrogenated form of $C_6N_3^-$ are suspected for the absorption detected. The absorption frequencies of $C_6N_3^-$ obtained by IRPD were already reported [118]. In the region of 2000 to 2350 cm-1, four absorption bands at 2244, 2228, 2178 and 2109 cm^{-1} were clearly attributed to $C_6N_3^-$. From the mass spectrometry the heavy anions should represent 86 % of the anions of 155 amu.

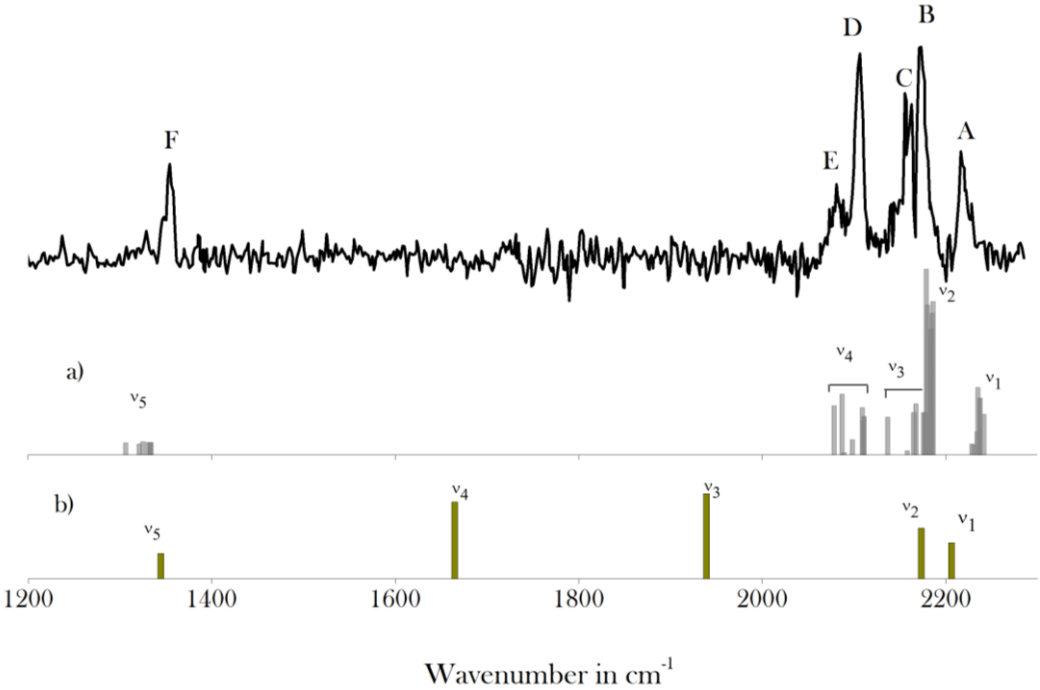

Figure 8.6: IRPD spectrum of the mass of 115 amu obtained by the sputtering of carbon target in presence of N_2. The B3LYP/ aug-cc-pVTZ calculations **a)** of the isotopomers and **b)** of the hydrogenated $C_6N_3H^-$

The isotopomers of $C_6N_3^-$

The structure of $C_6N_3^-$ has already been reported [118]. The three nitrogen atoms form three nitrile functional groups at the end of each branch of the anion. Two short branches find their junction on the fourth carbon of a long branch including four carbon atoms (figure 9.6 presents the geometries of hydrogenated anions affiliated with $C_6N_3^-$) The frequency of the stronger absorption (ν_2) resulted from the CC stretch located on the long branch. The strong influence of the three atoms of the branch provokes a red shift for absorption frequencies of absorption up to 20 cm^{-1}. The second absorption (ν_3) results from the two out of phase stretches of the nitriles groups located at the short branches. The absorption was estimated at 10 cm^{-1} deeper than ν_2. The isotopomers pattern corresponding to (ν_2) and (ν_3) stretches should build a broad and strong peak of absorption with a secondary maximum on the red region. The experimental double peak (B) and (C) at 2160 cm^{-1} and 2174 cm^{-1} match the predictions. Another absorption originates from CN stretches. The two nitrile functions located at the end of the short branches are also coupled in phase. The absorption is predicted at 2235 cm^{-1} and weaker than the two other nitrile stretches. The distribution of the influences of the heavy atoms is estimated as relatively small, presenting a spreading of approximately 8 cm^{-1}. The experimental band at 2223 cm^{-1} (A) matches the calculations. The third absorption resulting from the CN located at the end of the long branch experiences a strong influence of three heavy atoms. A 30 cm^{-1} large absorption pattern is expected from the calculations. The double peak at 2082 cm^{-1} (E) and 2104 cm^{-1} (D) match with respect to the calculated frequencies. The intensity at 2082 cm^{-1} is

stronger than expected. The fourth absorption band comes from the atom located at the junction of the branches. The influence of the heavy atoms is likely to enlarge this absorption band, so that it should reach at least 20 cm^{-1} width. The experimental band again agrees with the predicted frequency but the observed intensity is stronger than the predicted. The presence of the isotopomers is clearly detected.

Anion configuration	ν_1 CN	ν_2 CN	ν_3 CN	ν_4 CC	ν_5 CC j
N-C-C-C-C-(C-N)-C-N	2244(3399	2188(1320)	2179(361)	2113(291)	1336.3(102)
^{15}**N** -C-C-C-C-(C-N)-C-N	2237.1(231)	2178.6(1578)	2177.3(361)	2098.2(130)	1330.7(106)
N-^{13}**C** -C-C-C-(C-N)-C-N	2230.2(86)	2177(1819)	2165.2 (360)	2088.9(18)	1333.7 (105)
N-C-^{13}**C** -C-C-(C-N)-C-N	2228.3(93)	2179.9(1274)	2177.3(360)	2087.0(516)	1321.3(91)
N-C-C-^{13}**C** -C-(C-N)-C-N	2234.0(197)	2185.3(1204)	2177.4(360)	2078.3(417)	1325.2(112)
N-C-C-C-^{13}**C** -(C-N)-C-N	2241.4(334)	2186.1(1302)	2175.6(358)	2109.7(295)	1332.9(105)
N-C-C-C-C-(^{13}**C** N)-C-N	2234.8(573)	2183.6(999)	2136.6(321)	2108.8(402)	1332.9(105)
N-C-C-C-C-(C-^{15}**N**)-C-N	2237.1(481)	2183.9(169.3)	2167.5(433)	2110.6(326)	1333.3(104)

Table 8.4: B3LYP / aug-cc-pVTZ calculations of the $C_6N_3^-$ and the isotopomers of the mass of 89 amu.

The $C_6N_3H^-$

From the calculations, the structure, which presents the deepest ground state, carries the hydrogen atom attached to the third carbon atom from the extremity of the long branch. The structure with a hydrogen atom attached on the nitrogen atom of the long branch is energetically 0.67 eV higher. Likewise, all the other locations of the hydrogen were clearly underprivileged by at least 0.77 eV.

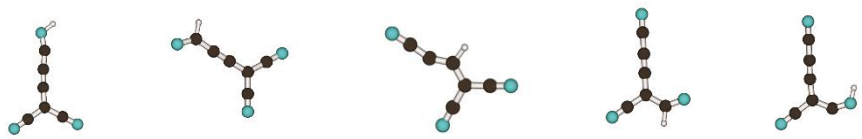

+ 0.67eV + 0.98 eV 0.0 eV + 0.77 eV + 1.02 eV

Figure 8.7: Structures of $C_6N_3H^-$ and the relative energies from the B3LYP / aug-cc-pVTZ calculations

In comparison with $C_6N_3^-$, the hydrogenated anion contains a bent long branch. Two angles, 130° and 156°, are located respectively at the third and the second carbon atom from the nitrile groups. The geometry allows three modes of vibration including the nitrile function at 2206 cm^{-1}, 2173 cm^{-1} and 1939 cm^{-1}. The (ν_1) and (ν_2) correspond to the two nitrile functions coupled, respectively in phase and out of phase, respectively. The intensity predicted by ν_2 is slightly stronger. The nitrile located at the end of the long branch should be responsible for an absorption at 1939 cm^{-1}, two times stronger than the other nitrile function. Two other intense vibration modes appear involving a third carbon atom where the hydrogen atom is attached and the precedent carbon (counting from the extremity of the branch (ν_4) at 1665 cm^{-1} and the fourth carbon atom (ν_5) at 1345 cm^{-1}. The absorption bands of $C_6N_3H^-$ are not detected on the spectra.

8.4. Conclusion

A series of systems of masses 75, 89 or 115 amu were examined by IRPD spectroscopy between 1400 and 2400 cm^{-1}. The absorption bands of $C_5N_2H^-$, C_6OH^-, and of the isotopomers of $C_5N_2^-$, C_5N^-, C_4O^- and $C_6N_3^-$ were clearly identified. Besides the identified systems, the calculations at the B3LYP aug-cc-pVTZ level, delivered structural information on other anions: C_5NH^- and $C_6NH_3^-$. The presence of a ^{13}C or a ^{15}N reduces the frequencies systematically up to 30 cm^{-1}. The distribution of the influence reveals the implication of the different locations of the heavy atoms on the vibration modes. Typically two atoms influence strongly the absorption and created an asymmetry on the red part of the absorption. Particularly on the C_6O^- and $C_5N_2^-$ linear chains, absorption patterns with two parts were observed. A narrower united pattern was detected for the C_5N^- and the branched $C_6N_3^-$, where the width of the pattern was estimated to be only 10 cm^{-1} broad for the vibration modes including a coupling of the two nitrile functions.

The presence of the hydrogen caused a modification of the bond lengths and eventually a flexure of the structure ($C_5N_2H^-$ and $C_6N_3H^-$). The absorption spectra were influenced with the modification of frequencies and intensities, the apparition of new stretching and bending modes. The addition of the hydrogen atom could influence the frequencies in different directions: red shifted for HC_6O^- and C_6N_3H-; blue shifted for C_5NH^- ; either red or blue shifted depending on the modes for $C_5N_2H^-$. The identification of the $C_5N_2H^-$ indicated its strong reactivity of formation, whereas the formation of C_5NH^- remains hypothetic. The formation of $C_6N_3H^-$ appears underprivileged. Contrary to the H-free structure, the presence of the dinitrile $C_5N_2H^-$ contaminating the HC_6O^- was unclear and remained minor. The reactivity of formation of C_6OH^- should be definitively stronger than of $C_5N_2H^-$ in the sputtering process in the presence of O_2.

The ensemble of information collected on the masses 75, 89, and 115 provides a solid foundation and will facilitate the future investigations of more complex molecules in gas the phase obtained by sputtering of a carbon target and are a first step towards the generation and interpretation of the IRPD spectra of these larger systems such as hopefully amino acids.

Chapter 9:

NCO^- and NC_3O^-

Recently, an abundant formation of CNO^- and C_3NO^- was observed through the fragmentation of DNA/RNA bases [181]. These fragmentations resulted from the collisions of nuclear bases with potassium ions, which carried an energy in the range of 13.5 eV to 23 eV. Thereby CNO^- was the major anion produced. In the chemistry, two isomers of CNO^- are fully employed in the chemistry and investigated: the cyanate $[O\text{-}C{\equiv}N]^-$ and the fulminate $[O\text{-}N{\equiv}C]^-$. The fulminate is unstable and is utilized as an explosive, the cyanate is a ligand used to form complexes including metal cyanato complexes and isocyanate. Ab initio calculations predicted in the gas phase a rearrangement of the fulminate form in the cyanate form [182]. The protonization of CNO^- could form different acids: the isocyanic acid (HNCO), the fulminic acid (HCNO), the cyanic acid (CNOH). These isocyanic acid and fulminic acid were identified in interstellar medium with a HNCO/HCNO ratio from 40 to 1000 depending of the dark clouds [183]. The cyanic acid, which is less favored than the isocyanic and the fulminic acid isomers, was also recently identified in the hot core Sgr B2 [184]. With two hydrogen atoms more, the formamide $HCONH_2$ was also identified in the same cloud [185]. Hydrogenated molecules, which include the same entail of carbon, nitrogen and oxygen atoms as C_3NO^-, were subject of theoretical investigations concerning the exogene origin of the life [31]. Indeed C_3NOH_7 presents many isomers and the amino aldehyde form was considered as precursor of alanine. Only an oxidation of the hydroxide functional group of this amino aldehyde forms a carboxyde group and the amino acid alanine is obtained as shown in the equation 9.1. However the precursor of alanine has been predicted energetically 1 eV higher in the gas phase than another isomer, the propamide. The IR absorption spectra of CNO^- in gas phase have been reported by diode laser absorption spectroscopy studies [186], which revealed an absorption band measured at 2124 cm^{-1} attributed to the asymmetric stretch mode. The IR absorption of the neutral C_3NO was reported in 2008 [187] presenting a CO stretch at 2096 cm^{-1} and a CN stretch at 2041 cm^{-1}. Previous IRPD measurements attributed an absorption band at 2127 cm^{-1} to C_3NO^-, which was present in the IR absorption spectra of carbon nitride anions [118].

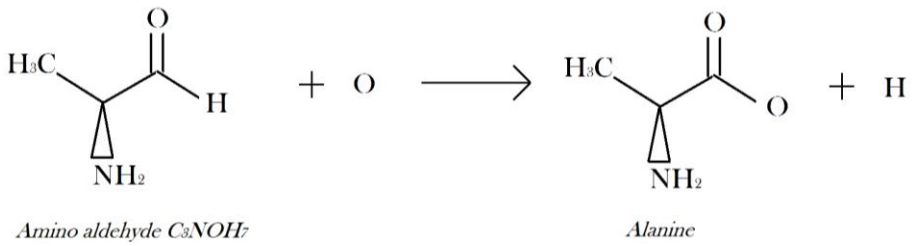

(9.1)

The two anions C_3NO^- and the CNO^- are structurally related to organic molecules. They are the fragments of organic bases or present the same composition in carbon, nitrogen and oxygen atoms as the precursors of amino acids. The C_3NO^- and CNO^- here investigated are

produced by the sputtering process in the presence of O_2, without the introduction of nitrogen. Their investigation is likely valuable in the effort to understand the chemistry of formation of organic molecules in gas phase. The IRPD investigations of C_3NO^- and CNO^- are presented in the next pages. In addition the theoretical predictions of the hydrogenated form of the two anions are presented below.

9.1 IRPD spectra of CNO^- and C_3NO^-

CNO^- and C_3NO^- are largely produced through the sputtering in the presence of O_2. Despite the minimal presence of nitrogen, available only through contamination of the target, the formation of these anions containing a nitrogen atom is significant. On the mass-spectra, the mass of 42 amu (corresponding to CNO^-) is the fifth mass in order of abundance and the mass of 66 amu (corresponding to C_3NO^-) is among the twenty most-produced masses (as shown in chapter 3). By the sputtering process in the presence of N_2, CNO^- and C_3NO^- were also produced although no O_2 was introduced. Indeed, not coinciding with any carbon nitride, the mass 42 amu of CNO^-, is produced in very great quantity in the nitrogen experiment. In similar conditions, one of the stronger absorption band observed in the IR spectra of the mass 66 was attributed to C_3NO^- [118]. The formation of these two anions is remarkably propitious in the gas phase, despite no oxygen or no nitrogen are properly introduced in the sputtering process indicating a strong reaction and a high stability of these anions. IR identification of CNO^- and C_3NO^- presented below originate from the sputtering in the presence of oxygen.

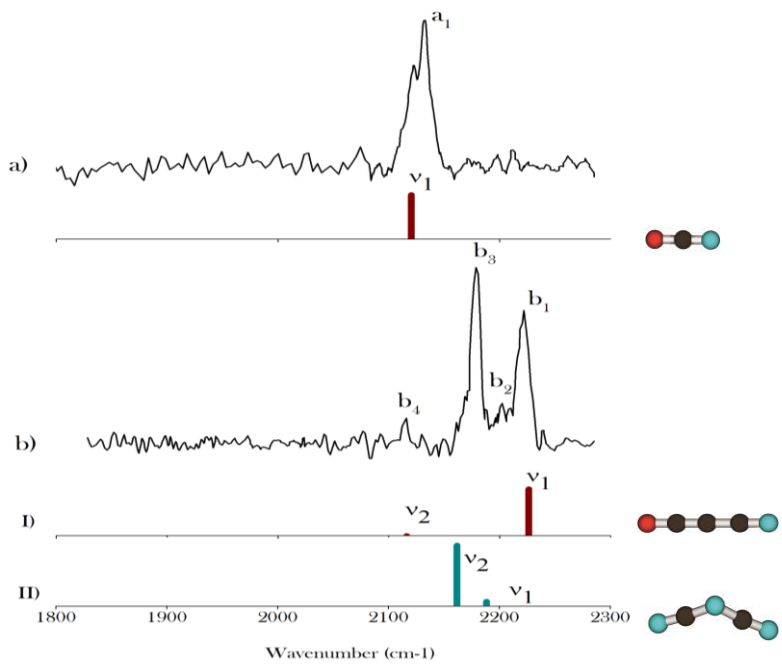

Figure 9.1: IRPD spectra of a) CNO^- and b) C_3NO^- . The B3LYP/ aug-cc-pVTZ predicted frequencies(with a scaling factor of 0.968) of a) CNO^- and b) C_3NO^- are presented as red bars. The green bars present the calculated frequencies for $C_2N_3^-$.

In the IR spectra, the CNO^- and C_3NO^- could be clearly identified. The agreement between the predicted and the experimental values lies within 10 cm^{-1} (figure 9.1 and table 9.1). A band at 2127 cm^{-1} is attributed to the asymmetric stretching mode of CNO^-, whereas the band at 2221 cm^{-1} and 2114 cm^{-1} are attributed to the CO stretch and CN stretch of C_3NO^-. On the spectra, which concern the mass of 66 amu (b), in addition to the peaks attributable to C_3NO^-, another strong peak (b_3) is observed. $C_2N_3^-$ having the same mass constitutes a plausible origin of the additional absorption. Since no gaseous N_2 was introduced in the sputter source, the presence of a high signal of anions containing three nitrogen atoms is highly hypothetic. The origin of the peak is discussed in more detail in the next paragraphs.

	Stretching mode	IRPD Experiment Freq	B3LYP Frequency(cm^{-1})
OCN^-	ν_1 O=C≡N asym	2127(49)	2120 (846)
	ν_2 O=C≡N sym	--	1210 (67)
CNO	N-O	--	2037 (265)
	C≡N	--	1048 (177)
C_3NO^-	ν_1 -C=O	2221(76)	2227 (2526)
	--	2200(25)	--
	--	2178(100)	--
	ν_2 C≡N	2114 (14)	2116 (6)
$C_2N_3^-$	--	2221(76)	--
	ν_1 -C≡N 1/2	2200(25)	2192 (63)
	ν_2 -C=N	2178(100)	2165 (110)
	--	2114 (14) / 7	--

Table 9.1: IRPD experimental absorption band frequencies. The relative IR intensities are given in parenthesis in percents. B3LYP /aug-cc-pVTZ geometries and frequencies with the predicted intensities given in parenthesis in km/mole.

9.2 Cyanate CNO^- and linear C_3NO^-

The B3LYP/aug-cc-pVTZ calculations reveal the cyanate structure $[N=C=O]^-$ as energetically lowest and privileged geometry. The bond lengths of 1.22 and 1.187 angstrom correspond respectively to a double CO bond and a partial triple CN bond. The absorption at 2127 cm^{-1} (a_1) match those already reported in the gas phase and in xenon matrix at 2124 cm^{-1} [186]. A second IR active stretch mode, which is symmetric, is expected at 1210 cm^{-1}, outside the investigated range in this work. The fulminate $[CNO]^-$ anion is also examined by B3LYP/aug-cc-pVTZ calculations. The structure is estimated with the NO bond length of 1.266 angstrom and the CN bond length of 1.187 angstrom. The vibration modes differs from the cyanate and two pairs of atoms form two separated stretching modes. The NO stretch is predicted to be IR active at 2037 cm^{-1} and the CN stretch at 1048 cm^{-1}. The predicted absorption band at 2037

cm^{-1} for fulminate is not observed, which is in accord with the clearly disfavored energy difference (predicted of 2.9 eV) between the two isomers.

The C_3NO^-

The energetically lowest C_3NO^- structure forms a linear chain presenting the oxygen and the nitrogen atoms at either terminal location of the chain. The structure presenting a nitrogen atom in the middle of the chain is estimated at least 1.87 eV higher in energy. The oxygen in the middle of the chain renders the structures clearly underprivileged, at least 4.06 eV higher (figure 9.2). The energetically favored structure of the C_3NO^- contains two double bonds, the CO and the CC adjacent, a single CC bond, and a partial triple CN bond with a length of 1,1734 angstrom. The CO function is responsible for the absorption at 2221 cm^{-1}, which matches the calculations very well, with a deviation of only 6 cm^{-1}. The small peak at 2114 cm^{-1} (b_4) is attributable to the CN vibration expected at 2116 cm^{-1}. The neutral molecule C_3NO absorbs at 2096 cm^{-1}, 2041 cm^{-1} and 1479 cm^{-1}. The charge influences principally the two absorptions assigned to CN and CO leading to a blue shift. The influence of the charge on the absorption frequency of the CC stretch should represent only a small red shift (with the reference to the predicted CC stretch of C_3NO^-).

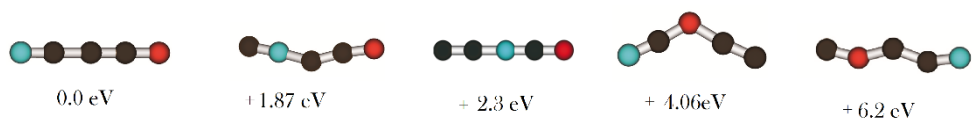

Figure 9.2: Predicted structure of the C_3NO^- isomer with the predicted relative energies from B3LYP/aug-cc-pVTZ calculations

9.3 Discussion for the absorption band at 2178 cm^{-1}

The strongest peak of the spectra at 2178 cm^{-1} originates clearly from a molecule other than the C_3NO^-. The B3LYP /aug-cc-pVTZ calculations of $C_2N_3^-$ (also 66 amu) predict a strong absorption at 2165 cm^{-1}. This represents a deviation of 13 cm^{-1} from the experimental results. This band originates from the out of phase vibration of the two nitrile functional groups. Another less intensive absorption should be observable at 2192 cm^{-1} from the in phase coupling of the nitrile groups in phase. The small intermediate peak observed at 2200 cm^{-1} (b_2) between the two strongest peaks is in agreement with this mode of vibration. The third nitrogen atom in the middle of the chain is predicted at the origin of absorption at 1375 cm^{-1}, which is outside the range of experimental measurement, employed here. From DFT calculations the presence of $C_2N_3^-$ remains highly probable. But the previous measurements [118] argue against this explanation, where through the sputtering process with N_2, the absorption spectra of the mass 66 revealed two strong bands at 2220 cm^{-1} and 2127 cm^{-1}. The first was attributed to the C_3NO^- and is completely in accord with the present experimental results. For the second band

at 2127 cm^{-1}, $C_2N_3^-$ was suspected. The B3LYP /aug-cc-pVTZ calculations had a deviation of 37 cm^{-1} from the experimental results. The attribution to the $C_2N_3^-$ was concluded through other calculations at the CCSD/6-6311+G (d,p) level, which presented a deviation of only 8 cm^{-1} from the experimental results.

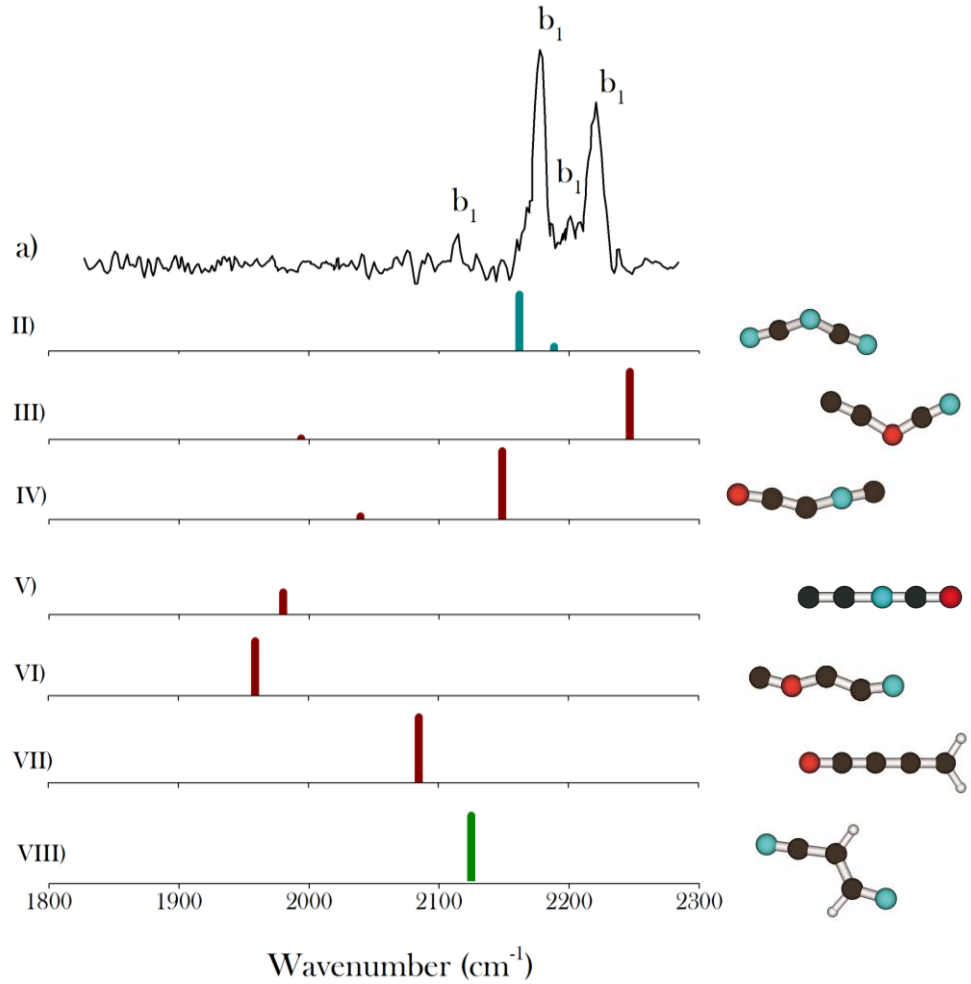

Figure 9.3: IRPD spectra of a) C_3NO^- and B3LYP/ aug-cc-pVTZ calculations values of II) $C_2N_3^-$. III) $CCOCN^-$, IV) OCCNC-, V) OCNCC-, VI) COCCN-, VII) $C_4OH_2^-$, VIII) $C_3N_2H_2^-$.

The main reason, which acts against assigning this peak to $C_2N_3^-$, is the observation of the peak at two different positions: at 2178 cm^{-1} and at 2127 cm^{-1} when sputtered with N_2 and O_2. Thus only one band can be attributed to $C_2N_3^-$, which question the assignment done previously. In the present work, the experimental conditions are disadvantageous for anions, which contain three nitrogen atoms. If the peak observed at 2127 cm^{-1} originates from $C_2N_3^-$, other species with 66 amu, should explain the absorption at 2178 cm^{-1}. The absorptions predicted for the C_3NO^- isomers are examined. The B3LYP/aug-cc-pVTZ calculations predict the following strong absorption bands in the region in question: 1959 cm^{-1} ($NCCOC^-$), 2246 cm^{-1} ($NCOCC^-$), 2149cm^{-1}($CNCCO^-$), 1982 cm^{-1} ($CCNCO^-$) as shown in figure 9.3. The failure to detect

these isomers was in accord with the predicted relative energies of the different isomers. Considering the possibility of hydrogen presence, two anions which include two hydrogen atoms also carry the mass of 66 amu. For example, $C_4OH_2^-$ is a candidate. The B3LYP/aug-cc-pVTZ calculations on $C_4OH_2^-$ also reveal an absorption pattern not concordant with the experimental band in question. The $C_3N_2H_2^-$ presents also the same mass of 66 amu. The computational calculations predicted a strong absorption at 2124 cm^{-1}. This expected band does not correspond to the absorption observed in this work but could correspond to the absorption observed at 2127 cm^{-1} in the previous measurement [118]. If the band at 2127 cm^{-1} originated from $C_3N_2H_2^-$, $C_2N_3^-$ could eventually explain the band at 2178 cm^{-1}. This constitutes an unlikely explanation, yet it remains the most plausible to date.

9.4 Predicted hydrogenised forms of C_3NO^- and CNO^-

Based on the observed mass spectra, the masses detected at 43 and 67 amu are attributed respectively mainly to $CNOH^-$ (with a minimum presence of the anions containing heavy isomers) and partly to C_3NOH^- (with the potential presence of the other anions as $C_2N_3H^-$). The reactivity of formation of the anions containing a hydrogen atom reveals itself strong. The $C_xNOH_y^-$ present the same composition in carbon, nitrogen, and oxygen atoms as several organic molecules. To foresee the molecules resulting from these anions, theoretical calculations have been carried out. The structures of the $CNOH_y^-$ (y = 1-4) and $C_3NOH_y^-$ (y = 1-7) are examined through B3LYP/aug-cc-pVTZ calculations. The ground states of each location of hydrogen are energetically compared to find the privileged structure. This predicted structure forms the base for the next calculations of anions containing a supplementary hydrogen atom.

The reactivity of hydrogen on the C_xNO^- is not yet well investigated, whereas the reactivity of hydrogen gathers extended reports [159, 171]. The simplest cases of hydrogenation could be associations of hydrogen atoms on the anions (9.1). A radiative association followed (9.2) by a radiative electron attachment (9.4) could also occur. Hydroxide association (9.3) followed by radiative electron attachment (9.4) is not to be excluded.

$$C_xNOH_y^- + H \rightarrow C_xNOH_{y+1}^- \quad (9.1)$$

$$C_xNOH_y^- + H \rightarrow C_xNOH_{y+1} + e^- \quad (9.2)$$

$$C_xNOH_y^- + H+ \rightarrow C_xNOH_{y+1} + e^- \quad (9.3)$$

$$C_xNOH_{y+1} + e^- \rightarrow C_xNOH_{y+1}^- + h\nu \quad (9.4)$$

Hydrogenated CNO^-

In the very limited presence of hydrogen atoms, the $HCNO^-$ observed in the mass spectra represent 4.3 % of CNO^- (isotopomers substracted). Through a sputtering experiment with an additional presence of H_2, anions containing more than one hydrogen atom are clearly expected. B3LYP/aug-cc-pVTZ calculations are carried out on $CNOH_y^-$ (y = 1-4) in order to reveal the privileged locations of the hydrogen atoms (figure 9.4). The first hydrogen is preferentially attached on the nitrogen atom. The second hydrogen is predicted preferably attached to the carbon atom The third hydrogen atom attaches also the nitrogen atom. The carbon atom is the privileged location for the fourth hydrogen. Through the sputtering in the presence of H_2, the $[H_2CNH_2O]^-$, which presents an amide function, (figure 9.4) is predictable. Its neutral form is known as formamide and represents the smallest molecule with a peptide bond. The formamide belongs to the list of interstellar molecules [185].

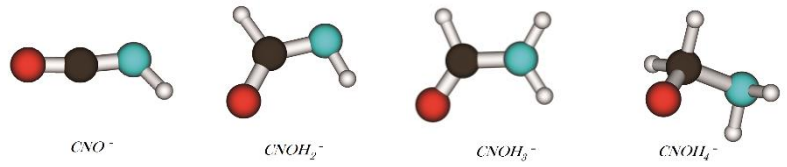

Figure 9.5: Predicted geometries of the $CNOH_y^-$ (y = 1 - 4) from B3LYP/aug-cc-pVTZ calculations.

Hydrogented C_3NO^-

With the same computational method, the $C_3NOH_y^-$ (y =1-7) anions are examined. The locations of the hydrogen atoms differ from that in the CNO as shown in the figure 9.6. The three first hydrogen atoms are predicted to be attached to the carbon chain. The location is predicted first on the carbon atom in center and successively on the carbon atoms located on the oxygen side and then on the nitrogen side. The fourth and the fifth hydrogen atoms are estimated to be preferably attached to the nitrogen atom. The two following hydrogen atoms should be attached on the two carbon atoms to the nitrogen side (again at first on the central carbon).

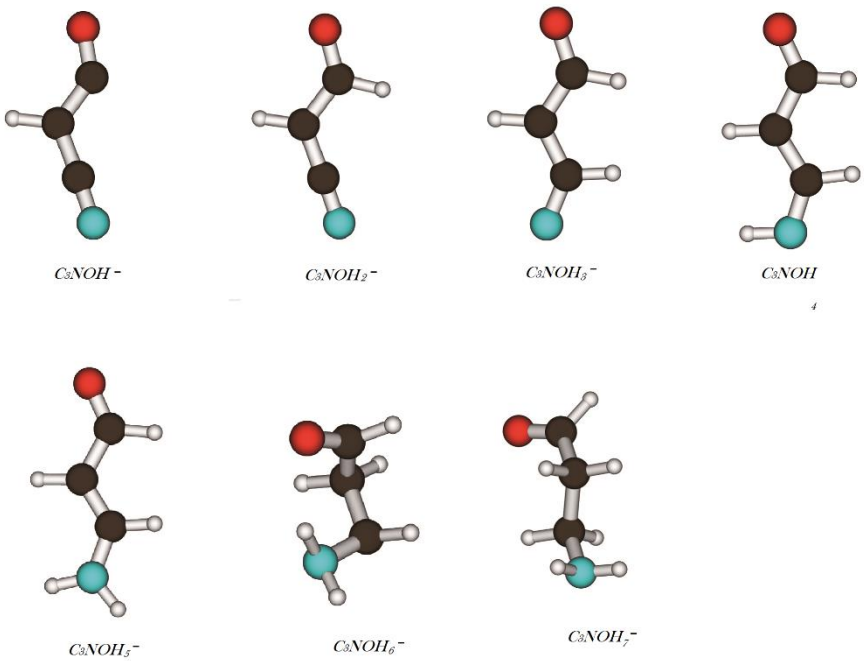

Figure 9.6: Predicted geometries of the $C_3NOH_y^-$ (y = 1 - 7) anions from B3LYP/aug-cc-pVTZ calculations.

The linear C_3NO^- through hydrogenations is predicted to form a carboxyl-amine structure $[NH_2CHCH_2CHO]^-$. These anions share a structure different from the precursor of alanine (the amino-aldehyde $[NH_2(CH_3)CHCHO]^-$) as presented in the figure 9.7. The amino aldehyde presents a branched-structure with the nitrogen atom attached to the central carbon atom.

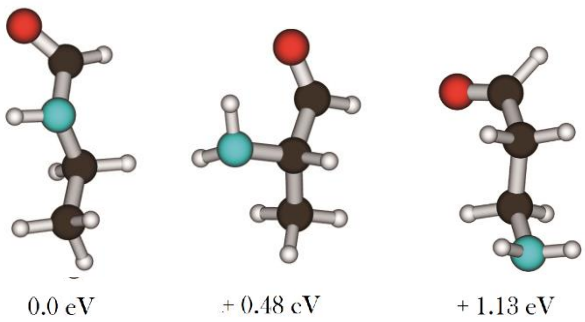

Figure 9.7: Predicted geometries of (form left to right) the propamide $C_3NOH_7^-$, the aminoaldehyde $C_3NOH_7^-$, the $C_3NOH_7^-$ with an amine and a carboxyl functional group (originating from the hydrogenation calculations) and their respective relative energies from B3LYP/aug-cc-pVTZ calculations.

The B3LYP/aug-cc-pVTZ calculations on the isomer of $C_3NOH_7^-$, reveal the negatively charged amino aldehyde structure as favored (predicted 0.65 eV deeper) in comparison with

the structure originating from the hydrogenation the linear C_3NO^-. The precursor of alanine is also not representing the global minimum. The structure presenting an amide function is estimated to be energetically favored (0.48 eV deeper in comparison with the amino aldehyde form).

9.5 Conclusion

CNO^- and C_3NO^- present a remarkable reactivity of formation by the sputtering process. Despite the absence of oxygen or nitrogen, respectively introduced in the source, they constitute two major species produced. The IR absorption spectra of the CNO^- and C_3NO^- obtain through the IRPD method reported here are in accord with precedent gas phase investigation [186] and with previous IRPD measurement [118]. Both anions present a linear chain with a carboxyl and a nitrile functional group at the extremities. Parallel to C_3NO^-, another specie is responsible for an additional strong absorption band in the spectra. Calculations are carried out on different anions carrying the mass of 66 amu. The structural isomers of C_3NO^- and anions with two hydrogen isomers ($C_3N_2H^-$ and $C_4OH_2^-$) are examined. Through this investigation, another origin is proposed for the band already reported and previously attributed to $C_2N_3^-$ [118]. The most plausible source for the band in question in this work remains $C_2N_3^-$. This explanation matches the computational results but reveals itself not completely satisfactory taking the experimental conditions into account. The expected hydrogenated anions deriving from the CNO^- and C_3NO^- have been theoretically examined as well. The negatively charged formamide is predicted as a product of hydrogenations of CNO^-. The formamide is the shortest molecule containing a peptide bond. The hydrogenations of C_3NO^- are predicted to form anions with carboxyl and amine functional groups at the extremities. However the negatively charged propamide isomer is predicted to be the energetically lowest structure. Thereby, in the sputtering in the added presence of H_2, it will be interesting to pay particularly attention to the mass of 73 amu. The presence of one or the other isomer of $C_3NOH_7^-$ could inform us about their formations. Under these isomers, an amino aldehyde is considered as precursor of alanine. However this isomer is disfavored by the predictions.

ANNEX

Amino acids embedded in Helium droplets

Complementary to the main experiment presented in this work, which approaches the formation of organic molecules in gas phase, another experience, which investigate directly organic molecules in helium droplets was carried out. Helium nanodroplets have the advantage of generating an isolation matrix in which the molecules conserve quasi-completely the vibrational and rotational freedom of the gas phase [188]. At temperatures below 2.17 Kelvin, liquid helium (^{4}He) adopts the superfluidity state, which corresponds to a fluid with zero viscosity. Through evaporative cooling via expansion in vacuum, helium nanodroplets reach a temperature of 0.38 K, which corresponds to their superfluidity state [189]. Nanodroplet beams allow for embedding and isolating all molecules coming into contact with the helium. In the droplets clusters of embedded molecules are suspended [190]. In this annex the attempt to embed several different amino acids in helium droplets is reported. Monomers as well as oligomers of amino acids are observed. The simultaneous pickup of different amino acids also allows the observation of heterodimers. The amino acids involved in this experience include glycine (gly), valine (val), histidine (his) and tryptophan (trp). Glycine is the smallest amino acid, in which the lateral chain is composed only of one hydrogen atom. Tryptophan is the heaviest proteogenic amino acid, composed of an indole cycle in the lateral chain. Histidine includes an imidazole cycle and valine a methylbutan on the lateral chain. Several previous studies already reported glycine [191, 192], valine [193], histidine and tryptophan [194] embedded in helium droplets. In this article, the ability of amino acids to form heteropolymers with other amino acids, fragments of amino acids and water is examined and enhance the information about the complex formation in helium droplets. The experiment was performed with a supersonic beam of ^{4}He achieved through a 5 μm nozzle cooled to 12 K at a pressure of 25 bars. This supersonic beam passes through a pick up cell that is designed with apertures of 2 and 3 millimeter diameter (respectively upstream and downstream). The pickup cell contains few milligrams of the amino acids, which are vaporized by a heating element allowing temperatures up to 200°C. The 10mm path through the cell remains long enough to permit the pickup of the amino acids of interest. The nanodroplet constituents are detected in their positively charged form by a Balzers QMG-420 quadrupole mass analyzer after the electron impact ionization performed by the source set at a voltage of 50 V (figure A1).

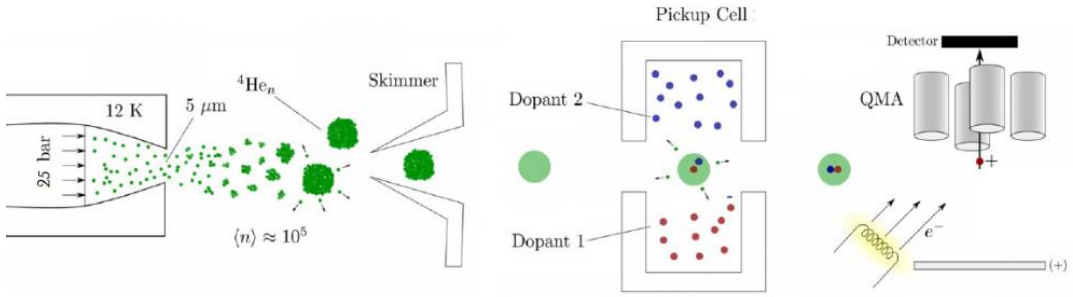

Figure A1: Illustration of the helium droplet experimental setup. Amino acids represent the dopant investigated here. Picture adapted from [8].

L-Glycine

Embedded glycine is detected in its protonized form [gly, H] at 76 m/z. In the presence of water vapor, glycine is also observed in complexes with water molecules. Figure A2 shows glycine complexes composed of up to 14 water molecules (where glycine remains in its protonized form). Complexes comprised of four water molecules and eight water molecules are clearly favored. The signals at 148 m/z [Gly, H, 4 H_2O] and at 220 m/z [Gly, H, 8 H_2O] are detected in greater quantity than their homologues with either one more or one less water molecule. At high water pressure, complexes formed with only one water molecule and a hydrogen nucleus exhibit a series of clusters. These water clusters clearly favored five- and ten-water-molecule groupings. In figure 2 the detections at 91 m/z [5 H_2O, H] and at181 m/z [10 H_2O, H] are more abundant than the other clusters in the series, which correspond to complexes with either one more or one less water molecule. In the gas phase the structure of $H^+/(H_2O)_n$ revealed a first shell of water molecules by n = 4 and subsequent shells which form clathrate cages with n = 21 and n = 28 [195,121]. The configuration of water clusters in helium droplets appears to remain different in comparison to the configuration in the gas phase.

.

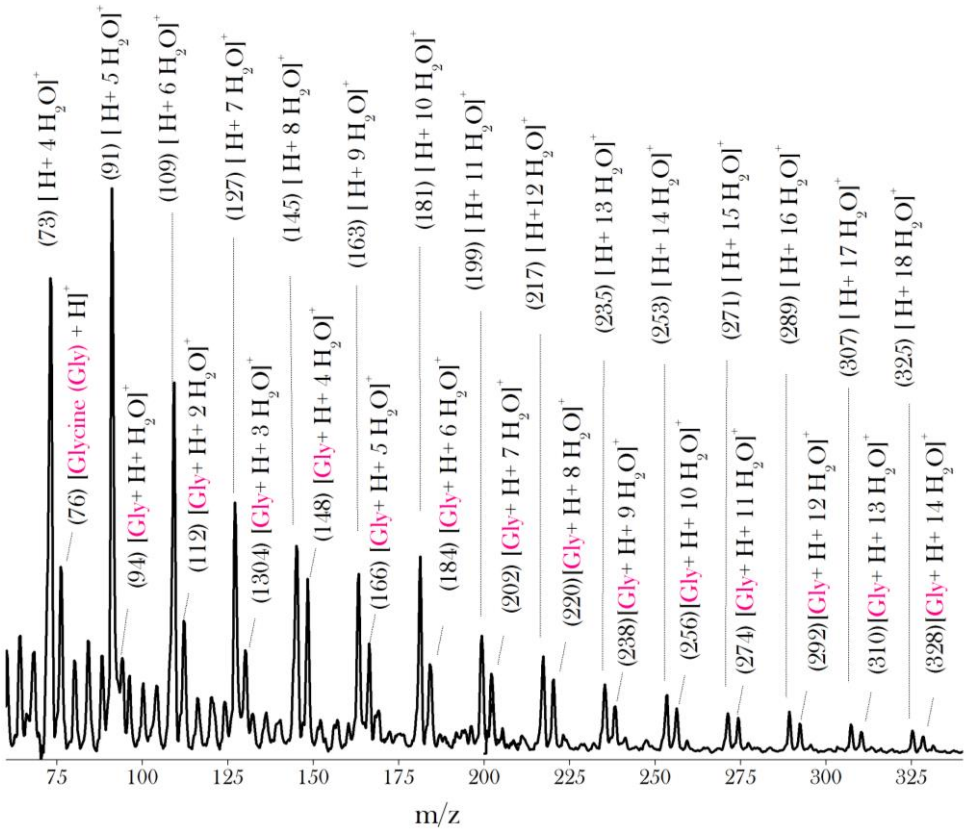

Figure A2: Mass spectrum of embedded molecules, which results from a helium droplet beam passing through the pickup cell containing glycine.

By itself, a unit composition of five water molecules is favorably detected. However, when added to protonized glycine, a unit composition of four water molecules is observed in great quantity. Amino acids experienced fragmentation through the electron impact ionization, particularly in their immonium ions. These ions correspond to the amino acids truncated from the carboxyl functional group [-COOH] (which represents fewer than 45 amu). The immonium ion of glycine is observed at 30 m/z, a low concentration in comparison to glycine (figure A3).

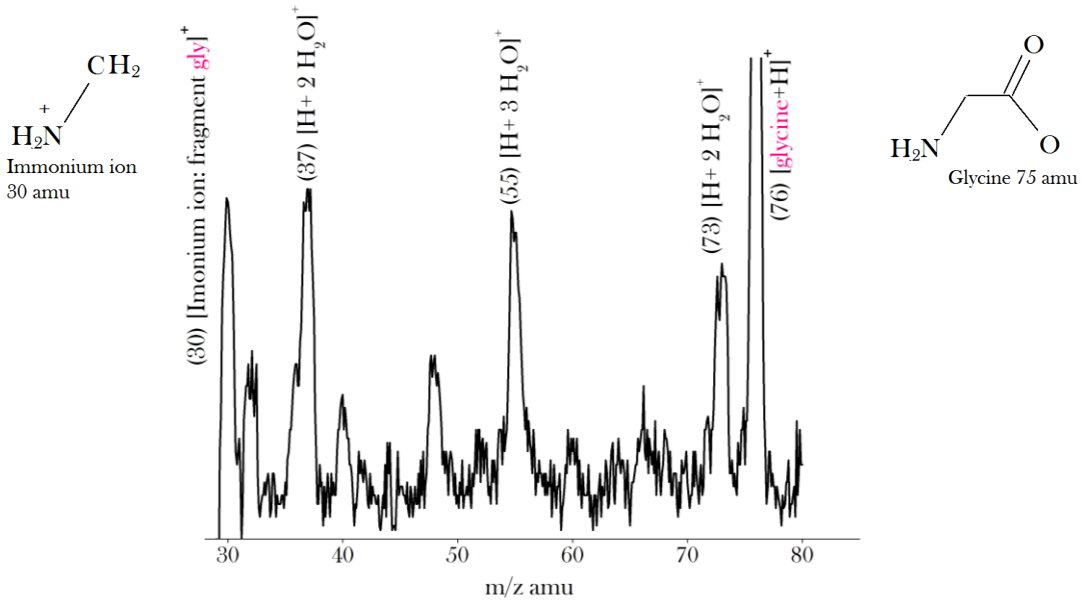

Figure A3: Mass spectrum of embedded molecules, which results from a helium droplet beam passing through the pickup cell containing glycine in the presence of fewer water compared to the spectrum presented in figure 2. A fragment of glycine is also detected

Electron impact ionization on helium droplets causes fragmentation of the embedded molecules through different processes than in the gas phase [196, 197]. Ionization of a helium droplet forms a migrating He^+ cation, which releases substantial energy and provokes fragmentation in the molecules. This fragmentation could be dramatically reduced by the presence of water in helium droplets. Different processes, which explain the protection caused by the water molecules, are suspected. A buffering effect, which originates from a solvation surrounding the fragile molecule, is presumed. Such an effect was reported by nucleotides solvated in water clusters [197]. In experiments, where the water is first embedded in droplets and forms clusters followed by the secondary pickup of the molecules, the reduction of fragmentation by the presence of water was still observed [197]. A study, which compares the fragmentation of glycine, polyglycine, alkanes and alkanethiols, proposes a concurrent process [191]. This study shows protection from molecular fragmentation by water molecules, which is particularly present when the embedded molecules exhibit a low electric dipole moment. The solvation remains favored by molecules that possess a large dipole moment. The suggestion is made that migrating He^+ cations are steered by water complexes located near fragile molecules. This protection originating from the water molecules remains limited when the fragile molecules possess a high dipole moment.

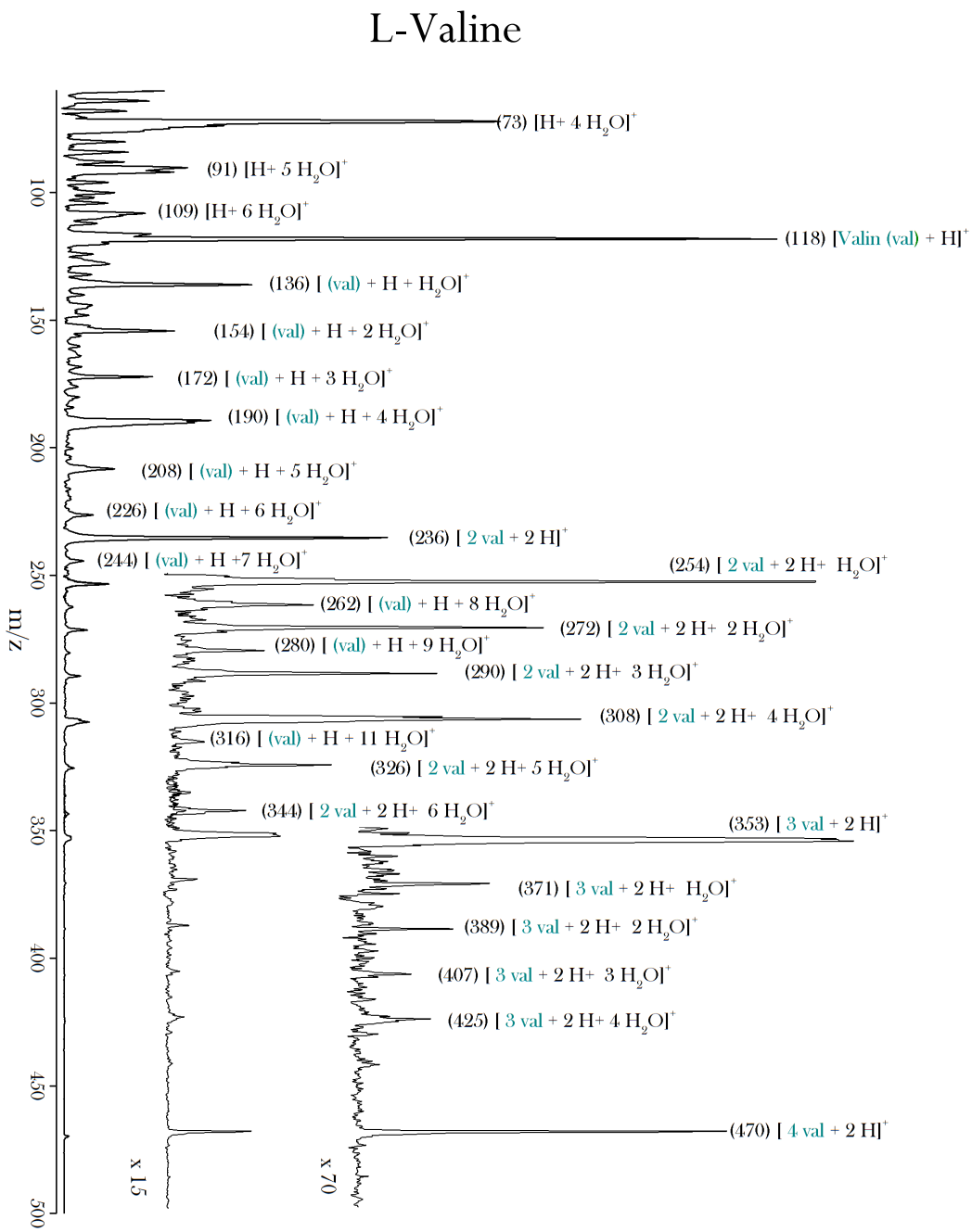

Figure A4: Mass spectrum of embedded molecules, which results from a helium droplet beam passing through the pickup cell containing valine. The mass spectrum is obtained through the difference of mass spectra in the presence and in the absence of helium droplets. The insets show the spectra with an enlargement of 15 times and of 70 times.

Several embedded polymers of valine are observable in helium droplets (figure A4). Valine monomers are detected in the protonized form at 118 *m/z*. Monomers are observed in complexes, which contain up to 12 water molecules. The fragment of valine, which corresponds to its immonium ion, is also detected in the protonized form at 73 *m/z*. Complexes composed of 4, 9 and 11 water molecules appear particularly favored. The dimers are observed with added hydrogen atoms [2 Val, 2 H]. The complexes with four water molecules are particularly privileged and up to six water molecules are abundantly detected in complexes including valine dimers. These clusters are favored when they contain four water molecules. The valine tetramer is also observed with only two added hydrogen nuclei. Tetramers appear with a ratio to trimers of 74%, whereas trimers represent 3 % of dimers. A recent study investigated valine embedded in helium droplets in the presence of heavy water D_2O [193]. Thereby the provenance of the added hydrogen from the water molecules was demonstrated. The protonization of amino acids usually occurs on the amine functional group of the amino acids (N-*terminus*). This suggests that amine functional groups are involved in the formation of the complexes made of three and four valine.

L-Valine and L-Tryptophan

In order to embed simultaneously two different amino acids, valine and tryptophan are introduced in the pickup cell. The vaporization temperature of valine is lower than that of tryptophan. In a small temperature window, the simultaneous detection of both amino acids remains possible (figure 5). At these temperatures, valine monomers at 118 *m/z* are also detected in complexes with water molecules. In these conditions, including a lower water vapor pressure, the favored complexes with four water molecules (observable in figure A4) are not any more remarkable. Tryptophan monomers are detected at 205 *m/z*, which like valine represents a protonized form of amino acids. The tryptophan also forms complexes with water molecules. The characteristic fragments of tryptophan are observed at 130 m/z and 160 m/z. The small fragment corresponds to the tryptophan, where the amide functional group [CH-NH_2-COOH] remains truncated. The larger fragment corresponds to tryptophan without the carboxyl functional group [COOH]. This decarboxylized fragment carries a mass of 159 amu and is detected in its protonized form. This confirms a location of the added hydrogen nuclei on the amine functional group. Neither fragment is detected in complexes with water molecules. A bond with water molecules located on the carboxyl functional group (C-terminal) of the amino acids could be suggested. In this condition no homodimer of tryptophan is registered, whereas the homodimer of valine is observed with two hydrogen nuclei [2 val, 2 H]. At a mass of 322 m/z, the heterodimer [val, trp, H] is observed. The difference in the number of hydrogen nuclei suggests different bonds involved in the homodimers of valine and the heterodimer valine-tryptophan.

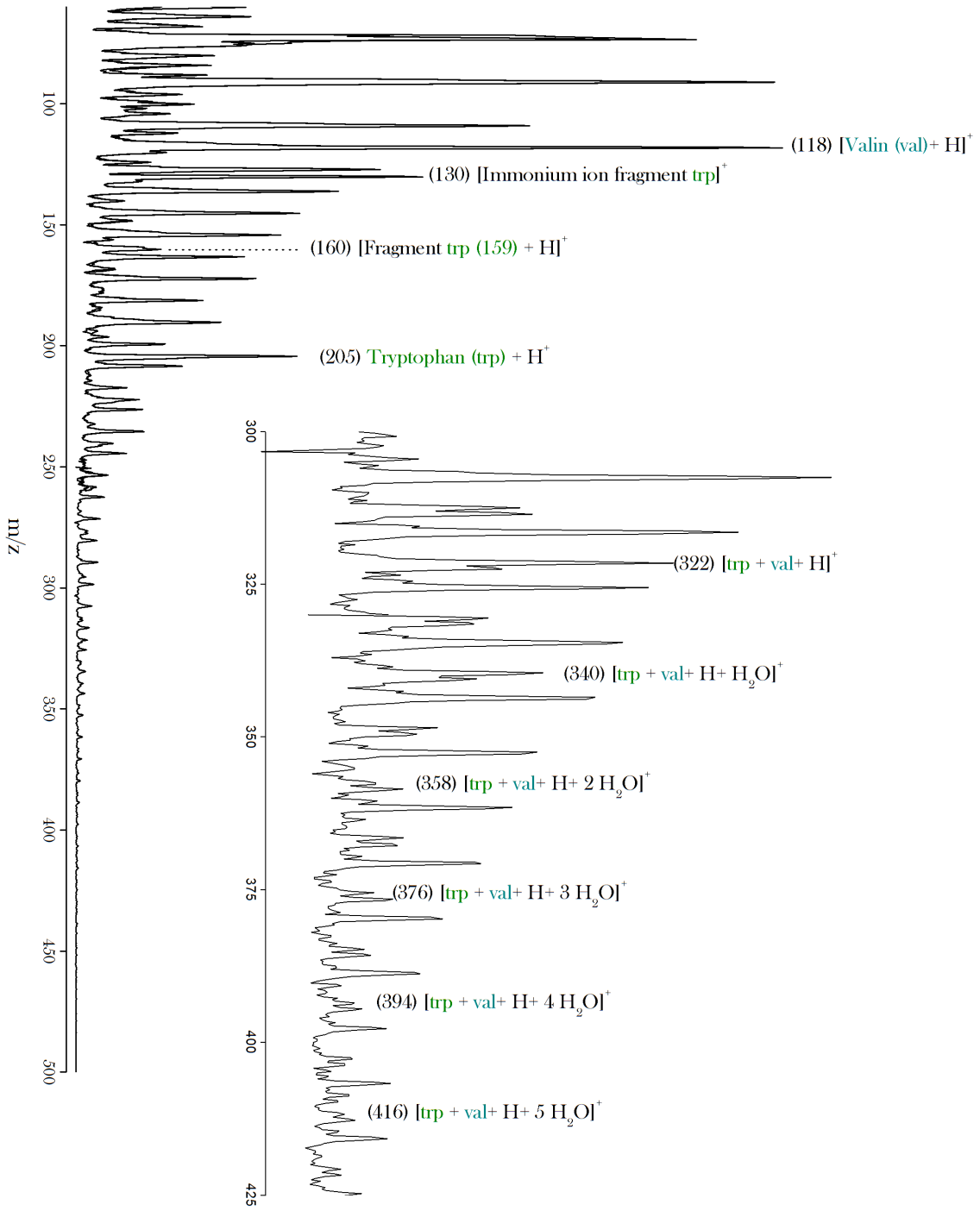

Figure A5: Mass spectrum of embedded molecules, which results from a helium droplet beam passing through the pickup cell containing both valine and tryptophan (in quantity following the respective molar ratio 2/1). The mass spectrum is obtained through the difference of mass spectra in presence and absence of helium droplets. The inset shows an enlargement of thirty times.

The peak detected at 304 *m/z* does not correspond to an expected complex of fragments, nor to a complex containing water molecules (figure.A6). This mass represents the mass of the complex [val, trp, H] shortened by 18 amu, which corresponds to the mass of a water molecule. The reaction of formation of a peptide bond between two amino acids (containing respectively R1 and R2 as side-chains) also form a water molecule as a co-product:

The peptide bond formation reveals itself as an endothermic reaction by 10 kJ mol^{-1} (ΔG at 273 K in water) [15] and presents an activation barrier of 54-84 kJ mol^{-1} [200, 201]. In the gas phase, amino acids could also exist in the cationic form without being protonized. In this case the positive charge is located at the carbon of the carboxyl functional group. These cationic amino acids are considered to more easily form peptide bonds via the free doublet located at the C-terminal with the amine function of another amino acid [31]. A scenario in which the electron impact ionization first forms a cationic amino acid could explain peptide bond formation.

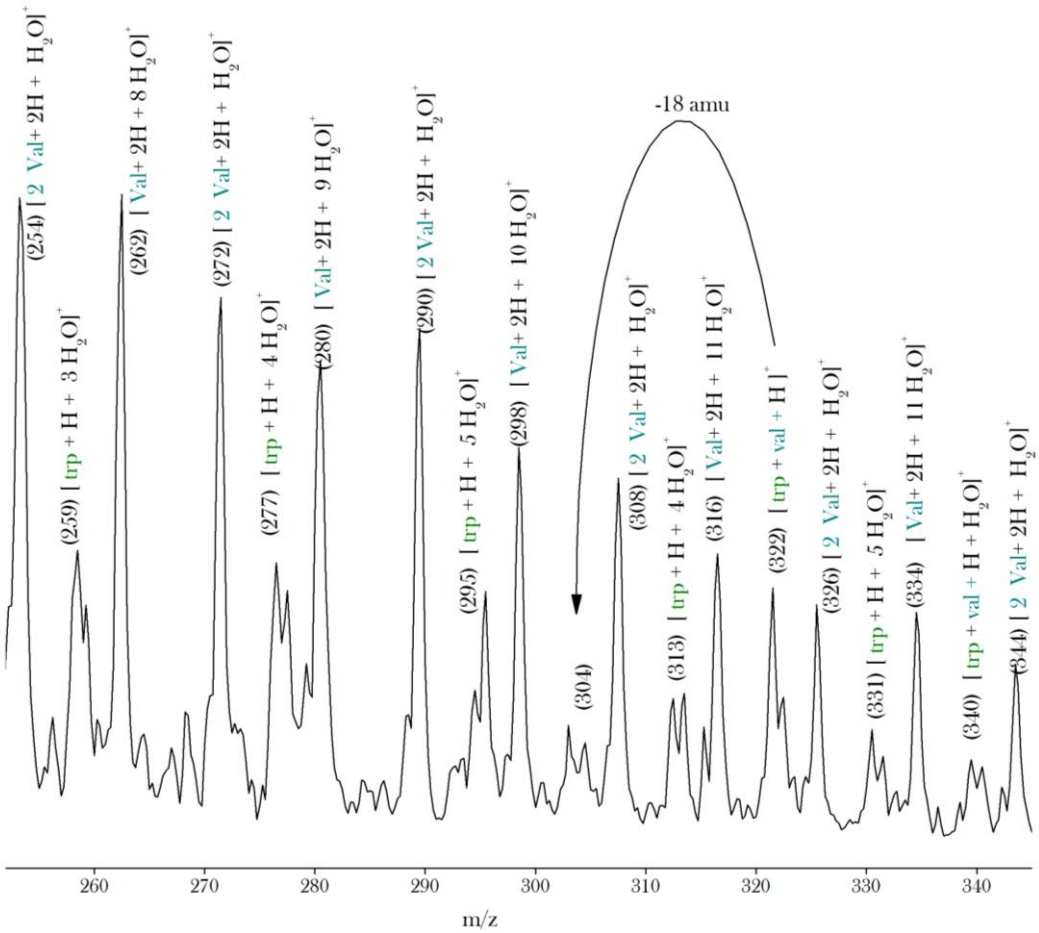

Figure A6: Range of 250-350 m/z of the mass spectrum presented in the figure A5

L-Histidine and L-Tryptophan

The peaks at 156, 110 and 82 *m/z* match the masses of histidine and its two principal fragments (figure A8). The tryptophan and its two fragments are also detected at 130, 159, and 205 *m/z*. Histidine and tryptophan, which carry the mass 155 and 204 in the neutral form, are here observed in a protonized form. The two species observed at 110 and 159 *m/z* represent the lateral chain of amino acids, which correspond to histidine and tryptophan where their carboxyl functional group [CO_2H] remains truncated (figure A7). The fragments at 82 *m/z* and at 130 *m/z* correspond to amino acids shortened from their amide functional groups [COOH-NH_2-CH-]. The smaller fragments are present in larger quantity than the immonium ion fragments from the two amino acids. However in comparison to its fragments, the tryptophan remains minor, whereas the histidine is present in greater quantity than the imidazole fragment. The quantity of fragments and amino acids detected is temperature-dependent. By increasing the temperature in the pickup cell, the fragments first appear in great quantity whereas the amino acids remain a minor product. At higher temperature the amino acids become the major embedded products. Studies on histidine embedded in helium revealed the linear temperature dependence of its fragments [194]. This linear temperature dependence of the histidine fragments remained limited by a plateau of stabilization after a temperature of 190° C. The histidine experienced a quadratic temperature dependency, which starts at a temperature 10 K higher than the fragments. The stabilization temperature of the fragments corresponded to the intersection of the two curves. The higher melting point of the tryptophan (290-295°C) than the histidine (287°C) could explain the observation of fragments of tryptophan in greater quantity than fragments of the histidine. Tryptophan is also detected in the presence of up to five water molecules. In the case of histidine in similar conditions, the complexes with water molecules are quasi-absent.

Embedded dimers

The presence of both amino acids and their two respective fragments offer several possibilities of dimer formation. Embedded homodimers were observed with both amino acids. The dimer/monomer ratios remain small, respectively 3% for histidine and 5% for tryptophan. The monomers are detected in the protonized form. In the case of the tryptophan dimers, 408 *m/z*, 409 *m/z*, and 410 *m/z* are detected, which correspond to [2 trp], [2 trp, H], and [2 trp, 2 H] complexes respectively. The forms with and without one hydrogen atom remain a minority in comparison with the complex including two hydrogen atoms. The histidine dimer is detected only at 315 *m/z* corresponding to two histidine molecules and an added hydrogen atom. Similarly to the monomer, the tryptophan dimer is also detected in the form of a complex with water. The heterodimer tryptophan-histidine is present at 360 *m/z* and 361 *m/z* corresponding respectively to complexes with one and two hydrogen atoms. The heterodimer complex with water molecules is observed in limited quantity, similar to the histidine monomers and dimers. Taking into account the importance of the carboxyl function in the water complex formation, the C-terminus of tryptophan implication in the heterodimer could be suggested. The homodimers of amino acid fragments are not observed as well as dimers composed of amino acids and fragments of histidine.

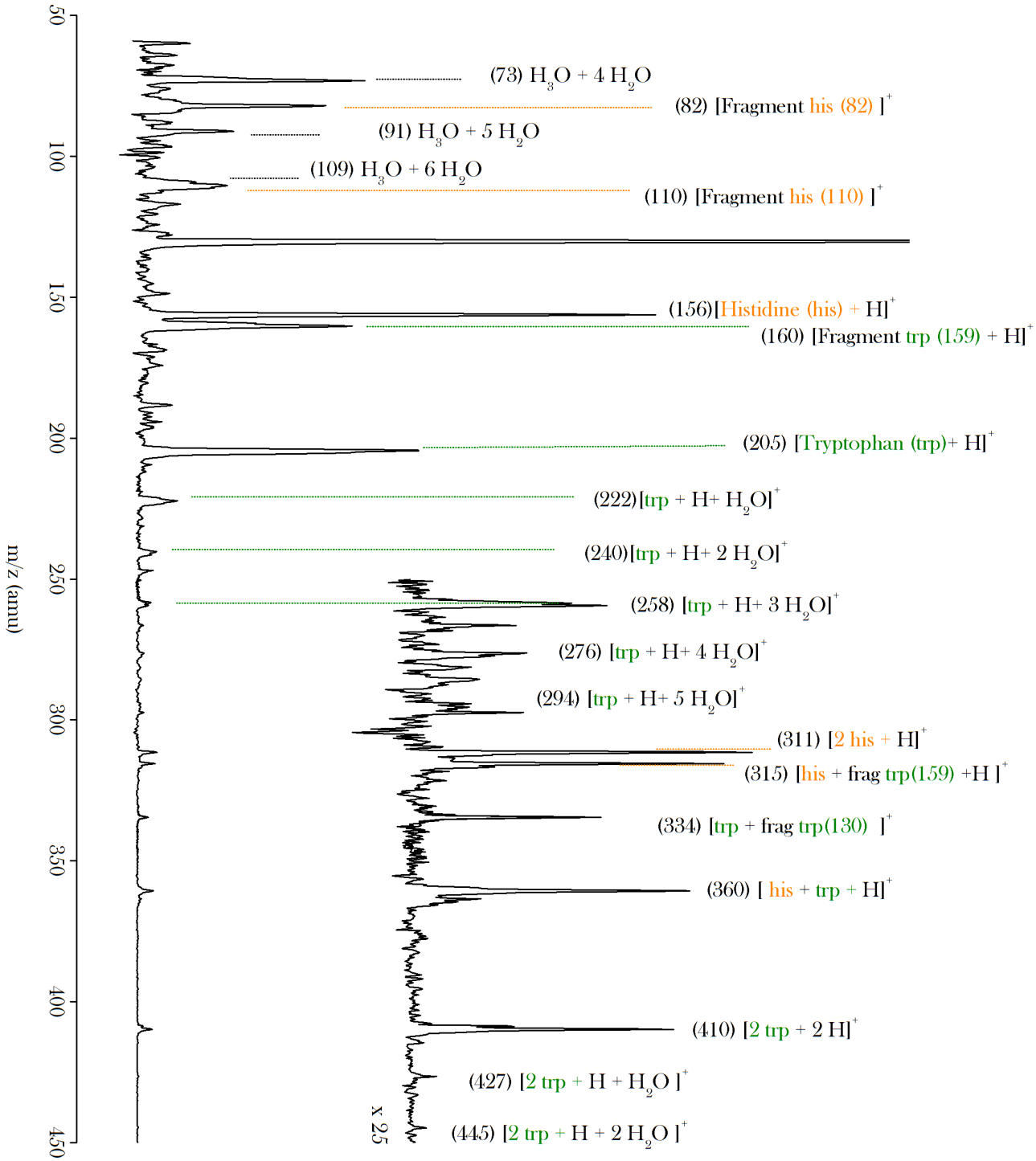

Figure A8: Mass spectrum of embedded molecules, which results from a helium droplet beam passing through the pickup cell containing tryptophan and histidine with a molar ratio of 1/2. The mass spectrum is obtained through the difference of mass spectra in the presence and in the absence of helium droplets. The inset shows an enlargement of the spectrum of twenty-five times

The two fragments of tryptophan abundantly form complexes. At 334 and 364 m/z the complexes of both fragments with tryptophan are detected with one of both amino acids: the indole fragment with tryptophan at 334 m/z. At 315 m/z the iminium ion of tryptophan with histidine is detected, whereas complexes of histidine with the (130) fragment of tryptophan are not observable. Tryptophan with histidine fragments is also observed, but only in very limited quantity at 286 m/z and 314 m/z. In all cases of heterodimers with fragments, complexes with water molecules are not observed. This confirms an implication of the C-terminus in the formation of water clusters. Tryptophan dimers are detected in complexes including 0 to 2 hydrogen atoms. Complexes with water are also observed. In this case the form with only one hydrogen atom remains favored. Two masses are detected at m/z = 390 and 392, which correspond to the mass of [2 trp] and [2 trp, 2 H shortened from 18 amu (figure A9). In accord with the equation A1, peptide bonds between two tryptophan molecules could be suspected. Another detection at 297 m/z is also not properly attributable to complexes of fragments also including water molecules (figure A10). This detection corresponds to the mass of 315 amu subtracted by the mass of a water molecule. The detection at 315 m/z is attributed to a complex of histidine with the decarboxylized fragment of tryptophan (159 amu) and a hydrogen nucleus. The fragment of tryptophan includes an amine functional group and potentially remains able to form a peptide bond with a carboxyl functional group of an amino acid. A molecule formed through peptide bonding between histidine and the decarboxylized tryptophan remains possible.

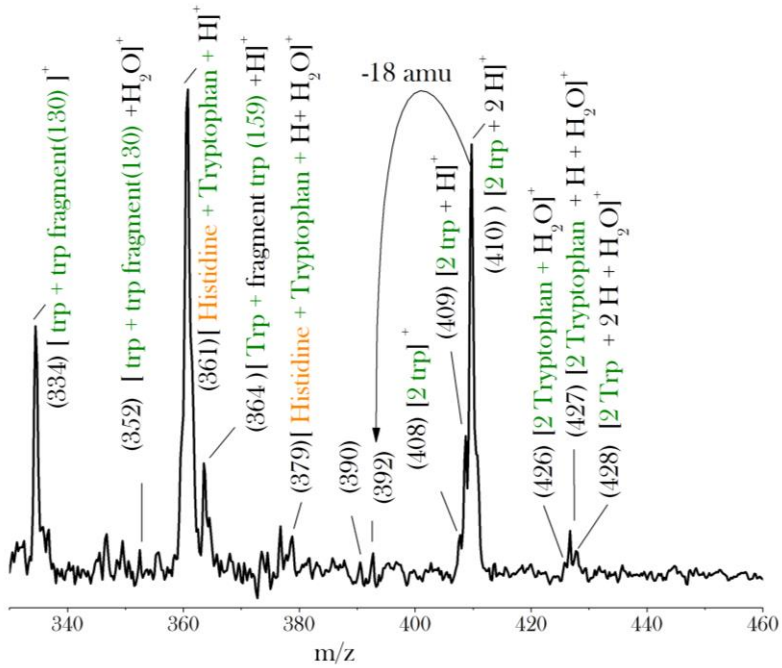

Figure A9: Range of 330-460 m/z of the mass spectrum presented in the figure A8

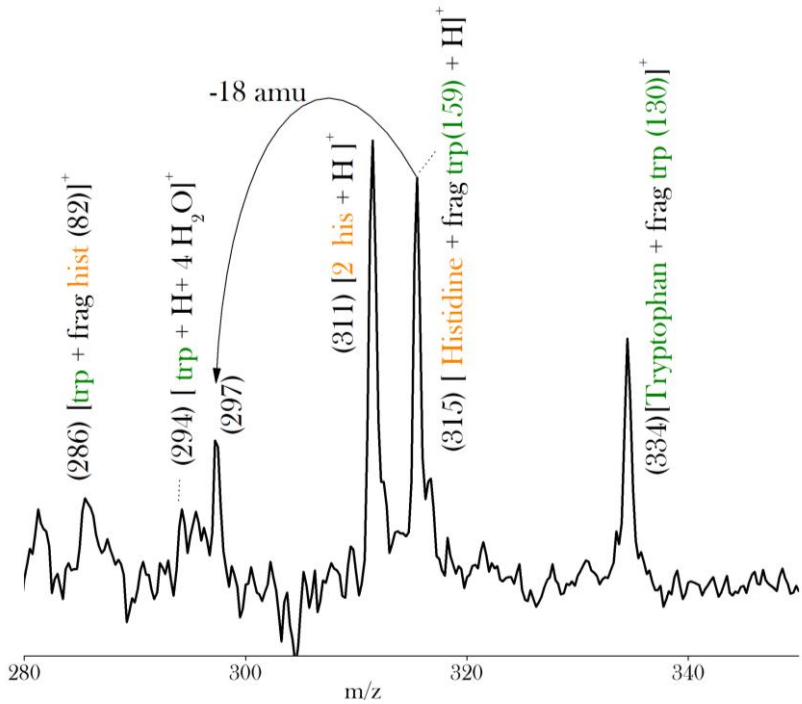

Figure A10: Range of 390-340 m/z of the mass spectrum presented in the figure A8.

Conclusion

Glycine, valine, histidine and tryptophan were embedded in helium droplets, through their vaporization in a pickup cell. The fragments of these amino acids first appeared at low temperature. These main fragments represent the amino acids shortened from the carboxyl functional group (-45 amu) or the amine functional group (-73 amu). By increasing the temperature, monomers and polymers of amino acids are successively detected. The cluster including a small number of amino acids appeared in greater quantity than the larger complexes. However the tetramers of valine appeared particularly privileged. Ionized monomers and polymers of amino acids are able to form complexes with water molecules. The absence of water complexes with the fragments indicates an implication of the C-terminus in the formation of water complexes. At a high water vapor pressure, complexes with four water

molecules are quasi-systematically favored independently from the size and the number of amino acids involved (monomer, dimer or trimer). This suggests stable clusters of four water molecules attached to the amino acids. Experiments were performed with two different amino acids in the pickup cell. The heterodimers of [tryptophan-valine-H] and [tryptophan-histidine-H] were observed. Tryptophan appears particularly suitable to form complexes with other amino acids, with fragments of amino acids, and with water molecules. Its immonium fragment also forms complexes with histidine. The fragment (130) truncated from the N-terminal amine function does not have the ability to from complexes with histidine. The configuration of tryptophan, which includes the two amine functional groups at N-terminus and in the indole cycle appears particularly likely to form clusters. Several complexes were detected at a mass indicative of amino acid dimers shortened from 18 amu. These masses are observed by tryptophan dimers and tryptophan-valine heterodimers. They are not explainable by other complexes of amino acids, fragments, and water molecules. The peptide bond formation generates water molecules as a co-product. The cationic (but not protonized) amino acids are considered to more easily form peptide bonds. Peptide bond formation resulting from this experiment is suspected.

Summary

The synergy of the sputtering technology and the messenger IRPD allowed the measurement of the IR spectra of a series of gas phase, mass-selected anions with high sensitivity and selectivity. Structural information on more than 25 anions, not yet IR investigated by gas phase IR spectroscopy could be obtained. Many of these systems play an important role for the interstellar chemistry and some of them have been already detected in the interstellar medium. This series of systems includes: a naked carbon chain [C_{11}^-], carbon nitrides with two nitrogen atoms [the $C_xN_2^-$(x = 1,3-11)] and four nitrogen atoms [$C_xN_4^-$(x = 3,4,6,8,10)], carbon chains containing one oxygen atom [C_xO^- (x = 6,8)], and two oxygen atoms [$C_4O_2^-$] and carbon chains including oxygen and nitrogen atoms [C_3NO^-]. The list also includes anions containing one hydrogen atom [C_4OH^- and $C_5NH_2^-$] and one ^{13}C or ^{15}N isotope [ispotomers of $C_5N_2^-$, C_4O^-, $C_6N_3^-$]. The identifications were carried out through the IR absorption originating essentially from C-C, C-N and C-O stretches and are responsible for absorptions in the region of 1200 to 2300 cm^{-1}.

Additionally, valuable data was presented which aid in understanding the chemistry of formation of these anions. Several valuable evidences were collected about the chemistry of formation of negatively charged clusters. The sputtering in a nitrogen atmosphere produced abundantly carbon-nitride anions [$C_xN_y^-$ (y = 1-5)]. An odd/even effect was observed with a clear preference for the formation of cluster anions with an odd number of carbon atoms for (y = 1,2) and an even number of carbon atoms for (y = 3,4,5). The formation of carbon nitride anions including one hydrogen atom was unexpectedly strong for several anions (only with the minimal presence of hydrogen). These $C_xN_yH_z^-$ revealed also an odd/even preference for the anions with y = 1,3, but inversed in comparison to those hydrogen-free homologues. The sputtering in the presence oxygen is less propitious and despite the minimal presence of nitrogen, the presence of several carbon nitrides could be detected as well. The IR spectra revealed the stronger reactivity for the formation of the $C_xN_2^-$ (x = 5, 7) than for the formation of the C_xO^- (x = 6, 8). Contrary to this, the formation of C_4OH is favored in comparison to $C_5N_2H^-$. The CNO^- and C_3NO^- were two of the most abundantly produced anions. They were formed despite the absence of introduced oxygen or nitrogen. The C, N and O atoms compose the structure of many organic molecules. Thereby, facilities of organic molecules' formation in such experiment could be forsee. The ensemble of the evidence and characteristics observed in this work supplement the understanding of synthesis of clusters in the sputtering source.

The B3LYP/aug-cc-pVTZ calculations applied on the ensemble of the systems presented below helped the structural assignment of the anions. The structures predicted as global minima were detected for all species. Linear geometries were detected for all investigated carbon cluster anions including up to 2 nitrogen or oxygen atoms (except for $C_xN_2^-$ (x = 3,4,5) with a bent geometry). The N and O atoms were preferentially located at the end of the chains, forming nitrile and carbonyl groups. The tendency to form nitrile groups at the end of the carbon chain appeared also by the anion including four nitrogen atoms. Tetra-branched structures were

observed for several $C_xN_4^-$, as for example for the well-known $C_6N_4^-$. The $C_xN_4^-$ (x = 8, 10) clusters anions present a similar structure as $C_6N_4^-$ where the elongation of the carbon cluster takes place in a single branch. When the number of carbon atoms included in the molecule was equal or inferior to the number of nitrogen atoms, the tetra-branched structure was not observed. $C_3N_4^-$ presents a tri-branched structure and includes one nitrogen atoms within the carbon chains forming an imine (C=N-C) functional group. $C_3N_4^-$ contains two imine functional groups within the chain, with alternating carbon and nitrogen atoms. In this report, the combination for the experiment with B3LYP/ aug-cc-pVTZ calculations was essential for the assignment of the structures, particularly for the uninvestigated systems.

The computational methods also delivered estimations of the length of the bonds. The anions presenting more than two successive carbon atoms present a structure corresponding to an intermediate between the cumulene-like (=C=C=) and the polyyne (-C≡C-) form. The preference for one of these two forms (cumulene like or to polyyne-like) is influenced by the parity of carbon atoms and the presence of other atoms types. Inclusion of a nitrogen atom with its five valence electrons predisposes the polyyne form, whereas inclusion of an oxygen atom with its six valence electrons favors the cumulene form. The structure influences the vibration mode, as for example in the case of naked carbon chain. Similar vibration modes of these C_x^- were attributed to IR frequencies regularly increasing or decreasing as function of the size of carbon clusters, an depending on the odd or even number of C atoms. This work furnished a solid basis for future structural studies of uninvestigated systems based on similar elements.

Numerous isomers of the detected systems were also subject to B3LYP/ aug-cc-pVTZ calculations confirming the assignment of the detected IR spectra to the lowest energy geometries. For example the disfavored cyclic isomers of C_x^- (up to C_9^-), linear and bend geometries of the $C_xN_2^-$, and many structural isomers of the $C_xN_4^-$ were theoretically examined, however not detected. The calculations of some systems containing two hydrogen atoms ($C_3N_2H_2^-$) or three oxygen atoms ($C_7O_3^-$) revealed the favored location of the hydrogen and oxygen atoms on the carbon chains. The calculations of the $CNOH_z^-$ (z =1-4) and $C_3NOH_z^-$ (z = 1-7) were particularly valuable to foresee the formation of organic molecules in case of sputtering in the presence of H_2. The predicted $CNOH_4^-$ corresponds to negatively charged formamide, which is the smallest organic molecule presenting a peptide bond. The calculations of simple hydrogenations of C_3NO^- predicted a structure of $C_3NOH_7^-$ with an amine (-NH2) and a carboxyl (C=O) functional group located at the ends of the hydrogenated carbon chain. The amino aldehyde (CHO-NH-) isomer of $C_3NOH_7^-$ is considered as precursor of alanine. From the calculations, a third isomer presenting an amide functional group (-CHO-NH2), is estimated to be clearly favored in comparison to the two precedents anions. These predictions propose future investigation of the chemistry in presence of hydrogen to be highly interesting. The absorption bands of several anions, which present the same masses as three of the amino acids (alanine, glycine and serine), were revealed [C_5N^- (with one substitute ^{13}C or one ^{15}N), $C_5N_2^-$ (with one ^{13}C or one ^{15}N), $C_6N_3^-$ (with one ^{13}C or one ^{15}N), and C_4O^- (with one ^{13}C), C_4OH^- and $C_5N_2H^-$]. These results are valuable for future IR based identifications of amino acids in gas phase.

In a complementary experiment, amino acids were examined in helium nanodroplets generating an isolation matrix in which the molecules conserve quasi-completely the vibrational and rotational freedom of the gas phase. Glycine, valine, histidine and tryptophan were embedded in helium droplets, through their vaporization in a pickup cell. The amino acid and their fragments were detected. These main fragmentation channels represent the loss of the carboxyl (-45 amu) or the amine functional group (-73 amu). Complexes of embedded molecules were also observed. The amino acids formed easily complexes with water or homopolymers and heteropolymers, which contained also fragment of amino acid. By comparing the capacity of truncated fragment to form complexes, an implication of the C-terminus in the formation of water complexes was suspected. In the case of complex with fragments, the configuration of tryptophan, which includes the two amine functional groups at N-terminus and in the indole cycle appeared particularly likely to form clusters. Several complexes were detected at a mass indicative of amino acid dimers shortened by 18 amu. These masses were observed for tryptophan dimers and tryptophan-valine heterodimers. They are not explainable by other complexes of amino acids, fragments, and water molecules. The peptide bond formation generates water molecules as a co-product. The cationic (but not protonized) amino acids are considered to more easily form peptide bonds. Peptide bond formation resulting from these experiments is suspected.

FUTURES PERSPECTIVES

The work presented here produced answers but also puts forth questions, inviting further investigations. The unexplained 80 cm^{-1} broad absorption band of $C_5N_2^-$ and the possible presence of a clearly unprivileged conformer (from the calculations) of C_3N_4- are examples, which particularly worth the effort to carrying out further investigations. The utilization of another messenger than D_2 in the photodissociation method may be one of the ways to follow in order to gain more information regarding these issues. The chemistry of anion formation in the sputtering process constitutes also a potential field of futures investigations. There remains much to be learned about the formation of carbon clusters containing oxygen and nitrogen atoms. The preferences for anions depending of the parity of the number of carbon atoms present in $C_xN_2^-$ and $C_xN_4^-$ cannot be directly explained solely by their structures. This work seems clearly indicate a cascade of reactions between the different species present. The sputtering source produced ions (positively and negatively charged) as well as their neutral homologues. Several cations produced were only briefly examined. Future investigations on the ensemble of molecules produced in the source will complete the understanding of reactive sputtering and of the formation pathways for the investigated molecules

Anions in Space

This experiment clearly demonstrates the suitability of the sputtering source for the synthesis of ions similar to those identified in the interstellar medium. The lack of IR information on this anions is one of the main reasons evocated by astronomers to explain the strong underrepresentation of negatively charged species identified in space. Thereby these results offer valuable information for the understanding of the interstellar chemistry. Indeed the telescope data require laboratory data for comparison. However, multiwavelength observations of space provide data also in microwave region. This region reveals, in addition to the rotational, also the vibrational levels of the molecules. This region presents a better resolution than the IR and is particularly propitious in the identifications of interstellar molecules. In the quest for interstellar anions identification, the μm absorption domain of the systems, which are presented in this work, should deliver complementary results. The abundance of hydrogen atoms in space favors the molecule including hydrogen (cf. the list of interstellar molecules published by NASA). Thereby the same experiment in the added presence of gaseous hydrogen is particularly promising. In the added presence of hydrogen in the sputtering process, polyhydrogenated carbon chains are expected. In the case of the sputtering experiment carried out with the presence of N_2, O_2. H_2, within the hydrogenated substituted carbon chain, organic molecules are strongly expected.

Amino Acids

The sputtering experiment came close to producing organic molecules. The negatively charged formamide is predictable if H_2 is added also to the reactive sputtering process. Theoretical studies predicted glycine and alanine (under their different forms including the anionic) as underprivileged in the gas phase [31] (by respectively 0.39 eV and 0.46 eV). In the present experiment, the privileged systems (predicted by the calculations) were persuasively detected. The experimental setup, utilized in this work, extracted species formed in the gas phase. According to the computational predictions, alanine and glycine will not appear (or will appear only in a negligible quantity). In the formation of glycine reported by Devienne et al., amino acids were identified in the gas phase, but their formation occurred on the carbon surface of the target. The charged products of sputtering were secondarily extracted from the target after hours of bombardment. In order to bridge the gap between Devienne experimental results and the present experiment, a complementary setup could be proposed. The concept of this setup takes elements from the two previously mentioned experiments. A mass selection applied to the products of the sputtering source is similar to the experiment presented in this work. The second step consists of depositing the selected ions on a solid surface. By the deposition, the species are formed on a location similar to the surface of the carbon target of Devienne's experiment. The next step constituted by the extraction of the molecules formed. An electromagnetic extraction (as in Devienne′s experimental setup) or a chromatographic examination of the constituents of the target could be carried out.

Such an experiment simulates the encounter of interstellar molecules (produced by sputtering) and dust or meteorites (by a solid target). It is now clear for astronomers, that dust plays an important role in interstellar chemistry. Theoretical predictions proposed the formation of amino acids on a graphene or ice surface as possible under interstellar conditions [31]. Indeed, DFT calculations revealed that different families of molecules: acid, ether, ester, aldehyde, cyanide and also precursors of amino acid could attach easily on the graphitic or iced surface of carbon grains. Such attachments were estimated possible in the accretion phase of meteorites fixing the ingredients of amino acid on their surface. A reaction for the formation of amino acids located on meteorites constitutes the most probable hypotheses also sustained by the comparative abundance of amino acids observed on meteorites concluded in these theoretical studies. Such a complementary experiment appears adapted to investigate these theoretical findings. Thereby, new understandings about the chemistry on solid surfaces in conditions approaching those of the interstellar medium may be expected. The difficulty encountered in observing amino acids in interstellar clouds and the paradoxical omnipresence of numerous amino acid on several meteorites and comets remains an open question.

References

[1] Elsila J. E., Glavin D. P., Dworkin J.P.: Cometary glycin detected in sample returned by Stradust, *Met. Plan. Sc.* ,44, 1323-1330, **2009**.

[2] Cronin J.R., Chang S.: The Chemistry of Life′s Origin, *Eds Greenberg, J.M. mendoza-Gomez, C.X. &Pirronello, V. (Kluwer, Dordrecht, The Netherlands)*, p 209, **1993**.

[3] Cronin J.R., Pizzarello S.: Amino acids of the murchison meteorite.III. Seven carbon acyclic primary a-amino alkanoic acids, *Goechim. Cosmochim. Acta,* 1, 50, 2419, **1986**.

[4] O Leavy M.: Anaxagoras and the origin of the life, *iUniverse publishing group*, **2008**.

[5] Pasteur L.: Examen du role attribué au gaz oxygene atmospherique dans la destruction des matières animales, *C.R. Acad. Sci.,* 56, 734-740, **1863**.

[6] Miller S.: A production of amino acids under possible primitiv earth conditions, *Science*, 117, **1953**.

[7] Miller S.: The mechanism of synthesis of amino acids by electric discharged, *Biochim. Biophys acta*, 23, 480, **1957**.

[8] Paschke R.: Probable Role of Gamma Irradaition in Origin of life, *Science,* 125, 881, **1957**.

[9] Groth M.: Photochemische Bildung von Aminosäuren und anderen organische Verbindungen aus Mischungen von H2O, NH3 und den einfachsten Kohlenwasserstoffen, *Angew Chem*, 68, 681, **1957**.

[10] Fox S. W., Haralda K.: Thermal copolimerisation of amino acids to product resembling protein, *Science*, 247, 951, **1958**.

[11] Kastin J. E., Earth′s early atmosphere, *Science*, 259,920, **1993**.

[12] Boniface M., Jenderzejewski N., Agrinier P., Humler E., Coleman M., Javoy M., The Chlorine Isotope Composition of Earth′s Mantle, *Science*, 318: 1518, **2008**.

[13] Altwegg K., Balsiger H., Bar-Nun A.,Berthelier J.J., Bieler A., Bochsler P., Briois C., Calmonte U., Combi M., De Keyser J., Eberhardt P., Fiethe B., Fuselier S., Gasc S., Gombosi T.I., Hansen K.C., Hässig M., Jäckel A., Kopp E., Korth A., LeRoy L., Mall U., Marty B., Mousis O., Neefs E., Owen T., Rème H., Rubin M., Sémon T., Tzou C.-Y., Waite H., Wurz P. : 67P/Churyumov-Gerasimenko, a jupiter family comet with a high D/H ratio, *Science*, 347, 6220, **2015**.

[14] Gibson D.G., Glass J.I., Lartigue C., Noskov V.N., Chuang R-Y., Algire M. A., benders G. A., Montague M. G., Ma L., Moodie M.M., Merryman C., Vashee S., Krisnakumar R., Assad-Garcia N., Andrews-Pfannkoch C., Denisova E. A., Young L., Qi Z-Q, Segall Shapiro T. H., Calvey C.H., Parmar P.P., Hutschinson C.A.III,Smith H.O., Venter C.J.: Creation of a Bacterial Cell Controlled by the Chemically Synthetized Genome, *Science*, 319, 5867, **2010**.

[15] Bernstein M., Dworkin J.P., Standford S. A., Cooper G.W., Allamandol L. J.: Racemic amino acids from the ultraviolet photolysis of interstellar ice analogues, *Nature* ,416, 401-403, **2002**.

[16] Pilling S., Seperualo Duarte E., da Silveira E. F., Balanzat H., Rothard H., Domaracka A., Boduch P.: Possible observation of Glycine during processing of NH_3:H_2O:CO ice by heavy cosmic ray analog, *Astr. Sci. Conf.*, **2010**.

[17] Devienne F.M., Barnabé C., Couderc M., Ourisson G.: Synthesis of biological compounds in quasi-interstellar conditions, *C.R. Acad. Sci.,* Paris, 1, Serie II, 435-439, **1998**.

[18] Devienne F.M., Teisseire M.: Total synthesis of interstellar chemical compounds by high energy molecular beam bombardment on pure graphite, Astron. Astrophys., 147,54-60,**1985**.

[19] NASA´s website, science.gsfc.nasa.gov, **2015**.

[20] Mc Carthy M.C., Gottlieb C.A., Gupta H., Thaddeus P.: Laboratory and Astronimical identification of the negative moleuclar ion C6H-, *Astroph. J*, 652, 141-144 , **2006**.

[21] Herbst E.: Can negative molecular ions be detected in dense interstellar clouds?, *Nature*, 289, 656-657, **1981**.

[22] Tulej M., Kirkwood D. A., Pachkov M., Maier J. P.: Gas Phase electronic transitions of carbon chain anions coinciding with diffuse interstellar bands, 506, 69, **1998**.

[23] Terzieva R., and Herbst E.: Radiative electron attachment to small linear carbon clusters and ist significance fort the chemistry of diffuse interstellar clouds, *Int. J.Mass Spectrom.*, 201, 135, **2000**.

[24] Blanskby S. J., Mc Anoy A. M., Dua S., Bowie J.H.: Cummulenic and heterocummulenic anions: potentiel interstellar species?, *RAS, MNRAS*, 328, 89-100, **2001**.

[25] Coll P., Guillemin J-C., Gazeau M-C., Raulin F.: Report and implications of the first observation of C_4N_2 in laboratory simulations of Titan's atmosphere, *Pl. Sp. Sci.,* 47, 1433-1440, **1999**.

[26] Teanby N.A., Irwin P.G.J., de Kok R., Jolly A., Bézard B., Nixon C.A., Calcutt S.B.: Titan's stratospheric C_2N2, C3H4 and C4H2 abundances from Cassini/CIRS far-infrared spectra, *Icarus*, 202, , 620-631, **2009**.

[27] Mc Carthy M., Molecular Anions in the laboratory and in Space, *ITAMP Workshop*, Dec **2012**.

[28] Lovas J. L. Kawashima Y., Grabow J.U., Sueram R. D., Fraser G. T., Hirota E.: Microwave spectra, hyperfine structure and electronic diplole moments for conformers I and II of glycine, *ApJ*, 455, 201, **1995**.

[29] Kuan Y.-J., Charnley S.B., Huang H.-C., Tseng W. L., Kisiel Z.: Interstellar Glycine, *ApJ.,* 593.848, **2003**.

[30] Jones P.A., Cunningham M.R., Godfrey P.D., Cragg D.M.: A search for biomolecules in Sagittarius B2 (LMH): with the Australia Telescope Compact Array, *MNRAS*, 374:579,**2007**.

[31] Lattelais M., Etudes théoriques à propos de l′origine exogène des molécules prébiotiques, PhD thesis, Université Pierre at Marie Curie, **2008**.

[32] Bernhardt K. H., Vaccum technology compendium, *Pfeiffer vacuum GmbH,* **2010**

[33] Wang X., Maeda K., Chen X., Takanabe K., Domen K., Hou Y., Fu X., Antonietti M.: Polymer Semiconductors For artificial Photosynthesis: Hydrogen Evolution of Mesoporous Graphitic Carbon Nitride with Visible Ligth, *J. Am. Chem. Soc.,* 131 1680-1681, **2009**.

[34] Liu A. Y., Cohen M. L.: Prediction of New Low Compressibility Solids, Nature, *Science*, 245, 841-842, **1989**.

[35] Li D., Shi J., Lai M., Li R., Yu D.: First-principle calculation on the structural and electronic properties of hard C11N4, *Phys. B.: Cond. Mat.,* 449, , 90-94, **2014**.

[36] Liu M., Artyukhov V.I., Lee H., Xu F., Yakobson B.I., Carbyne from first principles: Chain of C atoms, a nanorod or a nanorope*?, ACS Nano*, 7, 10075-10082, **2013**.

[37] Artyukhov V. I., Liu M., Yakobson B.I., Mechanically Induced Metal-Insulator Transition in Carbyne., *Nano Lett.,* 14, 4224-4229, **2014**.

[38] Movisyan L. D., Kondratuk D. V., Franz M., Thompson A. L., Tykiwinski R., Anderson H. L.: Synthesis of polyyne Rotaxanes. *Organics let.*,14, 3424-3426, **2012**.

[39] Sorokin P., Lee H., Antipina L.Y., Singh A. K. Yakobson B. I.: Calcium Decorated Carbyne Networks as Hydrogen storage media. *Nano Lett* , 11, 2660-2665, **2011**.

[40] Jacox M. E., Miligan D. E. Moll N. G., Thomson W.E.: Matrix-Isolation Infrared Spectrum of the free Radical CCO, *J Phys. Chem.*, 43, 3734, **1965**.

[41] DeKock R.L., Weltner W. Jr: C_2O CN_2 and C_3O molecules, *J. Am. Soc.*, 93, 7106, **1971**.

[42] Philippe L., Hirayama T., Ramage M.J., Comtet G., Rose M., Hellner L., Dujardin G., Molecular Reactions in condensed Carbon-Monoxide Studied by Ion Photodesorption, *J. Chem. Phys.*, 106, 7072-7079, **1997.**

[43] Maier G., Reisenauer H.P., U schäfer, Balli H.: C_5O_2(1,2,3,4,-pentatetraen-1,5-dion), ein neues Oxyd des Kohlenstoffs , *Angew. Chem.* 100, 590, **1988**.

[44] Maier G, Reisenauer H. P., Ulrich: Matrixspektroskopische Untersuchung zur Existenz von C_7O_2(1,2,3,4,5,6-heptahexaen-1,7-dion), *Tetrahedron Lett* 32, 4469, **1991**.

[45] Maier G., Reisenauer H. P., Balli H., Brandt W.:C_4O_2(1,2,3,-buitatrien-1,4-dion) das erste Dioxid des Kohlenstoffs mit einer geraden Anzahl C-atome, *Angew. Chem.* 102, 920, **1990**.

[46] Behrisch P.: Sputtering by particule Bombardment I, *Springer verlag*, Berlin **1981**.

[47] Honig R.E.: Sputtering of Surfaces by positive Ion beam of low energy, *J. Appl. Phys.*, 29, 249 **1958**.

[48] Hortig G. Mueller M.: Multiatomic Clusters Emerging from a Metal Surface under Ion Bombardment, *Z. Phys.,* 221,119, **1969**.

[49] Katakuse I., Ichiara T., Fujita Y., Matsuo T., Sakurai T., Matsuda H.: Mass Distribution of Negative Cluster Ions of Copper, Silver and Gold, *Int. J. Mass Spectr. Ion Process.*, 74, 33, **1986**.

[50] Staudt C., Wucher A.: Generation of Large Indium Clusters by Sputtering, *Phys. Rev. B.,* 82, 075419, **2002**.

[51] Wucher A., Wahl M.: The Formation of Clusters during Ion Induced Sputtering of Metals Nucl. *Inst. B*, 115, 581, **1996**.

[52] Wucher A., Wahl M., Oechsner H.: The Mass Distribution of Sputtered Metal Clusters I. Experiment Nucl. *Inst. Meth. B*, 83, 73, **1993**.

[53] Benninghoven A.: Developments in Secondary Ion Mass Spectroscopy and Applications to Surface Studies, *Surf. Sci.,* 53, 596, **1975**.

[54] Williams P., Evans, Jr C. A.: Anomalous Enhancement of Negative Sputtered Ion Emission by Oxygen, *Surf. Sci.,* 78, 324, **1978**.

[55] Mann K., Yu M. L.: Origin of the Chemical Enhancemnet of Postive Secondary Ion Yield in SIMS Secondary Ion Mass Spectrometry (SIMS V), *eds. A. Benninghoven, R. J. Colton, D. S. Simons, H. W. Werner (Springer, Berlin, Heidelberg),* p. 26, **1986**.

[56] Heinrich R., Staudt C., Wahl M., Wucher A.: Ionization Probability of Sputtered Custers Secondary Ion Mass Spectrometry (SIMS XII), *eds. P. Bertrand, A. Benninghoven, H.W. Werner (Elsevier, Amsterdam),* p. 111, **2000**.

[57] Gerhard W.: A Model Calculation of the Neutral Molecule Emission by Sputtering, *Processes Z. Phys. B*, 22, 31, **1975**.

[58] Sigmund P., Urbassek H. M., Matragrano D.: A Note on Rotational and Vibrational Motion of Sputtered or Desorbed Diatomic Molecules, *Nucl. Inst. Meth. B,* 14, 495, **1986**.

[59] Gerhard W., Oechsner H.: Mass Spectrometry of Neutral Molecules Sputtered from Polycrystalline Metals by Ar+ - Ions of 100- 1000 eV, *Z. Phys. B* 22, 41, **1975**.

[60] Urbassek H. M.: Sputtered Cluster Mass Distributions, Thermodynamic Equilibrium and Critical Phenomena*, Nucl. Inst. Meth. B,* 31, 541, **1988**.

[61] Bitensky I. S. Parilis, E. S.: Shock Wave Mechanism Cluster Emission and Organic Molecule Desorption under Heavy Ion Bombardment, *Nucl. Inst. Meth. B*, 21, 26 (**1987**).

[62] Landau L. D. and Lifshitz E. M.: Physical Kinetics, volume 10 of Course of theoretical physics. Pergamon Press, Oxford, **1981**.

[63] Smirnov B. M.: Processes involving clusters and small particles in a buffer gas. *Physics-Uspekhi,* 54, 691–721, **2011**.

[64] Bouchat V., Feron O., Gallez B., Masereel B., Michiels C., Van der Borght T.,Lucas S.: Carbon nanoparticles synthetized by sputtering and gas condensation inside a nanocluster source of fixed dimension, *Surface and coating technology*, 205, 5577, **2011**.

[65] Vietzke E., Refke A., Philipps V., Hennes M., Energy distributions and yields of sputtered C_2 and C_3 clusters, *J. Nucl. Mat.241*, 810-815, **1997**.

[66] Kashtanov P. V., Smirnov B. M., Hippler R.: Magnetron plasma and nanotechnology. *Physics-Uspekhi,* 50, 455–488, **2007**.

[67] Ganeva M.: Formation of metal nano-size clusters with a DC magnetron-based gas aggregation source, PhD Thesis,Ernst-Moritz-Arndt-Universität, Greiswald, **2013**.

[68] Smirnov B., Nanoclusters and Microparticles in Gases and vapors, Germany, De Gruyter, 2012.

[69] Majumdar A., Köpp D., Ganeva M., Datta d., Bhattacharyya S., Hippler R.: Development of metal nanocluster ion source based on dc magnetron plasma sputtering at room temperature. *Review of Scientific Instruments*, 80, 095103, **2009**.

[70] Smirnov B. M., Shyjumon I., Hippler. R.: Flow of nanosize cluster-containing plasma in a magnetron discharge. *Phys. Rev. E*, 75, 066402, **2007**.

[71] Smirnov B.M.: Fundamentals of Ionized Gases. *Wiley*, **2012**.

[72] WatanabeY.: Formation and behaviour of nano/micro-particles in low pressure plasmas. *Journal of Physics D: Applied Physics*, 39, 329, **2006**.

[73] Krimm S. and Bandekar J.: Vibrationnal Spectroscopy and conformation of peptides, polypeptides and proteines, *Adv. Prot. Chem*, 38, 181, **1986**.

[74] Taillandier E., Liquidier A, Ghomi M.: conformation transition of Nucleic acids studied by IR and Raman Spectroscopies, *J. Mol. Struct.*, 214, 185, **1989**.

[75] Coates J., Interpretation of Infrared Spectra, a Pratical Approach, *encyclopedia of analytical chemistry*, pp. 10815-10837, **2000**.

[76] Zhan C-G, Nichols J. A., Dixon A., Ionization Potential, Electron Affinity, Electronegativity, hardness and Electron Excitation Energy: Molecular Properties from Density Functional Theory Orbital Energies, *J. Chem. Phys. A.*, 107, 4184-4195, **2003**.

[77] Socrates G, Infrared and Raman Characteristic Group Frequencies: Tables and Charts, *J. Wiley & Sons,* **2012**.

[78] Larkin P., Infrared and Raman Spectroscopy, Principle and Spectral Interpretation, *Elsevier*, **2012**.

[79] Jacox M.E., Vibrational and Electronic energy Levels of polyatomic Transients Molecules, *J. Phys. Chem.*, 32, 1, **2003**.

[80] Cohen-Tannoudji C., Diu b., Laloe, Mecanique quantique, *Hermann*, **1973**.

[81] Hollas J. M. Symmetry in Molecules, *Chapman and Hall Ltd,* **1972**.

[82] Okumura M., Yeh L. I., and Lee Y.T., The vibrational predissociation spectroscopy of hydrogen cluster ions, *J.Chem. Phys.,* 83, 7, **1985**.

[83] R.L. Woodm, D.S. Bomse and J.L. Beauchamp: Multiphoton dissociation of molecules with low power continous wave infrared laser radiation, *J. Am. Chem. Soc.*, 100, 3248, **1978**.

[84] Asmis K. R., Sauer J.: Mass selective vibrational spectroscopy of vanadium cluster ions, *Mass Spectrom Rev.*, 26, 542-562, **2007**.

[85] Lehmann K.K., Scoles G., Pate B.H.: Intramolecular Dynamics from Eigenstate-resolved Infrared Spectra, *Annu. Rev. Phys. Chem.*, 45, 241-274, **1994**.

[86] Dunba R.C.: Kinetics of low – intensity infrared laser photodissociation. The thermal model and application of the Tolman Theorem, *J. Chem. Phys.,* 95, 2537, **1991**.

[87] Salomon K.E. and Brauman J.I., Infrared multiple-photon decomposition of methanol-solvated fluoride [CH3OHF]- and benzyl(1-), *J. Phys. Chem.,* 92, 6948, **1988**.

[88] Wysocki V, Kenttamaa HI, Cooks RG. Internal energy distributions of isolated ions after activation by variousmethods. *Int. J. Mass Spectrom. Ion Processes*, 75, 181, **1987**.

[89] Uechi G.T., Dunbar RC. The kinetics of infrared laserphotodissociation of n-butylbenzene ions at low pressure, *J.Chem. Phys.*, 96, 8897, **1992**.

[90] Van der Hart W.J., Studies of ion structures by photodissociation,*Int. J. Mass Spectrom. Ion Processes*,118-119, 617, **1992**.

[91] Okumura M., Yeh L. I., Meyers J.D., Lee Y.T.: Infrared spectra of the clusters ions H_7O^+ $3H_2$ and H_9O^+ $4H_2$, J. Chem. Phys., 85, 2328, **1986**.

[92] Kojima, T; Kudaka I, Sato T, Asakawa T. Akyama R., kawashima, Y. Hiraoka k., *Rap commun. Mass Spectrom,* 13, 2090-2097, **1999**.

[93] Sorin A.: Infrared photodissociation spectroscopy of ionic Hydrocarbons: microsolvation and protonation sites, PhD Dissertation, Würzburg, **2007**

[94] Mizuse K., Fujii A.: Infrared photodissociation spectroscopy of $H^+(H_2O)$. Mm (M= Ne, Ar, Kr, Xe, H_2, N_2, and CH_4): messenger-dependent balance between H_3O^+ and $H_5O_2^+$ core isomers, *Phys. Chem. Chem. Phys*, 13, 7129-7135, **2011**.

[95] Miller D. J., Lisy J.M., *J Am Chem soc*, 130, 15381-15392, **2008**.

[96] Stanca-Kaposta E., Schwaneberg F., Fagiani M. R., Wende T., Hagemann F., Wünschmann A.,Wöste L., Asmis K. R.: Infrared photodissociation Spectroscopy of C_{n2+1}^- anions with n=1-5, *Z. Phys. Chem.,* 228 , 351-368 **2014**.

[97] Heitler W., London F.: Wechselwirkung neutraler Atome und homöopolare Bindung nach der Quantenmechanik, *Zeit. für Phys.*, 44, 6-7,455, **1927**.

[98] Weigend F., Häser M.: RI- MP2: first derivative and global consistency. *Theor. Chem. Acc.*,

97, 331, **1997**.

[99] Christiansen O., Koch H., Jorgensen P. : For the approximate coupled-cluster singles and doubles model CC2, *Chem. Phys. Lett.,* 243, 409-418, **1995**.

[100] Hohenberg P., Kohn W., Inhomogeneous Electron Gas, *Phys. Rev.,* 136, B864, **1964**

[101] Kohn W., Sham L. J.: Self-consistent equations including exchange and correlation effects, *Phys. Rev.* **1965.**

[102] P.A.M. Dirac.: Note on exchange phenomena in the Thomas atom, *Proc. Cambridge Philos. Soc.*, 26, 376, **1930**.

[103] D.M. Ceperley and B.J. Alder.: Ground State of the Electron Gas by a Stochastic Method *Phys. Rev. Lett.,* 45: 1200, **1980**.

[104] Vosko S.H., Wilk L. and Nusair M.:Accurate spin-dependent electron liquid correlation energies for local spin density calculations: a critical analysis, *Can. J. Phys.* 58, 1200–1211. **1980**.

[105] F. Jensen. Introduction to computational chemistry, *John Wiley & Sons,* **1999**.

[106] Becke A. D.: Density-functional exchange-energy approximation with correct asymptotic behavior, *Phys. Rev. A,* 38 (6), **1988**.

[107] Lee C.,Yang W. and Parr R. G. : Development of the Colle-Salvetti correlation-energy formula into a functional of the electron density, *Phys. Rev. B,* 37, 785–789,**1988**.

[108] Wende T.: Gas Phase Photodissociation Spectroscopy of Mass-Selected Ionic Clusters: Metal Oxides and Microhydrated Anions, PhD Thesis, Freie Universität Berlin, **2012**.

[109] Grove, W.R.: On the Electrochemical polarity of gases, *Phil. Trans. Royal. Soc.*, london, B142, 87, **1852**.

[110] Plücker J.: Observation on the electrical Discharged Through Rarefied Gases, *The Lon. Edim. Dubl. Phil. Mag.,* 16, 409, **1858**.

[111] Thomson J.J.: Rays of positive electricity and their application to chemical analyses, Longmans Green and Co., London, 2nd edition, **1921**.

[112] Penning, F.M. "Coating by Cathode Disintegration," (filed December 1935 in Germany), U.S. Patent 2,146,025 (Feb. 7, 1939); also Physica (Utrecht), 3, 873 **1936**.

[113] Keudell A.: Einführung in die Plasmaphysik, Vorlesungsskript, Ruhr Universität Bochum, **2014**.

[114] Circular Sputtering Source, Torus® 2“ HV, Installation & Operation Manual, Kurt J. Lesker Compagny, version 3.1, 2006.

[115] Berg S., Larson T., Nender C., Blom H.-O.: Predicting thin-film stoichiometry in reactive sputtering *J. Appl. Phys.*, 63, 887, **1988**.

[116] Berg S., Särhammar E., Nyberg T., Upgrading the „Berg-model“ for reactive sputtering process, *Thin Solid Films*, 565, 186-192, **2014**.

[117] Luca A., Schlemmer S., Cermak I., Gerlich D.: On the combination of a linear field free trap with time-of-flight mass spectrometer, Rev. Sci Inst., 72, 2900-2908, **2001**

[118] Schwaneberg F.: Gasphasen-Infrarot-Photodissoziationspektroskopie von massenselektierten monohydrierten und nitrierten Kohlenstoffcluster-Anionen, PhD thesis, Freie Unviversität Berlin, **2014**

[119] Mathieu E.; Mémoire sur le mouvement vibratoire d’une membrane de forme elliptique, *Journal de mathématiques pures et appliqueés,*13,137-203, **1868**.

[120] Bosenberg W.R., Guyer D.R., Broadly tunable, single frequency optical parametric frequency-conversion system, *J. Opti. Soc. Am. B***,** 10, 1716-1722, **1993**.

[121] Heine N.: Vibrational Spectroscopy of Gaseous Hydrogen-bonded clusters: On the Role of Isomer Specificity and Anharmonicity, PhD Thesis, FU Berlin, **2014.**

[122] Depla D., Colpaert A., Eufinger K., Segers A., Haemers J., De Gryse R.: target behaviour during DC sputtering sputtering of silicon in an argon/nitrogen mixture, *Vaccum*, 66, 9, **2002**.

[123] Särhammar E., Strijkmans K., Nyberg T., van Steenberge S., Berg S., Depla D., A study of the process pressure influence in reactive sputtering aiming at hysteresis elimination,*Surf. Coat. Tech.*, 232, 357-361, **2013**.

[124] Depla D., Heirwegh S., Mahieu S., De Gryse R., Towards a more complete model for reactive magnetron sputtering, *J. Phys. D: Appl. Phys.,* 40, 1957-1965, **2007**.

[125] McKindra T., O′Keefe M., Cortez R., Reactive sputter-deposition of oxygenated amorphous carbon thin films in Ar/O2, *Diamond and related Materials,* 20, 509-515, **2011**.

[126] Jiang Z.Y., Xu X.-H., Wu H.-S., Zhang F.Q., Jin Z.-H.: First Principles Study of the Structure, Electronic State, and Stability of CmN_2 Clusters, *Int. J. Quant. Chem.,* 97, 876-882, **2004**.

[127] Belbruno J. J., Tang Z.-C., Smith R., Hobday S., The structure and energetics of carbon-nitrogen clusters, *Mol. Phys.* 99, 957-967,**2001**.

[128] Chen M., Liu J., Dang L., Zhang Q., Au C. T.: A Density Functional study on nitrogen doped carbon clusters Cn N3- (n=1-8), *J. Chem. Phys.* 121, 11661, **2004**.

[129] Maier J. P.: Electronic spectroscopy of Carbon Chains, *J. Phys. Chem. A.,* 102, 3462-3469, **1998**.

[130] Yang Z., Eichelberger B., Carpenter M.Y., Martinez O. Jr, Snow T.P., Bierbaum V.M.: Experimental and Theoretical Studies of Reactions between Atoms and carbanions of Interstellar relevance, *ApJ*, 723, 1325, **2010**.

[131]Yang Z., Snow T.P., Bierbaum V. M.,Computational Studies of gas phase reactions of carbon chain anions with N and O atoms, *Phys. Chem. Chem.Phys.,* 12, 13091-13098, **2010**.

[132] Diaz-Tendero S., Sánchez G., Hervieux P-A., Alcamí M., Martín F., Ionization Potentials, Dissociation Energies and Statistical Fragmentation of Neutral and Positively Charged Small Carbon Clusters, *Braz. J. Phys.* 36, 2B, **2006**

[133] Lépine F., Allouche A. R., Baguenard B., Bordas Ch., Aubert-Frécon M., Computed Eletron Affinity of Carbon Clusters C_n up to n = 20 and Fragmentation Energy of Anions, *J. Phys. Chem. A,* 106, 7177-7183, **2002**.

[134] Ito T., Otani Y., Namiki N., Electronic Separation of Carbon Dioxide by Ionization in Bifurcation Flow, *Aerosol and Air Quality Res.*, 4, 91-104, **2004**.

[135] Gennady L., Gutsev G.L., Bartlett J., Compton R. N., Electron affinities of CO_2, OCS and CS_2, *J. Chem. Phys.* 108, 6756, **1998**.

[136] Fulara J. Grutter M., Wyss M., Maier J.P., A 22E+<-X2P Electronic Absorption spectrum of CCO- in a Neon Matrix*, J. Phys. Chem.* A Vol 102, No 20, **1998**

[137] Comet′s poisonous tail, *New York Times*, february 08, **1910**.

[138] Atreya S.K.: The significance of trace constituents in the solar system, *Faraday Discuss*,147, 9-29, **2010**.

[139] Derenne D. , Coehlo C., Anquetil C., Szopa C., Rahman A.S.,McMillan P.F., Corà F., Pickard C.J.,Quirico E., Bonhomme C. New insigths into the structure and Chemistry of

Titan´s thiolins via ^{13}C and ^{15}N solid state nuclear magnetic resonance spectroscopy, *Icarus*, 221, 844-853, **2012**.

[140] Al Mogren M. M., El-Hazary A. A., Alkiali W. Z., A G3 structure of Carbon-Nitrogen Nanoclusters, *J. Chem. A*, 114, 12258-12268, **2010**.

[141] K. Chuchev, J.J. Belbruno: Electronic Structure of C_5N_2 and C_6N_2 and isoelectronic molecule, *J. chem. A*, 107, 1887-1890, **2003**.

[142] Thaddeus P., Gottlieb C. A., Gupta H., Brunken S., McCarthy, Agundez M., Guelin M., Cernicharo J.: Laboratory and astronomical detection of the negative molecular ion C3N-, *Astrophys. J.*, 677, 1132-1139, **2008**.

[143] Cernicharo J., Gelin M., Agundez M., McCarthy M.C., Thaddeus P.: Detection of C5N- and vibrational excited C6H in IRC +120216, *Astrophys. J. lett.,* 688, 83-86, **2008**.

[144] Jiang Z.Y., Xu X.-H., Wu H.-S., Jin Z.-H: Theoretical study of structures and stabilities of C_mN_2 (m = 1-14) ions, *Int. J. Mass Spec.,* 230, 33-39, **2003**.

[145] Manceron L, Le Quere A. M., Perchard J.-P.: Reinvestigation of the infrared spectrum of the tetraoxide anion in solid argon: structural implications*, J. Phys. Chem.*, 77, 801, **1973**.

[146] Maier G. Reisenauer H.P., Ruppel R.: Dicynocarbene and its isomers: A matrix Spectroscopy study, *J. Org. Chem,* 68, 2695, **2003**.

[147] Guo Z., Chen j., Chen J.-H., Wang P.-N., Li F-M., J. : DC Glow Discharge and its Reaction with a graphite Surface and the laser Ablation Plume of Graphite, *Kor.Phys, Soc.*, 23, 213-216,**1998**.

[148] Shimanouchi T.: Tables of Molecular vibrational Frequencies Consolidated Volume II, *J. Phys. Chem.*, 76, 993-1102, **1972**.

[149] Ming L. C., Zinin P., Meng Y., Liu X. R., Hong S.M., Xie L.Y. : A cubic phase of C_3N_4 synthesized in the diamond-anvil cell, *J. App. Phys.* , 99, 3, **2009**.

[150] Jeanmaire D.L.,Suchanski M. R., Van Duyne R. P., Resonance Raman Spectroelectrochemistry. I. The Tetracyanoethylene Anion Radical. *J.Am. Chem. Soc.*, 97, 7, **1975**.

[151] Frankowski Marcin, Spectroscopy of Unstable and Charged Species in Cryogenic Solid, PhD thesis, T.U. München ,**2006**.

[152] Brown T. S., Rienstra-Kiracofe J. C., Scheafer H. F.: A Systematic Application of density Functional Theory to Some Carbon-Containing Molecules and Their Anions, *J. Phys. Chem. A*, 103, 4065-4077, **1999**.

[153] Zergioti I., Alexandrou I., Sfounis A. Amaratunga G.A.J., Fotakis C., Velegrakis M. Synthesis of C3N4+ by the combination of laser ablation of graphite and N_2 molecular beam, *Appl. Sur. Sc.*, 197, 387-392, **2002**.

[154] Zhu X.: Geometries and electronic properties of carbon-nitrogen clusters C_8N_4 and $C_8N_4^{+-}$, *Spec. Ac. P. Mol. Part A*, 71, 1825-1829, **2009**.

[155] Kertes M., Koller J., Azman A.: A Initio Hartree-Fock Crystal Orbital Studies.II. Energy Bands of an Infinite Carbon chain.*J Chem. Phys.*, 68, 2779-2782, **1978**.

[156] Whittaker A. G.: Carbon a new view of high-temperature behavior, *Science*, 200, 763-764, **1978**.

[157] Tulej M., kirkwood D. A., Pachkov M., Maier J. P.: Gas-phase transitions of carbon chain anions coinciding with diffuse interstellar bands, *Astr. Phys. J.,* 506, 69, **1998**.

[159] Yang S., Taylor K.J., Craycraft M.J., Conceicao J., Pettiette C.L., Chesnovsky, Smalley R.E. : UPS of 2-30-atom carbon clusters: Chains and Rings, *Chem. Phys. Lett.*, 114, 431-436, **1988**.

[160] Ohara M. Kassuya D., Shiromaru H., Achiba Y.: Resonance-Enhanced Multiphoton Electron Detachment (REMPED) Study of Carbon Anions up to C_{21}^-, *J. Phys. Chem. A.*, 104, 8622-8626, **2000**.

[161] Faibis A. Kanter E. P. Tack L.L., Bakke E., Zabranski B. J.: Geometrical structure of carbon ion (C_3^+), *J. Phys Chem.,* 91, 6445-6447, **1987**.

[162] Szczepanski J., Auerbach E., Vala M., C_6^- Carbon Cluster Anion: An infrared Absorption and Resonance raman Isotopic Study*, J. Phys. Chem.A.,* 101, 9296-9301, **1997**.

[163] Szczepanski J., Hodyss R., Vala M.: Isotopic Infrared Absorption Study of C_5^-, C_7^-, and C_9^- Carbon Cluster Anions in Argon Matrices, *J. Phys Chem. A.*, 102, 8300-8304, **1998**.

[164] Freivogel P., Grutter M., Forney D.: Infrared bands of mass-selected carbon chains C_n (n=8-12) and C_n- (n=5-10,12) in neon matrices, *Chem. Phys.*, 216, , p 401-406, **1997**.

[165] Hastie J.W., Hauge R. H., Margrave J.L.: Spectroscopy in Inorganic Chemistry Band 1, *ed C.N.R. Rao and John R. Ferraro (New York Academic Press)*, p58-98, **1970**.

[166] Grundy W. M., Buie M. W. : Distribution and Evolution of CH4, N 2, and CO Ices on Pluto's Surface: 1995 to 1998, *Icarus*, Volume 153, 248-263, **2001**.

[167] Irvine, W. M. et al: "Confirmation of the Existence of Two New Interstellar Molecules: C_3H and C_3O", *Bulletin of the American Astronomical Society* 16, 877, **1984**.

[168] Ohishi M.,Suzuki H., Íschikawa S-I, Yamada C., Kanamori H., Irvine W. M. , Brown R. D., Godfrey P.D., Kaifu N: Detection of a new carbon chain molecule CCO, *Astr. J.*, Part 2 Letters, 380, 39-42, **1991**.

[169] Oshima Y., Endo Y., Ogata T.: Fourier-transform microwave spectroscopy of triplet carbon monoides, C_2O, C_4O, C_6O and C_8O, *J. Chem. Phys.* 102, 1493, **1995**.

[170] Ogata T., Oshima Y., Endo Y.: Rotational Spectra and Structures of carbon monoxides C_5O C_7O C_9O, *J. Am. Soc.,* 117, 3593, **1995**.

[171] Aoki K.: Possible interstellar anions: C_nS^- and C_nO^- (n = 2-8), *Adv. Sp. Res.*, 47, 2004-2008, **2011**.

[172] Oakes, J.M.; Jones, M.E.; Bierbaum, V.M.; Ellison, G.B., Photoelectron spectroscopy of CCO^- and $HCCO^-$, *J. Phys. Chem.*, 87, 4810, **1983** .

[173] AbsRiaplov, E.; Wyss, M.; Lakin, N.M.; Maier, J.P.: Electronic Absorption Spectra of C_4O^- and C_4S^- in Neon Natrix, *J. Phys. Chem. A*, 105, 20, 4894, **2001**.

[174] Garand, E.; Yacovitch, T.I.; Neumark, D.M., Slow photoelectron velocity-map imaging spectroscopy of C_3O^- and C_3S^-, *J. Chem. Phys.*, 131, 054312, **2009**.

[175] A. A. Korkin Balkova A., Bartlett R. J., Boyd R. J., Schleyer P. v. R. : The 28-Electron Tetraatomic Molecules: N_4, CN_2O, BFN_2, C_2O_2, B_2F_2, CBFO, C_2FN, and BNO_2. Challenges for Computational and Experimental Chemistry, *J. Phys. Chem.*, 100, 5702, **1996** .

[176] Burenin A. V. Karyakin E. N., Krupnov N., Shapin S. M.: Microwave observation of the vibration-rotation spectrum of the nonpolar C_3O_2 molecule, *J. Mol. Spectrosc.* 78, 181-184, **1979**.

[177] Rabalais and al.: Electron spectroscopy, *D. A. Shirley Ed.*, *North holland publishing Co.*, Amsterdam, **1972**.

[178] Janoschek R.: Theoritical Studies on Heterocumulated Double Bond Syytems, *Sulfur. Rep.* 21, 373, **1999**.

[179] Thomson W. E., Jacobs M. E.: The vibrational spectra of molecular ions isolated in solid neon VII. CO^+, $C_2O_2^+$ and C_2Oâa^2, *J. Chem. Phys.,* 95, 2, 735, **1991**.

[180] Jacobs M.E., thomson W.E., The production and spectroscopy of Molecular Ions Isolated in Solid Neon, *Res. Chem. Intermed.,* 12, 1, 33, **1989**.

[181] Ameida D., Bacchus-Montabonel M.-C., Ferreira Da Silva F., Garcia G., Limao-Vieira P.: Potassium-uracil/thymine ring cleavage enhancement as studied in electron transfer experiments and theoritical calculations, *J. Phys. Chem*., 118, 6547-52, **2014**.

[182] Li W.K., Baker J.,Radom L.: Rearrangement of the Fulminate Anion (CNO^-) to the Cyanate Anio (OCN^-). Possible Intermediacy of the Oxazirinyl Anion, *Austr. J. Chem.* 39, 913-921, **1986**.

[183] Brünken, S., Belloche A., Martin S., Verheyen L., Menten K.M.: Interstellar HOCN in the Galactic center region, *Astronomy &Astrophysics,* 516, 109, **2010**.

[184] Marcelino, Núria Cernicharo J., Tercero B., Roueff E.: Discovery of fulminic acid, HCNO, in dark clouds, *Astrophysical Journal,* 690, 27–30, **2009**.

[185] Hollis, J. M. , Lovas F.J., Remijan A.J., Jewell P.R., Ilyushin V.V., Kleiner I.: Detection of Acetamide (CH_3CONH_2): The Largest Interstellar Molecule with a Peptide Bond,*Astrophysical Journal,* 643, 25–28, **2006**.

[186] Gruebele M., Polak M., sayk ally R. J.: Velocity modulation infrared laser spectroscopy of negative ions. The Î½3, Î½3+Î½1â^'Î½1, Î½3+Î½2â^'Î½2, and Î½3+2Î½2â^'2Î½2 bands of cyanate (NCOâ^'), *J. Chem. Phys.,* 86, 6631, **1987**.

[187] Sumiyoshi Y.; Takada H.; Endo Y., FTMW spectroscopy of the NC_2O and NC_3O radicals and ab initio calculations,*Chem. Phys. Lett.,* 387, 1-3, 116, **2004**.

[188] Cronin J.R., Pizzarello S.: Amino acids of the murchison meteorite.III. Seven carbon acyclic primary a-amino alkanoic acids, *Geochim. Cosmochim. Acta,* 50, 2419, **1986**.

[189] Elsila J. E., Glavin D. P., Dworkin J.P.: Cometary glycin detected in sample returned by Stradust, *Met. Plan. Sc*. 44, 1323-1330, **2009**.

[190] Lehmann K.K., Scoles G.: The Ultimate Spectroscopic Matrix?, *Science*, 279, 2065, **1998**.

[191] Toennies J. P., Vilesov A. F.: Superfluid Helium droplets: A uniquely Cold Nanomatrix for Molecules and Molecular Complexes, *Ang. Chem.,* 43, 2622, **2004**.

[192] Hartmann M., Lindinger A., Toennis J.P., Vilesov A.F.: Laser-induced fluorescence spectroscopy of van der Waals complexes of tetracene-Ar_N $(N \leq 5)$ and pentacene-Ar within ultracold liquid He droplets, *Chem. Phys*., 239, 139, **1998**.

[193] Ren Y., Kresin V.V.: Suppressing the fragmentation of fragile molecules in helium nanodroplets by co-embedded with water: Possible role of the electric dipole moment, *J. Chem. Phys.* 128, 074303, **2007**.

[194] Ferreira da Silva F., Denifl S., Märk T.D.,Ellis A.M., Scheier P: Electron attachment to amino acid clusters in helium nanodroplets: glycine alanine serine, *J Chem. Phys.,* 132, 214306, **2010**.

[195] Denifl. S., Ferreira da Silva F., Zappa F., Märk T.D., Scheier P.: Electron impact ionization studies with thze amino acid valine in the gas phase and (hydrated) in helium droplets, *Eur. Phys. J. D*, 51, 73-79, **2009**.

[196] Bellina B., Merthe D.J., Kresin V.V.: Proton transfer in histidine-tryptophan heterodimers embededded in helium droplets, *J. Chem. Phys*, 142, 114306, **2015**.

[197] Wu C.C., Lin C-K.,Chang H-C, Jiang J-C., Kuo J-L., Klein M.L.: Protonated clathrate cages enclosing neutral water molecules: $H^+(H_2O)_{21}$ and $H^+(H_2O)_{28}$, *J.Chem. Phys.* 122, 074315, **2005**.

[198] Lindinger A., Toennis J.P., Vilesov A.F.: High resolution vibronic spectra of the amino acids tryptophan and tyrosin in 0.38K cold helium droplets, *J.Chem.Phys.*, 110,1429, **1999**.

[199] Ren Y., Moro R., Kresin V.V.: Changing the fragmentation pattern of molecules in helium nanodroplets by co-embedded with water, *Eur Phys. J.D*, 43, 2622, **2004**.

[200] Liu b., Brønsted S., Nielsen P., Hvelplund P., Zettergren H., Cederquist B., Manil B., Huber B.H.: Collision-Induced Dissociation of Hydrated Adenosine Monophosphate Nucleotide Ions: Protection of the Ion in Water Nanoclusters, *Phys. Rev. Lett.,* 97, 133401 (**2006**).

[201] Zang J., Germann M.W.: Characterisation of Secondary Amide Peptides Bonds Isomerization: Thermodynamics amd kinetics from 2D NMR Spectroscopy, *Biopolymers*, 95**,** 755-762, **2011**.

[202] Schroeder G.K. and Wolfenden R.: The Rate Enhancement Produced by the ribosome: An Improved Model, *Biochemistry*, 46, 4037, **2007**.

[203] Sievers A., Beringer M., Rodina M.V., Wolfenden R.: The ribosome as an entropy trap, *Proc Natl. Acad. Sci.,* U.S.A., 101, 7897, **2004.**

ABSTRACT

Anions in gas phase are now attracting renewed attention from astronomers. Slightly over a decade ago, the discovery of negatively charged interstellar molecules reoriented the expectations of the interstellar chemistry. Space contains anions. Propositions of potential anionic interstellar species were no longer discredited, but rather flourished. Astronomers require laboratory data for comparison with telescope measurements. Valuable experimental absorption results on anions in the gas phase remain thin and spectroscopic properties of anions, which have been not yet investigated, are necessary in order to identify interstellar molecules. The list of molecules, which have been identified in Space, contains several organic molecules as amino acids, already observed on comets and meteorites. Proteinogenic amino acids are considered as prebiotic molecules and their origin on Earth is of considerable scientific interest. This work attempts to enhance the infrared spectroscopic absorption information on negatively charged systems and to apprehend the chemistry leading to the formation of organic molecules in the gas phase.

In this work, the IR absorption spectra in the gas phase in the region of 1200 to 2400 cm^{-1} of more than 25 anions, which have been not yet investigated in this region, are reported and examined. This concerns the clusters including two and four nitrogen atoms ($C_xN_2^-$ and $C_xN_4^-$), one or two oxygen atoms (C_xO^- and $C_xO_2^-$) and one oxygen and one nitrogen atoms (C_3NO^-). This succession of anions is carried out in order to approach the organic molecules and understand the successively steps leading to their formation in the gas phase.

This work demonstrates the prolifically synergy of technologies. The sputtering of carbon target in gaseous oxygen and nitrogen reveals great facilities to produce ions relevant for astronomers. The low density of the charged sputter yield is investigated by the advanced Infrared Photodissocition (IRPD) method, which utilizes a weak-bonded messenger strategy.

The power of computational quantum methods is solicited in order to achieve in-depth interpretation of the results. The well-established B3LYP with cc-aug-pVTZ method allows for the identifications of anions investigated. The geometries and the stretch modes responsible for the absorptions of the anions are presented. The calculations were also employed to predict several polyhydrogenated systems and foresee the formation of organic molecules. The negatively charged formamide, the smallest molecule presenting a peptide bond, is predictable in a case of the sputtering experiment in added presence of hydrogen.

A complementary experiment, which performed the embedding of amino acids in helium droplets, is also presented. The electron impact ionization allows for detecting positively charged glycine, valine, histidine, tryptophan and their principal fragments. Monomers, polymers with up to four amino acids are reported. Heterodimers of tryptophan and valine or histidine are observed as well as heterodimers of included fragments. The ability of these associations of molecules to form complexes with water is examined. The presence of complexes corresponding to the release of water molecules suggests the formation of peptide bonds.

Finally to conclude, within the formation of molecules in the gas phase the attention is focused on the amino acids. The formation of glycine and alanine is predicted disfavored in the gas phase. Reported successful synthesis of glycine invites the consideration of potential complementary strategy to attempt the formation of these amino acids.

Zusammenfassung

Anionen in der Gasphase ziehen seit kurzem wieder die Aufmerksamkeit der Astronomen auf sich. Vor vierzehn Jahren hat die Entdeckung von negativ geladenen interstellaren Molekülen die Vorstellung der Interstellaren Chemie neu ausgerichtet. Das Weltall enthält Anionen. Die Behauptungen von potentiellen anionisch interstellaren Molekülen wurden nicht mehr diskreditiert, sondern vermehrten sich. Dafür benötigen die Astronomen Daten aus dem Labor, um Vergleiche mit den Messungen aus Teleskopen anzustellen. Die nützlichen experimentellen Ergebnisse für Anionen in der Gasphase bleiben begrenzt, und die spektroskopische Eigenschaft von Anionen, die bisher nicht erforscht ist, ist erforderlich, um interstellare Moleküle zu identifizieren. Die Liste von Molekülen, die bereits im Weltall identifiziert wurden, enthält organische Moleküle, wie Aminosäuren, die auf Meteoriten und Kometen entdeckt wurden. Die proteinogenen Aminosäuren werden als prebiotische Moleküle betrachtet und deren Ursprung auf der Erde ist von erheblichem Interesse. Diese Arbeit stellt einen Versuch dar, die Kenntnisse über die spektroskopische Absorption von negativ geladenen Molekülen zu erweitern und die Chemie, die zur Bildung organischer Moleküle führt, zu untersuchen.

In dieser Arbeit werden die IR Absorptionsspektren in der Gasphase in der Region von 1200 cm^{-1} bis 2400 cm^{-1} von mehr als 25 Anionen, die noch nicht in dieser Region untersucht worden sind, vorgestellt. Das betrifft Kohlenstoffcluster, die mit zwei und vier Stickstoff Atomen($C_xN_2^-$ and $C_xN_4^-$), mit einem und zwei Sauerstoff (C_xO^- and $C_xO_2^-$) oder mit einem Sauerstoff und einem Stickstoff Atom (C_3NO^-) dotiert sind. Die Reihenfolge von untersuchten Systemen ist aufgestellt, um die sukzessiven Stufen, die zur Bildung organischer Moleküle führen, zu erfassen.

Diese Arbeit beweist die produktive Zusammenwirkung von Technologien. Der Sputterprozess in Sauerstoff- und Stickstoffatmosphäre beweist die Relevanz der Produktion von Molekülen für die Astronomie. Die geringe Dichte von untersuchten geladenen Systemen aus der Sputterquelle wird bei Infrarot Photodissociation untersucht, die einen schwachen gebundenen Komplex als Indikator benutzt. Die etablierte Berechnungsmethode B3LYP mit cc-aug-pVTZ fördert die Identifikation der untersuchten Anionen. Die Geometrie und die in den IR Absorptionen involvierte Streckschwingung werden präsentiert. Es werden ebenfalls Rechnungen für etliche polyhydrogenierte Anionen durchgeführt, um Bildungen organischer Moleküle vorherzusehen.

Ein zusätzliches Experiment, das in Heliumtröpfchen eingebettete Aminosäure ermöglicht, wird präsentiert. Die Elektronenstoßionizierung gewährt die Detektion von positiv geladenem Glycin, Valin, Histidin, Tryptophan und ihren Hauptfragementen. Monomere, Polymere, die bis vier Aminosäuren enthalten, werden beobachtet. Heterodimere von Tryptophan und Valin oder Histidin werden so wie Heterodimere, die Fragmente von Aminosäure beinhalten, beobachtet. Die Eignung von Molekülen, um Komplexe mit Wassermolekülen zu binden, wird untersucht. Die Beobachtung von Komplexen, die einem Verlust von Wassermolekülen entsprechen, wies auf die Möglichkeit von Peptidbindungen hin.

Schlussendlich, richtet sich bei der Molekülbildung in der Gasphase die Aufmerksamkeit auf die Aminosäure. Die Bildung von Glycin und Alanin sind als unterprivilegiert in der Gasphase vorhergesagt. Vorhergehende erfolgreiche Glycin Synthesen führen zur Berücksichtigung komplementärer Strategien, um diese Aminosäure zu synthetisieren.

Acknowledgments

The years I have spent at the Freie Universtität of Berlin were extremely enriching for me on a scientific level as well as on a cultural and human level. I am appreciative to all the people who contributed to this project. It is through their support that this dissertation was made possible.

I am deeply grateful to Professor Lugder Wöste for giving me the opportunity to work in his laboratory and providing the conditions necessary for a productive work. His constant encouragement and support as well as his youthful mind and enthusiasm contribute greatly to the creative and positive atmosphere of the AG Wöste. I am deeply thankful to Eva Cristina Stanca-Kaposta for thematic guidance and competent support. Her engagement and perseverance never failed to assist in every phase of my work.

I am particularly grateful to Professor Knut R. Asmis, who permitted the use of his IR-PD experimental setup. His competent team allowed for the success of the measurement period. I am greatly thankful the Xaowei Song for her efficient support and help, Matias Fagiani for the practical teaching, and Tim Esser for his help with the laser system.

I am also greatly thankful to Albrecht Lindinger for giving me the opportunity to take measurements using his helium droplets source. His competence in the field greatly facilitated the efficiency of the work. For mounting the apparatus I would like to thank Georg Achazi.

I am grateful and indebted to all the colleges who never refused my requests for assistance. I want to thank Doctor Falko Schwaneberg for making himself available even far outside official working hours. His passionate knowledge of the rules of physics, as well as his courtesy and orderly attitude rendered the times shared with him especially enriching. I am also grateful to Frank Hagemann for his particularly clever advices as well as his sympathy, Adrian Dufour for sharing his deep theoretical knowledge, Alexander Patas for his helpful disposition, even for the chemistry labor inventory. I must also express my gratitude to Frau Odeh for her assistance with organization and administrative skills.

For advice and corrections concerning the English language I have to thank at first Kathleen Garner but also Pierce Warnecke, Paul Roth, Anne-Laure Arsac and Lory Dell'anna. For the realization microscopic picture I am grateful to Aouefa Amoussouvi. Sincer thanks go to Ingrid Sabatier and Stephan Schwarz from ISSSresearch for an informal and helpful support.

A special thanks to my family. I would like to thank all my friends who supported me in writing, and encouraged me to strive toward my goals.